Characterization of Electrochemically Formed Coloured Passive Layers on Titanium and

Zirconium: Optical, Surface and Corrosion Properties

By

Rebecca Jane Holmberg

A thesis submitted to the Graduate Program in Chemistry

in conformity with the requirements for the

Degree of Master of Science

Queen's University

Kingston, Ontario, Canada

September, 2011

Abstract

Electrochemically formed passive layers on titanium and zirconium, and their optical, surface and corrosion properties are presented. With the use of higher applied AC voltages, the passive layers become thicker and more protective of the underlying metal, as determined from thickness measurements by scanning electron microscopy and focused ion beam instruments, as well as passive layer corrosion resistance measurements by electrochemical polarization curve and inductively coupled plasma mass spectrometry experiments. The surface morphology of all samples was studied with atomic force microscopy, profilometry, visible light microscopy, transmission electron microscopy, and finally electron backscattered diffraction experiments. The passive layers were found to be uniform in their surface structure with no cracks or fractures. However, the samples prepared at V_{AC} = 60-80 V showed defects, which were increasingly prevalent at higher V_{AC}. These defects are thought to be attributed to a process of localized electrochemical breakdown. The aforementioned increase in corrosion resistance is in spite of the defects, which were observed for the samples prepared at V_{AC} = 60-80 V. Surface morphology, in relation to optical properties, was also investigated through reflectance spectroscopy measurements. A correlation between grain colouration and light reflected from the sample surface was observed through measurements using visible light microscopy as well as near infrared ultraviolet visible reflectance spectroscopy. These experiments showed a red-shift of wavelength maxima (λ_{max}) values as voltages, and therefore thickness, were increased. This is the reason that different colours are seen for different thicknesses; the red shift causes different wavelengths to be reflected constructively and destructively. Overall, these passive layers are protective of an already remarkable metal

and, with greater knowledge of their properties, their potential may be observed in a wide

range of applications.

Acknowledgements

I would like to present the initial and most substantial gratitude towards my supervisor Gregory Jerkiewicz. He has been an excellent support from my undergraduate studies up until the very end of my Masters; I would never have entered graduate school without his encouragement. I will always look back fondly, and appreciate the kindness and generosity bestowed upon me by Dr. Jerkiewicz. I would also like to thank my co-supervisor Diane Beauchemin for being not only an excellent support but an inspiring teacher as well. I am grateful to my committee members, Dr. Simon Hesp and Dr. Guojun Liu, for their precious time, valuable advice and suggestions.

I would like to express my gratitude to my colleagues and friends in Dr. Jerkiewicz's laboratory: Mr. Mohammad Alsabet, Mr. Andrew Munro, Mr. Yoseif Makonnen, Miss Julia van Drunen, and Dr. Liyan Xing for their continued aid, friendship and constant entertainment both inside of the lab and out.

I would finally like to recognize some amazing individuals within the Chemistry Department: Bill Newstead, Tom Hunter and Igor Kozin for always being amazing to work with and inspirational teaching leaders.

Table of Contents

List of Tables

List of Figures

List of Symbols and Abbreviations

Zr – zirconium

Ti – titanium

Pt – platinum

W – tungsten

AC – alternating current

DC – direct current

vis – visible

NIR – near infrared

UV – ultraviolet

K – Kelvin

°C – Celsius

T_m – melting temperature

T_f – freezing temperature

h – heat transfer coefficient

ρ – density or reflectivity

τ – transmittivity

α – absorptivity

δ – resolution

K – Kelvin

J – joule

Ω – ohm (resistance)

Hz – Hertz

W – watt

λ – wavelength

$\mathring{A}$ – angstroms

n – refractive index

R_a – roughness

UHV – ultra high vacuum

E_{corr} – corrosion potential

j_{corr} – corrosion current density

E_a – redox potential of the anode

E_c – redox potential of the cathode

V – volts

R – specular reflectivity

T – transmittance

wt. % – weight percent

AFM – atomic force microscopy

SEM – scanning electron microscopy

TEM – transmission electron microscopy

Ga^+ – gallium ion

LMIS – liquid metal ion source

FIB – focused ion beam

EBSD – electron backscatter diffraction

VLM – visible light microscopy

ICP-MS – inductively coupled plasma mass spectrometry

Ar – argon

ETV – electrothermal vaporization

LA – laser ablation

XPS – x-ray photoelectron spectroscopy

FCC – face centered cubic

BCC – body centered cubic

HCP – hexagonal close packed

Chapter 1   Introduction

Electrochemistry is a field of research that has crucial implications towards prominent technologies such as: fuel cells, solar cells, batteries, semiconductors, and corrosion studies, among others. Through further in-depth knowledge of electrochemical processes that occur at electrode interfaces, there can be staggering new improvements to many different important technologies in creating a greener enviroment, as well as a more efficient society. Through employing electrochemistry in the creation of better materials, light can be shed on the field of research and its many applications for more energy efficient and cleaner industrial processes.

Titanium (Ti) and zirconium (Zr) are valve metals that are known to develop coloured passive layers through oxidation at elevated temperatures, as well as through the application of direct current or alternating current in aqueous electrolytes. Previously, metals were passivated using thermal methods, where they were placed in a closed environment of oxygen and argon and heated to very high temperatures (800-2000ºC) in order to facilitate oxidation at the surface of the metal.[1,2] In the case of titanium and zirconium, this process produced coloured passive layers that were only comprised of a range of blue, purple, and brown colours. This was a very time-consuming process, taking hours and therefore requiring a large amount of energy input. When using electrochemical oxidation, a highly variable spectrum of colours is observed, this is obtained at room temperature in seconds. Passive layers owe their distinctive colouration to iridescence, which is the effect caused by incident light waves reflecting at upper and lower boundaries of a thin film, constructively interfering to form a new wave. This effect is further discussed in the section on colour. In particular, through the application

of alternating current (AC) voltage in aqueous electrolyte, there is a particularly wide

spectrum of colours observed, as is illustrated in Figures 1 and 2.
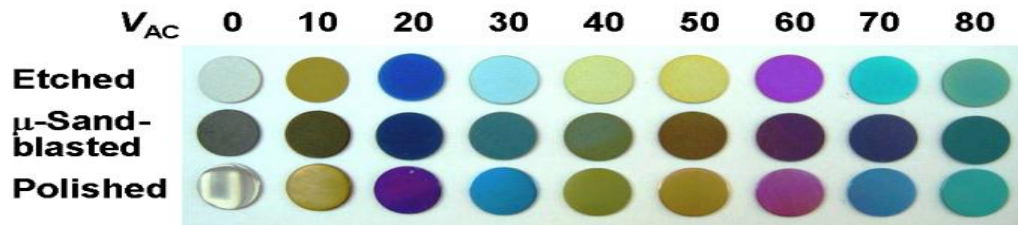
Figure 1. Titanium samples which were surface treated by etching, micro sandblasting or

polishing.[3] Coloured samples were passivated at V_{AC} = 10, 20, ..., 80 V.
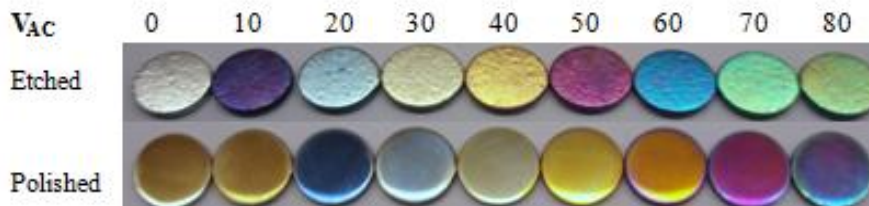
Figure 2. Zirconium samples which were surface treated with etching or polishing.

Coloured samples were passivated at V_{AC} = 10, 20, ..., 80 V.

The reason that different colours of passive layers are observed at different

voltages, is that film thickness changes with applied voltage. With higher applied voltage

values, the thickness of the passive layer increases.[4] These results are shown in

Figure 3. This will occur until a voltage where electrochemical breakdown occurs, which

happens to be over 80 V.
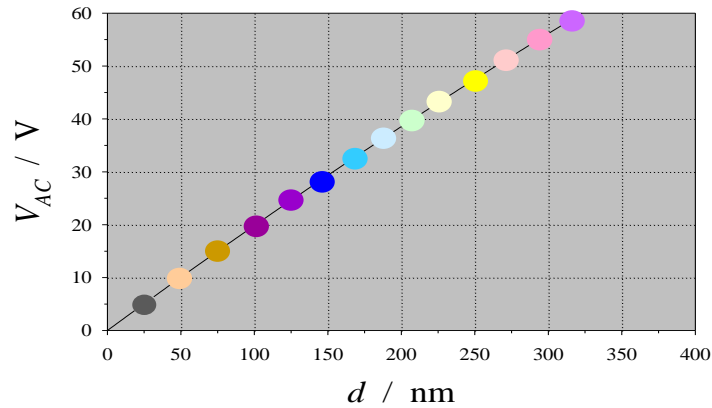
Figure 3. Thicknesses of passive layers on titanium samples with respect to voltage applied.[5]

For Ti, this thickness is dependent upon both the rate of oxide formation and the rate of dissolution caused by the chemically etching fluoride-containing ions in the electrolyte solution.[6] Thus, for this metal, a sample can be passivated at a certain V_{AC}, and re-passivated at another V_{AC}, consistently resulting in a specific thickness for a particular value of applied AC voltage, as illustrated in Figure 4.
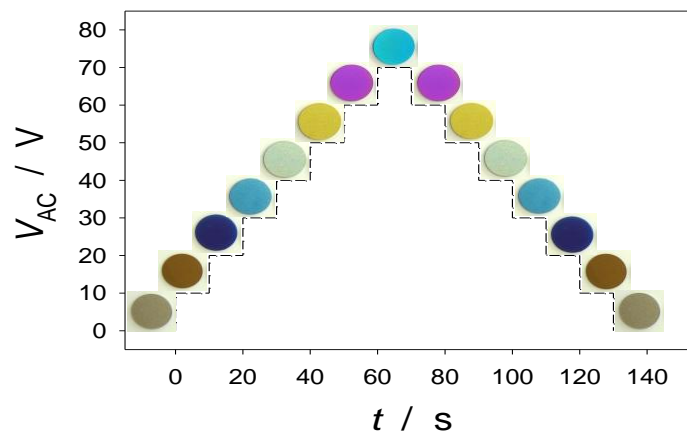
Figure 4. Thicknesses (colours) of passive layers on titanium with respect to voltage applied over time.[6]

These metals have low density (ρ), high melting temperature (T_m) and freezing temperature (T_f), low heat transfer coefficient (h), high fire resistance, excellent mechanical properties (strength, ductility, low thermal expansion coefficient), good performance at low and high temperatures, excellent resistance to abrasion and resistance to various forms of corrosion (including corrosion in halide-containing media, bio-corrosion, etc.). The main importance surrounding the use of Ti and Zr lies within their unique properties. Most importantly, Ti and Zr develop a surface passive layer, which becomes intrinsic protection. Therefore, when used in many applications (horology, spectacle frames and jewelry (aesthetics), aerospace and aviation industry (airframe components), architecture (structures, roofing, window frames), sporting equipment (mountain bikes, golf clubs), nuclear industry (waste storage containers), medicine, dentistry and orthodontics (medical and dental implants), electrocatalysis (anode materials), metal extraction equipment, heat exchangers, seawater piping, steam turbines, gas turbine engines, etc.), these passive layers would greatly improve the material for their purposes by offering corrosion protection. The interest in colour is also due to the fact that paint will not adhere to these two metals, therefore another colouration method is required.

Chapter 2   Literature Review

2.1 Overview

Titanium and zirconium are materials that are commonly employed in many industries, not only for manufacture, but often even the equipment employed in industry is made from such materials. This is because of their incredible properties. Titanium and zirconium have made names for themselves within many industries for their strength, resistance to abrasion and corrosion and their other valuable mechanical properties. Most importantly for this project, these metals both develop surface oxide layers for intrinsic protection from abrasion as well as corrosion and bio-corrosion. As will become apparent, these metals can be studied using electrochemical techniques in order to improve the depth of knowledge about their properties, but also, remarkably, electrochemistry can be employed to improve some of these properties. Thus, from this project, the immense variability of electrochemistry as an area of research can be seen.

2.1.1   Titanium

Titanium is the 9th most abundant element in the crust of the Earth, while also being the 4th most abundant structural metal.[7]   Titanium occurs in the minerals *rutile, ilmenite,* and *sphene*, and is present in titanates and many types of iron ore.[8]   These minerals can be found all over the world, more specifically in North America, South Africa, Australia, Norway, Malaysia, India and China. Also, Ti can be found in coal ash, certain plants, and within the human body.[8] The nickname "valve metal" is used for Ti, as well as Zr and many other metals. This nickname derives from passivating metals that

could only pass current in one direction, resulting in the ability of the passive layer to not be reduced (in moderate cathodic currents).[9]

The widespread employment of this metal can be attributed to properties such as: high tensile strength (comparable to martensitic stainless steels and better than austenitic or ferritic stainless steels),[7] low density, nonmagnetic properties, high melting point, as well as the fact that it can be forged or wrought by standard techniques, it can be joined through many different means, and it is machinable, as shown in Figure 5. The boiling temperature of Ti is 3533 K, and its melting point is 1941 K.[7] Titanium has an atomic mass of 47.867 g/mol and a density of 4.506 g/cm^3.[7] These properties illustrate that Ti is 45% lighter than steel.[10] It also has the highest strength to weight ratio of any metal.[7] Titanium has an oxidation state of +4, and is able to obtain states of +3 and +2. The isotopes of Ti are: ^{46}Ti, ^{47}Ti, ^{48}Ti (most abundant), ^{49}Ti, and finally ^{50}Ti. Titanium is very corrosion resistant, including resistance to both acidic and saline solutions. This resistance to common corrosive media allows Ti to be a crucial material in areas that rely on strength as well as a lack of degradation in solution. Titanium also develops a thin oxide film on its surface for further protection.[11] The naturally formed oxide is responsible for the corrosion-resistant properties of Ti, and thus has been extensively studied. The thickness of the oxide grows over time, from one to hundreds of nanometres, and is mainly composed of non-crystalline TiO$_2$.[12,13,14,15] It is not resistant to fluorine-containing compounds such as hydrofluoric acid, which therefore can be used as a chemical etchant for this metal.
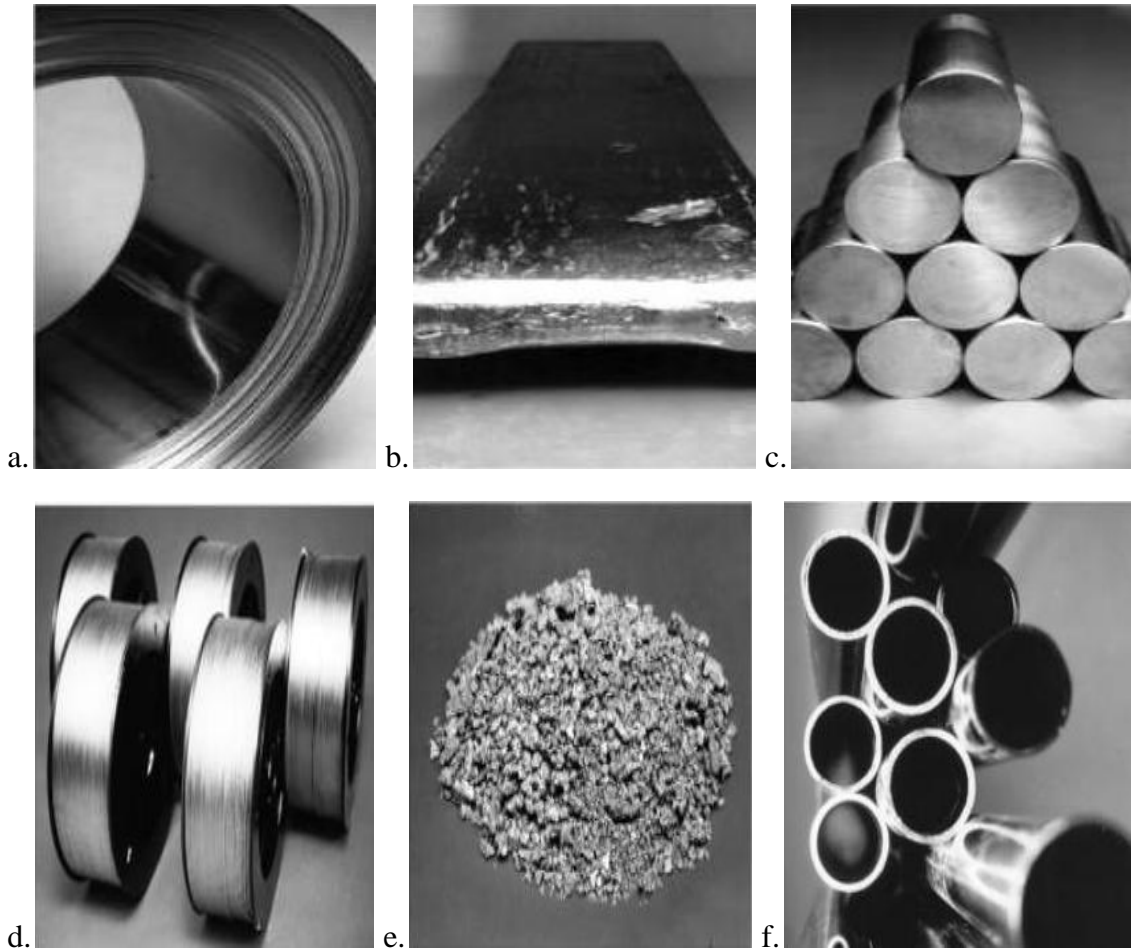
Figure 5. Titanium and Ti alloy product forms: (a.) strip, (b.) slab, (c.) billet, (d.) wire, (e.) sponge, (f.) tube.[7]

Very pure Ti is produced through thermal decomposition of TiI_4 under vacuum conditions, and the resulting Ti crystals are then deposited on a hot thin wire. Another method of production is through calcium chloride electrolysis in the presence of TiO, calcium reacting with the oxide to form Ti,[16] as can be seen in the cathodic reaction below.

$$TiO + Ca^{2+} \rightarrow Ti + CaO + 2e^-$$
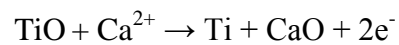
Titanium dioxide is most often found as a white powder, whereas pure titanium dioxide is transparent and has a very high index of refraction, with an optical dispersion higher than diamond.[8]

The structures of Ti can be defined as either alpha (hexagonal close packed, HCP), or beta (body centered cubic, BCC). Beta Ti is only found at very high temperatures (above 1153 K) or within certain alloys.[8] These crystal conformations are akin to those of Zr. Cubic lattices allow slippage to occur more easily, meaning that HCP crystals are less ductile than cubic and face centered cubic (FCC) lattices.[17] Thus, Ti and Zr are unlikely to deform under expansion and contraction due to their crystal structures. All of the properties of Ti make it a very desirable metal to work with.
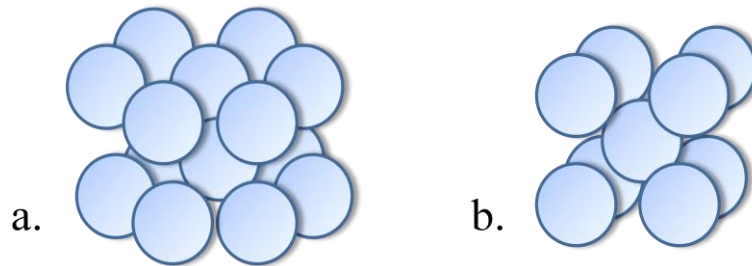
Figure 6. Appearance of Ti and Zr crystal structures at the atomic level. (a.) Hexagonal close packed, (b.) Body centered cubic.[7]

The applications of Ti metal span over a broad range, and fall under categories such as: aerospace, power generation, chemical processing, nuclear waste storage, automotive and marine, oil/gas and petroleum processing, biomedical, architectural, sports, as well as apparel and jewellery. High purity Ti is employed in applications

requiring corrosion resistance, whereas low purity and alloyed Ti (ex. Ti_6Al_4V) materials are employed in applications where strength is prioritized. Pure Ti application examples would be: armoured vehicle materials, heat exchangers, reactor vessels, and medical and dental implants. Titanium alloys would be, contrastingly, employed for offshore drilling applications and geothermal piping.[18] There are also applications requiring both corrosion resistance and strength properties: automotive, marine and aerospace industries. Since both corrosion resistance and strength are needed, a combination of factors must be considered to optimize the Ti material for these applications. Titanium and Zr have been alloyed together as well as with other metals. Tensile strength and hardness tests performed by Kobayashi revealed that alloying Ti and Zr together in equal mole fractions presented the best results.[19] Titanium oxide is also employed in many areas, such as: use as a photoanode,[4] as sunscreen, food colouring and in paints. As can be seen, the mechanical properties of Ti allow for its use in many applications that require a strong and corrosion resistant metal.

2.1.2 Zirconium

Zirconium is the 19th most abundant element on the planet,[20] while also being the 11th most abundant structural metal. The mineral source of Zr is zircon, $ZrSiO_4$, which is found as either a dark powder, or as a gray metallic crystal. This mineral is found in North America, Australia, South Africa, as well as other regions.

Like Ti, Zr has mechanical properties that are remarkable for many applications. It has an atomic mass of 91.224 g/mol and density of 6.52 g/cm^3 at standard temperature

and pressure. These properties indicate that Zr, like Ti, is also lighter than steel.[21] Zirconium most often has an oxidation state of +4, and is able to obtain states of +3 and +2. The boiling temperature of Zr is 4682 K, and its melting point is 2128 K.[22] The isotopes of Zr are: ^{90}Zr (most abundant), ^{91}Zr, ^{92}Zr, ^{94}Zr, and finally ^{96}Zr. Like Ti (see Figure 6), Zr has an alpha crystalline structure, which is hexagonal close packed, and a beta crystalline structure, which is body centered cubic, and is found at very high temperatures (1136 K).[23] Zirconium is very corrosion-resistant, and develops an oxide film on its surface for further protection, like Ti. Zirconium is resistant to attack in many solutions: chromic acid, phosphoric acid, sulphuric acid, hydrochloric acid, nitric acid, most organic acids as well as many saline solutions.[21] Thus, Zr is an excellent choice for applications that require not only strength and temperature resistance, but also corrosion resistance. The interest in corrosion properties of Zr arose from its employment in the nuclear industry. It is not resistant to fluorine-containing compounds such as hydrofluoric acid. Thus, fluorine-containing solutions can be used as chemical etchants for this metal. The corrosion of Zr in mixtures of HF and HNO_3 has been studied by James *et al*,[24] the overall reaction being:

$$Zr_{(s)} + bHF_{(aq)} \rightarrow ZrF_b^{4\text{-}b}{}_{(aq)} + bH^+{}_{(aq)} + 4e^-$$
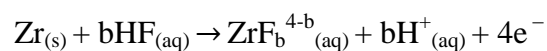
Where b is between 2.5 and 4 in value. This is specifically for 0.001 - 0.004 M HF in 1.2M HNO_3 solution. This reaction is of interest since a combination of HF and HNO_3 is employed as an etchant for Ti and Zr metals in this project.

The applications of Zr originated and are still mainly comprised of usages within the nuclear industry. Zirconium, with its low cross section for absorption of neutrons, is

useful in nuclear fields for cladding fuel rods.[8] Zirconium oxide with its high index of

refraction is often used as gem material (zirconia). It is also useful in: corrosion-resistant

applications, magnetic alloys, steel alloying, lamp filament productions, etc. When doped

with yttrium (Y), ZrO_2 is an oxygen ion conductor, and is thus applied in solid oxide fuel

cells and as a solid electrolyte in gas sensors.[25] Like Ti, the mechanical properties of Zr

allow for its use in many applications that require a strong and corrosion resistant metal.

2.1.3 Passivation

Corrosion resistance of metals can be enhanced using certain techniques, such as:

alloying, precious metal surface treatments, inhibitor addition, cathodic and anodic

protection, and finally thermal or electrochemical passivation in order to form passive

layers.[26] Although Ti and Zr both naturally form oxide layers on their surfaces very

rapidly, the layers are not always chemically stable, and will often undergo additional

reactions. Hence, they are not always protective of the metal itself. Thus, a more stable

coating is necessary, and thermal and electrochemical methods of passivation become a

desirable alternative.

Thermal oxidation, which was previously discussed, would often produce passive

layers that were not uniform, and contained cracks due to the high temperatures applied.

The reasoning for the formation of cracks is that the metal and oxide have different molar

volumes and thermal expansion coefficients, thus developing cracks upon cooling.[5]

Because of these downfalls of thermal oxidation, another passivation method was

developed, which involved using electrochemistry instead. Electrochemical passivation

will occur when a potential is applied, at which oxidation takes place. Depending on the

process, the passive layer formed will change in thickness and consistency throughout its formation. Mott and Cabrera's theory of growth by migration describes the growth of these passive layers.[1] The theory of Mott and Cabrera is valid for thin films, with several extensions to apply to thicker films. An important assumption of the Cabrera-Mott model is that electrons can pass freely from the metal to the oxide surface, in order to ionize oxygen atoms.[27] The electrons continue to cross the film in order to maintain zero electrical current. Electrons are assumed to pass through the film via tunnelling within the Cabrera-Mott model. This assumption restricts the model to thin films.

This anodizing technique involved direct current (DC) as a potential source, applied for mere seconds, in an open cell at ambient temperature. This process was therefore preferable to thermal oxidation since it was quicker and less energy-consuming. It was overall a much more practical technique, which was also able to form even layers without defects. Direct current passivation also produced passive layers in various hues, not merely blue, violet and brown. Experimentation was done by our laboratory using AC instead of DC, which resulted in much more varied, uniform and brightly coloured passive layers.[4] Thus, AC polarization became the preferred method for our laboratory to coat metals with protective passive layers.

Optimization was performed in order to create bright and well-defined colours on Ti under AC voltage conditions. Four electrolytes were compared: sulphuric acid (H_2SO_4), sodium chloride (NaCl), trisodium phosphate (Na_3PO_4), and ammonium tetrafluoroborate (NH_4BF_4).[4] Because colouration using NH_4BF_4 was brighter and better defined, it was chosen for Ti passivation from this point onward.

Zirconium was investigated by Burgers *et al.* who initially found that anodic polarization of the metal in aqueous media produced a layer of ZrO_2 atop the surface of the metal.[28] The passivation process was studied in different electrolytes for Zr by Charlesby, the preferred electrolyte being a sodium sulphate solution.[29] Thus, Zr is passivated in a Na_2SO_4 solution.

Through testing frequencies, passivation duration, and passivation voltages, the optimal parameters were chosen according to their formation of the brightest, best defined and most uniform passive layer colours: frequency of 60 Hz, passivation time of 10 s, and an applied AC voltage up to 80 V.[4] Beyond $V_{AC} = 80$ V, electrochemical breakdown occurs. The voltage at which electrochemical breakdown occurs depends on electrolyte composition, concentration, and conductivity.[30] Electrochemical breakdown was defined by Dyer and Leach as a sudden decrease in current efficiency for film formation.[31] Dyer and Leach attributed oxygen evolution to the increase in electrical conductivity of the film accompanying crystallographic transformation. Thus, growth of the film is limited by high current density, causing breakdown of the layer, which is accompanied by partial oxide evaporation, allotropic transformation of the stable anatase to the rutile oxide, and finally formation of a microporous structure.[32] Anodic films on Ti have increasing conductivity with oxygen vacancies present in the oxide structure.[33] The conductivity of the anode can change further with voltage, due to the piezoresistive effect.[34] This resistance leads to changes in morphology of the layers, as there are oxygen vacancies in the oxide structure, leading to a less consistent surface structure.

The properties of passive layers allow them to be not only coloured, but also protective of the underlying metal. In particular, passive layers on Ti have very unique

properties. The composition of the layer, to a degree, is dependent upon the electrolyte composition, the atmosphere and purity of the metal.[35] Through the employment of X-ray photoelectron spectroscopy, XPS, the passive layer atop Ti was found to be composed of: fluoride ions due to passivation occurring in NH_4BF_4 electrolyte, a layer of TiO-Ti_2O_3 and TiF_2-TiF_3, and finally a layer of TiO_2 and TiF_4.[36] This composition can be seen in Figure 7.

Outer layer: TiO_2 + TiF_4 (Ti^{4+})

Inner layer: TiO-Ti_2O_3 + TiF_2-TiF_3 (Ti^{2+}-Ti^{3+})

F at the inner metal/passive layer interface
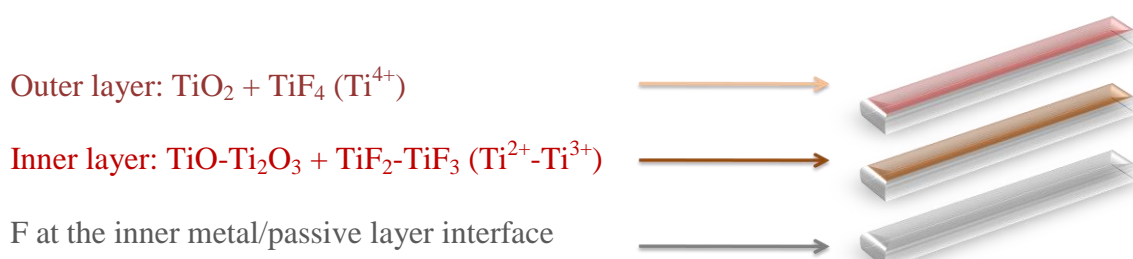
Figure 7. Titanium passive layer composition.

Thus, Ti is protected by more than one passive layer, which means that its overall passive coating is most likely thicker than that of Zr. This is because the passive layer atop Zr has been found to be composed only of ZrO_2,[37] which is seen in Figure 8.

Outer layer: ZrO_2 (Zr^{4+})

Figure 8. Passive layer composition of zirconium.

There is no fluorine present for Zr because it is passivated in a different electrolyte (Na_2SO_4). This difference in electrolyte is also why Ti, and not Zr, has the ability to

switch back and forth between different layer thicknesses, and thus the ability to switch colouration,[6] as shown in Figure 4.

Uniquely, Ti is able to change colours even after initial passivation, to both lower and higher thickness values, depending on applied AC voltage. This effect is due to the electrolyte used (NH_4BF_4). Fluorine-containing compounds are chemical etchants for Ti, and thus, with passivation in this electrolyte, there is both a rate of passive layer formation as well as a rate of passive layer dissolution.

Due to the relevance of Ti in medical and dental industries, it has been studied extensively. Titanium has been found to be a biocompatible material, meaning that it can be used in implants for medical and dental industries. Some important aspects of a medical or dental implant are: strength, corrosion resistance, non-toxicity, and ability to integrate with cells and tissues. Jerkiewicz and Zhao published findings on their work with passivated Ti in Hank's balanced salt solution, which is a simulated body fluid, where they examined corrosion behaviour, ion leaching, surface roughness and wettability over time.[3] These tests allowed them to quantify the potential for passivated Ti to be employed primarily in dental science. The results indicated that passivated Ti would be a more preferable material for dental implants than unpassivated Ti, as it is more resistant to bio-corrosion than the latter. This is also relevant to Zr, as Ti-Zr alloys are often used in the dental industry.

2.1.4 Colouration

Colour is a term used to describe a property observed through the human eye, which is from the visible spectrum. The visible wavelengths and their corresponding colours are illustrated in the visible light spectrum, which is shown in Figure 9.
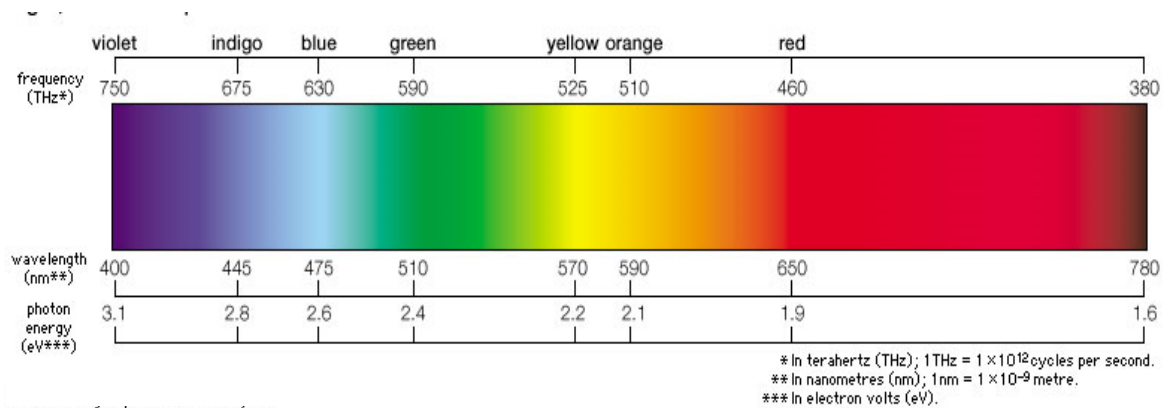
Figure 9. Wavelength, frequency and photonic energy assignments of the visible region of the electromagnetic spectrum.[38]

The colour of an object is dependent upon its physical properties and those of its environment, as well as the physical characteristics of the perceiving ocular system. Objects are often said to have the colour of the light that is leaving their surface, as reflected light prompts the colouration observed by the human eye. By this definition, colour is dependent on the spectrum and angle of incident light, surface reflectance properties, and the viewing angle.

A colour can be defined by certain specifications, which allow for the description of its appearance and unique characteristics. Hue, colourfulness, chroma, saturation, lightness and brightness are all properties corresponding to colouration. Hue is defined as

the degree of red, green, blue and yellow present within a colour.[39] However, in the colour theory of paint, hue refers to a colour that is absent of tint or shade. Tint refers to the combination of a colour with white, thus increasing the value of lightness. Shade, conversely, refers to the combination of a colour with black, thus decreasing the property of lightness. Thus, mixing a colour with any neutral (such as black or white) reduces the colourfulness or chroma, while the hue remains unchanged. Lightness is often referred to as tone. This property defines the position of a colour along a scale of lightness-darkness. The importance of defining these colour characteristics is that often hue, tint, shade and tone are terms that are mistakenly used as replacements for colour, when they should solely describe its properties.

Colour is important to this project because the passive layers on both Ti and Zr are coloured. This colouration is attributed to a light interference phenomenon (Table 1) called iridescence, which is illustrated in Figure 10. Iridescence is the effect that leads to the colouration of soap bubbles, rainbows and oil on water.
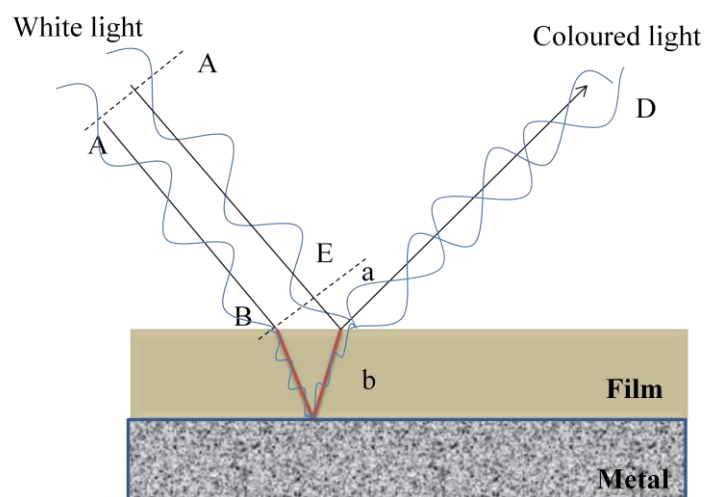
Figure 10. Interference of light beams reflected from front and back surfaces of a thin film.[40]

17

Table 1. Examples of the fifteen causes of colour.[40]

#	Cause of Colour	Example
	Vibrations and Simple Excitations	
1	Incandescence	Flames, lamps, carbon arc, limelight
2	Gas Excitations	Vapour lamps, lightening, auroras, some lasers
3	Vibrations and Rotations	Water, ice, iodine, blue gas flame
	Transitions Involving Ligand Field Effects	
4	Transition Metal Compounds	Turquoise, many pigments, some fluorescence, lasers, phosphors
5	Transition Metal Impurities	Ruby, emerald, red iron ore, some fluorescence and lasers
	Transitions between Molecular Orbitals	
6	Organic Compounds	Most dyes, most biological colourations, some fluorescence and lasers
7	Charge Transfer	Blue sapphire, magnetite, lapis lazuli, many pigments
	Transitions Involving Energy Bands	
8	Metals	Copper, silver, gold, iron, brass, "ruby" glass
9	Pure Semiconductors	Silicon, galena, cinnabar, diamond
10	Doped or Activated Semiconductors	Blue and yellow diamond, light-emitting diodes, some lasers and phosphors
11	Color Centers	Amethyst, smoky quartz, desert "amethyst" glass, some fluorescence and lasers
	Geometrical and Physical Optics	
12	Dispersive Refraction	Polarization, etc: rainbow, halos, sun dogs, green flash of sun, "fire" in gemstones
13	Scattering	Blue sky, red sunset, blue moon, moonstone, Raman scattering, blue eyes, some other biological colours
14	Interference	Oil slick on water, soap bubbles, coating on camera lenses, some biological colours
15	Diffraction	Aureole, glory, diffraction gratings, opal, some biological colours, most liquid crystals

Iridescence is also taken advantage of in devices such as interference filters, liquid crystals and lens coatings. The colouration arises from the interaction between light

waves. Importantly, upon closer observation, an incident light source will arrive at a surface with parallel waves. The light waves are reflected from inner and outer surfaces of a thin film, causing their phases to change. As is shown in Figure 10, beam A-A splits when it arrives at the film surface, beam B traverses a distance of 2b through the film, and beam E travels through air a distance of a. The path difference should keep them in phase since they differ by a factor of 4, however, the refractive indices of the film and air are different, causing phase-shifting. The phase-shifting in this case leads to destructive cancellation, thus no light of this wavelength is observed. With a different film thickness, the interference would change. Thus, depending on refractive index and thickness of the thin layer material, the properties of the photons will change and different colouration will be observed. This is the cause of colouration in passive layers, and the reasoning behind the observed colour changes with layer thickness.

2.2 Corrosion

Titanium and Zr are reputable in their corrosion and bio-corrosion resistant properties. In order for these materials to be employed in areas where they will be exposed to corrosive media, it is important to understand the level of resistance in a given solution, as well as how much of the metal is dissolved into solution through corrosion reactions. This is especially important within applications in dental and medical science, where corrosive dissolution of metals into the human body is harmful and toxic to health. Corrosion of metals is a seriously grievous occurrence for any application, because of change in dimensions, loss of strength, toxicity in biological applications, etc. There are

many different processes through which corrosion can occur on metals; they are visualized in Figure 11, and described in the text that follows.
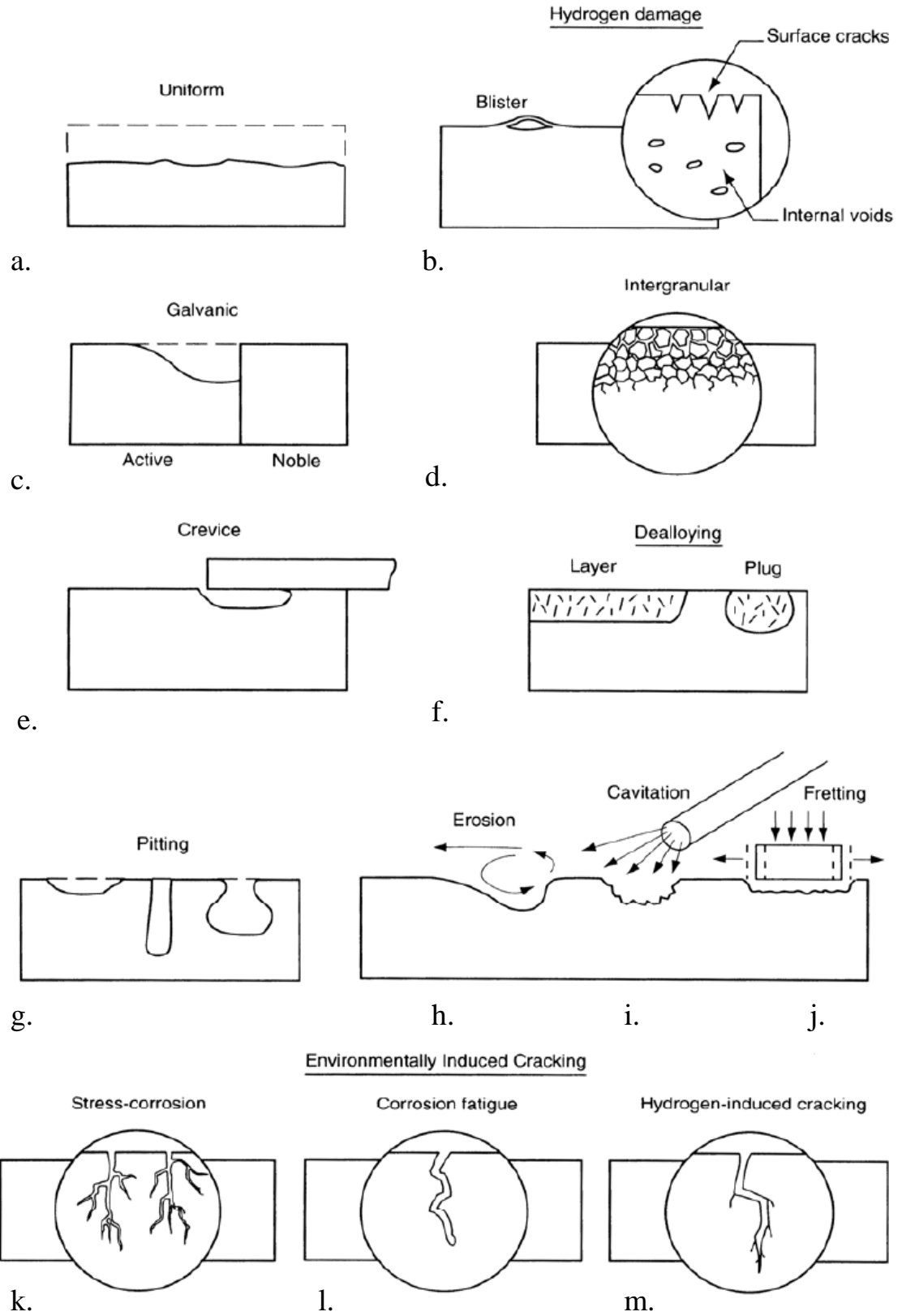
Figure 11. Forms of metallic corrosion illustrated.[41]

The first diagram (Figure 11a) illustrates what is known as uniform corrosion, which is able to degrade very large metallic volumes. This is the most common form of corrosion, as it occurs over an entire surface; however, it may be less noticeable since other forms of corrosion often work in a more localized and rapid manner. Since this form of corrosion is not localized to a small area, it is easier to predict and not as rapid, and therefore is classified as being less harmful than other corrosion methods. Examples of uniform corrosion are: general atmospheric corrosion and seawater corrosion. The aggressive factors that cause atmospheric corrosion, in addition to oxygen, are moisture, water, ultraviolet light and temperature. Hydrogen damage (Figure 11b) includes hydrogen-induced cracking, hydrogen blistering and hydrogen embrittlement. Atomic hydrogen migrates from the surface of the metal (or alloy), and diffuses towards internal defects and inclusions, where it reacts with carbon or other impurities and forms gaseous products. Hydrogen corrosion is dangerous since it is an internal process, which is not often observed before the metal is already greatly weakened in mechanical strength. Galvanic corrosion (Figure 11c) occurs when two differing metals or alloys are in electrical contact. The different potentials of the respective redox couples that can form cause a reaction in solution. Intergranular corrosion is observed in Figure 11d, and is of major concern in regard to alloyed metals. Pure metals can occasionally be subject to this type of corrosion that depends on the presence of reactive impurities which often accumulate in grain boundaries, i.e. the areas where intergranular corrosion takes place. Crevice corrosion (Figure 11e), occurs in small, sheltered areas. This type of corrosion is characteristically found when fasteners such as screws and bolts are used, though crevices created by poor application of coatings can be subject to this as well. Titanium is susceptible to crevice corrosion in brine solutions where oxidizers are present. This

susceptibility is heightened with increased temperature and chlorine concentration, as well as at lower pH value.[18] Dealloying is observed in Figure 11f, and can occur in an alloy when there is a substantial difference in the redox potentials of the elements within the alloy. A good example of this type of corrosion is the removal of zinc from brass.[42]

Pitting corrosion (Figure 11g) shares the same mechanism as crevice corrosion, in that the electrolyte is relatively isolated in the pit and becomes more acidic, thus increasing the rate of corrosion. Erosion-corrosion (Figure 11h) occurs when the corrosive medium is moving at a high flow velocity, and thus sweeps away layers of the metal or the protective coating atop the metal. This effect is worsened when abrasives are present. In seawater, the critical velocity for Ti to exhibit erosion-corrosion is extremely high compared to other metals (27 m/s).[18] Cavitation (Figure 11i) is a type of erosion-corrosion that occurs when the flow velocity of the medium is so high that water vapour is able to form bubbles that crash against the surface and implode. Fretting (Figure 11j) is another type of erosion-corrosion, which occurs when a metal or alloy is in contact with another solid, and they experience movement abrasion.

Stress corrosion cracking (Figure 11k) occurs mainly in alloys, as pure metals are relatively resistant. It occurs when a static tensile stress (a stress leading towards expansion) on the metal exists and certain dissolved species are present in the solution. Examples of this are stainless steels in hot chlorides, and brass in ammonia.[42] Corrosion fatigue cracking (Figure 11l) occurs when a cyclic stress (a stress that changes over time in a repetitive fashion) is present on a metal in a corrosive environment. Finally, environmental hydrogen induced cracking (Figure 11m) is a structural failure caused by

the presence of external hydrogen during tensile stresses, weakening a material. This type of cracking is a problem for alloyed metals.

Titanium specifically is susceptible to uniform, crevice, anodic pitting, hydrogen damage, stress-cracking, fatigue, fretting, galvanic and intergranular forms of corrosion.[41,43] Corrosion of metals in aqueous media almost always involves electrochemical reactions, as a change in electrochemical potential at the surface of a metal has a significant effect on corrosion reaction rates.[41] Through the understanding of metallic corrosion and the specific corrosion behaviour of the materials under scrutiny, corrosion can be prevented through innovative and effective methods (ex. alloying, precious metal surface treatments, inhibitor addition, cathodic and anodic protection, and finally thermal or electrochemical passivation in order to form passive layers.[26]).

2.3 Measurement Techniques to Assess Corrosion and Other Properties

2.3.1 Visible-Light Microscopy

Visible light microscopy, VLM, is a technique that was implemented many centuries ago. This technique employs visible light and optical lenses to enlarge the image of an object in order to allow the human eye to observe it in greater detail. This has been a popular technique, as it employs readily available visible light and is very simple to use, producing excellent results. As much as one century ago, the technique was practically perfected in terms of optical principles and lens design for magnification.[44] However, the light microscope took a significant dip in employment

when the electron microscope became prevalent, due to the more advanced magnification capabilities of the latter. Electron microscopy had the ability to explore objects on such a minute scale with significant detail, and thus it seemed as if VLM would be replaced completely. In the last few decades, VLM has once again been adopted for use in many applications. Medicine and research especially have found it an essential tool for exploration, especially with the use of fluorescent tags for imaging.[44] New developments have been made in VLM since its reputation was reestablished as being a useful technique. Most importantly, light sources were developed in order to improve image quality. Using advanced micromachining, computer chips, storage devices and other advances in technology, VLM can be improved using advanced lenses, electro-optical and electromechanical devices.[44] It is a useful technique, as developments in spatial resolution and magnification allow for identification and study far beyond the means of the human eye. Magnification and spatial resolution are defined as:[45]

$$\text{Magnifying power of instrument} = \frac{\text{visual angle of image observed with instrument}}{\text{visual angle of object seen directly}}$$

The smallest resolution possible for VLM is defined by Rayleigh's criterion: [46]

$$\delta = \frac{0.61\lambda}{n\,sin\theta}$$

In this equation, λ represents wavelength, and n sinΘ is the numerical aperture. Basically, the resolution would be about half of the wavelength of visible light, as the numerical aperture can be assumed as 1. This means that the resolution at best would be about 200-300 nm.[46] The numerical aperture value is dependent upon the angle of the

maximum cone of light that the lens can take from a point of the object.[45] The prevalent problem with VLM comes from the use of light waves, and thus diffraction.

There are two main types of VLM instruments: a simple microscope that consists of only one lens, or a compound microscope that has more than one lens. Since the microscope itself is static, the sample or lens can be moved in order to change the focal length, and thus gain another perspective of focus. Compound microscopes are beneficial, as they have improved numerical aperture, reduced chromatic aberration and multiple lenses, which can often be adjusted for different levels of magnification. Chromatic aberration is a similar effect to spherical aberration, where not all wavelengths of light are focused into the same focal point by a lens. Thus, this effect is undesireable because the image becomes distorted.

A visible light microscope will most basically consist of a light source, a lens and an objective for magnification of the sample being studied (Figure 12). Most commonly, it consists of an eyepiece, light source, condenser lens and objective, as well as a stage and focus wheels. An eyepiece consists of multiple lenses designed to focus the image for observation by the human eye. The light source could be outside light; however, modern microscopes often employ a halogen light source, which has been built into the microscope. The objective contains multiple lenses that are made from glass, and are responsible for collecting light from the sample. In high magnification applications, where a higher numerical aperture is required, some objectives can be oil or water immersion. These immersion objectives have oil/water between the objective lens and sample; thus, they have a refractive index matching that of oil or water instead of air. This works on the principle that oil and water have higher refractive indices than air, thus

allowing the numerical aperture to be higher. The stage is used to hold samples; often, it holds glass slides, and light will pass through from underneath the stage. However, some microscopes have a light source above the sample for non-transparent sample studies. A condenser lens is employed for focus of the light source onto the sample, thus allowing this light to be taken up by the objective lenses. There can also be filters, which are employed in order to manage quality and intensity of the light source. Computers and digital cameras are used to capture and process microscopy images, instead of merely observing with the human eye. This is convenient for processing of images, as well as the recording of images for publication and reference.
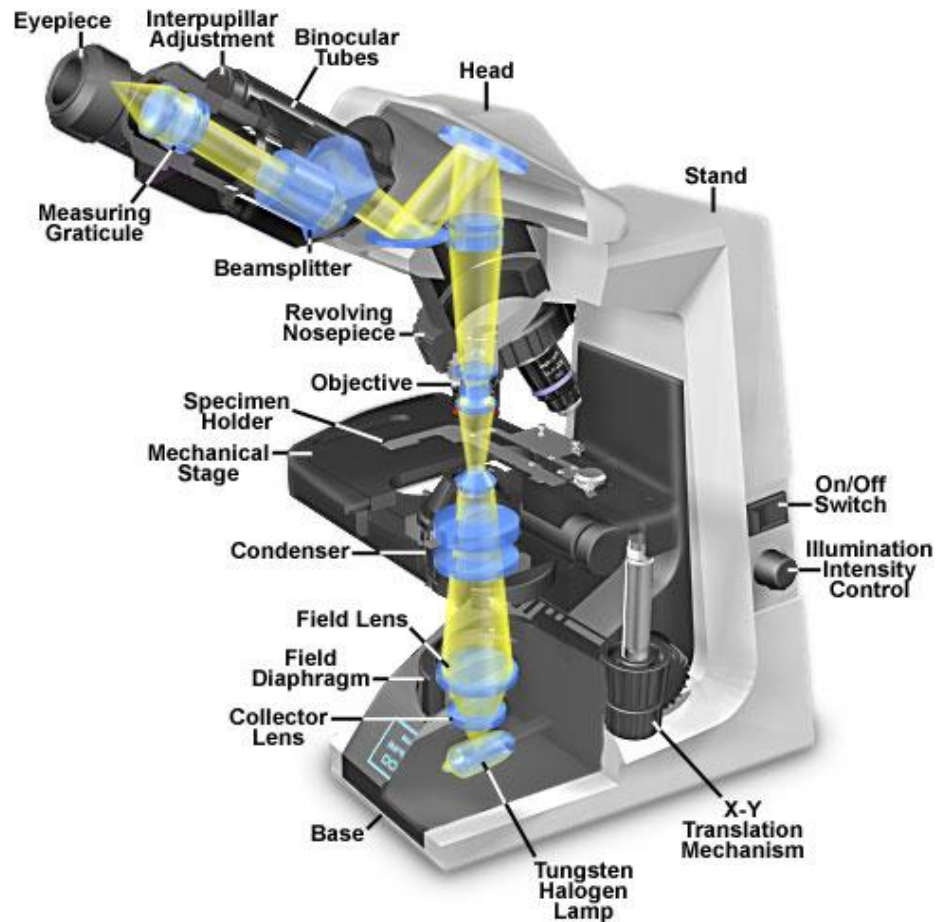
Figure 12. Basic layout of a visible light microscope.[47]

Visible light microscopy is useful to determine whether the surface of the passive layers are uniform and defect-free, and thus that the passive layer protects and fully coats the metal surface. A complete and crack-free coating allows for corrosion resistance and intrinsic protection of the underlying metal. This technique can also be employed to see any changes between polished and etched surfaces, as well as the change in surface morphology between samples passivated at different applied AC voltages. Some instruments, such as the Zeiss AXIO VLM have a very high resolution and image quality,

thus illustrating the significant instrumental improvements made using more recent technology.

This technique is useful in order to determine the surface morphology of passive layers and whether they are fully coating the underlying metal. It is important to understand surface defects, as they can promote abrasion and corrosion. Visible light microscopy is also useful in studying the relationship between surface morphology and V_{AC}. Finally, VLM can also be employed in comparison of coloured grains on the surface of the passive layer with the light reflected from the surface studied using reflectance spectroscopy.

2.3.2 NIR-UV-Vis Reflectance Spectroscopy

Reflectance is measured by recording the percentage of incident light that is reflected from the surface with which it has interacted. Specifically, this effect refers to thin films, as the reflection can vary upon the layer thickness. When referring to thicker bulk samples, reflectivity is the term most often used. This means that reflectivity would refer to the material, whereas reflectance refers to each specific sample. The aforementioned nomenclature rule is also true for transmittance and absorbance, which are sample-specific, whereas transmittivity and absorptivity refer to bulk material properties. Upon interaction with a surface, light will be transmitted, reflected or absorbed. The fraction of light that is transmitted, reflected or absorbed is expressed by the transmission coefficient (τ), reflection coefficient (ρ), and the absorption coefficient (α). Altogether, the relationship becomes:[48]

$$\tau + \rho + \alpha = 1$$

When reflected light is scattered, it may either be diffuse, specular (in the mirror direction), or a combination of the two. The reflectance factor, R, is defined as the amount of light reflected by the sample, compared to that which is reflected by a perfect diffuse mirror under identical conditions.[48] This is why a special mirror is employed to set up a background for calibration of the reflectance software.

Refractive index, n, is the speed at which light travels through a medium, compared to its speed through vacuum. It is a very important factor in the optics of photon interaction with matter. Refractive index is also an important factor in understanding the mechanism of passive layer colouration being observed due to iridescence. When refractive index of a substrate is larger than that of the film, phase changes are cancelled at front and back surfaces. Thus, for even valued waves (constructive interference), reflection is enhanced, and, for odd valued waves (destructive interference), the reflection is weakened.[49]
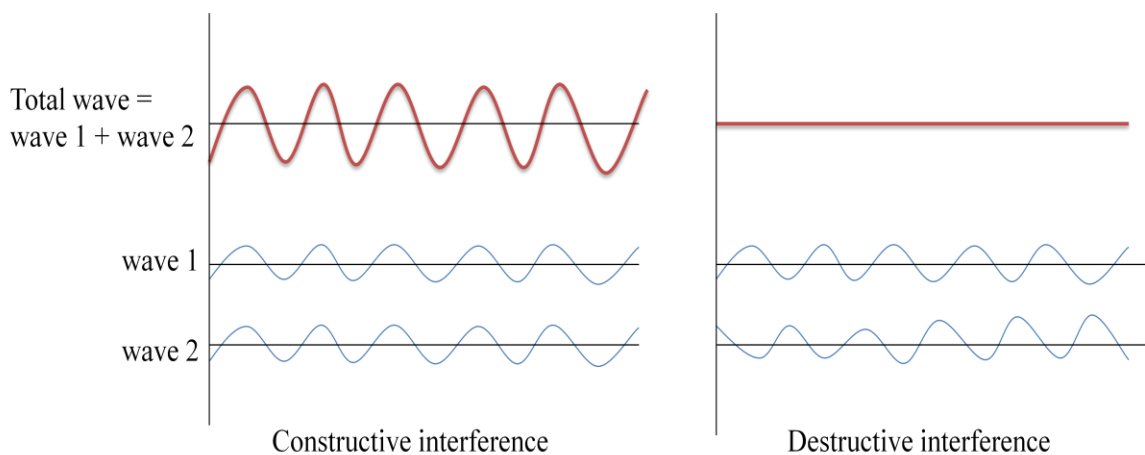
Figure 13. Schematic of constructive and destructive light wave interactions.

Light waves will propagate in a pattern, with the possibility of either constructive or destructive interference with one another (Figure 13). Constructive interference occurs when two waves are in phase, and thus their amplitudes combine. In a sense, constructive interference is similar to two waves working together to gain larger overall amplitude, whereas destructive interference involves two waves instead combining to cancel each other out partially or completely. In the case of complete destructive interference, the waves are out of phase by 180 degrees, thus causing their amplitudes to subtract and result in the overall amplitude being zero. Interference will affect the overall colouration caused by iridescence, since some waves will interfere constructively to enhance reflectance intensity at certain wavelengths, while others will interfere destructively and diminish reflectance intensity at other wavelengths. Thus, through reflectance spectroscopy, light regions showing positive constructive peaks, and light regions showing negative destructive peaks can be studied, adding up to the observed colouration.

The set-up of a reflectance spectrometer can be seen in Figure 14, which shows the Tungsten Halogen Deuterium light source, as well as the near infrared ultraviolet-visible (NIR UV-Vis) detector attached to a reflectance probe, which has optical fibers to carry the light emitted by the light source, as well as capture the reflected radiation. Thus, if light is scattered diffusely, fewer photons will reach the detector, and the intensity of reflection shown in the spectrum will consequently be smaller.
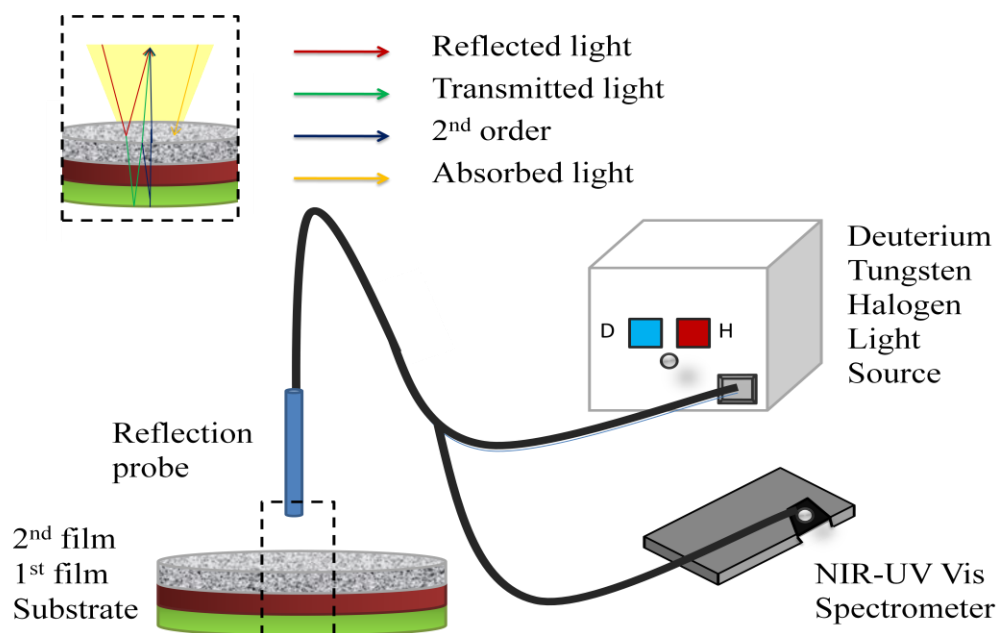
Figure 14. Set-up of reflectance spectrometer and light source is shown schematically. The magnified probe shows the interactions of the light source with the sample. There are reflected incident photons, reflected second order photons, transmitted photons and absorbed photons.

Reflection spectroscopy has been found to be useful in many areas, one of which is solar cell research, where it has been employed in quantification of the porosity of TiO_2 surface films.[49] Near infrared ultraviolet-visible reflectance spectroscopy has been employed in this project in order to examine the optical properties of the observed colour depending on the passive layer thickness. Reflectance spectra are derived through normal angle halogen and deuterium light being reflected by a sample, back to the detector. Thus, the outcome of constructive and destructive light interferences can be assessed in the form of a spectrum, which indicates the component colours that are responsible for the overall colouration of each sample.

2.3.3 Profilometry

Profilometry is a technique that probes the surface of a sample with a stylus in order to gain roughness measurements on the meso scale (hundreds of nanometers). The stylus used is diamond tipped and stationary, as the stage (and thus the sample) moves horizontally and a few nanometers in the vertical (z) direction, through a specifically programmed pattern of scan length, scan speed and stylus force. Variable surface defects shift the position of the stylus, thus producing electrical signals proportional to the position change. These signals are stored and processed for analysis. Thus, through the maps of set parameters, information is gained, which can be used to illustrate a profile of the surface under scrutiny.

Resolution will be dependent on both vertical and horizontal components. Horizontal resolution depends on scan length, stylus size, as well as the number of data points per scan. Vertical resolution is dependent on the motor that is responsible for moving the stage, and thus each instrument would have different vertical resolution. The size of the stylus employed is important as is its shape. Depending on the sample being studied, a different stylus could be beneficial. The standard stylus diameter is 12.5 μm, and the force may be adjusted between 1-15 mg.[50] As the point pressure will be higher for a smaller tip radius, the pressure must be adjusted for smaller or larger styli, as well as for softer or harder samples.

The roughness is calculated from the data of vertical displacement of the stylus according to the following equation, where L is the horizontal scan length.[51]

$$R_a = \frac{1}{L} \int_{x=0}^{x=l} |y| dx$$

This technique is beneficial because it takes a large area measurement of roughness across a surface. Compared to roughness measurements made through AFM, profilometry takes a broader map of the sample. The maps taken for roughness measurements were 2.5 mm by 2.5 mm. For comparison purposes, the largest possible square map taken with AFM would have a side length of 15 μm.

2.3.4 AFM

Atomic force microscopy is a technique that uses the attractive and/or repulsive forces between surface and tip to create an image. Through the use of scanning probe techniques, such as AFM and scanning tunneling microscopy (STM), the ability to gain atomic resolution of surfaces has arisen. Thus, these two methods of analysis have opened a window into detailed surface morphology experimentation. This is extremely useful for many applications including electrochemistry, as the understanding of the surface is essential to knowing how it will react under applied potentials. The truly unique part of these scanning probe methods is that they both are able to be operated without an ultra high vacuum (UHV) enclosure. This allows for ease of operation, much faster experimentation, as well as much more reliable operation, in contrast to UHV, which requires frequent and expensive maintenance. AFM in particular is useful for many applications, as it does not require the sample to be conducting or semiconducting; thus, insulating samples may also be studied.
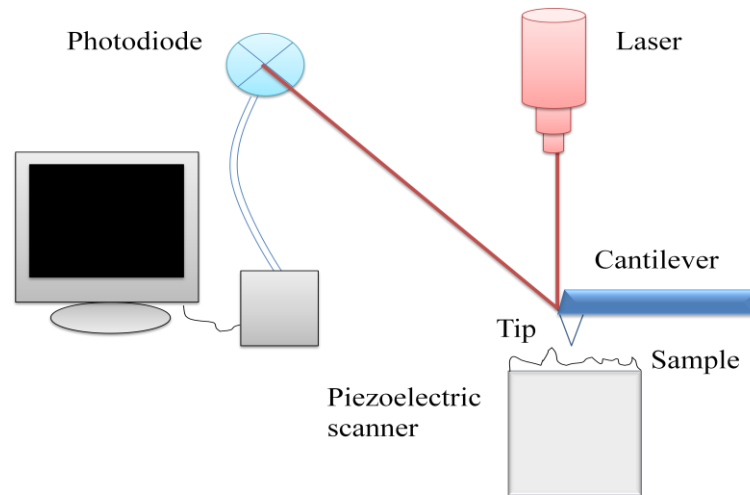
Figure 15. Schematic diagram of a typical AFM.[52]

An AFM instrument, whose diagram is shown in Figure 15, operates through the use of van der Waals, capillary and electrostatic forces[53,54,55] exerted between the tip and a sample, which is held at a close range to the tip. The force measurements are made using displacement of a very sensitive spring, proportionality between force and displacement being from Hooke's Law:[52]

$$F = -kx$$

In this case, F is the force, k is the force constant and x represents the displacement. The effect of attractive and repulsive forces on the tip is illustrated in Figure 16.
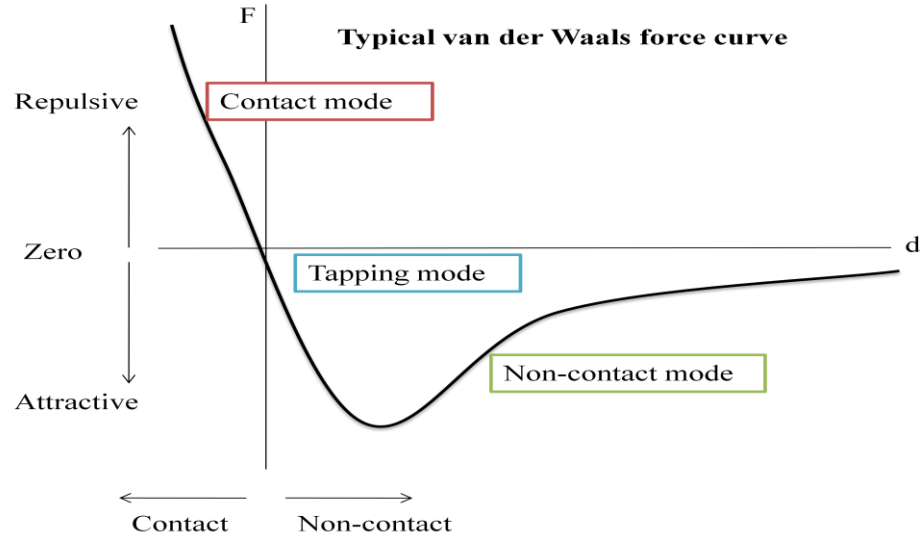
Figure 16. The attractive and repulsive force regimes applied on an AFM tip, as it approaches a surface.

The measurements of tip displacement due to surface interactions are taken using specific strain gauges.[56] The distance between the sample and cantilever must therefore be maintained to a point where there will be deflection; thus, the sample rests on a piezoceramic base. Piezo materials hold a charge in response to strain, so they are said to be piezoelectric in their responses. These materials are used in AFM as scanners; the x, y, and z directions of motion are controlled using different electrodes. Voltages are applied to these electrodes to facilitate expansion or contraction of the piezo depending upon the desired position of the sample surface with respect to the tip. The activation of the piezoelectric scanner is due to a feedback mechanism, which is driven by the monitoring of cantilever deflection, thus retaining constant deflection needed for measurement. Often, the deflection monitoring is done through optical means, using a laser. The laser is focused on the tip at the cantilever end, which will reflect the light to a

photodiode and thus, with changes in the photocurrents, the deflection is monitored.[52]
The tip needs to be inert and robust, and will typically be made of tungsten. There are
also silicon tips manufactured for further accuracy of measurements, as they can be
micromachined and oxide sharpened.

There are three modes of operation for an AFM system: contact, non-contact and
tapping. Contact mode operates on the principle of the tip touching the surface through
an adsorbed fluid layer on the sample surface.[57] In this case, the force between the tip
and the sample remains constant through maintenance of constant cantilever deflection.
The distance of the scanner's movement laterally (x, y) forms the image of the sample
surface. In tapping mode, the cantilever is oscillating at, or slightly below, its resonance
frequency in order for the tip to lightly tap across the surface. The vertical position (z) of
the scanner at each data point (x, y) is recorded in order to form the sample surface
image. Non-contact mode is where the cantilever is oscillated above its resonance
frequency in order to maintain an alternating current signal. The tip never comes into
contact with the sample in this method of experimentation. Van der Waals forces
decrease the oscillation frequency. The image is created using the distance the scanner
moves vertically (z) at each data point (x, y).[57] These methods of AFM operation all
have their advantages and disadvantages. Contact mode has high scan speed capabilities,
can study rougher samples and is the only mode in which atomic resolution is possible.
However, lateral forces can distort the image, contact can be damaging to soft samples
and normal forces to the tip can be high, thus reducing spatial resolution. In tapping
mode, there is higher lateral resolution, lower forces and less sample damage; however,
the scan speed is slower. Non-contact mode has no force exerted on the surface, which

saves the sample from any possible damage or force interactions. However, it has low lateral resolution, slow scanning speed, and it only works well on hydrophobic samples, as a large amount of adsorbed fluid on the surface traps the tip.[57]

Naturally, the technique has drawbacks like any other method of analysis. Specifically and most importantly, the high resolution is difficult to obtain, especially with rough samples because the tip is large and not always capable of differentiating all of the imperfections in the surface structure. Also, under UHV conditions, the interactions are limited because there is difficulty minimizing tip-sample charging, thus causing sample characterization to be problematic.[52] The electrostatic force between tip and sample in this case dominates over the weaker van der Waals forces.

2.3.5 SEM-FIB

Scanning electron microscopy (SEM) and focused ion beam (FIB) are very similar techniques, which have a range of applications in materials science when employed either together or separately. They can be used in many industries and areas of research, as they image down to very small spot sizes, and can provide detailed information of surface morphology. FIB is most frequently employed in materials science and in the study of semiconductors, as it has the ability to give information on the surface as well as below the surface through milling with an ion beam. The FIB instrument also has the ability to deposit material on the surface, thus broadening the applications further. A schematic representation of the differences and similarities between the set-up of an SEM system versus that of a FIB system can be seen in Figure 17.
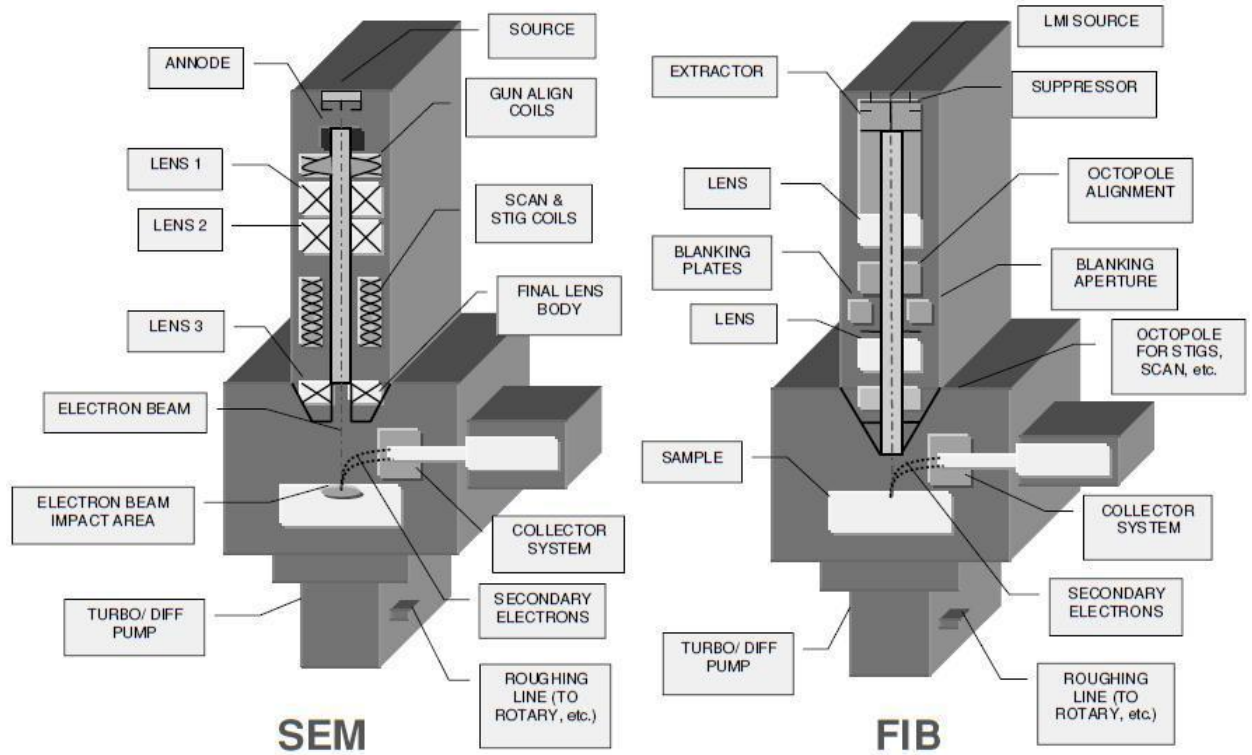
Figure 17. Schematic comparison of the SEM and FIB machines.[58]

Because one of the techniques employs a beam of electrons and the other employs a beam of ions, and the properties of electrons and ions differ, so does the instrumentation that controls the beams, as well as the effect that these beams have on a sample. The most obvious difference between the two instruments is that the sources of each beam are different. The ion beam is produced through the use of a liquid metal ion source, and the electron beam is produced from a filament. The FIB system also has additional components designed for ion beam control, such as the blanking aperture, which is designed to avoid sample erosion by deflecting the beam from the center of the column, and the octopole lenses, which perform deflection, alignment and stigmation correction. Table 2 illustrates the specific differences between gallium (Ga^+) ions, most frequently

used in the FIB system, and electrons in the SEM system. This information gives a quantitative representation of how these differences in particles will change the requirements of the system.

Table 2. Quantitative Comparison of FIB Ions and SEM Electrons.[58]

Particle:	FIB	SEM	Ratio
Type	Ga^+ ion	Electron	
Elementary charge	+1	-1	
Particle size	0.2 nm	0.00001nm	20000
Mass	1.2×10^{-25} kg	9.1×10^{-31} kg	130000
Velocity at 30 kV	2.8×10^{5} m/s	1.0×10^{8} m/s	0.0028
Velocity at 2 kV	7.3×10^{4} m/s	2.6×10^{7} m/s	0.0028
Velocity at 1 kV	5.2×10^{4} m/s	1.8×10^{7} m/s	0.0028
Momentum at 30 kV	3.4×10^{-20} kgm/s	9.1×10^{-23} kgm/s	370
Momentum at 2 kV	8.8×10^{-21} kgm/s	2.4×10^{-23} kgm/s	370
Momentum at 1 kV	6.2×10^{-21} kgm/s	1.6×10^{-23} kgm/s	370
Beam:			
Size	Nm range	Nm range	
Energy	Up to 30 kV	Up to 30 kV	
Current	pA to nA range	pA to nA range	
Penetration depth:			
In polymer at 30 kV	60 nm	12000 nm	0.005
In polymer at 2 kV	12 nm	100 nm	0.12
In iron at 30 kV	20 nm	1800 nm	0.11
In iron at 2 kV	4 nm	25 nm	0.16
Average signal per 100 particles at 20 kV:			
Secondary electrons	100-200	50-75	
Backscattered electron	0	30-50	0
Substrate atom	500	0	infinite
Secondary ion	30	0	infinite
X-ray	0	0.7	0

Ions weigh more than electrons, meaning they gain more momentum over time, but are slower to accelerate. Magnetic lenses are employed for electron beams because they have superior optics and are not easily degraded through the constant use of high

voltages. Magnetic lenses in SEM systems use coils of magnet tuned to a particular electron wavelength, which will focus the electrons at that wavelength. As magnetic lenses are less efficient for ion beams, the FIB system uses electrostatic lenses instead. Indeed, because the focusing plane in magnetic lenses is dependent on the mass-to-charge ratio, focusing of ions would be much less efficient. Also, as ion acceleration is low and the momentum is high, there is difficulty in focusing the high powered Ga^+ ions using a magnetic field. Thus, electrostatic lenses are better for FIB, as they aid in transport of charged particles by employing electrostatic fields to guide them into a desired formation. Hence, they work in a similar manner to glass lenses focusing light, instead using electrodes to which different potentials are applied to focus charged particles. Electrostatic lenses can be used to focus both ion and electron beams, and can therefore be used in FIB and SEM systems that have both ion and electron beams, also referred to as dual beam systems. The schematic diagrams of both the FIB and SEM systems (Figure 17) show that each technique employs at least two lenses, SEM often having three.

Another important factor in ion beam optimization is that space charge effects will limit the source size. These effects are the proportional relationship between repulsion of same-charged particles and their speed. They will increase the energy distribution width of the ions being emitted. This leads to chromatic aberration, which is a limiting factor in FIB resolution,[59] where different wavelengths cannot be focused onto a desired location, and instead separate slightly, causing broadening.

2.3.5.1 SEM System

The basic SEM system consists of a high vacuum system, an electron beam source, electron beam manipulation, a sample stage where the beam interacts with a specimen, and finally the detectors and computer. The vacuum system in place within electron beam imaging systems is about 10^{-7} Torr.[60] The electron beam source has three components: a cathode filament often made from tungsten, a bias to control electron flow (grid cap), and finally an anode plate to accelerate the attracted electrons towards the sample stage. The voltage can be altered to obtain higher resolution; however, there will be more heat generated and delicate samples may be damaged. The reason why higher accelerating voltage has a positive effect on resolution is that it generates a shorter wavelength of electrons. Beam current may also be altered in order to change the bias between the anode and cathode, thus changing the amount of electrons hitting a sample at one time. This can also cause sample heating and damage. Electrons are released from the tungsten filament via an emission method. This emission method may be through filament heating, which involves applying a current across the filament, exciting electrons to be emitted through filament heating. Another method is field emission, where a large potential difference is applied to extract electrons from the filament. Field emission is a cold technique, as it requires no heating; thus, the filament will last longer and the beam is of a smaller diameter, which promotes better resolution. The biggest disadvantage to this method, over filament heating, is that it requires a higher vacuum, which is expensive and difficult to maintain.

In order to control the electron beam, there must be a system in place to manipulate the electrons into a desired spot for sample analysis. As electrons are affected

by both electrostatic and magnetic fields, both of these methods can be employed in the control of an electron beam. Magnetic lenses can be used after the electron emission stage for control and focus of the beam itself. Electrostatic lenses have a possibility of causing arcing in the beam, and thus are not employed in SEM beam focusing.[61] The electromagnetic lenses employ a copper wire with current flowing through it to focus the beam; thus, they are called condenser lenses. The final condenser lens has two magnetic fields that allow for x, y plane movement or scanning, which is why the instrument has its name.[61] There is also a lens to correct for astigmatism of the beam, i.e. a beam with a non-circular shape, which is detrimental to resolution. Finally, there are apertures to control the electrons that have strayed from the beam. Essentially, these apertures are holes, which have a diameter for the purpose of stopping electrons that have strayed outside the desired distance from the beam center. These apertures are sized depending on the spot size desired for specific analyses.

The beam will interact with a specimen on the sample stage. The interaction involves a primary electron, from the electron beam, travelling into the specimen under study until it collides with a particle, thus propelling it in another direction. This is called scattering, and the resulting effects can be seen in Figure 18. First, electrons can be backscattered; these electrons are considered to be primary, as they have not gone through a specimen, and thus still have very high energy from their original emission. Next, there are secondary electrons, which are released when a primary electron enters and expels another electron from the surface of the studied specimen. These electrons have very low energy, and thus must be detected near the sample surface where they were dislodged. Secondary electrons can be used for imaging, as their low energy allows for high

resolution, and they provide topography information.[61]   Thirdly, there will be X-rays

generated through the emission of electrons from certain atomic orbitals. An advantage

of X-ray detection is that the energy and wavelength values are representative of

elemental species, and can thus be used for species identification. Transmitted electrons

occur with thin samples and are the basis of transmission electron microscopy (TEM),

imaging. These electrons pass through the sample completely, and give information on

atomic density within the specimen. Photons can also be emitted, usually through

fluorescent molecules.
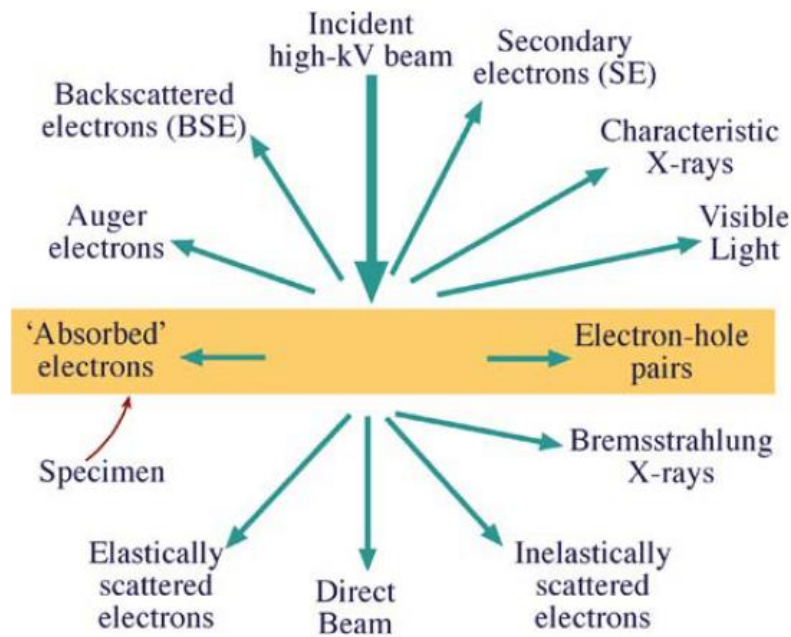
Figure 18. Signals generated by an electron beam interacting with a specimen.[46]

As was mentioned before, secondary electrons are usually detected for the purpose

of gaining information about topography, and thus are most commonly used in SEM for

imaging of surfaces. The secondary electron detector applies an attractive potential in

order to capture secondary electrons, which are converted into photons by the scintillator,

and sent to a photomultiplier for signal amplification. The surface image is dependent upon surface area. Thus, a flat surface with less surface area than a rougher surface will emit fewer electrons; this is why an image of topography can differentiate between surface structures. Backscattered electrons are detected using a very precisely positioned detector, which is normally very near to the primary beam so as to detect primary electrons that have bounced back from the sample surface. Ideally, the detector surrounds the beam, catching backscattered electrons from all directions. These electrons give information on atomic density, because more electrons bounce away from dense materials, in contrast to less dense materials where some electrons will pass through the specimen. X-rays may also be detected for information about elemental composition.

2.3.5.2 FIB System

The basic FIB system consists of a high vacuum system and a chamber, a liquid metal ion source, an ion column, a sample stage, a computer, and detectors. The beam of ions is produced through a liquid metal ion source (LMIS), most commonly made with gallium. The other possible sources can be of gold or iridium. The LMIS is liquid metal under a strong electrical field from an extractor, thus removing metal ions from the source, which can be seen in Figure 19. Gallium is most frequently used as the LMIS due to its properties: low melting point (roughly room temperature), low volatility (conserves metal supply and yields long source life), low vapour pressure (allows pure Ga to be used), as well as excellent electronic and emission characteristics. Gallium ion emission occurs over two concurrent steps. Initially, the heated Ga flows and wets a tungsten (W)

needle, the Ga remaining molten for extended time periods due to the above properties. An electric field applied to the end of the W needle will cause a point source in the shape of a Taylor cone to appear as a result of the electrostatic forces and surface tension produced by the electric field.[59] Secondly, the extraction voltage can pull Ga from the W tip, where it will then be ionized.
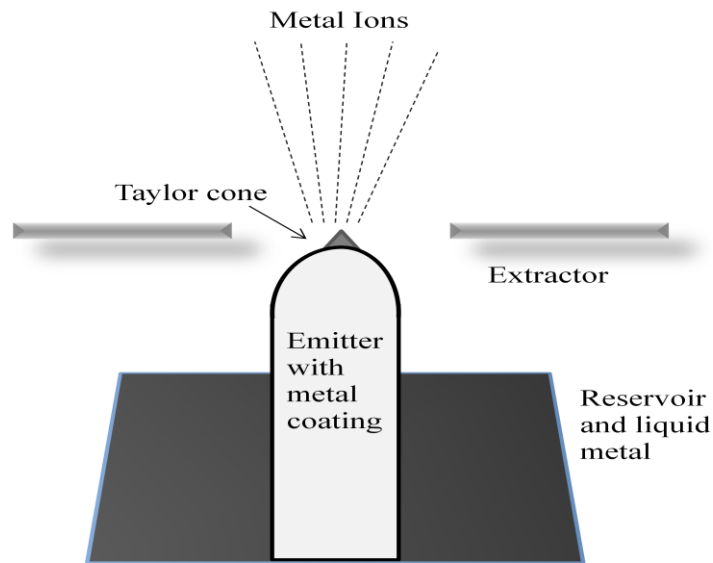
Figure 19. FIB LMIS schematic diagram of emitter and extractor electrodes.

Maintenance of the ion beam source is required. As the ion emission current rises, there is an increase in the chance of dimers, trimers, charged clusters and charged droplets in the beam. As the source becomes older, the suppressor voltage increases in order to maintain the beam current that is necessary. When this is no longer sufficient to create a working beam current, the system must be heated. This is done through a larger extraction voltage being applied, and then brought down to normal. The source may only be heated a certain number of times since the reservoir size is small.[59] Heating the

system will clear the source of contaminants and excess build-up, and allow the instrument to work cleanly and efficiently again.

Once the ions are extracted from the LMIS, they are accelerated using a potential through an ion column. There are usually two lenses, the condenser and the objective. The condenser is the beam forming lens and, the objective lens focuses the beam onto the sample surface. Beam optimization can be achieved through centering each aperture, tuning the lenses, and tuning the beam. The typical FIB instrument will often have three vacuum pumping regions, one for the source and ion column, one for the sample and detectors, and one for the sample exchange.[59] The source and column have a high vacuum (10^{-8} Torr) in order to avoid contamination, beam scattering and electrical discharge in the ion column.[62] When the ion beam leaves the column, it strikes the target surface to generate sputtered atoms and molecules, as well as secondary electrons and ions. The angle can be changed through rotation of the sample stage. The sample stage of a FIB instrument is typically able to provide motorized movement along five axes, i.e. x, y, z, rotation and tilt for various perspectives on a secured sample.

Since there is constant sputtering occurring while the ion beam images, the system is kept at a low beam current in order to minimize sample damage. Typically, there are two different detectors employed in the FIB system to collect secondary electrons for image formation: a multi-channel plate, which is mounted above the sample, and an electron multiplier, which sits at an angle of 45° to the incident angle on one side of the ion column. The electron multiplier can detect either secondary electrons or secondary positive ions. Secondary ions give a different image contrast from secondary electrons.

Secondary electron imaging capabilities are directly proportional to the surface effects of the collision.

It is also possible to have a dual platform system, which has both an ion and electron column (FIB and SEM essentially), as shown in Figure 20. This allows electron beam imaging without unwanted sputtering damage of the sample. This system has additional capabilities to FIB or SEM alone, such as creative milling, in-situ selective deposition, three dimensional imaging information, etc.
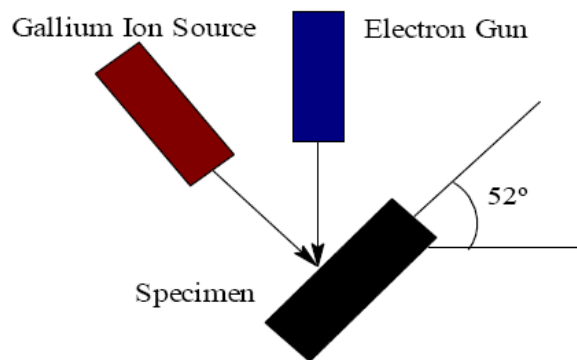
Figure 20. Simple schematic diagram of a dual platform, electron and ion beam, system.

One major attraction of dual-beam FIB/SEM is precision cross-sectioning for defect analysis, process and materials characterization, process control and monitoring, etc. Indeed, the dual beam instrument is ideal for cross-sectioning as it is able to use the electron beam to view a face, while the ion beam mills normal to the surface of the sample. This allows for milling to be stopped at the precise moment when desired, when the feature of interest is exposed. With the capabilities in creative milling, the sample can be rotated along with milling in order to cut a certain shape, or to design a custom pattern.
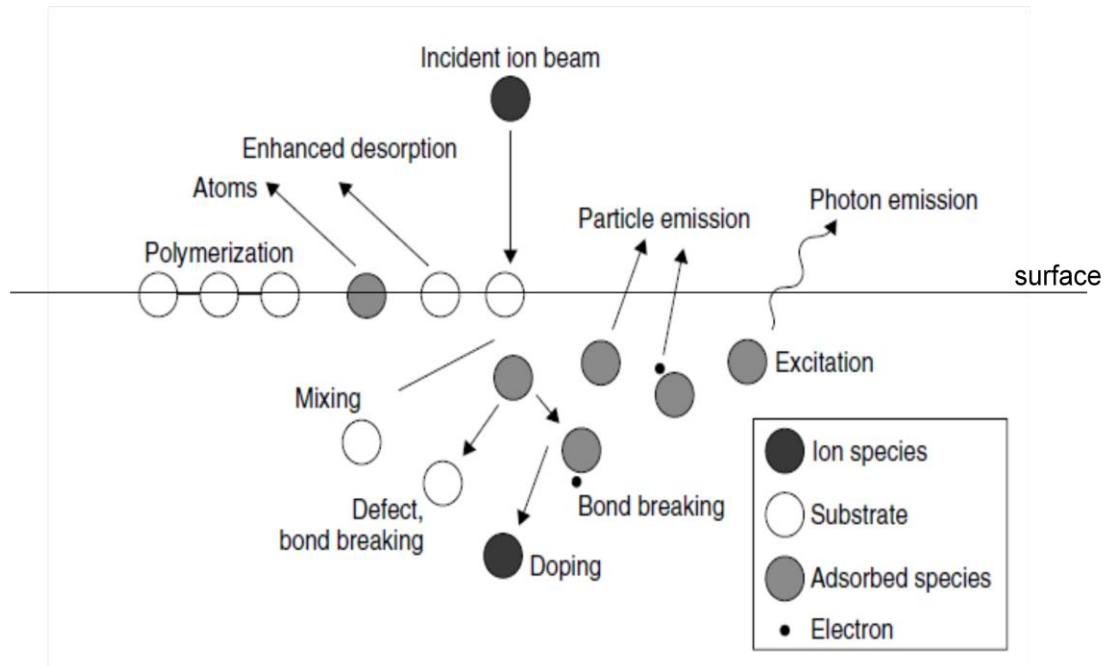
Figure 21. Possible interactions of the incident ion beam with the sample. [63]

Figure 21 illustrates some of the possible interactions at a surface under ion beam bombardment. Sputtering can result from a series of elastic collisions where momentum is transferred from the incident ions to the surface atoms over a collision cascade region;[62] where a waterfall of particles have collided at a point and begun to change direction with fluidic movement. Inelastic interactions also occur during bombardment. This can result in production of phonons, plasmons (in metals), and in the emission of secondary electrons. In general, the number of secondary electrons generated per incident ion is 1, which is 10 to 1000 times greater than the number of secondary ions generated per incident ion.[64]

Often FIB is not only used as a milling device to remove material, but as a tool to create or add material. An area being milled has sputtered ions that are implanted and/or

redeposited around the milled area. Redeposition is a function of: a leaving atom's kinetic energy, the sticking coefficient of the target, target geometry, and sputtering yield. This is the reasoning given for a square milled area tapering down to a point or "v" at the bottom, the sputtered atoms being deposited back onto the surface around where they were milled, creating a limited aspect ratio in the milled hole. If this is not a desired effect, it can be countered through reaction with a gas, such as chlorine, iodine or xenon fluoride, which reacts with the sputtered material, allowing it to be volatized into the vacuum system. The gas may however react with the sample material as well. Hence, it is desirable to alter the incident angle to one which, depending on the material, will lessen the v-shaping effect.

In Figure 24, the images show a progression of redeposition as the aspect ratio increases. The trench that is most shallow is also more smooth and even, whereas there is a gradual roughening in the next trench, and finally the third case has an obvious rough v-shape due to redeposition.
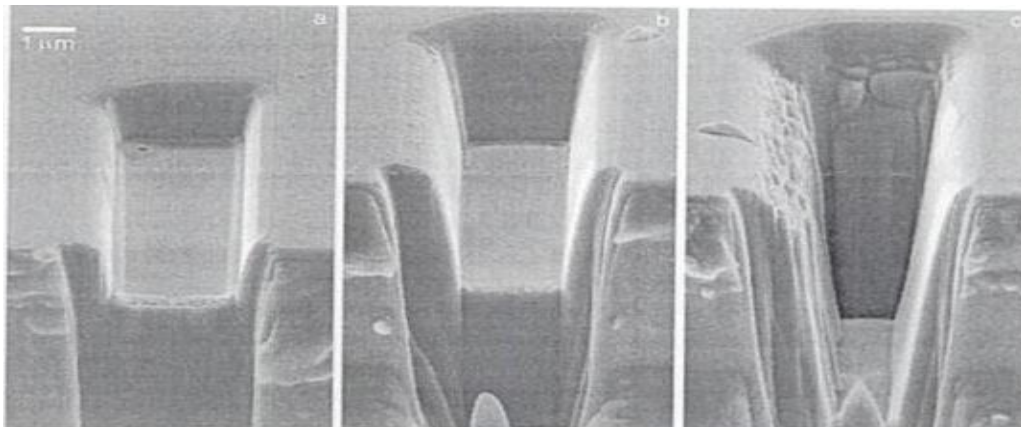
Figure 22. Rectangular FIB of (100) Si trenches milled at normal incidence by applying: (a) single fluence, (b) double fluence, and (c) triple fluence of Ga+ ions at 25 keV.[62]

2.3.6 TEM

Transmission electron microscopy (TEM), is a technique that is similar to SEM, but detects mainly transmitted electrons, which pass through the specimen being studied, and are detected beneath the sample stage (Figure 18). The sample employed must therefore be quite thin, in order to allow a majority of electrons to pass through and be detected. These transmitted electrons will provide information about the atomic density of the material under scrutiny; thus, an image of the structure of the material is reported. Improvements in the technique are constantly being made through the implementation of better lenses to control the electron beam and avoid things like spherical and chromatic aberrations. Through these improvements, the images become more resolved, and, through filtering out electrons of certain wavelengths, thicker samples can now be studied. Compared with SEM, TEM has much higher resolution. However, SEM has a larger depth of field and can study thicker samples.

Akin to visible light microscopes, electrons also have resolution limits. The resolution of electron microscopes is limited to wavelength, as is observed by de Broglie:

$$\lambda = \frac{1.22}{\sqrt{E}}$$

Where *E* represents energy. The wavelength of an electron is thus related to its energy. More specifically for a 100 keV electron, the wavelength would be around 4 picometres; thus, the resolution can be much smaller than the diameter of an atom.[46]

An interesting feature of TEM is the focus, where both top and bottom surfaces are in focus at the same time. This is especially unique compared to the VLM that, unless

a specimen is flat, can only focus on one area, not the entire field of view. This opens up possibilities for TEM as a technique for field of view mapping. On the other hand, the technique can only analyse a very small sample area. Thus, it is not an excellent technique for bulk analysis. This means that TEM analyses must be combined with SEM or VLM measurements in order to get a more comprehensive picture of the material under investigation. TEM has, however, been expanded into a scanning transmission electron microscope, which scans over more area than one field of view. Another disadvantage of TEM is that the two dimensional images can be difficult to interpret correctly, as there is no sensitivity to sample depth. Also, depending on the voltage used, the electron beam can damage the sample, and thus not provide accurate original imaging of the specimen.

The depth of the sample is dependent upon its atomic number as well as the electron energy. In practice, a sample that is under 100 nm in thickness should be employed.[46] TEM samples are often prepared using FIB, which can precisely mill material from a greater specimen. Thus, one of the main purposes of a FIB instrument is its employment in preparation of samples for TEM analysis. However, having to purchase a TEM instrument for analysis, as well as a FIB one to prepare TEM samples would be a very costly endeavour. Furthermore, FIB employs an ion beam to remove material from the surface through sputtering, meaning that the surface will no longer be the same after a sample is prepared. This problem can be reduced through the application of protective layers, which are composed of metals, such as platinum (Pt) and W, which prevent sputtering from redepositing material to the area of interest, hence altering the surface structure. Because these protective layers are not ideal, the surface of the material will most likely still be altered.

FIB sample preparation for TEM begins after a sample has been mechanically cut into suitable dimensions for placement into the FIB system. The ion beam mills at vertical incidence to the sample, milling the front and back sides of the sample using a gradient of beam diameter and current settings.[65]   Once the sample has undergone the finest milling and is thin enough for TEM study, it is placed on a TEM grid at the appropriate angle for TEM study, or into the TEM system if separate.
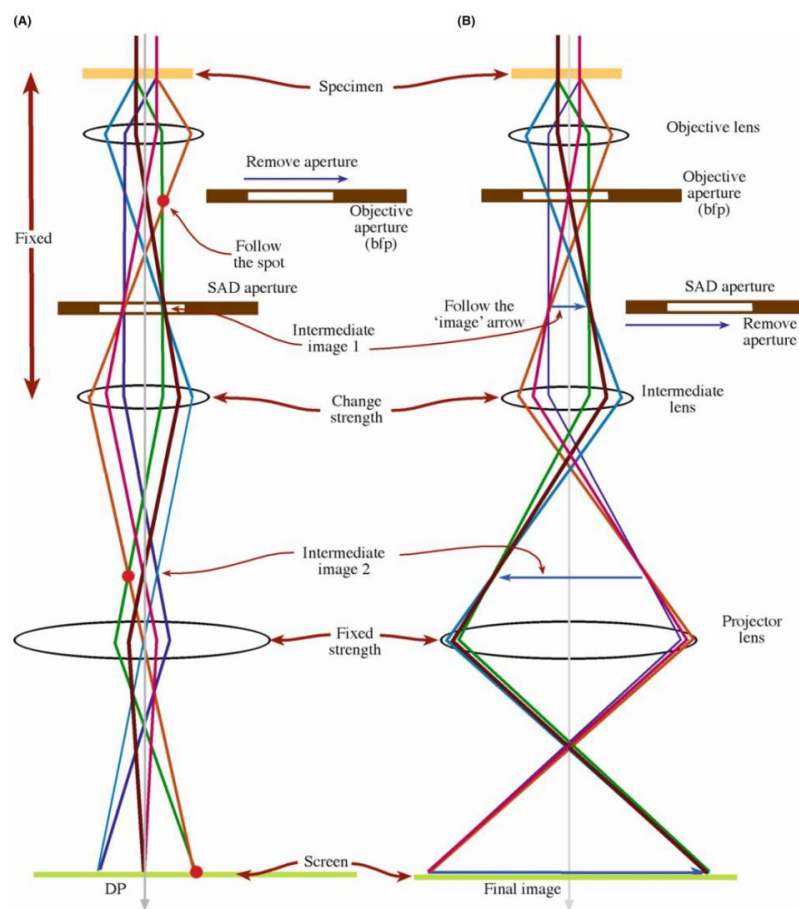
Figure 23. TEM system with the two operations: (A) Diffraction mode, which shows electron diffraction patterns, and (B) Imaging mode, which will show the image plane of the lens.[46]

Figure 23 illustrates the operating principles of the TEM system, which has the capability to image as well as to report diffraction patterns. These patterns will be explained further in the section on electron backscattering diffraction (EBSD). It uses the same electron beam system as described in the previous section on SEM and FIB. However, because SEM does not require electrons to be transmitted for detection, much lower beam energy (1-30 keV)[66] is used than in TEM (100-300 keV).[60]

2.3.7 EBSD

Electron diffraction experiments are essential when studying the crystal structure of materials. Through the study of converging beam patterns, the crystalline symmetry or whether a material is crystalline can be determined. Analysis stems from the knowledge that the greater the angle of scatter, the further off center an electron will hit the film; thus, distances correspond to scattering diffraction. As thicker materials will result in electrons being scattered in many directions, there is a requirement for a technique to analyse the angle of their Bragg diffraction. This technique was described in 1928 by Kikuchi, and employs Kikuchi lines to calculate the Bragg diffraction of incoherently scattered electrons.[46] Kikuchi bands correspond to the lattice planes, and thus represent the miller indices of a crystal lattice.

Electron backscattering diffraction, EBSD, is a separate technique that also employs Kikuchi lines to study crystal structure of materials. However, in this case, SEM is employed instead of TEM.
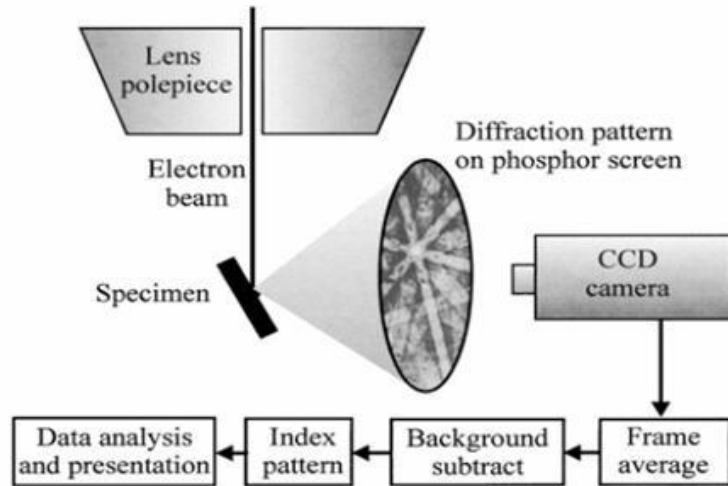
Figure 24. Schematic diagram of EBSD within an SEM system.[67]

As shown in Figure 24, the specimen is tilted about 70° towards a CCD camera, and a phosphor screen focuses the electron image on the camera.[68] The electrons backscatter from the material until they exit according to the atomic lattice present in the crystalline structure. Backscattered electron signal will increase with the atomic number of the specimen, as does the spatial resolution and quality of the diffraction pattern.[68] Kikuchi bands are then employed for analysis, most often using software for mathematical calculations in order to gain information about the crystal structure. Patterns are identified using a Hough Transform, and are then mapped accordingly. The patterns can be seen with and without Kikuchi lines in Figure 25.
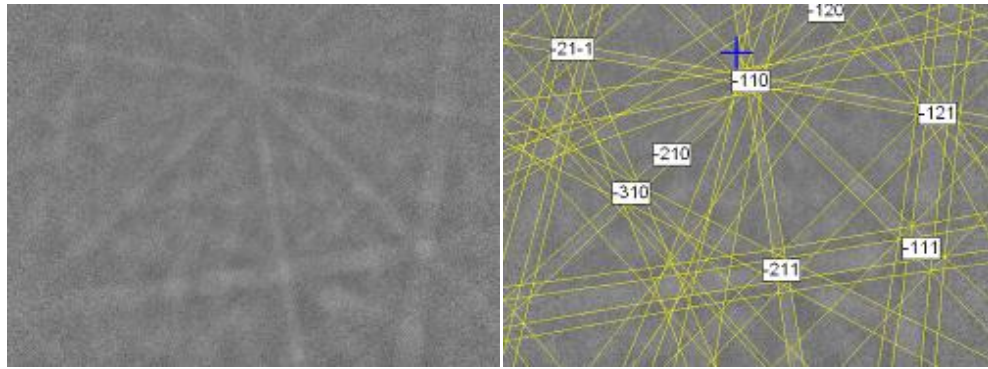
Figure 25. EBSD pattern on left, and the same pattern analysed with Kikuchi lines on right.

Compared with TEM electron diffraction, this technique is advantageous because it does not require thin film samples to be prepared using expensive equipment such as FIB. However, the spatial resolution is inferior, data acquisition takes longer, and single defects cannot be examined. Another drawback of this technique is that the sample preparation is not overly simple; although simpler than for TEM, it still requires time-consuming polishing techniques. Mechanical polishing is not sufficient because it will alter the surface structure of the crystal, and the backscattered electrons will only interact with the surface portion of the sample. Therefore, complex chemical polishing processes must be employed in order to maintain as much of the crystal lattice structure on the surface as possible.

2.3.8 ICP-MS

Inductively coupled plasma mass spectrometry (ICP-MS) is a technique with many applications, especially in identification of specific elements and their

concentrations.   Because it can be used for multielement ultra-trace analysis, it has

become prevalent in many areas.   Some advantages of the technique lie in its ability to

determine many elements at once with precision and accuracy, as well as the ability to

work with all phases of samples, especially those in solutions.   It also enables the

measurement of isotope ratios, which further broadens the range of application to tracer

and provenance studies, for example.   A typical setup of an ICP-MS system is shown in

Figure 26.
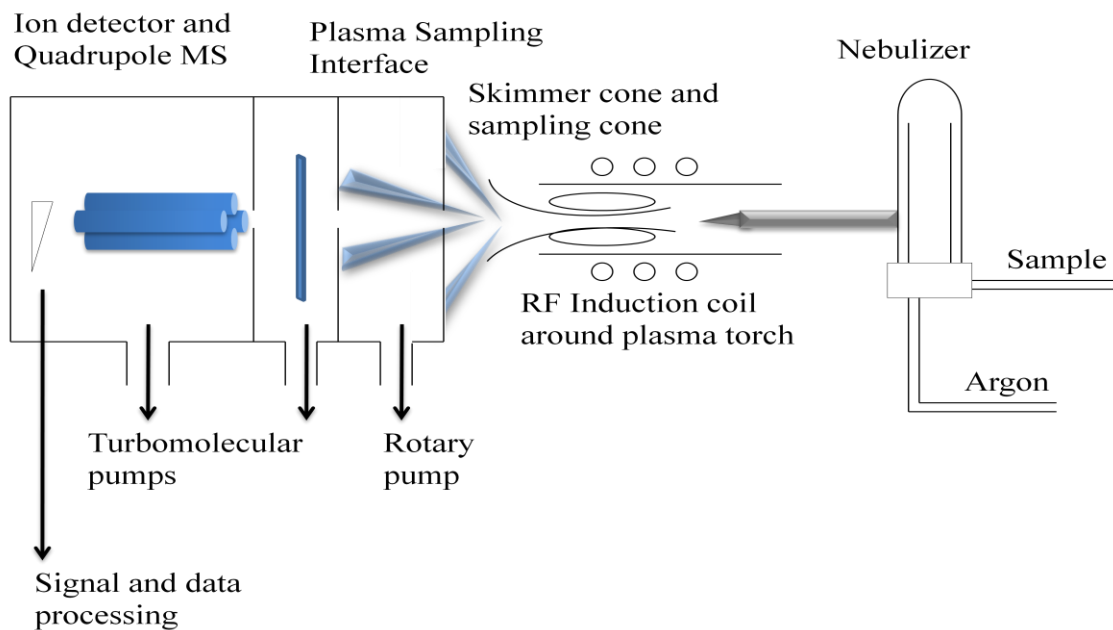
Figure 26. Schematic diagram of a typical ICP-MS instrument.

Typically, the sample is introduced via a peristaltic pump for consistent and even

flow to a nebulizer, which transforms it into an aerosol.   This nebulizer then traverses a

spray chamber, which ensures that only the smallest droplets will make it into the plasma,

larger droplets going down the drain after colliding with the walls of the chamber.   The

heart of the ICP-MS instrument is the plasma, which is composed most commonly of argon (Ar), and generated in a quartz torch, as can be seen in Figure 27.
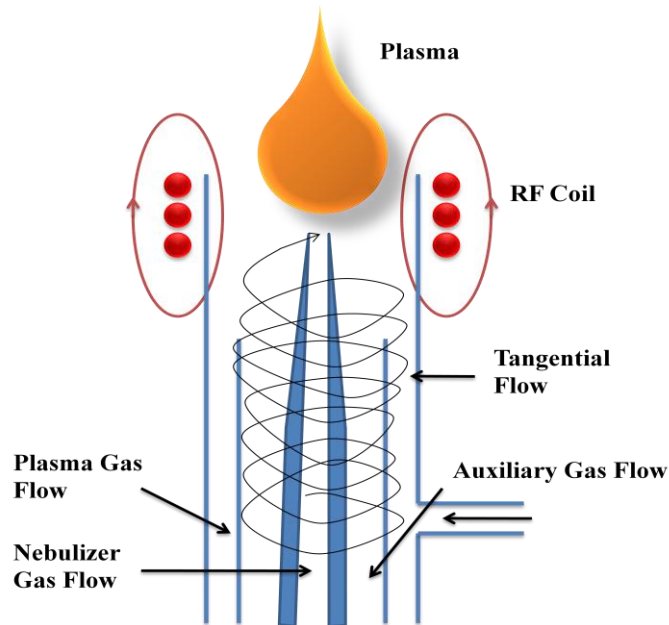
Figure 27. Plasma torch for ICP-MS.[69]

The plasma temperature is about 5000-10000 K. The main plasma gas, which has a flow rate of about 15 L/min, flows through the outermost tube of the torch, sustaining the plasma and also preventing it from coming in contact with the walls of the torch, which could then melt. The auxiliary gas flows at about 0.75 L/min in the intermediate tube, and controls the position of the plasma relative to the front of the torch. The nebulizer gas flow transforms the sample into an aerosol and introduces it into the plasma at a rate of 1 L/min. Several processes sequentially take place in the plasma: desolvation, vaporization, atomization and ionization. Ions are extracted into the mass spectrometer through two cones: the sampler and skimmer cones. The former is in contact with the plasma, of which it takes a sample, while the latter only allows the centerline of the

58

plasma to enter the MS (thus skimming out the bulk of the Ar). The mass spectrometer used most commonly for ICP-MS is a quadrupole because they are compact and simple in design. However, double focusing and time of flight instruments may also be employed. Quadrupole analysers only provide low mass resolution, which can complicate the analysis by requiring additional steps to remove the source of spectroscopic interference, where ions of similar mass-to-charge ratio as the analyte are erroneously measured as analyte ions.

Inductively coupled plasma mass spectrometry can also be employed to analyse solid samples using laser ablation or electrothermal vaporization techniques. Laser ablation employs a laser to expell material from the sample surface, which is then transported by a carrier gas (often Ar) into the ICP-MS analyser. This technique allows direct sample introduction, without the use of a nebulizer or spray chamber, thus reducing contamination. Electrothermal vaporization (ETV) is a technique where analytes are volatized in a furnace prior to their introduction into the plasma, thus leaving the plasma with more energy for atomization and ionization. Electrothermal vaporization can also reduce interferences due to its ability to separate matrix components from the analyte. Furthermore, it can analyse both solid and liquid samples, and is thus more practical than laser ablation if both phases of samples are under scrutiny.

Some limitations of ICP-MS as a technique include: physical, chemical, spectroscopic and finally non-spectroscopic interferences. Physical interferences involve different solutions being nebulized differently due to variations in their viscosity. This issue can be minimized using a peristaltic pump. Chemical interferences, where refractory compounds are not atomized, are often not an issue due to the high temperature

of the plasma, and can only become an issue with very high matrix concentrations. Spectroscopic interferences occur when there is another analyte, matrix element or polyatomic ion with the same mass-to-charge ratio as the analyte, and must thus be taken into consideration when using ICP-MS. With proper knowledge of sample composition, these interferences can be predicted and avoided by, for instance, measuring at another m/z. Collision reaction interfaces can also be employed to break up polyatomic species and thereby reduce their interference. Lastly, non-spectroscopic effects occur when the analyte signal is suppressed or enhanced by the sample matrix. That is why non-spectroscopic interferences are also called matrix effects. Often, if there is a large concentration of a heavy element in the matrix and a light element is the analyte, analyte signal suppression of large magnitude may result. Mass discrimination plays an important role in suppression, where space charge effects result from repulsions between like charges in the ion beam. The greater the ion beam current, the more extensive will be the space charge effects.

Several calibration methods can be employed for quantification, such as: external calibration curves, standard addition, and isotope dilution. The most appropriate method depends on the sample and the number of isotopes that are free of spectroscopic interference for each analyte. Occasionally, a drift correction may be required, usually using internal standardization.

Another important limitation of ICP-MS is a low tolerance to dissolved solids. Since the technique is limited by the amount of dissolved solids in samples, it can require pretreatment methods to remove the matrix and/or preconcentrate the analytes, especially in the case of saline solutions. Flow injection, which involves discrete sample injections

into a continuous flow of carrier, is often used for saline solution analysis. This technique minimizes sample consumption and contamination, as it is performed on-line, in a closed manifold.

2.3.9 Polarization Curves

Determining the corrosion behaviour of metals is very important in studying their optimal performance. Electrochemical analysis methods are practical for corrosion quantification since the corrosion process occurs through an electrochemical mechanism. An effective and rapid method, which is often employed, is the study of potentio-dynamic polarization curves that are performed in a controlled environment for a given time and can thus be used for comparative analysis. The potential and rate of corrosion can be determined. This electrochemical method is thus ideal for the study of corrosion properties, performed efficiently and effectively.

Polarization refers to the process resulting from the overpotential (η), which is the difference between the electrode potential and its zero-net value at equilibrium. Because the current density, j, is related to overpotential, if η is positive, j will be positive and the overall current is anodic; inversely, if η is negative, j will be negative and the current is cathodic. Through electrochemical methods, both anodic and cathodic polarizations can be studied. In order to obtain kinetics information on corrosion, anodic polarization curves are often recorded. The polarization curve can be expressed by the Butler-Volmer equation.[70]

$$j = j_0 \left[e^{\frac{\alpha nF\eta}{RT}} - e^{\frac{((1-\alpha)nF\eta)}{RT}} \right]$$

Where R is the gas constant, T represents the absolute temperature, j_0 is the exchange current density, n is the number of electrons transferred, α is the transfer coefficient (assumed to be 0.5), and η is the overpotential ($\eta = E - E_0$). When anodic overpotential is high, the metal cation deposition becomes negligible, thus:

$$j = j_0\, e^{\frac{\alpha nF\eta}{RT}}$$

Consequently, the Tafel relationship is shown below:

$$\eta_a = \beta_a\, log^{\frac{j_a}{j_c}}$$

$$\beta_a = \frac{2.303RT}{\alpha nF}$$

The Tafel coefficient (β) is determined from the slope of η_a versus log of the anodic current density (j_a) over the cathodic current density (j_c).

A polarization curve typical of a metal undergoing an active to passive transition is shown in Figure 28. This image shows the division of a polarization curve into distinct regions defined by letters A to F. Region AB shows the hydrogen generation region (cathodic polarization), region BC shows the active region (metal dissolution), and region C shows the end of increasing current density and thus the onset of passivation. Point C is characterized by both the primary passive potential (critical potential, E_{pp}) and the critical current density (j_{cc}).[26]   The critical current density is the value required to produce a sufficient amount of metal cations on the surface for a surface film to develop.

Thus, this is the beginning of passivation, and where the primary passivation potential lies (E_{pp}). Region CD experiences rapid decreasing current density as the passive film forms. Region D completes the active-passive transition, and the surface is fully passivated. Region DE is the passive region (metal dissolution) where current is independent of potential, and finally region EF is the transpassive region. At point E, the potential at the onset of the transpassive region is called the breakdown potential (E_b), where current increases above the passive value and the oxide film begins to dissolve or break down. For passivation to occur, two conditions should be met; (i) the equilibrium potential of the cathodic reaction must be greater than E_{pass}, and (ii) the cathodic reaction must be able to drive the anodic reaction to a current density of equal or greater value than j_{cc}.[70]
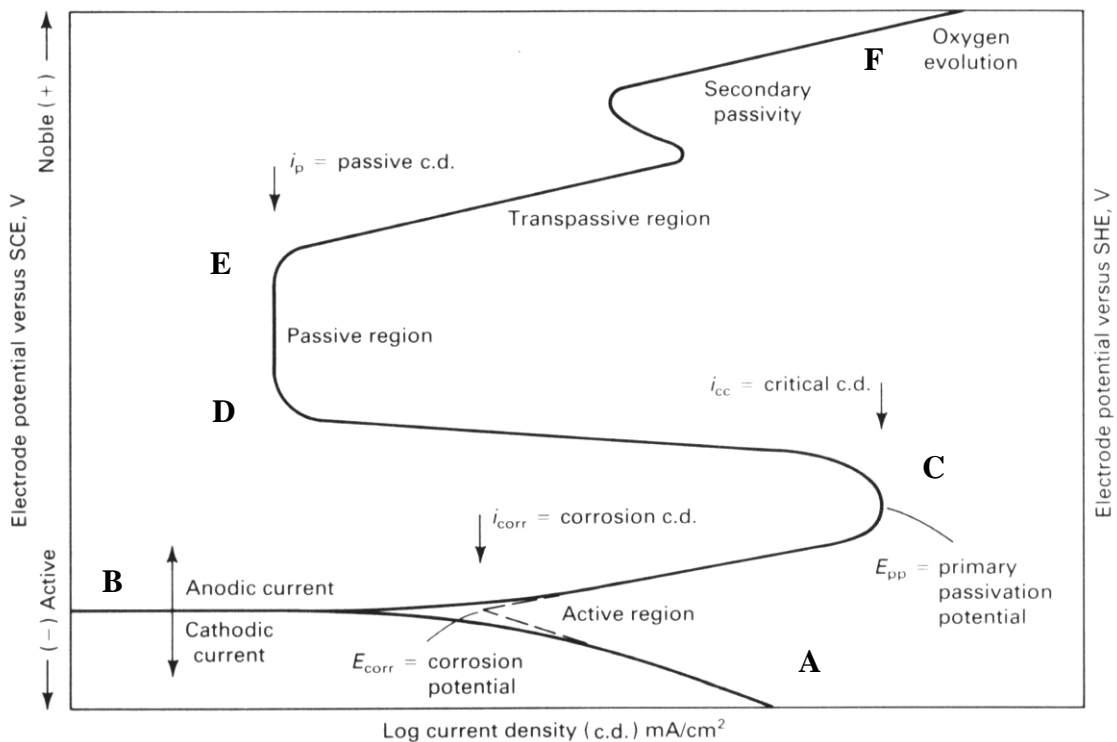
Figure 28. Hypothetical anodic and cathodic polarization behaviour for a material undergoing anodic passivation.[71]

Through the Tafel extrapolation of the ABC regions, the corrosion potential (E_{corr}), and the corrosion current density (j_{corr}) can be obtained. The Tafel relationship can be seen in Figure 29.
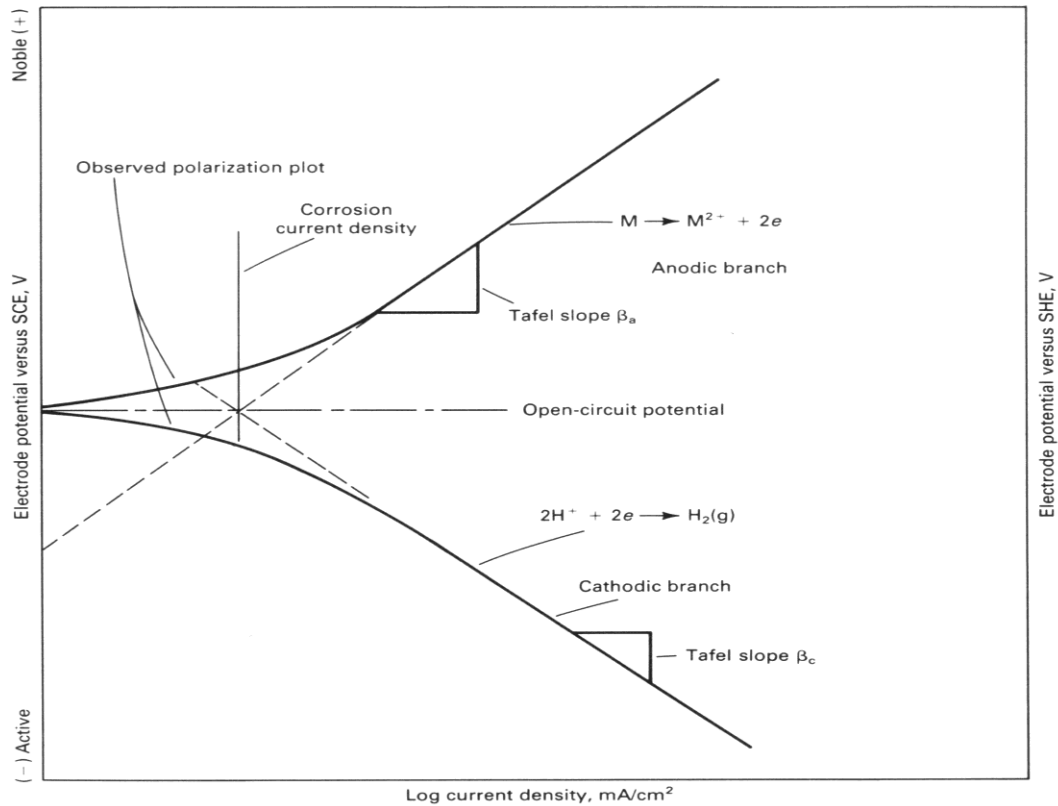
Figure 29. Illustration of Tafel extrapolation to estimate corrosion current density, j_{corr}.[72]

The above graph shows how to calculate the corrosion current density (j_{corr}), as well as the open–circuit potential. The open-circuit potential in this case can also be called the corrosion potential (E_{corr}). Each half of the cell reaction must polarize to a common intermediate potential where they are equal; thus, anodic dissolution (i_a) and cathodic current (i_c) are equal at E_{corr}. Corrosion current density refers to the material lost

due to corrosion, per unit time. With a higher value of j_{corr}, more corrosion is occurring over time. Electrochemical corrosion rates can be calculated either as weight loss per unit area or in terms of current density.[73]

The potential-current density plot is relatively linear within 50 mV of the corrosion potential (E_{corr}).[73] Through the obtained value of slope, a measure of potential resistance may be obtained, and related to the corrosion current density.

$$\frac{j_{net}}{E} = \frac{1}{R_p} = \frac{j_{corr}}{2.3}\left(\frac{\beta_a + \beta_c}{\beta_a\beta_c}\right)$$

In the above equation β_a and β_c are magnitudes of Tafel slopes (anodic and cathodic).[73] The net current density is shown as j_{net}, and the potential resistance is R_p. This method is attractive due to the ease and speed of information gain. Electrochemical methods of analysis such as linear sweep polarization provide information on corrosion point, corrosion rate and stability of the working electrode under study. These tests are performed in the specific closed environment of an electrochemical cell. The cell can be designed in a few different fashions, but the basic principles are the same. A drawing of a three-compartment electrochemical cell can be seen below, in Figure 30.
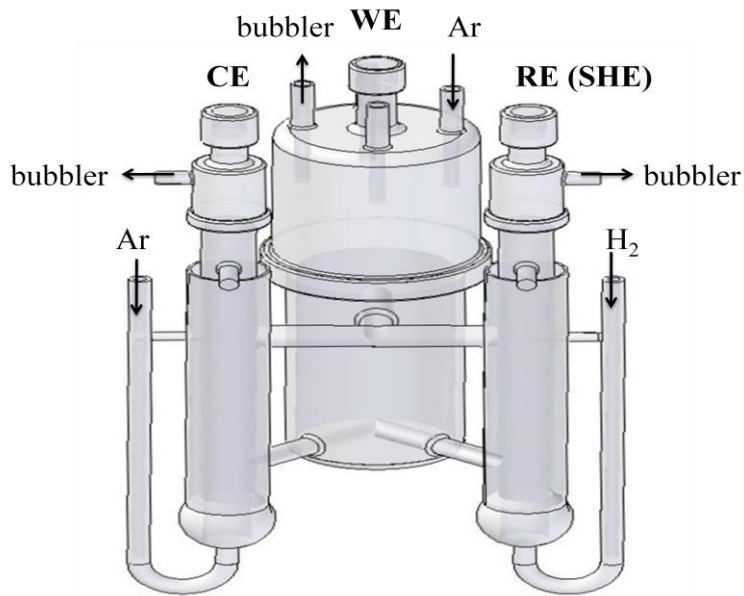
Figure 30. Schematic representation for the standard three-compartment electrochemical cell used for electrochemical measurement. CE: counter electrode; WE: working electrode; RE: reference electrode.[26]

Cells are most commonly fabricated from glass or occasionally from quartz. This is to allow for visual inspection and monitoring, as well as extensive cleaning procedures using permanganate, hydrogen peroxide and sulphuric acid. There are glass tubes on the outer regions of the cell, responsible for transporting gases into each compartment. The reference compartment is bubbled with hydrogen gas in order to saturate the solution surrounding the reference electrode with hydrogen. The main compartment in a two-compartment cell, or the two other compartments in a three-compartment cell, are bubbled with inert gas (argon or nitrogen), to remove reactive gases in solution. Both compartments are connected by a Luggin capillary to facilitate ion interaction and therefore ionic conductivity in both solutions. The Luggin capillary is responsible for

minimizing IR drop,[74] which is a potential loss due to electrolyte resistance between the Luggin and working electrode. It is possible to separate compartments with membranes and other devices, as well as to employ three compartment cells instead of two. However, it is advantageous to keep the working electrode and counter electrode near one another for minimal cell resistance.[74] There are three electrodes; working, counter and reference. The working electrode is the material of interest, and is where reactions take place. The counter electrode is commonly made of platinum wire with high surface area compared to that of the working electrode. The potential of the working electrode is measured with respect to the reference electrode, which can be made of specific materials in order to fulfill a redox couple, such as platinum, mercury (calomel), copper, and silver nitrate. Often a standard hydrogen electrode is employed for simple reference. The potential of the reference electrode is constant, and the current flows between the working and counter electrodes.

2.4 Thesis Objectives

Since experimentation in the area of medical and dental implantation was performed by previous group members, this project instead focuses more on gaining further insight into corrosion in saline solutions relating to other industries, such as: automotive, marine and aerospace. There is also a goal to look in detail at morphology and thickness values of Zr passive layers, and their optical properties to better understand the colouration of passive films. Thickness results were previously concluded for Ti passive layers, and will be investigated for Zr through experiments using scanning

electron microscopy (SEM) combined with focused ion beam (FIB). The surface properties will be studied using reflectance spectroscopy in the near infrared (NIR) ultraviolet (UV) visible region, visible light microscopy (VLM) techniques, profilometry, and finally atomic force microscopy (AFM). Corrosion studies will be performed in order to examine the stability of these passive layers in aggressive aqueous media using electrochemical experimentation methods as well as inductively coupled plasma mass spectrometry (ICP-MS).

AFM is a useful technique for this work because it has the ability to probe very specific surface defects using its high resolution capabilities, in order to study the surface of passive layers more closely than profilometry. However, profilometry provides a broader roughness value and surface map. Differences that applied AC voltage create on the oxide layer surface can be observed, which can be used to determine whether thicker passive layers are smoother, or whether they become too close to electrochemical breakdown to be defect-free.

SEM and FIB techniques will be used to analyse the passive layers on Ti and Zr. Since these are metals, they are conductive and thus simple to prepare as samples for SEM and FIB analysis. Through the milling capability of FIB, it is possible to create a crevice in which the layers of metal and surface oxide become clearly visible, and thus can be measured in size due to the precision of the instrument. Scanning electron microscopy can be employed for imaging as FIB will continue to sputter material away from the surface. Another important application is in fabrication of samples for TEM analysis. TEM was a useful technique to study the material closer, and look at the structure of both substrate metal and the thin passive layer. The studies done using TEM

allowed for speculation into whether the structure of the passive layer was crystalline, and thus electron backscatter diffraction (EBSD) became an essential technique in order to prove this hypothesis, and to see whether the structure of the oxide layer atop Zr was not amorphous as was initially speculated.

In reference to this project, ICP-MS is a useful technique in order to gain information on corrosion resistance properties in aqueous media. Specifically, samples can be immersed in solutions and aliquots of solution taken over time in order to see the gradual metallic ion release. This provides information on how metals react with and without passive layers, while in contact with solution. The specific relevance is to many applications of Ti and Zr, where the materials come into contact with saline media such as salt water (boats), winter water conditions and salted water (aircraft), and finally bodily fluid (medical and dental implants). Knowing the corrosion properties of passive layers compared to the unpassivated metals in salt-containing solution becomes relevant to many applications, and important to future employment of electrochemically-formed passive layers. Flow injection ICP-MS was employed for the experimentation in this project, since saline solution was prevalent.

Electrochemical analyses were essential since the knowledge of corrosion properties is a measure of how protective passive layers are of the underlying metal. The ability to employ any desired electrolyte as the medium in which the material will be studied allows for the design of experimentally practical comparisons to realistic corrosion situations. A salt solution (1% NaCl) can be used as electrolyte, as it is common in many applications of Ti and Zr such as in medical and dental implants (bodily fluids), marine use (seawater), aviation use (road/environmental salt), and other

applications. Through the use of these results and those for ion release over time obtained by ICP-MS, a comprehensive picture can be obtained of the corrosion properties for metals and passive layers.

Chapter 3   Experimental

3.1 Electrode Preparation and Passivation

The Ti and Zr foils used were 0.890 mm (0.035 in) thick, 99.7% (metals basis 0.0875 wt.% Fe, 0.1225 wt.% O, 0.0015 wt.% N, 0.0095 wt.% C, 0.0023 wt.% H), and 1.00 mm (0.039 in) thick, 99.2% (metals basis including Hf of 4.5% max), respectively. Titanium and Zr wires were 0.810 mm thick, 99.7% (metals basis 0.031 wt.% Fe, 0.054 wt.% O, 0.009 wt.% N, 0.012 wt.% C, 67 0.0047 wt.% H), and 1.0 mm thick, 99.2% (metals basis 4.5 wt.% Hf max), respectively. These wires (chemically etched) were employed in polarization curve experiments, as the working electrode. All metals were purchased from Alfa Aesar, a division of Johnson Matthey.

The Ti and Zr foil samples were cut into two different types of samples: discs of 7 mm diameter, and squares 5 mm in side length. All samples were then refluxed in acetone (three hours) for degreasing; half of the samples were chemically etched, and the other half were mechanically polished. The samples that were chemically etched were placed in an aqueous solution of 3% wt/v hydrofluoric acid (HF, Aldrich A.C.S. reagent, of 48 wt.% purity) and 5% wt/v nitric acid (HNO_3, Caledon, of 68-70 wt.% purity) to remove the native oxide on the surface and the outer layers of the metal, so as to reveal grain structure. Five to ten minutes are required for the surface to become evenly etched

and show crystalline morphology. Care must be taken to not allow the surface to etch unevenly, so as to promote a smooth surface morphology for even colouration. Thus, the samples were constantly moved while immersed in the etchant, using plastic tweezers. The mechanical polishing process employed a Struers mechanical polisher (model LaboPol-5). The polishing was done with silicon carbide abrasive papers of different grades down to 4000, followed by polishing with soft felt and alumina (1 µm to 0.3 µm) to obtain a mirror-like surface.

The samples were sonicated in Millipore water (resistance of 18.2 MΩ·cm, purified with Millipore Milli-Q system) for 1 minute, followed by a thorough cleaning with Millipore water. All samples were refluxed a second time for further cleaning and degreasing, prior to passivation. The samples were either loosely attached to a wire or welded onto a wire. The difference between these approaches is shown in Figures 31 and 32. Titanium samples were held by or spot-welded (Omicron Spot Welding Tool OM-97, 110 V, 50 Hz) onto a Ti wire for electrical contact, which is necessary for the passivation procedure, and Zr samples were held by or spot-welded onto a Zr wire.
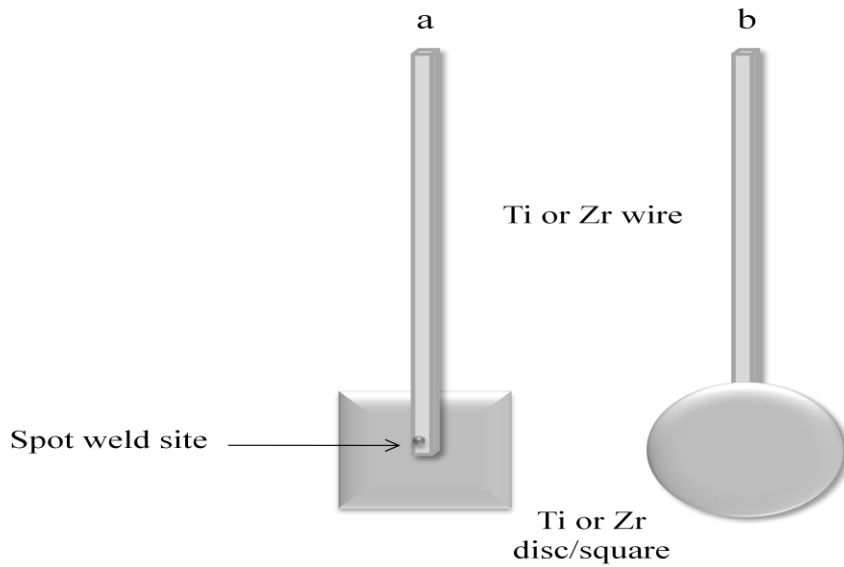
Figure 31. Layout of the (a) back and (b) front of the Zr and Ti disk- and square-shaped electrodes. All investigations and characterizations were carried out on the front face of the disk.
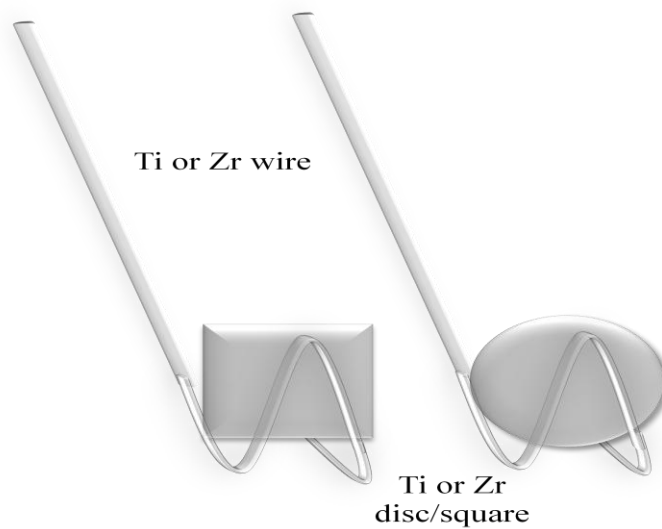
Figure 32. Layout of the Zr and Ti disk- and square-shaped loose electrodes. All investigations and characterizations were carried out on either face of the disk.

The samples were passivated in their respective electrolyte solutions. For Ti, the electrolyte was aqueous ammonium tetrafluoroborate (wt.% 7.5% NH_4BF_4, Aldrich, of 97+ wt.% purity), and, for Zr, the electrolyte was aqueous sodium sulphate (wt.% 10% Na_2SO_4 powder, Aldrich A.C.S. reagent, of 99+ wt.% purity). Both the circular and wire-shaped Zr electrodes were immersed in a single compartment electrochemical cell where the growth of a coloured passive layer was carried out by application of a required AC voltage, V_{AC}. The counter electrode was made of platinum (Pt) foil spot-welded to a Pt wire (Johnson-Matthey, 99.9 wt.%); its real surface area was at least 10 times greater than that of the Zr one. The distance between the Zr electrode and the Pt one was ca. 5 cm. This separation was sufficient to allow for effective circulation of the electrolyte between the electrodes and for removal of the gases generated during the AC polarization. In general, the preparation procedure applied in the course of research ensured good reproducibility of the experimental results. The samples were passivated by applying AC voltages at a frequency of $f = 60$ Hz, for ten seconds. The AC voltage applied was in the 10 to 80 V range. The variable power supply used was 3 KVA AC Power Source Model 3001iM, California Instruments, San Diego, CA. The solution was magnetically stirred in order to expel any gases evolved during colouring and to maintain electrolyte mixing, and it was kept at a temperature of 25 °C (298 K). Stirring and temperature control lead to more evenly coloured layers. The electrochemical setup used to colour Ti and Zr is shown in Figure 33. All glassware involved in experiments and measurements went through a cleaning procedure involving a three-step soaking process in $KMnO_4$ and H_2SO_4 for 24 hours, 30% wt/v H_2O_2 for 24 hours and finally in concentrated H_2SO_4. Between each step in the glassware cleaning process, the specimens were washed with Millipore water a minimum of eleven times, before moving on to the next treatment.
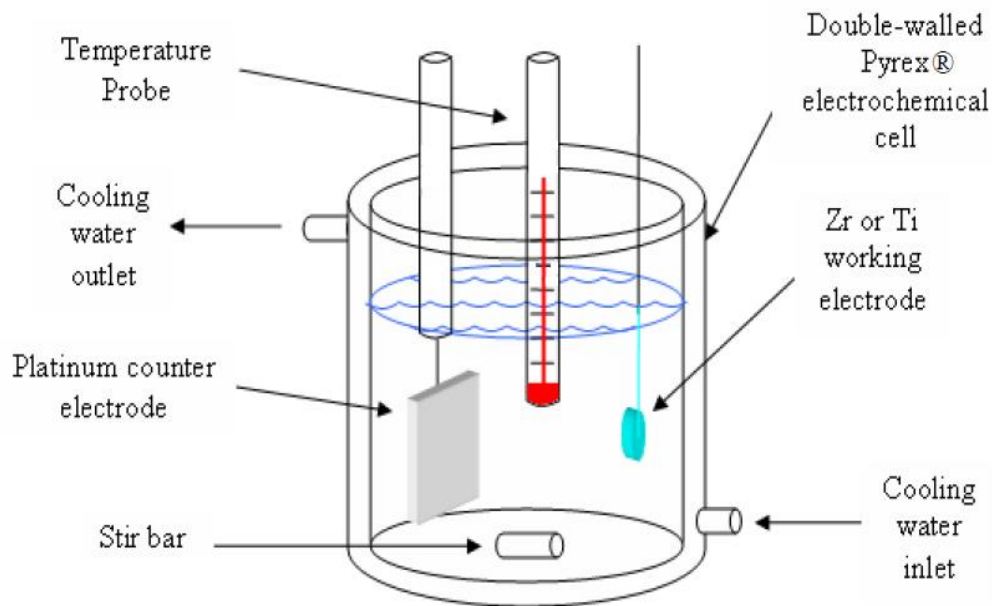
Figure 33. Apparatus for electrochemical passivation of Zr and Ti electrodes.[42]

For electrochemical studies, the wire-shaped electrodes were made of Ti or Zr wire (described above). They were connected to a copper wire through an electric connector and sealed with epoxy resin (Struers); only the Ti/Zr wire was in contact with electrolyte. Upon the resin hardening, the Ti/Zr wire was cut to a length of 1.0 cm and the incision was polished with sandpaper using a mechanical polisher (Struers) to reach a nice, flat end. The wire-shaped electrodes were subsequently degreased in acetone and rinsed with Millipore water. Then, they were treated in the etching solution described above, rinsed with water, and sonicated in an ultrasonic bath (Branson) for 1 min prior to experiments taking place.

74

3.2 Visible Light Microscopy

Quality, grain structure, and colouration of the passive layers on Ti and Zr were studied using a visible light microscope (Seiwa Optical SDMTR, bulb: 20 W and 6 V) capable of 400x magnification.

Additional surface morphology, colouration and grain structure studies were performed on etched Zr samples using a high-resolution Zeiss AXIO Imager M2 MAT visible light microscope. This microscope has a unique ability for automated focus, allowing it to make measurements at different focal lengths, and select the ideal focal length for the desired area of study. If a sample is not uniformly flat, it will crop the image in order to remove the out-of-focus areas, thus centering on the region of interest.

3.3 NIR-UV-Vis Reflectance Spectroscopy

Reflectance spectroscopy measurements were conducted using a UV-Vis-NIR light source (DH-2000-BAL) through an optical fibre connected to a high-resolution spectrometer (HR-4000) from Ocean Optics. The spectrometer was capable of detecting in the 200-1100 nm range. The light source, with a range of 215-400 nm (deuterium bulb), and 360-2000 nm (tungsten halogen bulb), had a 400 μm High-SR fibre optic cable. The use of this combined tungsten halogen and deuterium light source allows for elimination of saturation and signal-to-noise problems that can be associated with a deuterium light source. A mirror (STAN-SSH High-reflectivity Specular Reflectance Standard) was employed to supply a background spectrum before any measurements were taken. The software utilized to collect the data was Spectra Suite (Ocean Optics Inc.).

During data acquisition, an integration time of 200 ms was used, along with an average of 50 acquisitions and a boxcar average of 10 data points. The software was operated in specular reflection (RS) mode.

3.4 Surface Profilometry

Surface profiling and roughness measurements were taken using a stylus profiler (Veeco Dektak® 8 Stylus Profiler) along with the associated software (Veeco Instruments Inc. 73 Software Version 8.32.001, and Veeco Vision32® Software, © 2001-2002). A high-precision programmable positioning system permits *x-y* positioning to any location over a 200.0 mm diameter area, with +/-5 μm repeatability and 3.175 μm resolution.[50] The stylus diameter is 12.5 μm, with adjustable stylus force from 1 mg to 15 mg, allowing profiling on soft or hard surfaces. The manufacturor has reported the vertical resolution of the instrument employed as 40Å. The horizontal scan length was 2.5 mm when acquiring surface roughness data. In the measurements conducted, one data point was acquired every 0.292 μm for a linear density of 3.425 data points/μm.[42] Therefore, there were roughly 8561 data points collected per scan with the above parameters.

3.5 AFM

The AFM system used for this work (Veeco Instruments MultiMode® 8 Scanning Probe Microscope) was placed on an air table for vibration isolation, and inside an acoustically insulated room, for suppression of potential vibrations due to acoustic noise.

For tapping mode measurements, a Veeco Phosphorous (n) doped silicon tip (Model: RTESP) was employed with a spring constant in the 20-80 N/m range. Resonance frequency was in the 248-357 kHz range, and the nominal tip radius of curvature was ca. 5-10 nm. For contact mode experiments, a Veeco silicon tip on a nitride lever (Model: SNL-10) was employed with a spring constant of 0.12 or 0.58 N/m depending on which side was employed. The tip radius of curvature is in the range of 14-75 nm. Scan sizes varied from 1 μm to 15 μm, with the 15 μm maps being shown in the results section, and employed for roughness measurements. Scan rate, integral gain and proportional gain were altered in order to optimize the parameters and image quality for each scan.

3.6 SEM-FIB, TEM

Scanning electron microscopy, FIB and TEM measurements were done at the Zeiss Application Laboratory in Oberkochen, Germany, using an AURIGA® Cross Beam instrument, which can be seen in Figures 34 and 35.
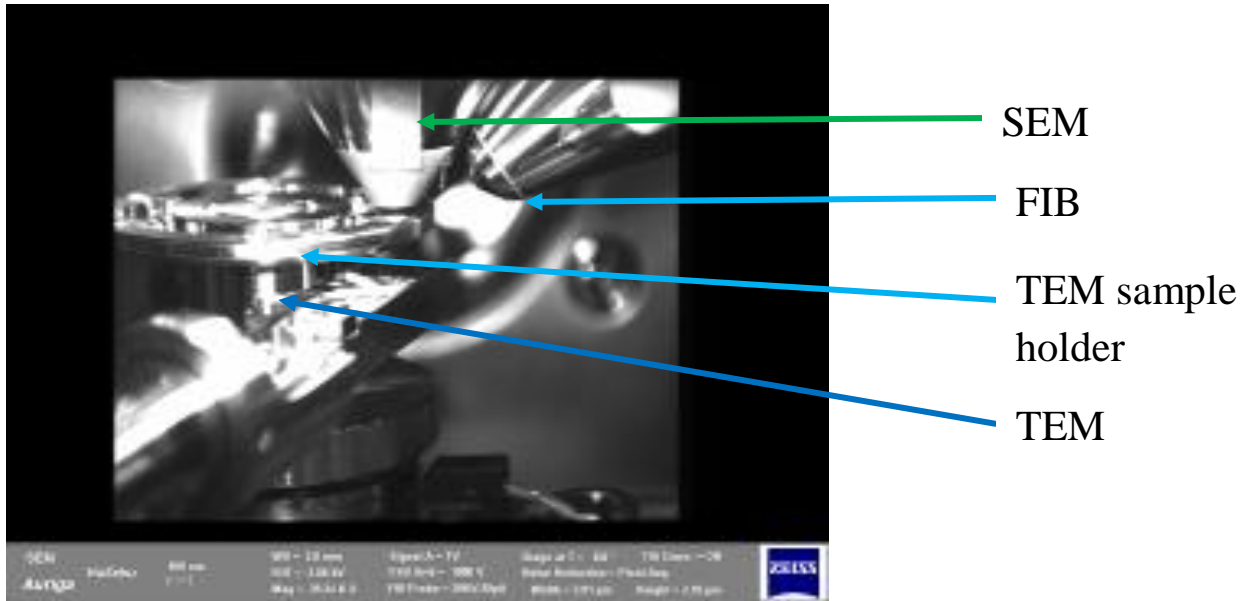
Figure 34. Clear chamber scope view of the Zeiss SEM, FIB, TEM.
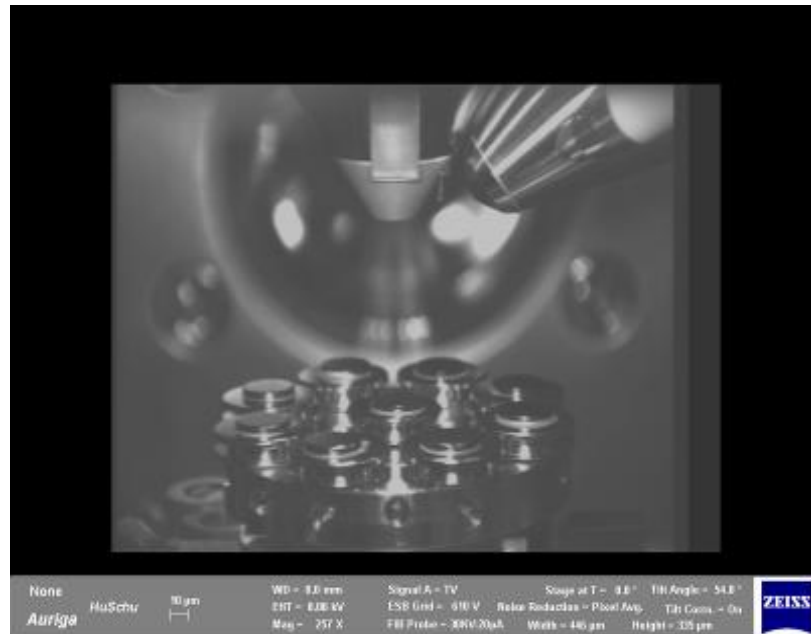
Figure 35. Chamber scope view of sample holder in Zeiss SEM, FIB, TEM.

This instrument was employed to apply a protective layer of Pt over the region of interest, using electron beam deposition, followed by ion beam deposition. Depending on

the beam settings, one method may be suited to a faster deposition process, while another

may be suited to a thicker deposited layer. The reasoning for the protective layer of Pt is

that Ga^+ often implant themselves within a material under ion beam bombardment, thus

changing the chemical composition and structure of the material. Platinum atop the

surface will prevent Ga^+ from penetrating the surface. Another reason for this protective

layer is to prevent redeposition of sputtered material onto the surface under scrutiny, as

this would also change the near-surface region from its original composition. Finally, the

Pt protective layer is employed for TEM sample preparation, where there is a Pt wire that

is attached to the protective layer in order to lift the sample away from the overall

structure, as shown in Figure 36.
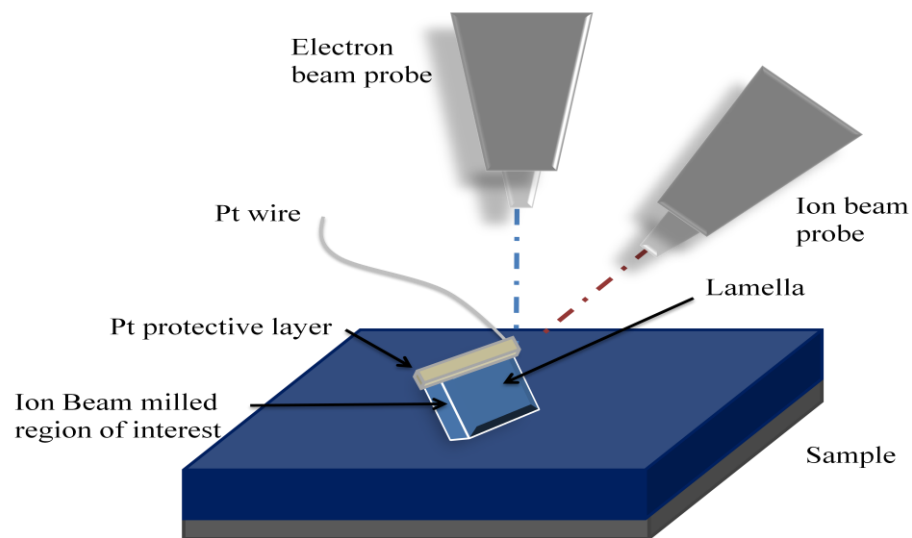
Figure 36. Schematic diagram of the procedure for ion-beam milling of sample, and simultaneous electron beam imaging.

Once the Pt protective layer has been applied, a milling procedure with the ion

beam takes place to cut out a three dimensional rectangular section of the overall sample.

Each face of the lamella is milled individually and, once a face is completed, the beam is

repositioned to mill another region. A Pt wire is attached to the platinum protective layer

on the lamella. Finally, once all four faces have been relieved from the overall sample,

the beam is rotated in order to cut the attachment below, and free the lamella to be

removed using the Pt wire. Once the lamella has been milled away, the ion beam current

is lowered and the surface is polished using the ion beam. An advantage of having SEM

and FIB in one system is that the electron beam is able to image the surface as the ion

beam is busy milling, thus allowing precise changes to be made.
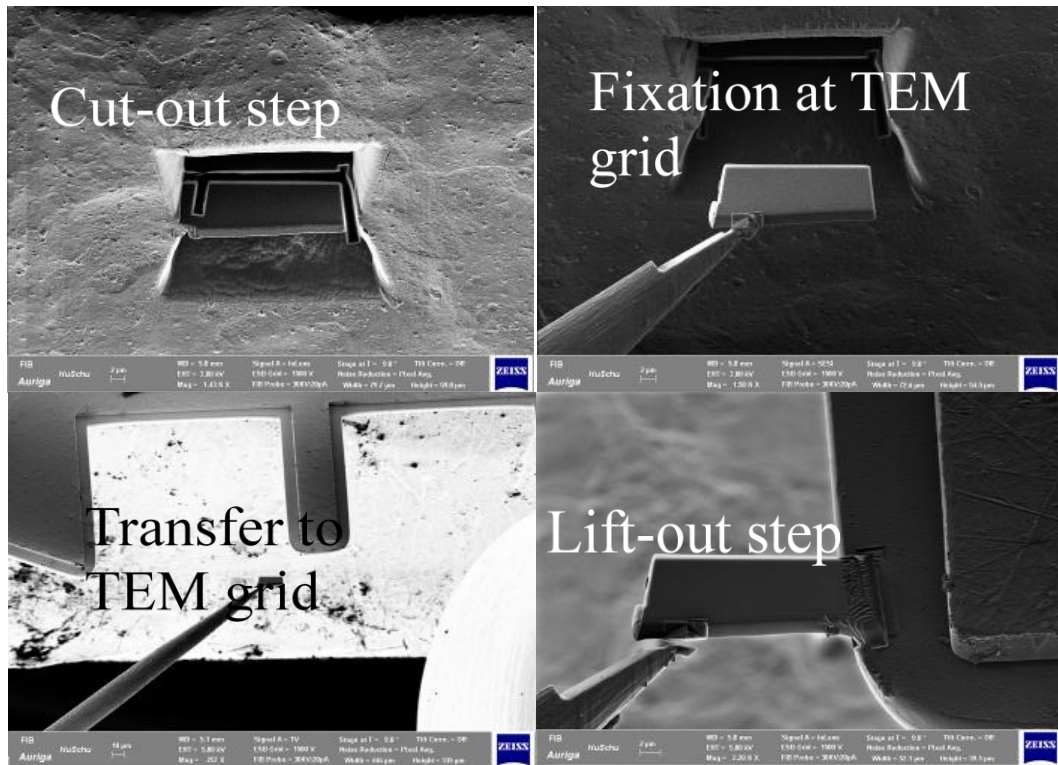
Figure 37. SEM/FIB lamella preparation from etched and coloured Zr sample prepared at
$V_{AC} = 80$ V.

Figure 37 shows TEM sample preparation using the ion beam to mill and cut a

thin wafer-like specimen of acceptable dimensions and thickness. This milling process is

followed by the attachment of a platinum wire to the platinum protective layer atop the sample. This wire is employed in transporting the thin TEM sample to the grid for further study.

3.7 ICP-MS

Inductively coupled plasma mass spectrometry experiments were performed using a Varian 820-MS instrument, with a Dionex 600/BioLC liquid chromatography system equipped with a GS50 gradient pump, a Rheodyne 9750E injector and a 50μL sample loop, employed for flow-injection. The matrix was a 1% NaCl solution. The specimens were all placed in test-tubes containing 25.0 mL of 1% NaCl solution, and were sealed with a silicone stopper. The pump was stabilized by pumping a carrier solution (Millipore water) for 60 minutes. The torch was aligned using a tuning solution containing 5 μg/L of Be, Mg, Co, In, Ce, Pb and Ba in 1% HNO_3 DDW solution prepared by dilution from a 10 μg/L Varian tuning solution (Spectropure[TM], St Louis, Missouri, USA). For mass optimization, the nebulizer, torch, sampler and skimmer cones were cleaned and a full optimization procedure was performed, including plasma alignment, mass calibration, mass resolution and trim, detector setup and ion optic settings.

The samples were run in time-resolved mode (peak hopping), with a sample uptake rate of 1mL/min. A five point external calibration was employed (linear regression through origin): blank, 1ppb, 10ppb, 50ppb and finally 100ppb. The conditions given in Table 3 were used for the quantitation of ^{47}Ti and ^{91}Zr species in real samples.

Table 3. ICP-MS Operating Conditions.

	Parameter	Setting
ICP	Ar plasma gas flow rate (L/min)	18.0
	Ar auxiliary gas flow rate (L/min)	1.80
	Ar nebulizer gas flow rate (L/min)	0.86
	Ar sheath gas flow rate (L/min)	0.02
	Plasma RF power (kW)	1.38
	Monitored m/z	47, 91
	Dwell time (s)	0.5
	Sampling depth (mm)	7.0
	Sampling time (s)	30
Sampling interface	Sampler cone; tip i.d. (mm)	Ni; 0.9
	Skimmer cone; tip i.d.(mm)	Ni; 0.4
Spray chamber	Temperature (ºC)	20
	Draining pump rate (mL/min)	2.0
Ion optics	First extraction lens (V)	-36
	Second extraction lens (V)	-189
	Third extraction lens (V)	-191
	Corner lens (V)	-260
	Mirror lens left (V)	39
	Mirror lens right (V)	24
	Mirror lens bottom (V)	29

	Entrance lens (V)	-7
	Fringe bias (V)	-2.4
	Entrance plate (V)	-25
	Pole bias (V)	0.0

The detection limit was 0.1 µg/L for Ti and 0.1 µg/L for Zr solutions. The ICP-MS standards (SCP Science, Champlain, New York, USA) were used to prepare calibration standards in 1% NaCl, which was also used as a blank. The error values on the slopes of the calibration curves shown in Figures 38 and 39 are: 6830 ± 110 (1.7%) for Ti and 23490 ± 680 (2.9%) for Zr. Flow injection peak analysis was performed by measuring area under the curve using SigmaPlot 10.0.
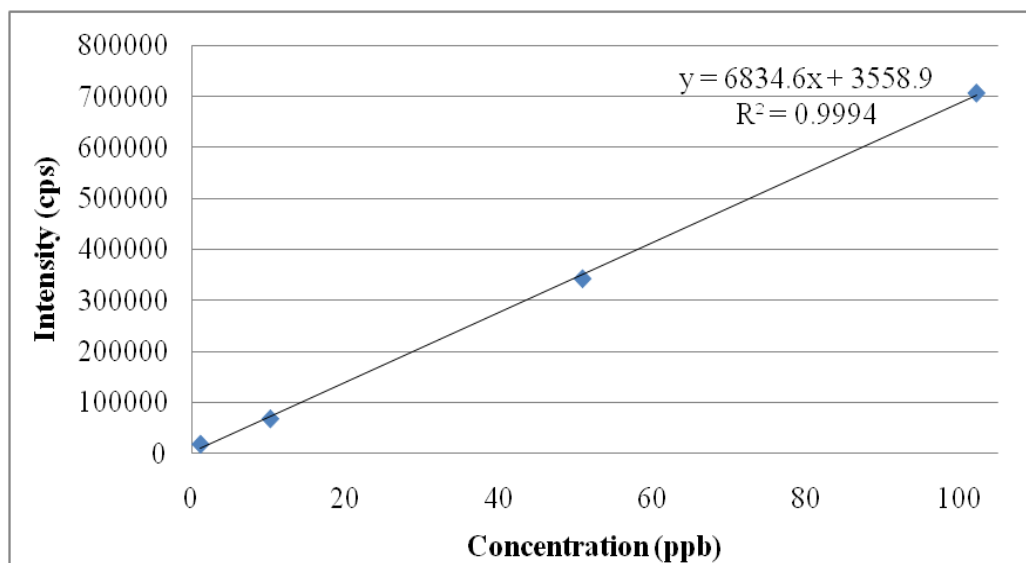
Figure 38. Titanium (^{47}Ti) five point external calibration (linear regression through origin): blank, 1 ppb, 10 ppb, 50 ppb and finally 100 ppb.
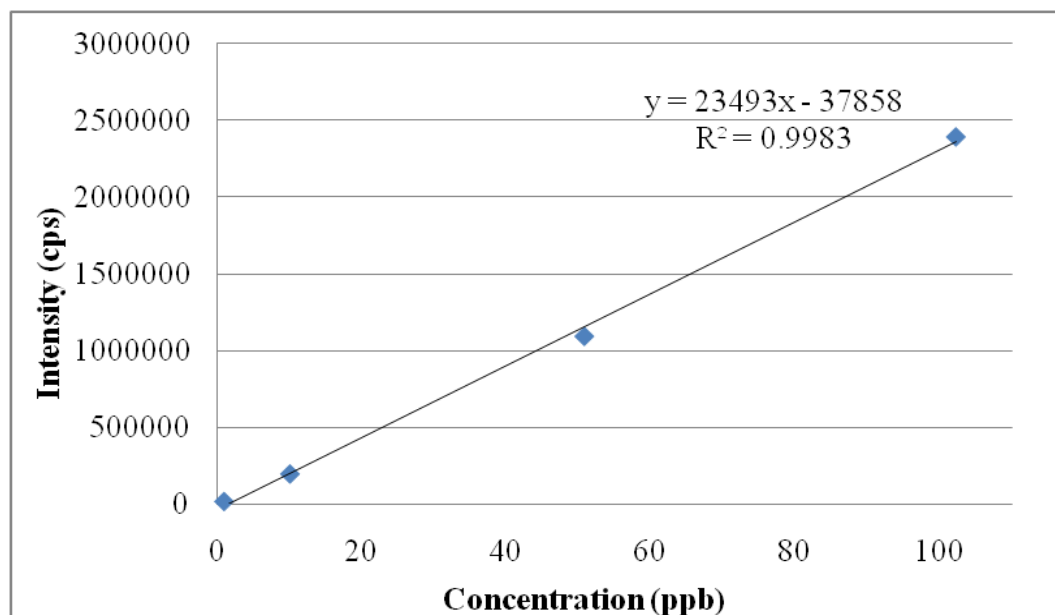
Figure 39. Zirconium (^{91}Zr) five point external calibration (linear regression through origin): blank, 1 ppb, 10 ppb, 50 ppb and finally 100 ppb.

3.8 Polarization Curves

Polarization curve experiments were carried out using an electrolyte solution of 1% NaCl (Fisher Scientific A.C.S certified crystals) in Millipore water (resistance of 18.2 MΩ·cm, purified with Millipore Milli-Q system). The scan rate used was 1.00 mV/s, with a potential range of -1 to 3 V. The polarization curves were recorded in 1% aqueous NaCl solution in a standard, two-compartment electrochemical cell. A stream of Ar gas (99.99 wt.%) was passed through electrolyte to expel any gases generated during electrochemical characterization. A Pt/Pt black reversible hydrogen electrode (RHE) was used as a reference electrode in the electrochemical characterization (polarization curves). A 1% aqueous NaCl was selected as the electrolyte for electrochemical characterization of the coloured Ti passive layers in order to relate their electrochemical characteristics to

the potential applications in medical and dental implantation, automotive, marine and aerospace industries, as well as any other saline solution exposed applications.

The calculations of E_{corr} and j_{corr} were performed using the linear extrapolation method shown in Figure 40.
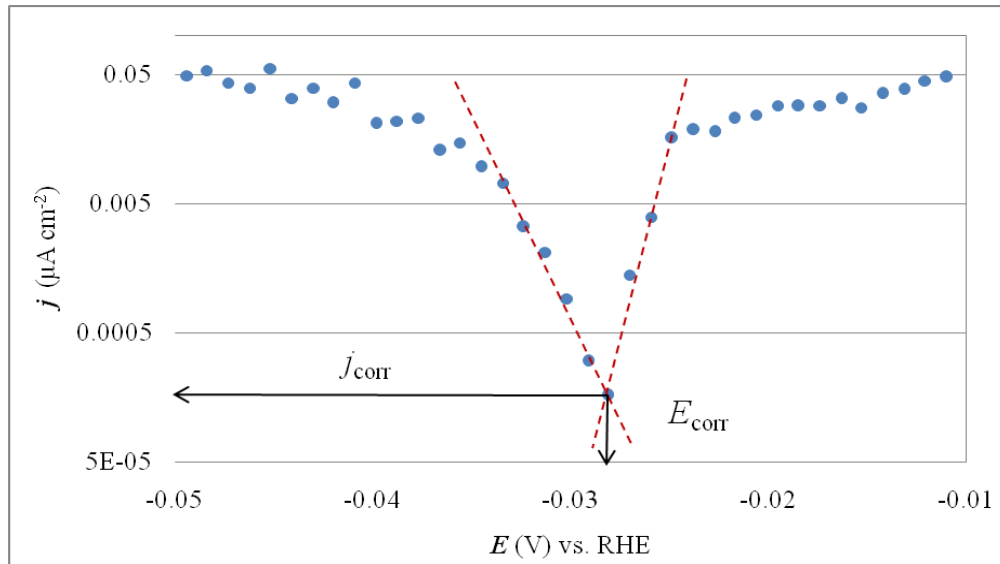
Figure 40. Method of determining the values of E_{corr} and j_{corr} through linear extrapolation of transients.[37]

4.0 Project Results

4.1 Light Microscopy

Surface morphology studies performed on both Ti and Zr metal samples were completed using a VLM capable of 400× magnification. Figures 41 though 48 show the colouration and surface morphology of four sets of samples: (i) etched, and etched and coloured Ti, (ii) etched, and etched and coloured Zr, (iii) polished, and polished and coloured Ti and (iv) polished, and polished and coloured Zr, through magnifications of

50×. The results for polished samples of passivated Ti and Zr show little difference between the metals, as they were each polished in the same fashion prior to being passivated. Through profilometry measurements, which will be discussed later in this section, average roughness values (R_a) are reported. The average R_a value after polishing for Ti samples was 0.254 µm, and the average R_a value after polishing for Zr samples was 0.204 µm. The results for the polished samples, which can be seen in Figures 41 and 43, illustrate that the morphology of passivated metals portrays a smoother surface appearance as higher voltages are applied (V_{AC}). Conversely, the etched samples, shown in Figures 45 and 47, illustrate the differences in the surface morphologies and metal fabrication methods employed. The average R_a value after etching for Ti samples was 0.986 µm, and the average R_a value after etching for Zr samples was 0.528 µm. These differences arise from the fact that chemical etching will maintain the order of the underlying metallic structure, whereas polishing is a more invasive process, which will disorder the surface in order to create a smoother appearance. Zr is very smooth when etched and therefore has finer grains than Ti, which has been shown to be quite rough. The difference in their formation is most likely due to the process of nucleation being different for each metal. The number of clusters of a certain size is dependent upon the total atoms in a system, the free energy required to create a specific cluster size and temperature. Overall, the number of clusters is linearly proportional to temperature value.[75] Using VLM, the Zr samples appear to have a granite-like appearance, which is due to the grains having different colours under close observation, thus eliciting a mosaic-like appearance. The different grains present in the surface structure of Zr have different surface orientations from a variation in their growth rates. Thus, varied granular growth

rates result in different grain thicknesses, leading to different grain colours and the mosaic appearance of the surface structure of Zr.

Each set of samples appears to have a uniform morphology in their oxide coatings, with no cracking or flaking defects as revealed by VLM at 5-100× magnification. This is important if these passive layers, in addition to offering visual characteristics (colour), are to reduce metallic corrosion. Indeed, the presence of surface defects would hinder their protective properties.
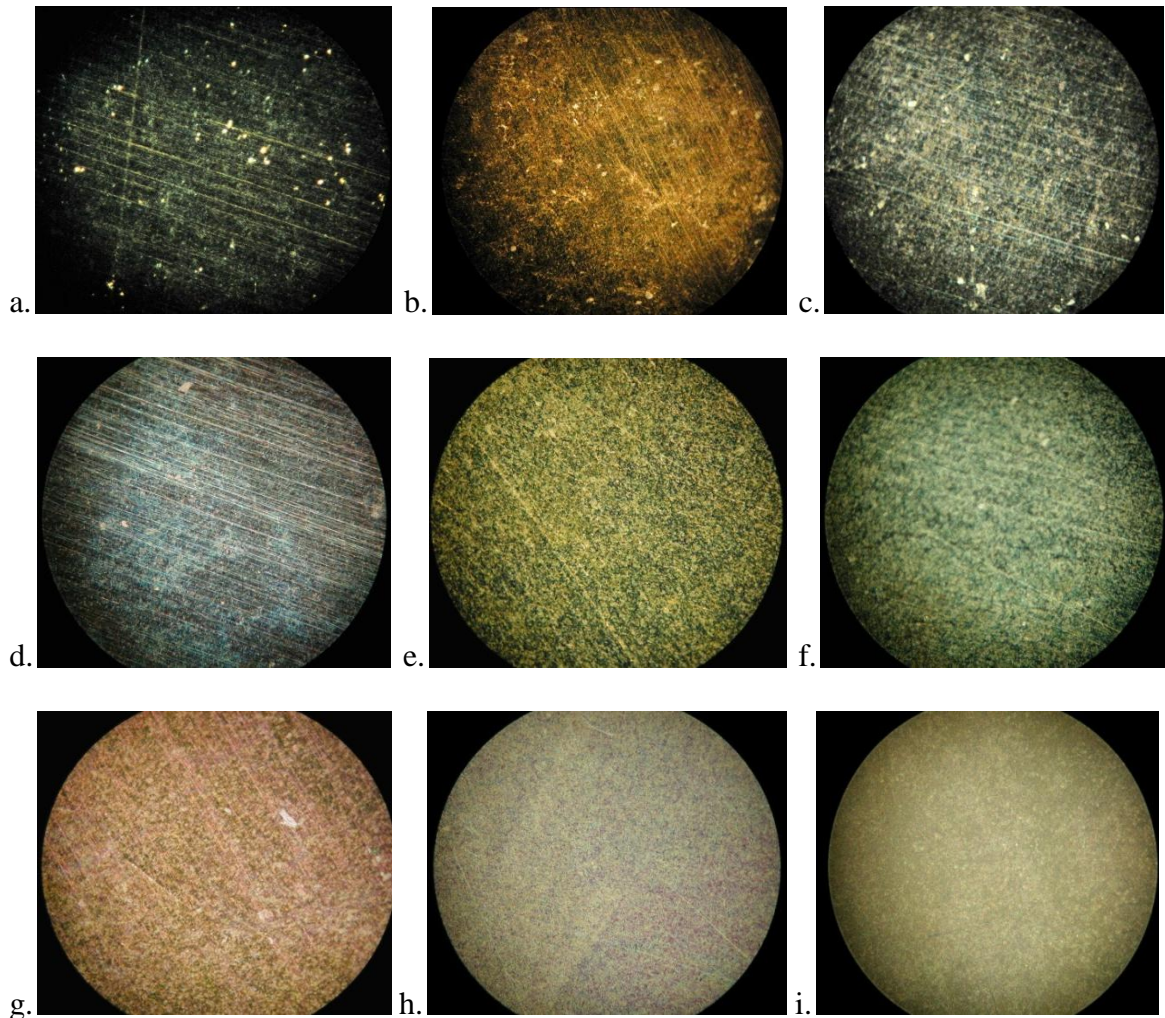
Figure 41. Visible light microscopy images of polished (a), and polished and coloured (b - i) Ti. From b to i, the passivation voltage is V_{AC} = 10, 20, ... , 80 V. Passivation was performed in aqueous 7.5 wt.% NH_4BF_4 electrolyte for 10 s at T = 298 K.

Figure 41 shows the polished, and polished and coloured Ti samples and their observed colouration under 50× magnification. A direct colouration comparison between the naked eye and VLM images for polished Ti can be seen in Figures 41 and 42 and is summarized in Table 4. Table 5 illustrates that there is a contribution of grain colourations combining to create an overall appearance. This will be studied closely

when reflectance data display the reflected colours of light contributing to the overall colour of each sample.

V_{AC} (V) =

| 0 | 10 | 20 | 30 | 40 | 50 | 60 | 70 | 80 |

Figure 42. Photography of the polished, and polished and coloured Ti samples. Coloured samples were prepared at V_{AC} = 10, 20, ..., 80 V. Passivation was performed in aqueous 7.5 wt.% NH_4BF_4 electrolyte for 10 s at T = 298 K. Samples placed on white background (above) and black background (below) due to the appearance being altered by variation in background colour.

Table 4. Summary of the colouration observed with naked eye and VLM in relation to the applied V_{AC}. Passivation was performed in aqueous 7.5 wt.% NH_4BF_4 electrolyte for 10 s at $T = 298$ K.

V_{AC}	Colour seen with naked eye	Colour observed using VLM
0	Bluish gray	Bluish gray
10	Reddish brown	Reddish brown, orange
20	Dark blue	Bluish violet
30	Light blue	Blue
40	Light green	Yellowish green
50	Yellowish orange	Bluish green, some yellow
60	Violet	Violet
70	Bluish green, some violet	Bluish green, some violet
80	Greenish blue	Greenish blue, some yellow
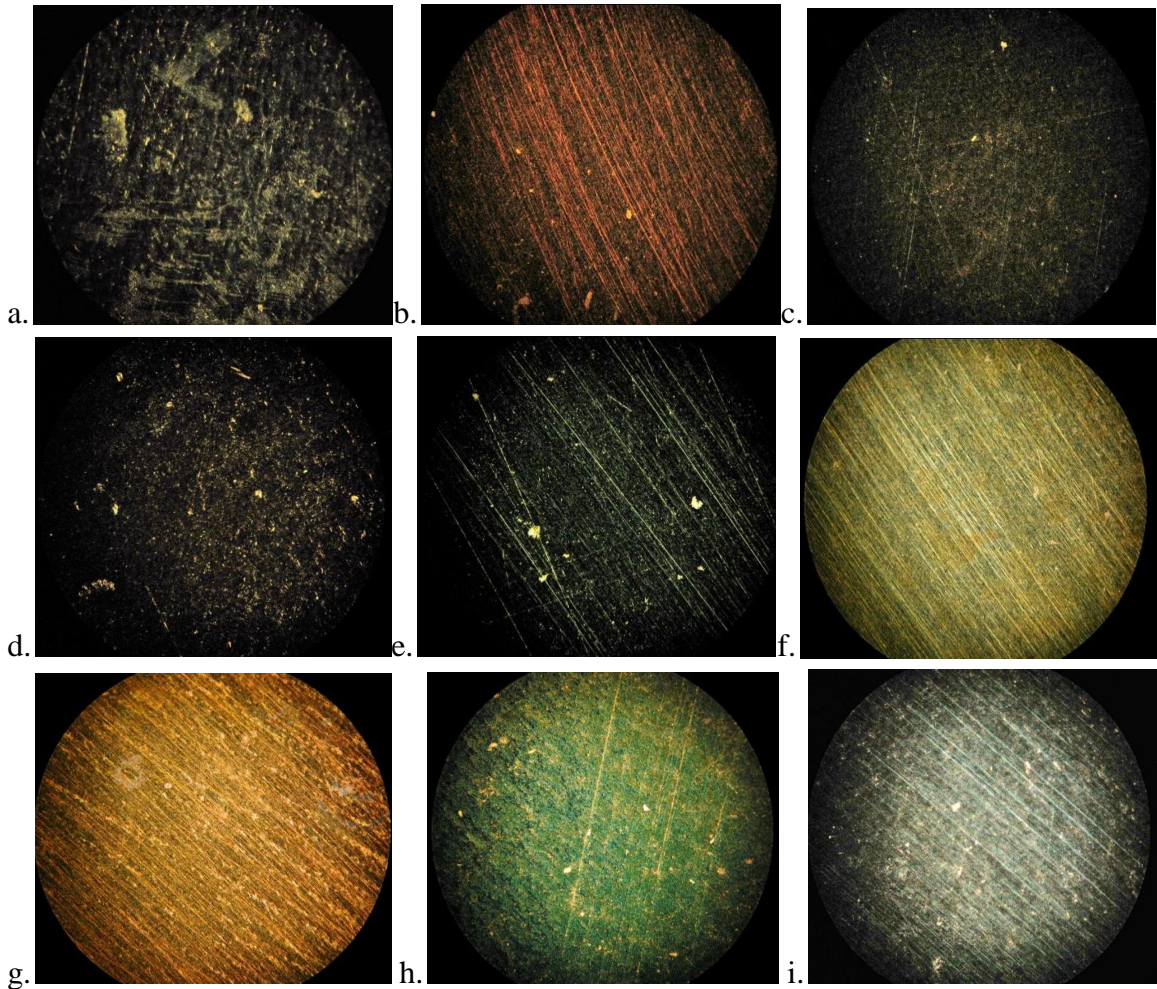
Figure 43. Visible light microscopy images of polished (a), and polished and coloured (b - i) Zr. From b to i, the passivation voltage is $V_{AC} = 10, 20, ... , 80$ V. Passivation was performed in aqueous 10 wt.% Na_2SO_4 electrolyte for 10 s at $T = 298$ K.

Figure 43 shows the VLM images for the polished, and polished and coloured Zr samples. Observed colouration and that seen by VLM are summarized in Table 5. Clearly, the microscopy images in Figure 43 are once again similar to what is observed using the naked eye.

V_{AC} (V) =

| 0 | 10 | 20 | 30 | 40 | 50 | 60 | 70 | 80 |
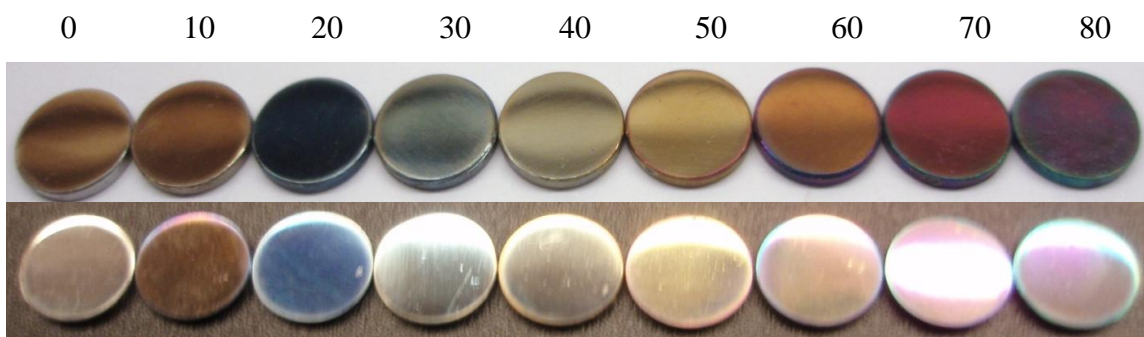
Figure 44. Photography of the polished, and polished and coloured Zr samples. Coloured samples were prepared at V_{AC} = 10, 20, ..., 80 V. Passivation was performed in aqueous 10 wt.% Na_2SO_4 electrolyte for 10 s at T = 298 K. Samples placed on white background (above) and black background (below) due to the appearance being altered by variation in background colour.

Table 5. Summary of the colouration as observed with naked eye and VLM in relation to the applied V_{AC}. Passivation was performed in aqueous 10 wt.% Na_2SO_4 electrolyte for 10 s at T = 298 K.

V_{AC}	Colour seen with naked eye	Colour observed using VLM
0	Bluish gray	Bluish gray
10	Reddish brown	Reddish brown
20	Dark blue	Bluish violet
30	Light blue	Blue
40	Light green	Blue, slight green
50	Yellowish orange	Yellowish orange
60	Orange, Violet	Orange, Violet, red
70	Magenta, Greenish blue	Greenish blue
80	Bluish Green	Bluish green
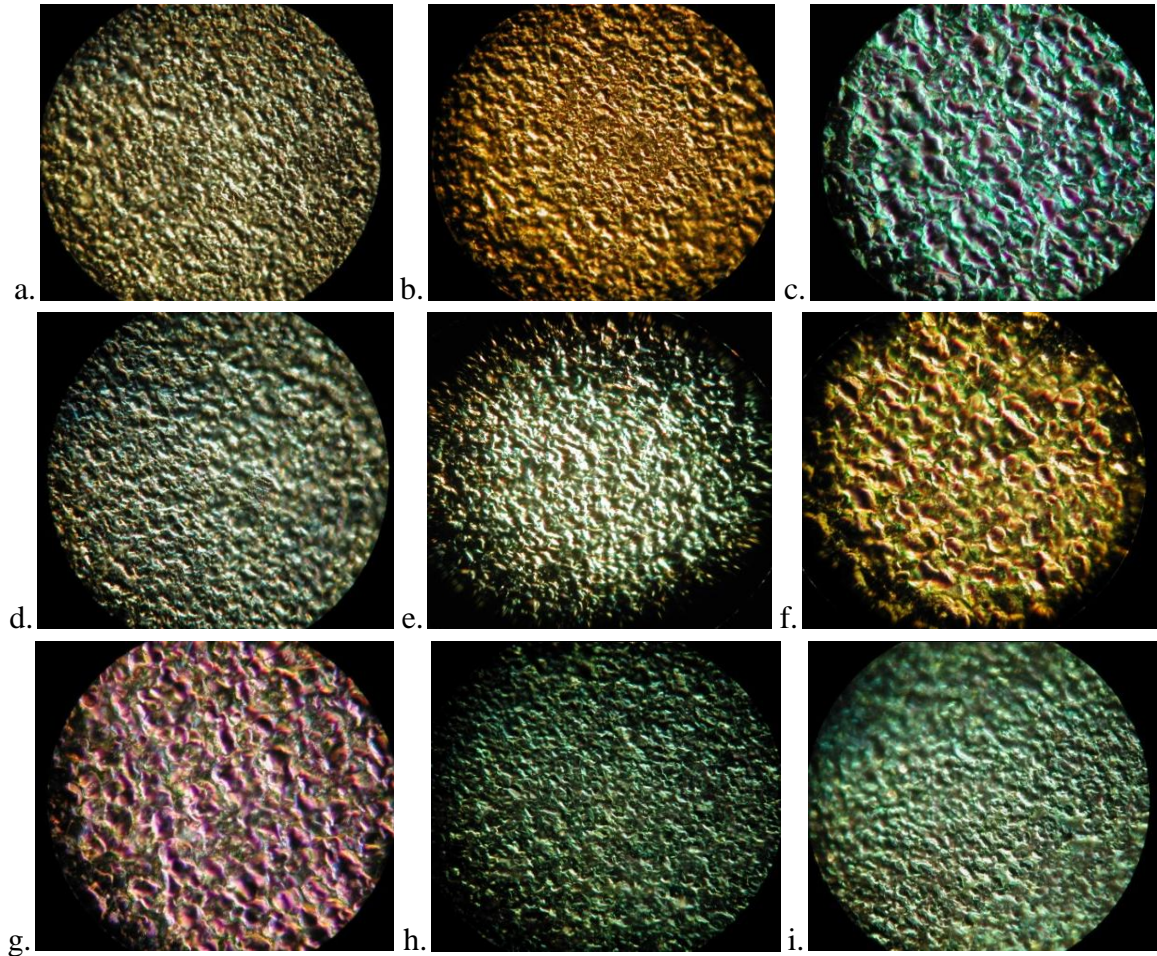
Figure 45. Visible light microscopy images of etched (a), and etched and coloured (b - i) Ti. From b to i, the passivation voltage is V_{AC} = 10, 20, ... , 80 V. Passivation was performed in aqueous 7.5 wt.% NH_4BF_4 electrolyte, for 10 s at T = 298 K.

Figure 45 shows the etched, and etched and coloured Ti samples. An immediate difference is observed, as the etched Ti samples have clear, bright colours. All of the samples observed through VLM, in Figure 45, correspond in their colouration to that seen using the human eye, in Figure 46, and summarized in Table 6. Clearly, with etching of the sample, the observed colouration comes from several colours, each originating either

from a different grain or a grain boundary, and working together to yield an overall colour.

V_{AC} (V) =

| 0 | 10 | 20 | 30 | 40 | 50 | 60 | 70 | 80 |
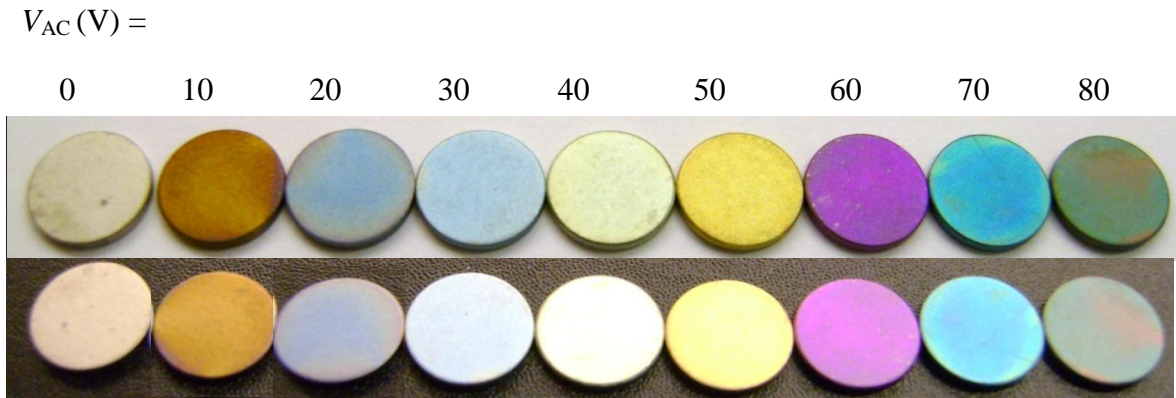
Figure 46. Photography of the etched and etched and coloured Ti samples. Coloured samples were prepared at V_{AC} = 10, 20, ..., 80 V. Passivation was performed in aqueous 7.5 wt.% NH_4BF_4 electrolyte for 10 s at T = 298 K. Samples placed on white background (above) and black background (below) due to the appearance being altered by variation in background colour.

Table 6. Summary of the colouration as observed with naked eye and VLM in relation to the applied V_{AC}. Passivation was performed in aqueous 7.5 wt.% NH_4BF_4 electrolyte for 10 s at $T = 298$ K.

V_{AC}	Colour seen with naked eye	Colour observed using VLM
0	Bluish gray	Bluish gray, slight green
10	Reddish brown	Reddish brown, orange
20	Dark blue	Bluish violet
30	Light blue	Blue
40	Light green	Bluish green
50	Yellow	Yellowish green, orange
60	Violet	Violet, orange, red, yellow, blue
70	Greenish blue	Greenish blue
80	Bluish Green	Bluish green, some yellow
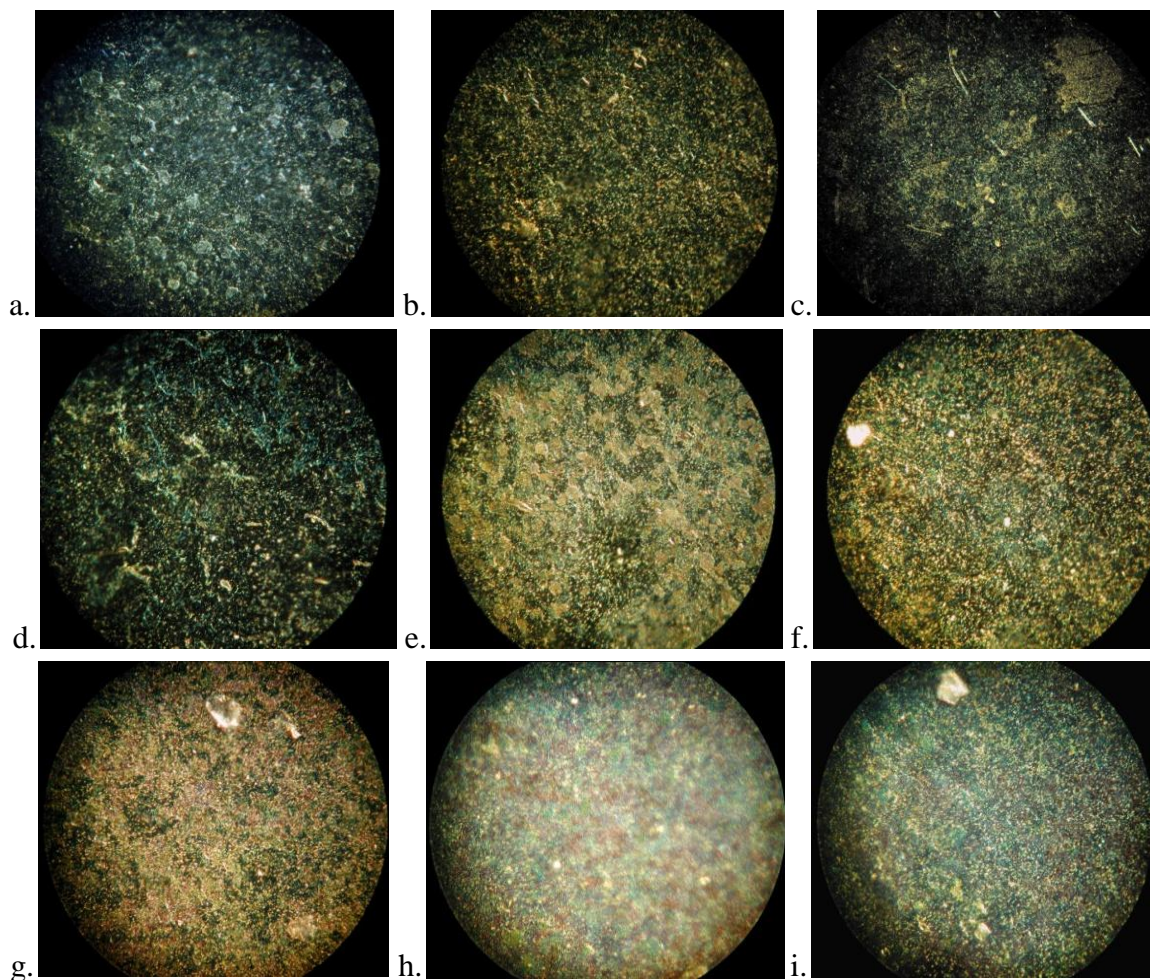
Figure 47. Visible light microscopy images of etched (a), and etched and coloured (b - i) Zr. From b to i, the passivation voltage is V_{AC} = 10, 20, ... , 80 V. Passivation was performed in aqueous 10 wt.% Na_2SO_4 electrolyte for 10 s at T = 298 K.

Figure 47 shows the VLM images of the etched, and etched and coloured Zr samples. These samples are clearly much smoother than the etched Ti samples, which is due to the fineness of their grains, as was previously discussed. These samples under microscopy have a granite-like appearance. Visible light microscopy images (Figure 47) can be compared with and the overall observed colourations (Figure 48), and are summarized in Table 7, as well as from the photography in. The application of high-

96

magnification VLM in the next section reveals additional information with regards to the grain size and colouration.

V_{AC} (V) =

| 0 | 10 | 20 | 30 | 40 | 50 | 60 | 70 | 80 |
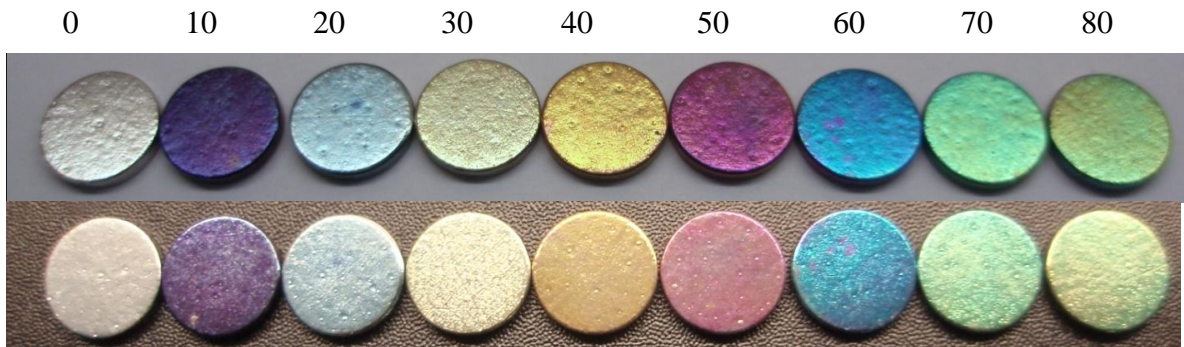
Figure 48. Photograph of the etched and etched and coloured Zr samples. Coloured samples were prepared at V_{AC} = 10, 20, ..., 80 V. Passivation was performed in aqueous 10 wt.% Na_2SO_4 electrolyte for 10 s at T = 298 K. Samples placed on white background (above) and black background (below) due to the appearance being altered by variation in background colour.
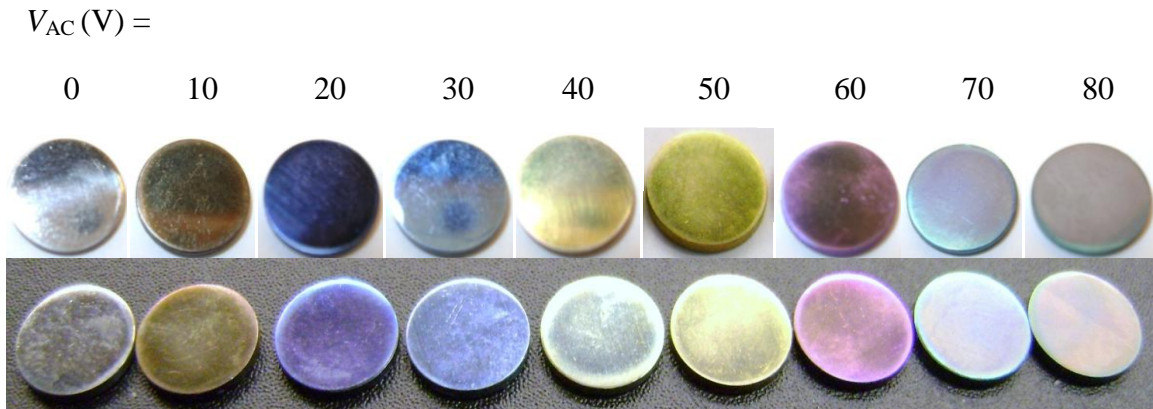
Table 7. Summary of the colouration as observed with naked eye and VLM in relation to the applied V_{AC}. Passivation was performed in aqueous 10 wt.% Na_2SO_4 electrolyte for 10 s at $T = 298$ K.

V_{AC}	Colour seen with naked eye	Colour observed using VLM
0	Dark bluish gray	Bluish gray, violet
10	Very dark Violet	Reddish brown, green, blue, orange
20	Blue	Blue
30	Light bluish green	Bluish green
40	Yellow	Greenish blue, yellow
50	Violet	Yellow, green, orange, red
60	Bright teal	Bluish violet
70	Greenish blue	Greenish blue, yellow, violet
80	Yellowish green	Bluish green, yellow, violet

4.2 Zeiss Light Microscopy

Surface morphology studies using more powerful VLM resulted in the images shown in Figures 49 and 50. The Zeiss VLM was able to clearly demonstrate sample colouration on a smaller scale, bringing forth the component colours that combine to make the observed sample colour. Comparison with reflectance spectroscopy will be able to confirm whether these component colours are related to reflected light colourations. The unpassivated sample of etched Zr has a slight violet colour among the overall gray; this was also seen in a previous microscopy analysis, and is expected since the overall colouration of the sample is a darker gray. The etched and coloured samples show clear and well defined component colours. The image for the sample prepared at $V_{AC} = 10$ V

has an overall colouration of dark blue, with violet and red grains visible on the surface. For the sample prepared at $V_{AC} = 20$ V, an overall blue colouration is due to there being more blue grains than violet grains. The sample prepared at $V_{AC} = 30$ V no longer has an overall blue appearance; it is instead a yellowish green colour, with yellow, orange and green grains present. Similarly, the sample prepared at $V_{AC} = 40$ V appears to be yellow; however, there are orange and red grains prevalent across the surface as well. Grains of violet, blue and red are observed for the sample prepared at $V_{AC} = 50$ V, creating an overall violet colouration, whereas the sample prepared at $V_{AC} = 60$ V appears entirely blue from the microscopy image. The samples prepared at $V_{AC} = 70$ and 80 V are bluish green and greenish blue respectively, and have green, blue, yellow and red grains contributing to the surface appearance. In the next section, these samples will be studied using reflectance spectroscopy to determine whether these colours correspond to reflected wavelengths.

The VLM results indicate that with passive layers prepared using higher values of V_{AC}, the surface of the metal becomes less rough. However, when an AC voltage greater than 60 V is applied, pores become prevalent across the surface. The passive layer is still providing full coverage at these higher voltages; however, these pits, which could be liable to the occurrence of pitting corrosion and abrasion, are likely caused by the onset of electrochemical breakdown (see Introduction page. 38) of the metal, which is why passivation is studied only up to $V_{AC} = 80$ V. When passivation is performed at voltages above 80 V, the metal deteriorates due to electrochemical breakdown.
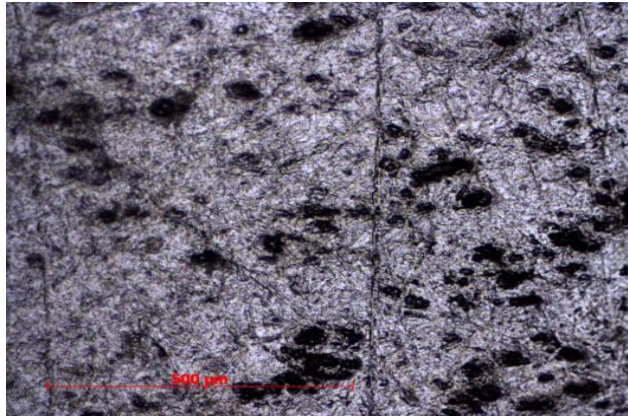
Figure 49. VLM image of etched Zr, obtained using a Zeiss AXIO Imager M2 MAT microscope.
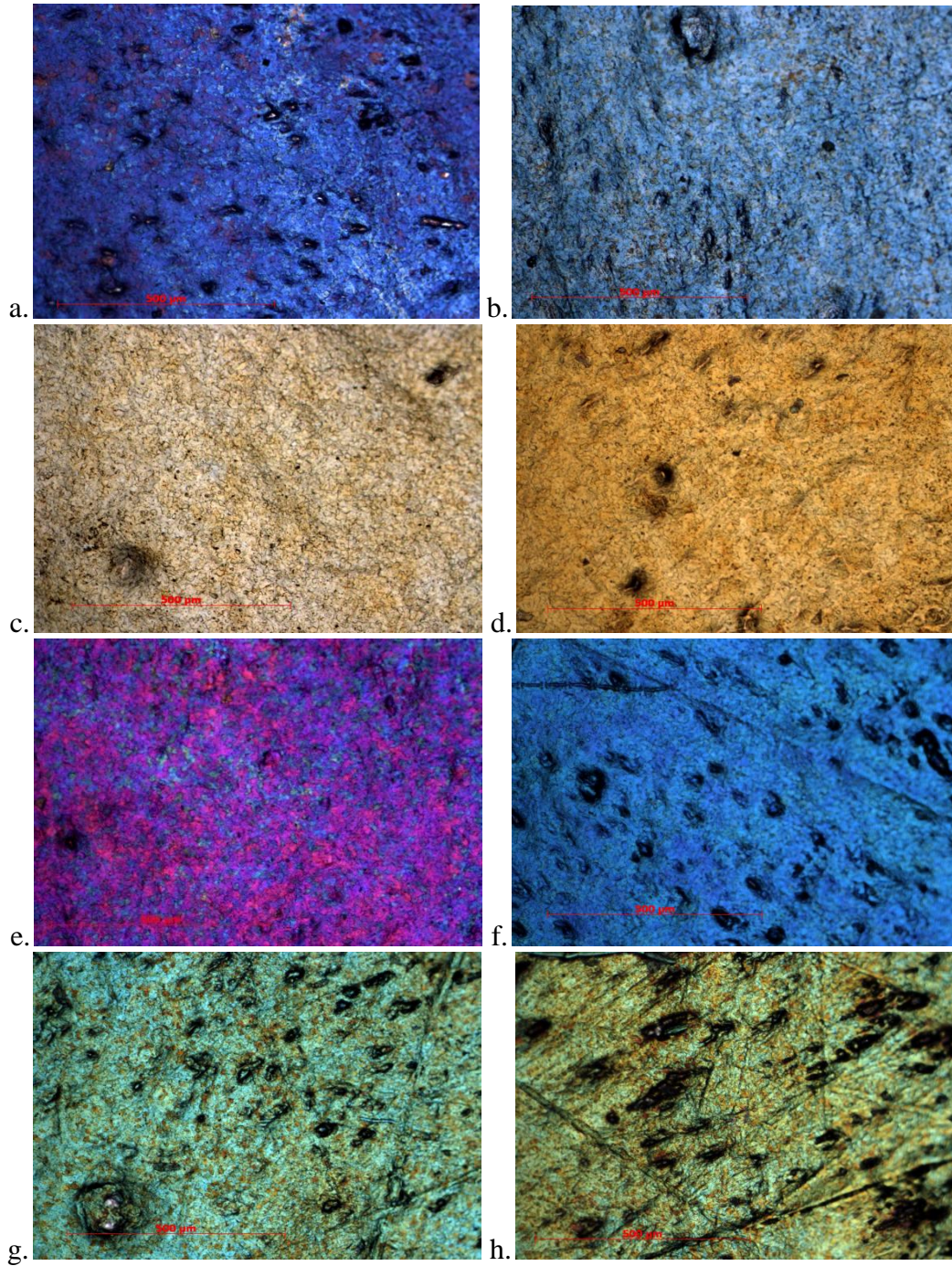
Figure 50. VLM images of etched and etched and coloured Zr, obtained using a Zeiss AXIO Imager M2 MAT microscope. From a to h, the coloured samples were prepared at V_{AC} = 10, 20, ..., 80 V. Passivation was performed in aqueous 10 wt.% Na_2SO_4 electrolyte for 10 s at T = 298 K.

Similar surface defects were reported to be present with passive layers on Ti by di Quarto *et al.*[76] They hypothesized that because oxide formation on Ti is always simultaneous to oxygen evolution, pores would be caused by oxygen evolution proceeding until an electrically insulating gas filled these spaces. A similar effect was found by Y. T. Sul *et al.* for Ti, where increased voltages lead to more and larger pores,[77] as can be seen from their results in Figure 51 using DC, instead of AC, anodization. The effect is the same overall: pores are developing at a certain applied voltage, and increase in size and frequency with higher applied voltages. However, differences lie in the surface structures. The pores caused in DC anodized samples can penetrate the metal itself, destroying any corrosion-resistant properties of the passive layer, because passive layers prepared with DC voltage are thinner than those prepared using AC voltage. The rate of formation for DC is 2.0 nm/V, whereas it is 5.2 nm/V for AC.[26] This thickness difference is most likely due to the fact that the DC-formed passive layers are only composed of one oxide (TiO_2), whereas the AC-formed passive layers are composed of two (TiO_2 and Ti_2O_3). [26, 78] The results for pore sizes will be discussed layer, in the section on AFM.

(a) Group I   (b) Group II   (c) Group III
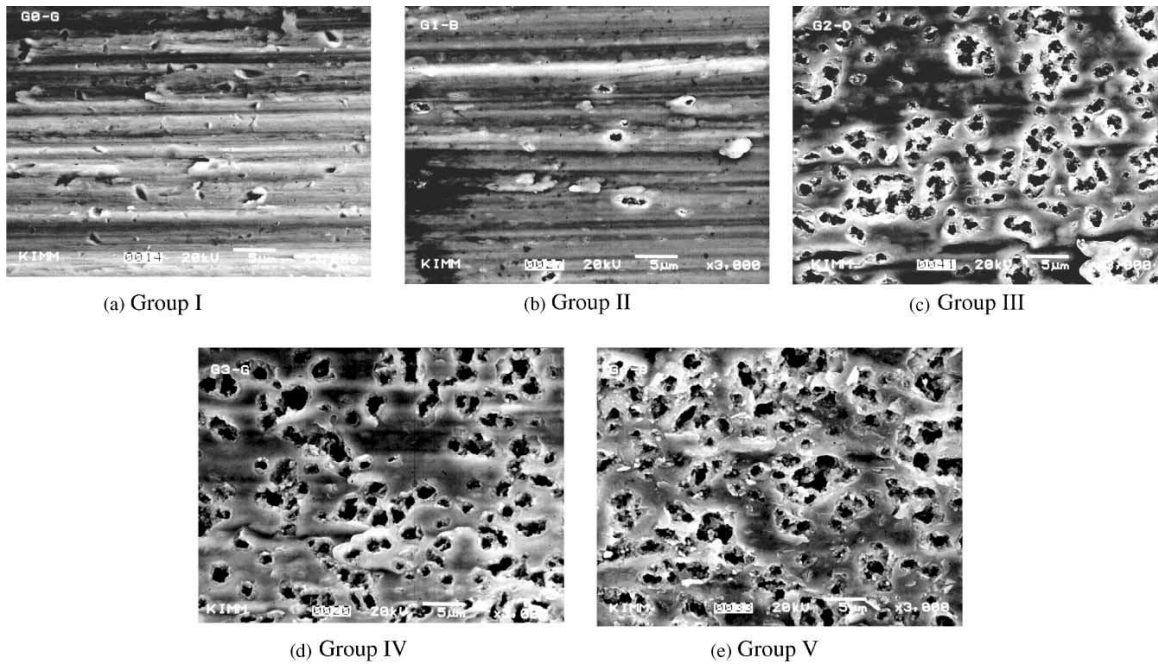
(d) Group IV   (e) Group V

Figure 51. SEM pictures show non-porous (Group I and II) and porous microstructure (Group III–V): Group I; turned surface, Group II; anodized surface at 100 V, Group III; anodized surface at 200 V, Group IV; anodized surface at 280 V, Group V; anodized surface at 380 V.[77]

The above results confirm the previously reported trend that pores being formed are due to higher applied voltages. This group used much higher voltages and thus gained very porous surfaces. As was explained in the introduction, the conductivity of the anode can change with voltage, due to the piezoresistive effect.[34] This resistance leads to changes in morphology of the layers, since there are oxygen vacancies in the oxide structure, leading to a less consistent surface structure. This is consistent with the results observed, as well as the work done by di Quarto.

A benefit of this structure would be in medical and dental implantation, where pores are important to cell adhesion and tissue acceptance of the material. Osseointegration is an important process for dental implants, prostheses as well as joint implants. Porous materials have been shown to allow formation of vascular systems within the porous area, thus facilitating the integration process.[79] Specifically, roughened surfaces increase bone-implant contact, promote tissue and bone ingrowth, create and increase the interlock between the ingrowth bone and implants, thereby improving overall bone healing.[80] Thus, using electrochemical breakdown potentials in order to create porous surfaces for implant, passivation could be a beneficial technique.

4.3 NIR-UV Vis Reflectance Spectroscopy

Four sets of samples were studied; (i) etched, and etched and coloured Ti, (ii) etched, and etched and coloured Zr, (iii) polished, and polished and coloured Ti and (iv) polished, and polished and coloured Zr. The wavelength range covered in reflectance spectroscopy measurements was from 200 nm to 1100 nm. Intensity of reflectance (R) is shown as values between 0 and 1, with 1 being perfect reflection. The spectra displayed below were recorded with a halogen-deuterium light source, in order to gain information about the spectrum from UV to IR wavelengths. These measurements will reveal whether the light wavelengths that are being reflected from the material correspond to the grain colours observed using VLM. Any uncertainties associated with the following reflectance measurements are derived from information loss along the fibre-optic cable, as well as certain quantities of scattered and diffusely reflected light, which was detected and taken as specularly reflected light.[42]

Table 8. Comparative reflectance results for polished and polished and coloured, and etched and etched and coloured Zr samples.

V_{AC} (V)	Spectra for Etched Zirconium	Spectra for Polished Zirconium
0		
10		
20		

30		
40		
50		

60		
70		
80		
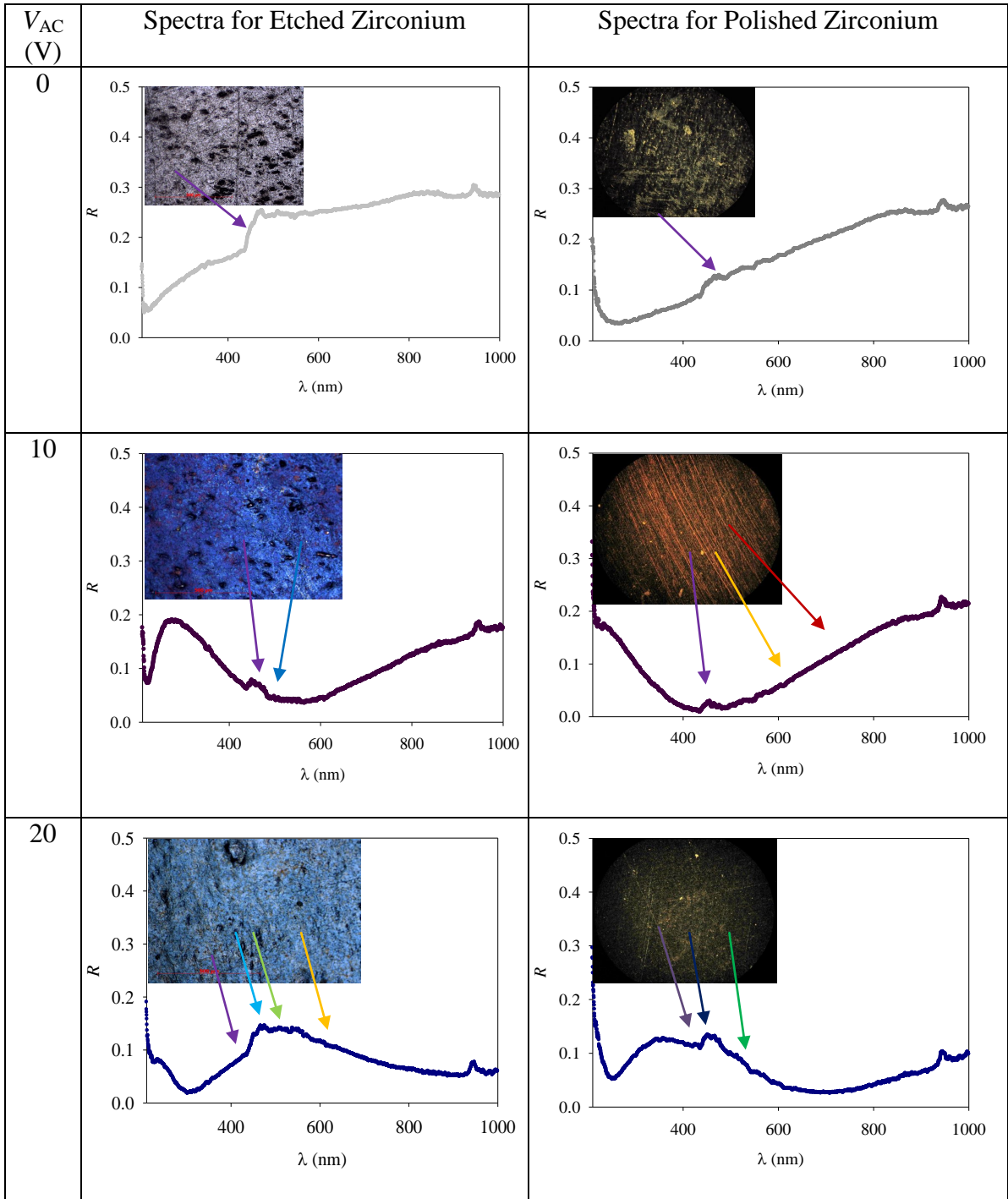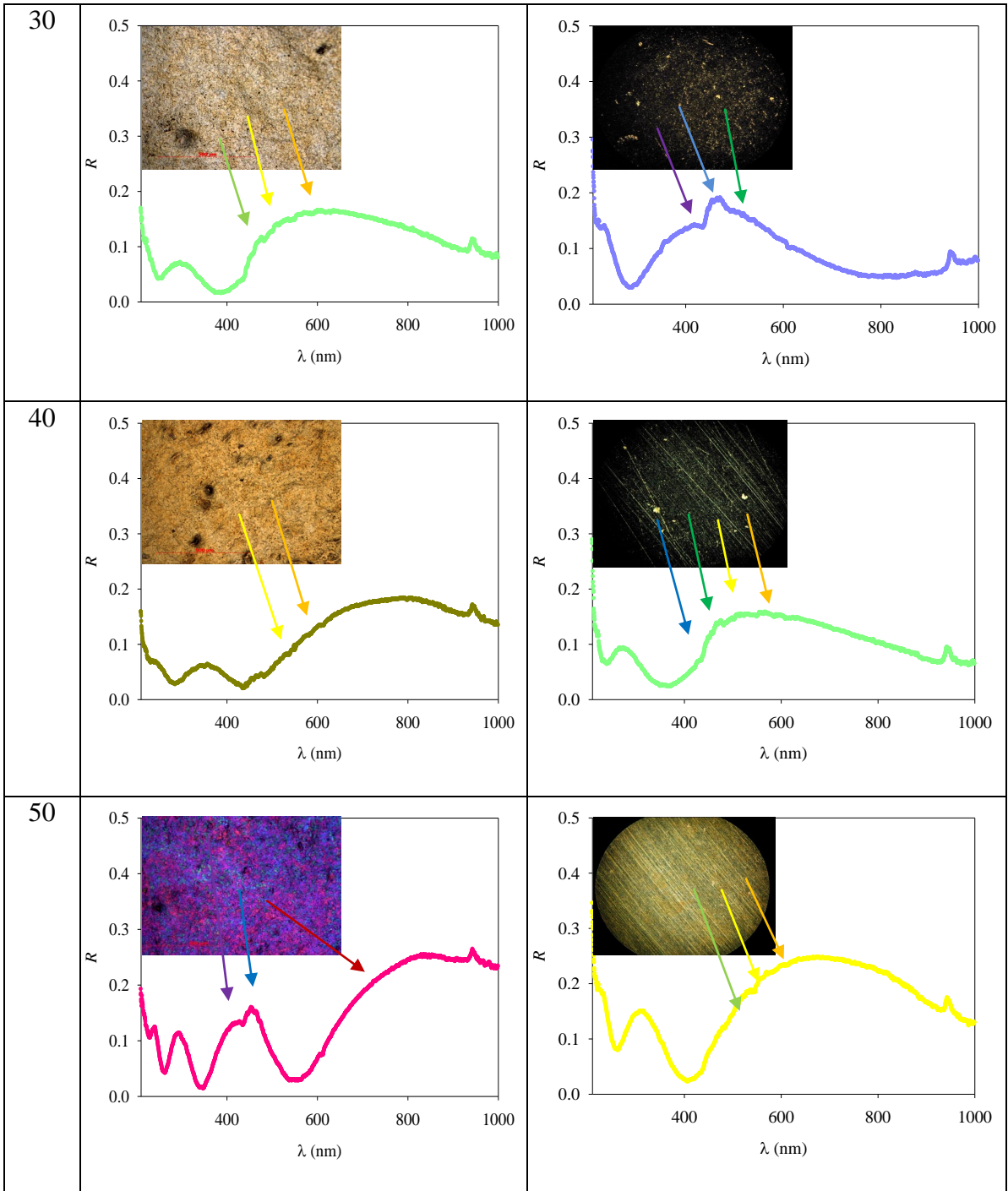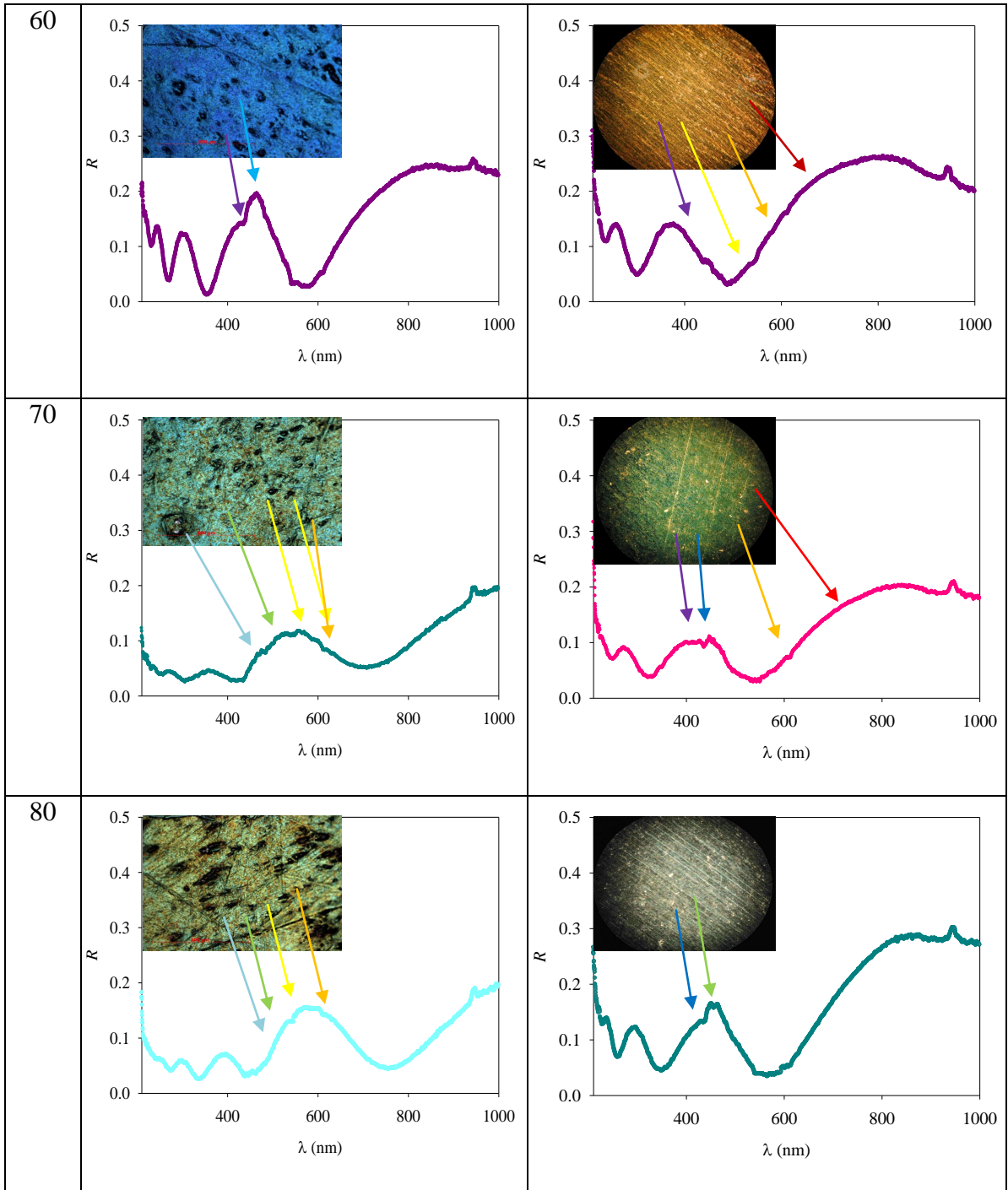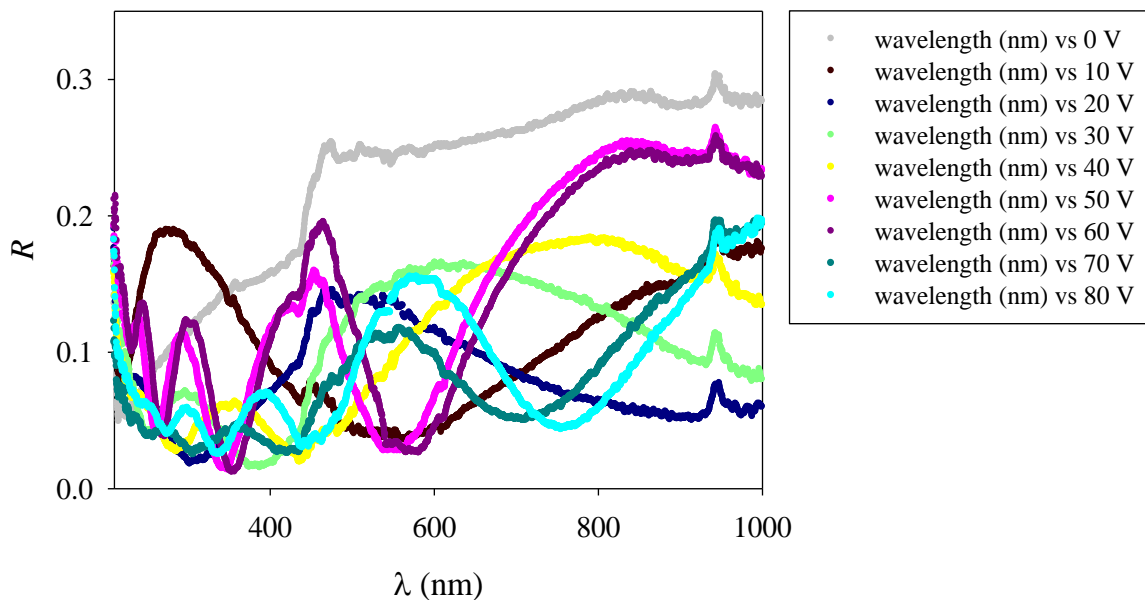
Figure 52. Reflectance spectra for the etched, and etched and coloured Zr samples obtained using a UV-Vis-NIR light source (DH-2000-BAL) that was fibre optically connected to a high-resolution spectrometer (HR-4000), Ocean Optics. Coloured samples were prepared at V_{AC} = 10, 20, ..., 80 V. Passivation was performed in aqueous 10 wt.% Na_2SO_4 electrolyte for 10 s at T = 298 K.

3-D Reflectance of Etched Zirconium Samples
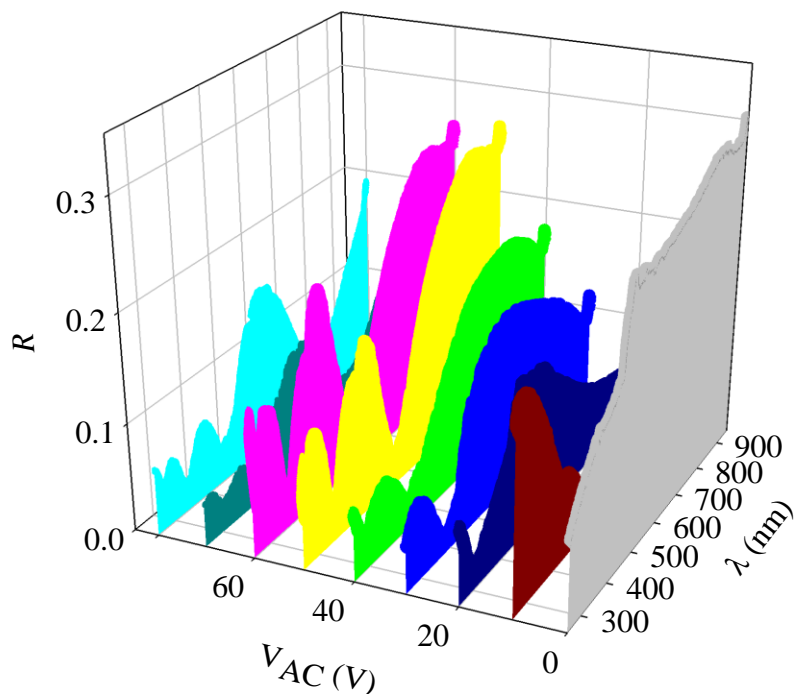
Figure 53. 3-D representation of reflectance spectra for the etched, and etched and coloured Zr samples obtained using a UV-Vis-NIR light source (DH-2000-BAL) that was fibre optically connected to a high-resolution spectrometer (HR-4000), Ocean Optics. Coloured samples were prepared at V_{AC} = 10, 20, ..., 80 V. Passivation was performed in aqueous 10 wt.% Na_2SO_4 electrolyte for 10 s at T = 298 K.

Reflectance spectra of the etched, and etched and coloured Zr samples can be seen in Figure 52. These spectra are also shown in Figure 53 as a three-dimensional representation for clear comparison of the relationship between the maxima and minima of each spectrum. The spectra of the etched and polished Zr samples are shown as a complete set of individual spectra inlaid with VLM images, which are used to interpret individual spectral characteristics, as well as to relate the reflectance results to the

colouration as analyzed by VLM, in Table 8. Etched Zr has a higher overall reflectance than etched Ti, which is due to the difference in their surface finish (smooth versus rough). The higher roughness factor of etched Ti causes more photons to be dispersed, thus reducing the number that reaches the fibre-optic cable and are detected. This increased roughness decreases the overall intensity of reflectance, as the rough surface is not directly reflecting as much light as the mirror-like surface of Zr.

Unpassivated Zr is more reflective than the coloured Zr samples. Etched Zr reflects more light in the 420-525 nm range, where blue and violet are present, which confirms the violet and blue grains seen in the VLM image, that lead to an overall violet shade in the gray metal. The reflectance of unpassivated Zr increases monotonically with wavelength because the refractive index is dependent upon wavelength and therefore frequency. The metal becomes shinier in appearance with higher wavelengths, as the refractive index increases.

The passivated samples can be seen beginning with the sample prepared at $V_{AC} =$ 10 V. This sample showed a broad maximum within the UV region, as well as an almost linear increase in reflectance at higher wavelengths, as seen in the case of unpassivated Zr. There is a feature in the 420-490 nm region that can be attributed to the blue and violet grains observed in the VLM image inset, the reflected violet and blue colours leading towards a dark violet passive layer. For the sample prepared at $V_{AC} = 20$ V, the spectrum differs from those previously examined; instead of an overall gradual increase in reflectance with wavelength, a broad maximum is observed at approximately 400-600 nm, followed by a monotonous decrease in R. This sample will thus have less reflected red light. The sample prepared at $V_{AC} = 20$ V has an additional feature in the 410-490 nm

range, and thus reflects more violet and blue colours, as can be seen in the inset VLM image, where violet and blue grains are predominant. There is also a previously mentioned broad peak in the 400-600 nm wavelength range, which corresponds to the reflection of green, yellow and orange light. The observed colouration is a dark blue, from a combination of violet, blue and most likely some green reflected light. The sample prepared at $V_{AC} = 30$ V has the same declining trend as wavelength increases, as was seen in the case of the sample prepared at $V_{AC} = 20$ V. This sample showed a broad reflection in the 450-650 nm range, which leads to reflectance of blue, green, yellow, orange and some red light. The inset VLM image predominantly shows grains that are orange, yellow and green, which creates an overall appearance of yellowish green. For the sample prepared at $V_{AC} = 40$ V, a very similar spectrum to that of the sample prepared at $V_{AC} = 30$ V is seen, but shifted towards higher wavelengths. This means that the sample prepared at $V_{AC} = 40$ V has increased intensity in the yellow, orange and red light range (590-780 nm). It also has decreased intensity in the violet and blue light regions (400-460 nm). This sample has a bright yellowish orange colour overall, which is derived from the yellow and orange grains observed in the VLM image inset. The spectra for samples prepared at $V_{AC} = 50$ and 60 V are very similar in shape, but once again the spectrum of the sample prepared at $V_{AC} = 60$ V is shifted to higher wavelengths than that for the sample prepared at $V_{AC} = 50$ V. The sample prepared at $V_{AC} = 50$ V has a feature in the 415-480 nm range, and thus reflects violet and blue light. There is also a maximum in the 350-550 nm range followed by a gradual increase in R from 600 to 780 nm, that correspond to violet and red colours; this is corroborated by the VLM image inset. There are blue, violet and red grains across the surface, which contribute to the overall appearance. Finally, there is a minimum (low intensity) centered at 535 nm, which means

that there is very little green light being reflected. Overall, this sample has a magenta colouration. The sample prepared at V_{AC} = 60 V has low intensity in the green light range, and high intensity in the blue, violet and red light ranges. There is a broad maximum in the 400-540 nm range, as well as a feature from 420-480 nm, which are reflecting blue and violet light. There is also a broad increase in R up to 780 nm, which indicates red light being reflected. A minimum (low intensity) at 560 nm allows for more green light to be reflected than was seen in the spectrum of the sample prepared at V_{AC} = 50, resulting in a different colouration overall. The sample prepared at V_{AC} = 60 has an overall teal and violet colouration from blue and violet grains seen in the inset VLM image. Finally, the samples prepared at V_{AC} = 70 and 80 V have a similar shape, both being less reflective overall than the previously discussed passivated samples. The sample prepared at V_{AC} = 70 V has a broad maximum centered at about 540 nm, which covers the blue, green and yellow light ranges. A side feature at 460 nm indicates an important blue contribution. There is a minimum (low intensity) centered around 690 nm, indicating that there is low reflectance of red light, but an increase in R up to 780 nm corresponds to dark red light being reflected. These results are confirmed in the VLM image inset, where blue, green, yellow and orange grains are prevalent across the surface to create an overall turquoise (bluish green) colouration. The spectrum of the sample prepared at V_{AC} = 80 V is once again shifted towards higher wavelengths than in the case of the sample prepared at V_{AC} = 70 V. The sample prepared at V_{AC} = 80 V has high intensity in the green light range, with low intensity observed in the violet and red light regions. There is a broad peak in the 450-700 nm range, which means that blue, green, yellow and orange light is being reflected, and a feature (shoulder) at 525 nm emphasizing the reflection of green light. This is shown in the VLM image inset, where

blue, green, yellow and orange grains create an overall colouration of light greenish blue. These results overall are very consistent with what was observed with VLM experiments.

The correlation between the etched, and etched and coloured Zr samples as a whole reveals a trend of wave patterns (maxima and minima in the spectra). The sample prepared at V_{AC} = 10 V has a half wave in the UV region and at the beginning of the visible wavelengths. The sample prepared at V_{AC} = 20 V shows a full wave near the centre of the spectrum, and the sample prepared at V_{AC} = 30 V similarly shows a wave, just shifted slightly to the higher wavelengths. In the spectrum for the sample prepared at V_{AC} = 20 V, half of a new wave appears in the UV region whereas, in the spectrum for the sample prepared at V_{AC} = 30 V, there is a full wave in the UV region. For the sample prepared at V_{AC} = 40 V, the spectrum is almost identical to that of the sample prepared at V_{AC} = 30 V; however, the spectrum is shifted towards higher wavelengths. The waves for the samples prepared at V_{AC} = 50 and 60 V are very similar: both have an additional wave appearing in the UV region, and the three remaining waves observed are also present, but shifted. The spectrum for the sample prepared at V_{AC} = 60 V is once again shifted towards higher wavelengths (red light region), as compared to that of the sample prepared at V_{AC} = 50 V. Finally, the spectra of the samples prepared at V_{AC} = 70 and 80 V are similar to one another, with the large peak near the IR region beginning to disappear, and another peak appearing in the UV region. These observations lead to the conclusion that, with a higher applied AC voltage, the wave propagates across the spectrum towards higher wavelengths (red-shifted). Thus, each higher applied AC voltage generates a further shift towards higher wavelengths. As a wave becomes near to the IR region, a

new wave appears within the UV region. This is thought to be due to the thin film interference reinforcing and cancelling wavelengths as the oxide layer thickens.[42]
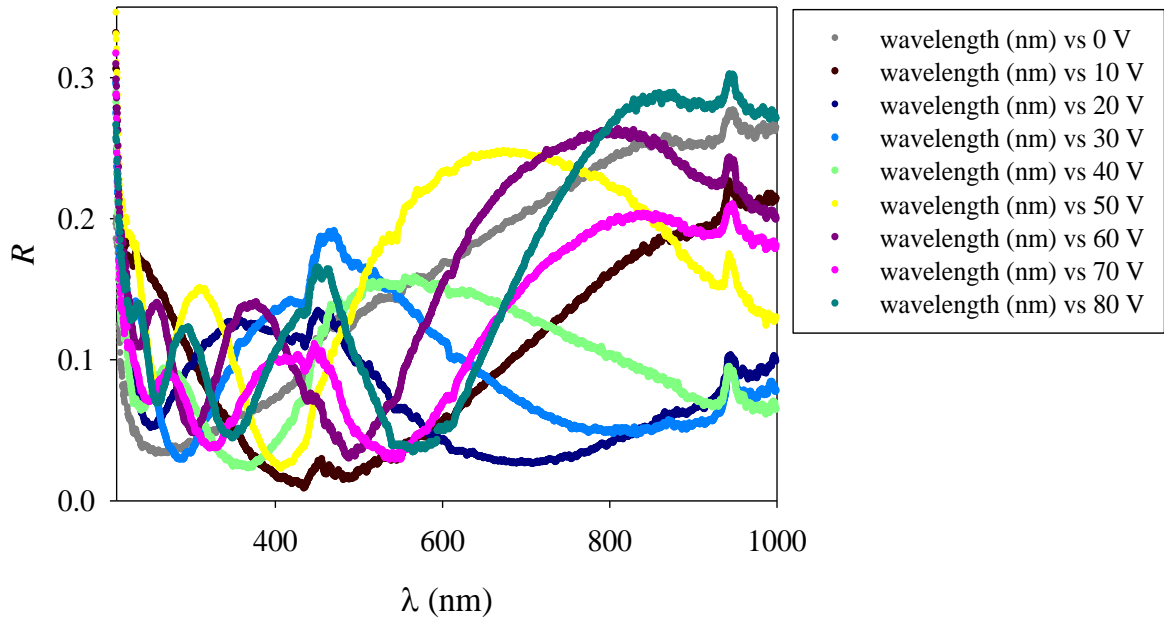
Figure 54. Reflectance spectra for the polished, and polished and coloured Zr samples, obtained using a UV-Vis-NIR light source (DH-2000-BAL) that was fibre optically connected to a high-resolution spectrometer (HR-4000), Ocean Optics. Coloured samples were prepared at V_{AC} = 10, 20, ... , 80 V. Passivation was performed in aqueous 10 wt.% Na_2SO_4 electrolyte for 10 s at T = 298 K.

3-D Reflectance of Polished Zirconium Samples
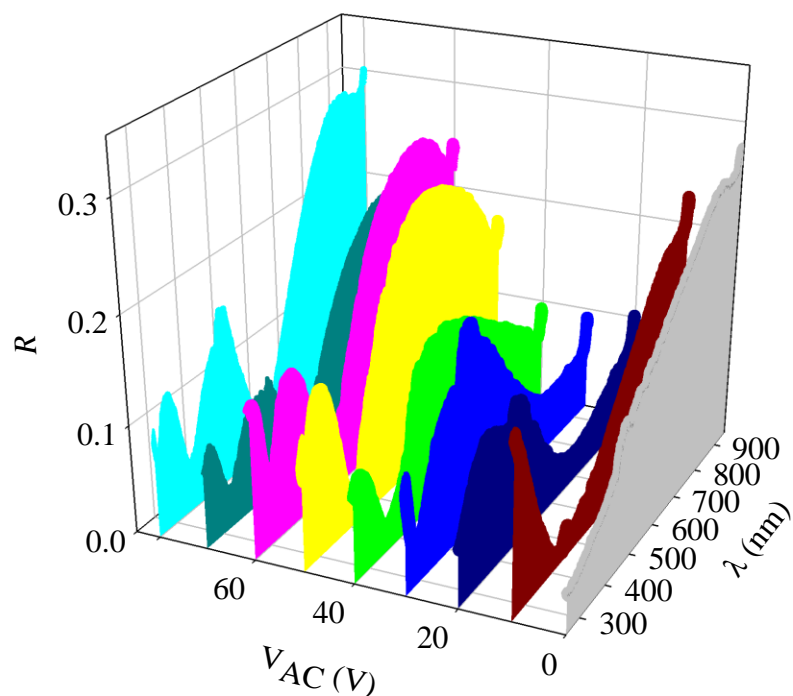
Figure 55. 3-D representation of reflectance spectra for the polished, and polished and coloured Zr samples, obtained using a UV-Vis-NIR light source (DH-2000-BAL) that was fibre optically connected to a high-resolution spectrometer (HR-4000), Ocean Optics. Coloured samples were prepared at V_{AC} = 10, 20, ... , 80 V. Passivation was performed in aqueous 10 wt.% Na_2SO_4 electrolyte for 10 s at T = 298 K.

Reflectance spectra of the polished, and polished and coloured Zr samples can be seen in Figure 54. These spectra are also shown in Figure 55 as a three-dimensional representation for clear comparison of the relationship between the maxima and minima of each spectrum. The spectra of the polished Zr samples are shown as a complete set in Table 8 in order to compare their overall shapes. The figures in Table 8 are individual

spectra inlaid with VLM images, which are used to interpret individual spectral characteristics, as well as to relate the reflectance results to the colouration as analyzed by VLM. The reflectance spectra of the two sets of Zr samples; (i) etched, and etched and coloured, and (ii) polished, and polished and coloured samples, are similar. Since etched Zr has a smooth, mirror-like surface when chemically etched due to fine underlying grain structure, a reflective surface presents on both polished and etched Zr samples.

Unpassivated polished Zr shows a relatively linear relationship between reflectance and wavelength because the refractive index increases with wavelength, as mentioned previously. A small region of increased light reflectance (a hump) in the 425-500 nm range indicates reflection of violet and blue light, which contributes to the overall dark gray colouration of unpassivated Zr. This is consistent with the reflectance results obtained for etched Zr, as well as VLM images.

The passivated samples can be seen beginning with the sample prepared at V_{AC} = 10 V. This sample showed a decrease in R within the UV region, as well as a monotonous increase in R from approximately 450 nm, as observed in the case of unpassivated Zr. There is a feature in the 420-490 nm range that can be attributed to blue and violet colours present in the VLM image inset. Due to the monotonous increase in R up to 780 nm, reflected orange and red light is observed as well, giving a reddish brown final colouration. The spectrum of the sample prepared at V_{AC} = 20 V shows high intensity in the 400-600 nm region, followed by a monotonous decrease in R. Because the sample prepared at V_{AC} = 20 V has an additional feature in the 440-490 nm range, it reflects more blue and violet light, as can also be seen in the VLM image inset, where blue and violet regions are predominant, giving an overall deep blue colouration. The

116

spectrum of the sample prepared at V_{AC} = 30 V has the same shape as the sample prepared at V_{AC} = 20 V, but there is an increase in intensity in the 400-700 nm range, which leads to reflection of violet, blue, green and yellow light. A feature in the 425-550 nm range can be assigned to a greater reflection of blue and green light. These results are confirmed by the VLM image inset, which shows blue, green and some yellow coloured clusters, resulting in an overall blue colouration. For the sample prepared at V_{AC} = 40 V, the spectrum shows increased intensity in the green, yellow and orange light region (475-650 nm), and low intensity in the region of violet light (400-450 nm). The VLM image inset shows the presence of green, yellow and orange colours. Consequently, this sample has a yellowish green colouration overall. The spectra of samples prepared at V_{AC} = 50 and 60 V are very similar in shape. The spectrum for the sample prepared at V_{AC} = 50 V shows low intensity in the 400-470 nm range, followed by a region of high intensity (500-780 nm) that covers the blue to red light range. The VLM image inset shows green, yellow and orange colouration, thus leading to an overall golden orange colour. The spectrum for the sample prepared at V_{AC} = 60 V is shifted towards higher wavelengths than the sample prepared at V_{AC} = 50 V; there is a region of low intensity in the blue light range (470-500 nm), and a region of high intensity in the violet, yellow, orange, green and red range, producing an overall orange and violet colour, which is confirmed by the VLM image inset, which shows violet, yellow, orange and red colours predominantly. Finally, the spectra of the samples prepared at V_{AC} = 70 and 80 V are very similar in shape. For the sample prepared at V_{AC} = 70 V, there is increased intensity in the 400-500 nm range (violet and blue light), as well as in the 650-780 nm range (orange and red light), with a small feature (hump) present in the 450-500nm region, which points to a greater contribution of violet and blue light. The VLM image inset shows violet, blue,
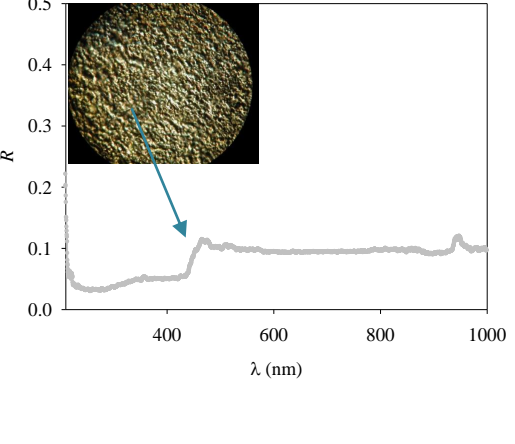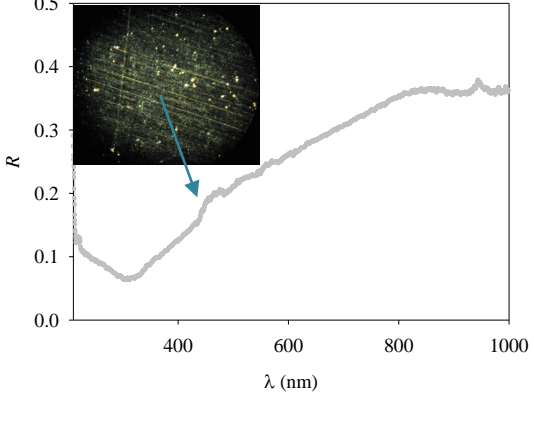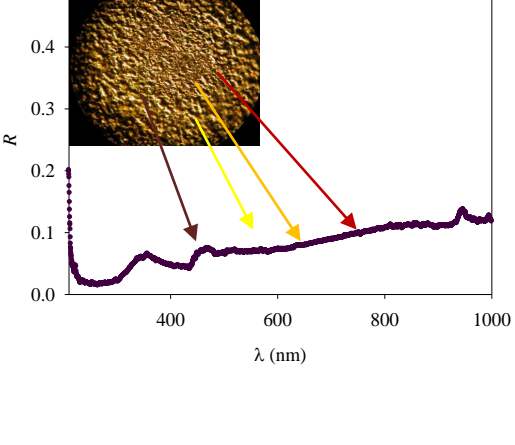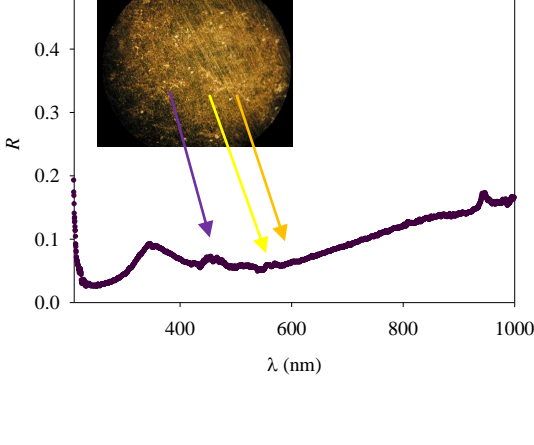
orange and red colours, producing an overall magenta colouration. For the sample prepared at $V_{AC} = 80$ V, the spectrum is shifted towards red wavelengths as compared to that of the sample prepared at $V_{AC} = 70$ V. This spectrum shows a broad peak in the 400-550nm range, which indicates the presence of violet, blue and green light. Rising intensity in the 625-780nm region indicates that red and orange light is being reflected. The overlapping feature in the 450-520 nm range is representative of blue and green light. These results are consistent with the VLM image inset, which shows blue and green light predominantly, producing an overall teal colouration.

Thus, the results are different to those of etched Zr; with the observed colourations and reflected light being different between the two surface treatment variations. This difference is most likely attributed to the thickness of the passive layer as well as the different surface morphologies. Since the observed colouration is due to iridescence, thickness as well as surface defects will affect the overall appearance of the light being reflected. The wave propagation towards higher wavelength with increased applied AC voltage is present in both polished and etched Zr samples. Thus, each higher applied AC voltage generates a shift further towards higher wavelengths. As a wave becomes near to the IR region, a new wave will appear within the UV range of wavelength.

Reflectance spectra of the etched, and etched and coloured Ti samples are shown above in Figure 56. These spectra are also shown in Figure 57 as a three-dimensional representation for clear comparison of the relationship between the maxima and minima of each spectrum. The spectra of the etched Ti samples are shown as individual spectra inlaid with VLM images, which are used to interpret individual spectral characteristics, as well as to relate the reflectance results to the colouration as analyzed by VLM, in Table 9

in order to compare their overall shapes. Etched Ti has a high dispersion of visible light since the surface structure is quite rough. This roughness translates into the reflectance intensity being low, since fewer photons are reaching the detector. Thus, etched Ti has much lower overall reflectance than etched Zr, which has a smoother surface structure.

Table 9. Comparison between etched and etched and coloured and polished and polished and coloured Ti samples using VLM images inlaid within reflectance spectra.

V_{AC} (V)	Spectra for Etched Titanium	Spectra for Etched Zirconium
0		
10		

20

30

40

50		
60		
70		
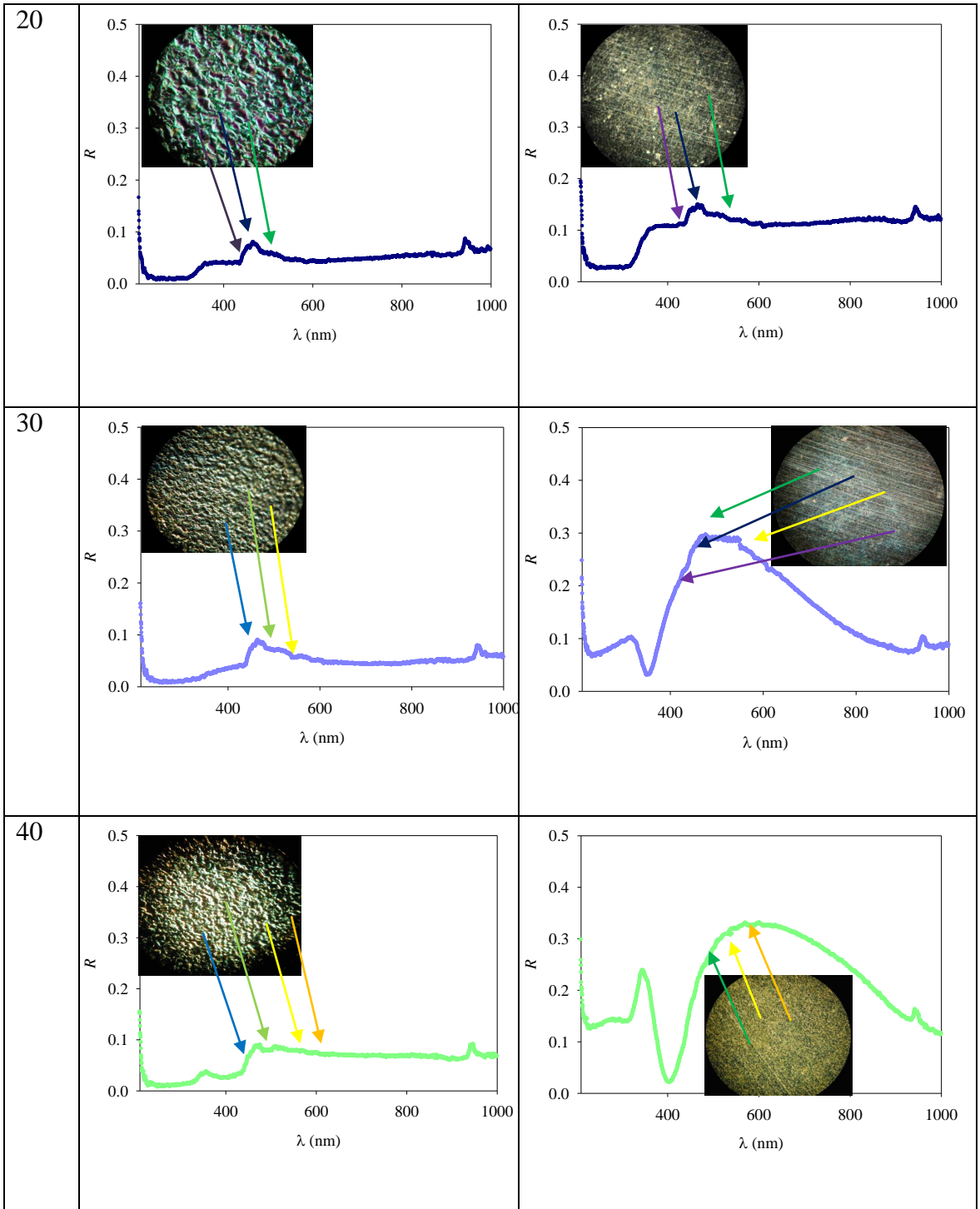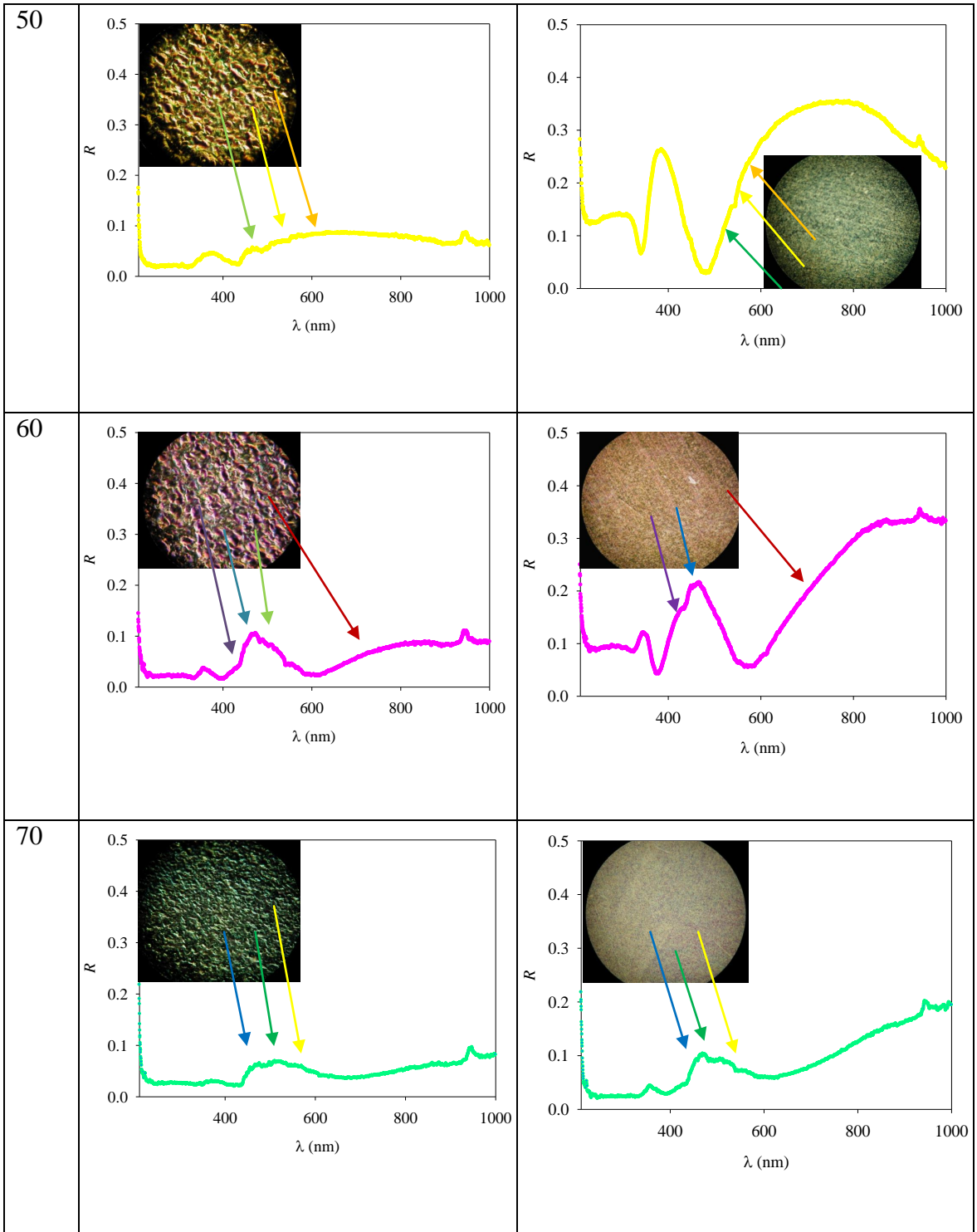
Figure 56. Reflectance spectra for the etched, and etched and coloured Ti samples, obtained using a UV-Vis-NIR light source (DH-2000-BAL) that was fibre optically connected to a high-resolution spectrometer (HR-4000), Ocean Optics. Coloured samples were prepared at V_{AC} = 10, 20, ..., 80 V. Passivation was performed in aqueous 10 wt.% Na_2SO_4 electrolyte for 10 s at T = 298 K.

3-D Reflectance of Etched Titanium Samples

Figure 57. 3-D representation of reflectance spectra for the etched, and etched and coloured Ti samples, obtained using a UV-Vis-NIR light source (DH-2000-BAL) that was fibre optically connected to a high-resolution spectrometer (HR-4000), Ocean Optics. Coloured samples were prepared at V_{AC} = 10, 20, ..., 80 V. Passivation was performed in aqueous 10 wt.% Na_2SO_4 electrolyte for 10 s at T = 298 K.

The spectrum of unpassivated Ti metal, shows a very slight increase in reflectance with wavelength. A step wise increase in R is present in the range of 450-500 nm, as well as a small overlapping feature in the 475-500 nm range where blue light is present. This feature is a confirmation of the blue areas observed in the inset VLM image, leading to a blue shade in the overall gray metal. This is unlike Zr, which reflects more violet light in

unpassivated samples. Titanium has a lighter overall gray colouration than that of Zr; thus, without the reflectance of violet light, it appears as a lighter gray colour.

The passivated samples can be observed beginning with the sample prepared at $V_{AC} = 10$ V. This sample shows a gradual increase in reflection as wavelength increases. This trend is showing that the passive layer becomes shinier with higher incident wavelengths, due to the increase in its refractive index, which was also true of Zr. There is a feature in the 420-500 nm range, which indicates the reflectance of violet and blue light. There are also contributions from yellow, orange, and red light reflection, which is confirmed by the VLM image inset, leading to a reddish brown appearance. The spectrum of the sample prepared at $V_{AC} = 20$ V shows a feature in the range of 440-550 nm, indicating the presence of violet, blue and green light reflection. This is confirmed by the VLM image inset, showing violet, blue and green regions, thus producing a dark blue colouration overall. The spectrum for the sample prepared at $V_{AC} = 30$ V shows a feature in the 450-600 nm range, which represents reflection of blue, green and yellow light, thus producing an overall light blue colouration. These findings are corroborated by the VLM image inset, which shows regions of blue, green and yellow colours. The spectrum for the sample prepared at $V_{AC} = 40$ V shows a step-wise increase in R, creating a region of high intensity in the 475-610 nm region, which reflects blue, green, yellow and orange light. This leads to a light green overall colouration which is derived from the presence of blue, green, yellow and orange clusters shown in the inset VLM image. The spectrum for the sample prepared at $V_{AC} = 50$ V has a contoured shape, as opposed to the step-wise increase observed in the spectrum for the sample prepared at $V_{AC} = 40$ V. This sample predominantly reflects orange and yellow light (580-650 nm), producing a golden

124

orange colour. The inset VLM image shows the contributions from green, yellow and orange reflected light. The sample prepared at V_{AC} = 60 V has a broad maxima in the 400-600 nm range, a gradual increase in R as λ reaches 780 nm, indicating the presence of red and violet light, as well as some blue and green light to produce an overall magenta colour. The inset VLM image illustrates the component violet, blue, green and red colours. Finally, the spectra of the samples prepared at V_{AC} = 70 and 80 V are similar in shape. The sample prepared at V_{AC} = 70 V has a region of high intensity in the 450-600 nm range, thus there are contributions from green, yellow, blue and red reflected light. As the inlaid VLM image shows, there is an overall greenish teal colouration made up of blue, green and yellow colours. The spectrum of the sample prepared at V_{AC} = 80 V is shifted slightly to higher wavelengths than that of the sample prepared at V_{AC} = 70 V. The sample prepared at V_{AC} = 80 V contains a broad region of high intensity in the range of 450-700 nm. Thus, this sample has blue, green, yellow and some orange reflected light. The inset VLM image shows blue, green and yellow colours, which produce a bluish teal colouration.

The spectra of the Ti samples were red-shifted with higher applied AC voltage, which was consistent with the findings for the Zr samples.
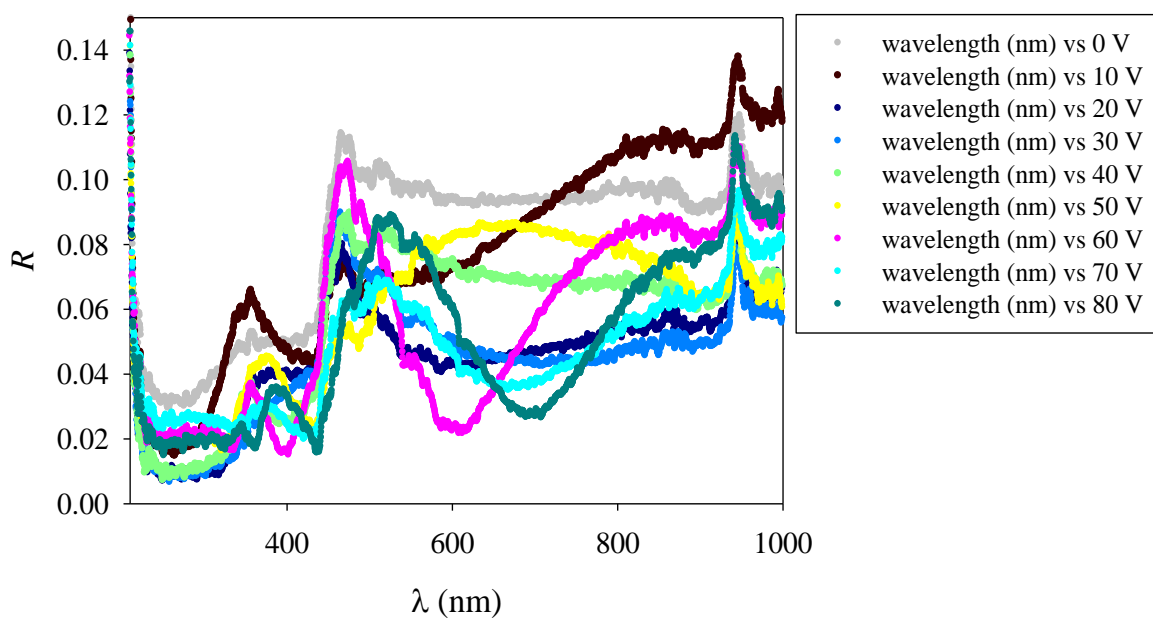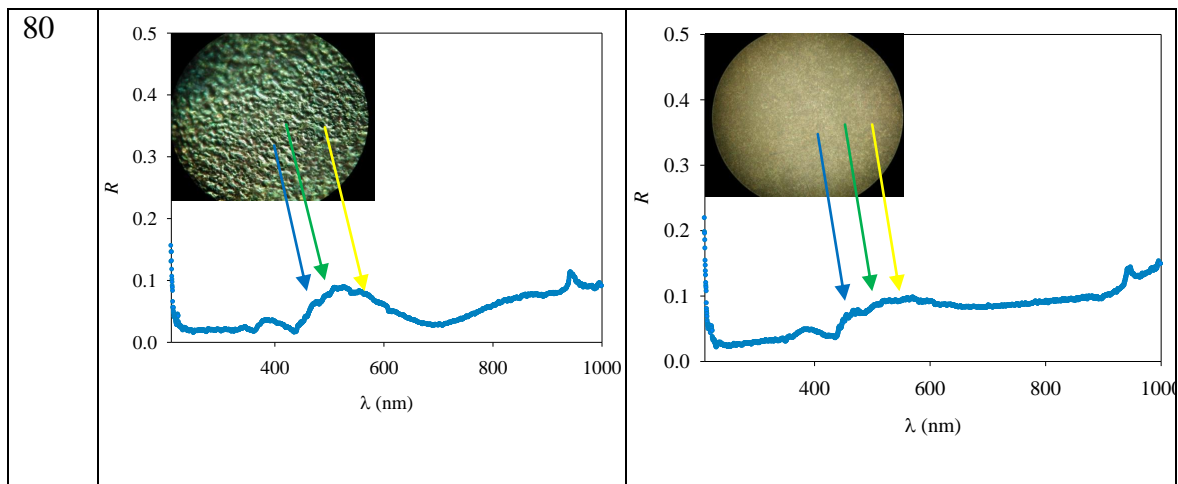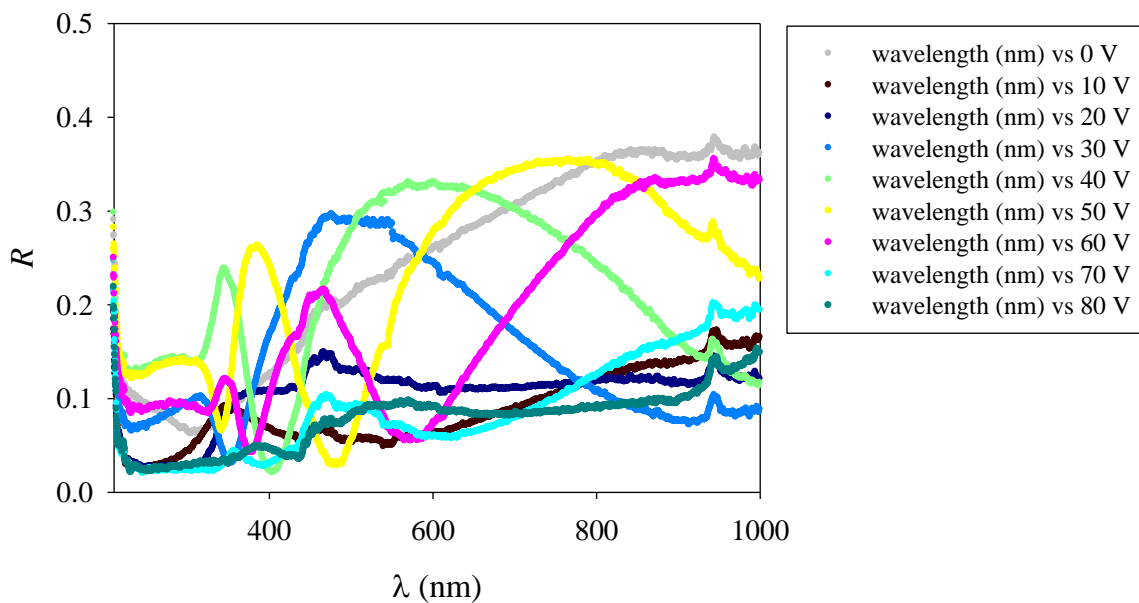
Figure 58. Reflectance spectra for the polished and polished and coloured Ti samples, obtained using a UV-Vis-NIR light source (DH-2000-BAL) that was fibre optically connected to a high-resolution spectrometer (HR-4000), Ocean Optics. Coloured samples were prepared at $V_{AC} = 10, 20, ..., 80$ V. Passivation was performed in aqueous 7.5 wt.% NH_4BF_4 electrolyte for 10 s at $T = 298$ K.
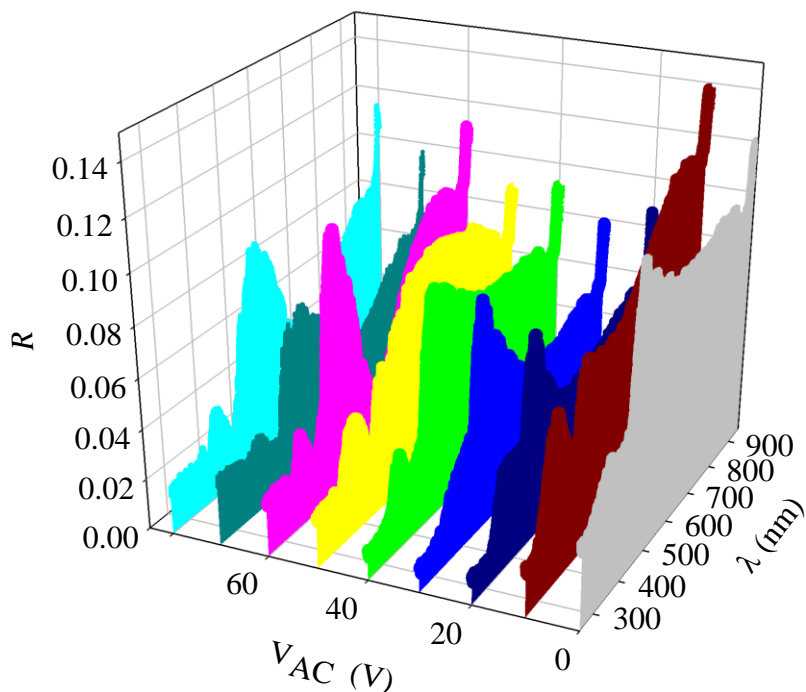
3-D Reflectance of Polished Titanium Samples
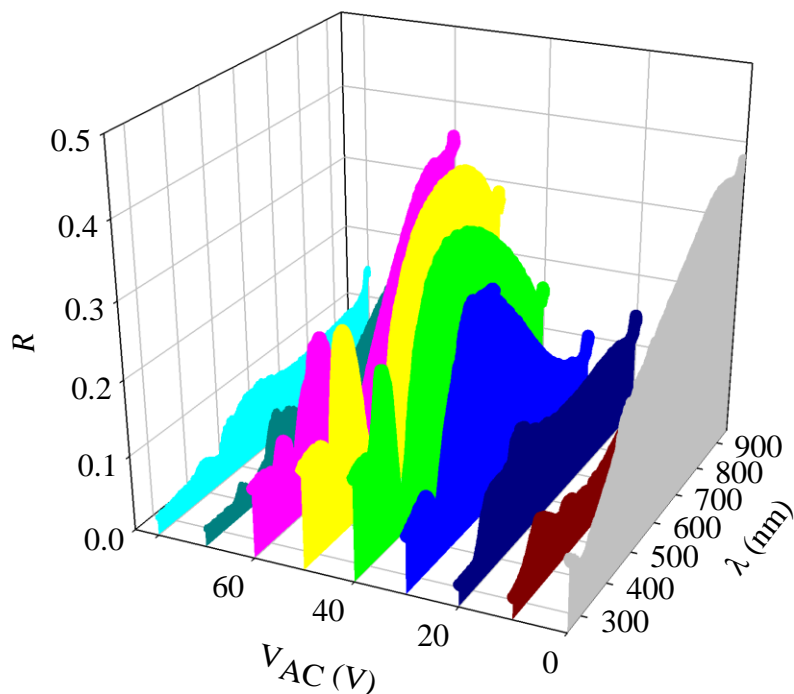
Figure 59. 3-D representation of reflectance spectra for the polished and polished and coloured Ti samples, obtained using a UV-Vis-NIR light source (DH-2000-BAL) that was fibre optically connected to a high-resolution spectrometer (HR-4000), Ocean Optics. Coloured samples were prepared at V_{AC} = 10, 20, ..., 80 V. Passivation was performed in aqueous 7.5 wt.% NH_4BF_4 electrolyte for 10 s at T = 298 K.

Reflectance spectra of the polished, and polished and coloured Ti samples can be seen in Figure 58. These spectra are also shown in Figure 59 as a three-dimensional representation for clear comparison of the relationship between the maxima and minima of each spectrum. The spectra of the polished Ti samples are shown as a complete set in Table 9 in order to compare their overall shapes. These spectra are individual spectra inlaid with VLM images, which are used to interpret individual spectral characteristics as

well as to relate the reflectance results to the colouration as analyzed by VLM. The spectra for polished Ti samples show a very reflective surface due to mechanical polishing, which creates a mirror-like finish. This is unlike the etched Ti samples, where the roughness translated into low reflectance intensity. Thus, the overall intensity in the spectra of polished Ti is higher than that of the etched Ti samples.

The spectrum of the unpassivated Ti (V_{AC} = 0 V) sample shows the trend of monotonous increasing R with wavelength; thus, the material is becoming more reflective at higher wavelengths. Polished Ti reflects slightly more light in the 450-500 nm range (hump), illustrating that there is a bit more blue light being reflected. This is confirmed in the VLM image inset, where blue colouration is observed, creating an overall lighter gray colour than that of unpassivated Zr. This is consistent with the results for etched Ti, as well as the appearance of the metal in general.

The passivated samples can be observed beginning with the specimen prepared at V_{AC} = 10 V. The spectrum for this sample also illustrates a slight increase in R with higher wavelength. There is a feature in the 420-500 nm region (violet and blue light), as well as some small features in the 560-625 nm region (yellow and orange light). The inset VLM image shows violet, yellow, orange and red colours, creating an overall colouration of reddish brown. For the sample prepared at V_{AC} = 20 V, violet, blue and green light are reflected in the 400-550 nm range, producing an overall dark blue colour. This is confirmed in the VLM image inlaid, where violet, blue and green regions are observed. The sample prepared at V_{AC} = 30 V has a very broad region of high intensity in the visible spectrum range (400-780 nm). This large maximum points to all visible light being reflected. However, the visible light range that is being reflected at the highest

intensity will be the most prominent contribution towards overall colour. The largest intensity is found in the 425-570 nm range, where violet, blue, green, and yellow light are reflected. The inset VLM image shows that there are violet, blue, green and yellow coloured areas contributing to the overall light blue colouration. The sample prepared at $V_{AC} = 40$ V has a similar shape to that of the sample prepared at $V_{AC} = 30$ V, however, there is a shift to higher wavelength values. The sample prepared at $V_{AC} = 40$ V has low intensity in the 375-425 nm range, thus violet light is not being reflected. The broad region of high intensity has also shifted to cover the 475-780 nm range, which is reflecting blue, green, yellow, orange and some red light. The VLM image inset shows blue, green and yellow colours predominantly, which produce an overall light green colouration. The spectrum for the sample prepared at $V_{AC} = 50$ V has low intensity in the 450-510 nm region, which indicates a lack of blue light being reflected. This spectrum is similar to that of the sample prepared at $V_{AC} = 40$ V, however, it is shifted to higher wavelength values. Thus, there is high intensity in the 525-780 nm region (green, yellow, orange, red), as well as the 400-445 nm region (violet). The VLM image inset shows contributions from green, yellow and orange to create an overall golden orange colour. The spectrum of the sample prepared at $V_{AC} = 60$ V is similar to that of the sample prepared at $V_{AC} = 50$ V, however, there is once again a shift towards higher wavelength values. Due to this shift, there is more violet, blue, and red light reflected, which elicits an overall magenta colouration. This is confirmed in the VLM image shown inlaid, which shows regions of violet, blue and red colours. Finally, the spectra for the samples prepared at $V_{AC} = 70$ and 80 V are similar. The spectrum for the sample prepared at $V_{AC} = 70$ V shows high intensity in the blue and green light regions (450-560 nm), as well as an increase in R as λ reaches the red light region (650-780 nm). The inset VLM image

129

shows blue, green and yellow regions, which create an overall teal colour. For the sample prepared at V_{AC} = 80 V, there is prominence of blue and red light in the spectrum, with the same amount of green light being reflected. The inset VLM image shows blue, green and yellow coloured regions which produce a greenish blue colour.

We observe that for Ti the polished and etched samples prepared at the same V_{AC} have the same overall colouration, which is derived from the reflected component colours. This is different from what was observed for Zr, where the colouration was different between etched and polished samples. Another difference lies in the intensities of reflectance. The polished Ti samples clearly showed a higher overall R intensity as compared to the etched samples. Zirconium, however, showed little difference between polished and etched samples in regards to intensity. This was explained previously, and is due to the fine grain structure of Zr.

Overall, from the reflectance results, two distinct trends arise: (i) the regions of high reflectance intensity and their corresponding wavelength values are consistent with the surface colouration observed using VLM experiments, and (ii) there is a red-shift as the applied AC voltage is increased; waves are reappearing in the UV region as soon as they become depleted beyond the IR region. Zirconium and Ti show different trends between the colourations of their etched and polished samples. Since Ti has two oxide layers, with Zr only having one, it is possible that the passive layer thickness on Ti is more consistent in formation, even with different surface treatments. Thus, the colourations, which are caused by iridescence, would be the same for polished and etched Ti samples prepared at the same V_{AC}. This trend is observed for Ti, while Zr samples are not consistent in their colouration between polished and etched samples of the same $V_{AC.}$

4.4 Profilometry

Surface profiling and roughness measurements were taken using a stylus profiler. Surface topography maps (2.5 mm by 2.5 mm) are shown in Table 10 and 12. These experiments provided roughness (R_a) values for each of the four topographical maps taken per sample, which were then averaged and summarized in Table 10 for four sets of samples; (i) etched, and etched and coloured Ti, (ii) etched, and etched and coloured Zr, (iii) polished, and polished and coloured Ti and (iv) polished, and polished and coloured Zr. As was previously discussed at the beginning of the results section (VLM), etched Ti is rougher than etched Zr because of the fine grain structure of Zr compared with Ti. The mechanically polished Ti and Zr specimens were similar in roughness. Etched Zr was only slightly rougher than the polished samples due to its smooth mirror-like finish after chemical etching. The overall roughness values are representative of the VLM and AFM (see next section) results, where pores were observed on the surface of samples prepared at high V_{AC} (60-80 V). The roughness values were higher overall for these samples prepared at V_{AC} = 60, 70, and 80 V due to the surface pores present, which cluster together to become larger with higher applied AC voltage. The inconsistent values of R_a for the samples prepared at V_{AC} = 10 and 20 V; are larger than expected. Roughness increases with passivation voltage, a trend which was also observed by Zhao.[26]

Table 10. Profilometry results for surface roughness (R_a) of four sets of samples; (i) etched, and etched and coloured Ti, (ii) etched, and etched and coloured Zr, (iii) polished, and polished and coloured Ti and (iv) polished, and polished and coloured Zr. The error is expressed as a standard deviation (m = 4).

V_{AC} (V)	R_a etched titanium (µm)	R_a etched zirconium (µm)	R_a polished titanium (µm)	R_a polished zirconium (µm)
0	1.220 ± 0.099	0.505 ± 0.023	0.369 ± 0.021	0.33 ± 0.18
10	1.29 ± 0.12	0.46 ± 0.10	0.140 ± 0.010	0.217 ± 0.022
20	0.870 ± 0.026	0.458 ± 0.023	0.2330 ± 0.0075	0.164 ± 0.021
30	0.813 ± 0.055	0.506 ± 0.054	0.254 ± 0.020	0.161 ± 0.020
40	0.879 ± 0.052	0.41 ± 0.11	0.1650 ± 0.0015	0.066 ± 0.013
50	0.839 ± 0.061	0.414 ± 0.065	0.152 ± 0.051	0.149 ± 0.010
60	1.055 ± 0.021	0.580 ± 0.010	0.450 ± 0.079	0.277 ± 0.023
70	0.991 ± 0.025	0.696 ± 0.033	0.30 ± 0.14	0.2890 ± 0.0074
80	0.921 ± 0.017	0.727 ± 0.058	0.219 ± 0.019	0.188 ± 0.091

Titanium samples can be observed in Table 11. Due to the nature of chemical etching, the metal is dissolved in surface layers, evenly, thus the profiles for etched samples have an overall level surface. Conversely, the polished samples have a different shape due to the nature of mechanical polishing. There are uneven surfaces caused by a variation in the applied pressure and instability of the sample during the polishing procedure. The polished samples, thus, have overall lower values of R_a, but have a contoured appearance. A similar trend is observed for Zr samples in Table 12.

Table 11. Three-dimensional (3D) profilometry profiles of two sets of samples; (i) etched, and etched and coloured and (ii) polished, and polished and coloured Ti samples. Coloured samples (b – i) prepared at V_{AC} = 10, 20, ..., 80 V. Passivation was performed in aqueous 7.5 wt.% NH_4BF_4 electrolyte for 10 s at T = 298 K.

V_{AC} (V)	3-D profile for Etched Titanium	3-D profile for Polished Titanium
0		
10		
20		

133

30		
40		
50		

60		
70		
80		
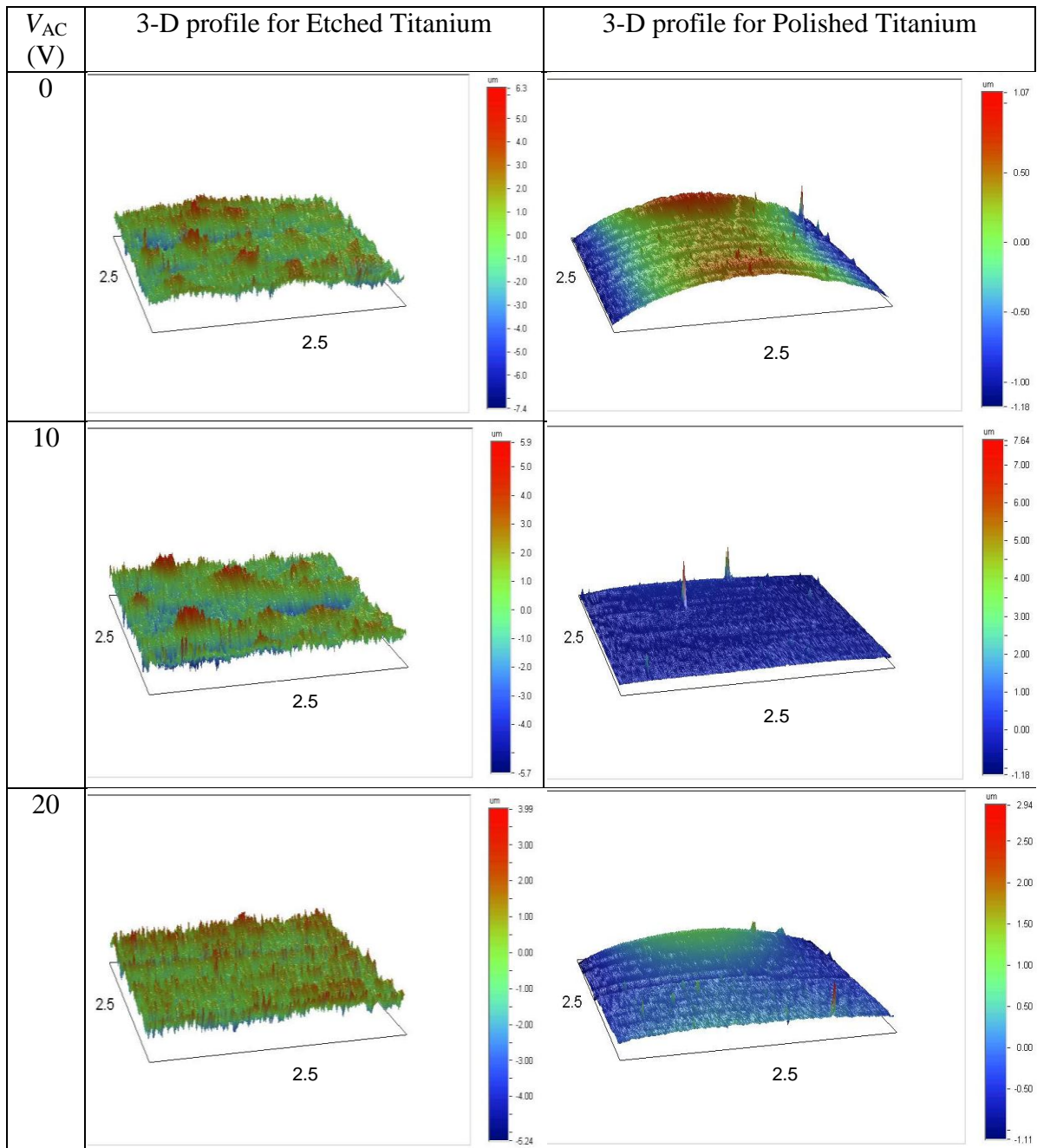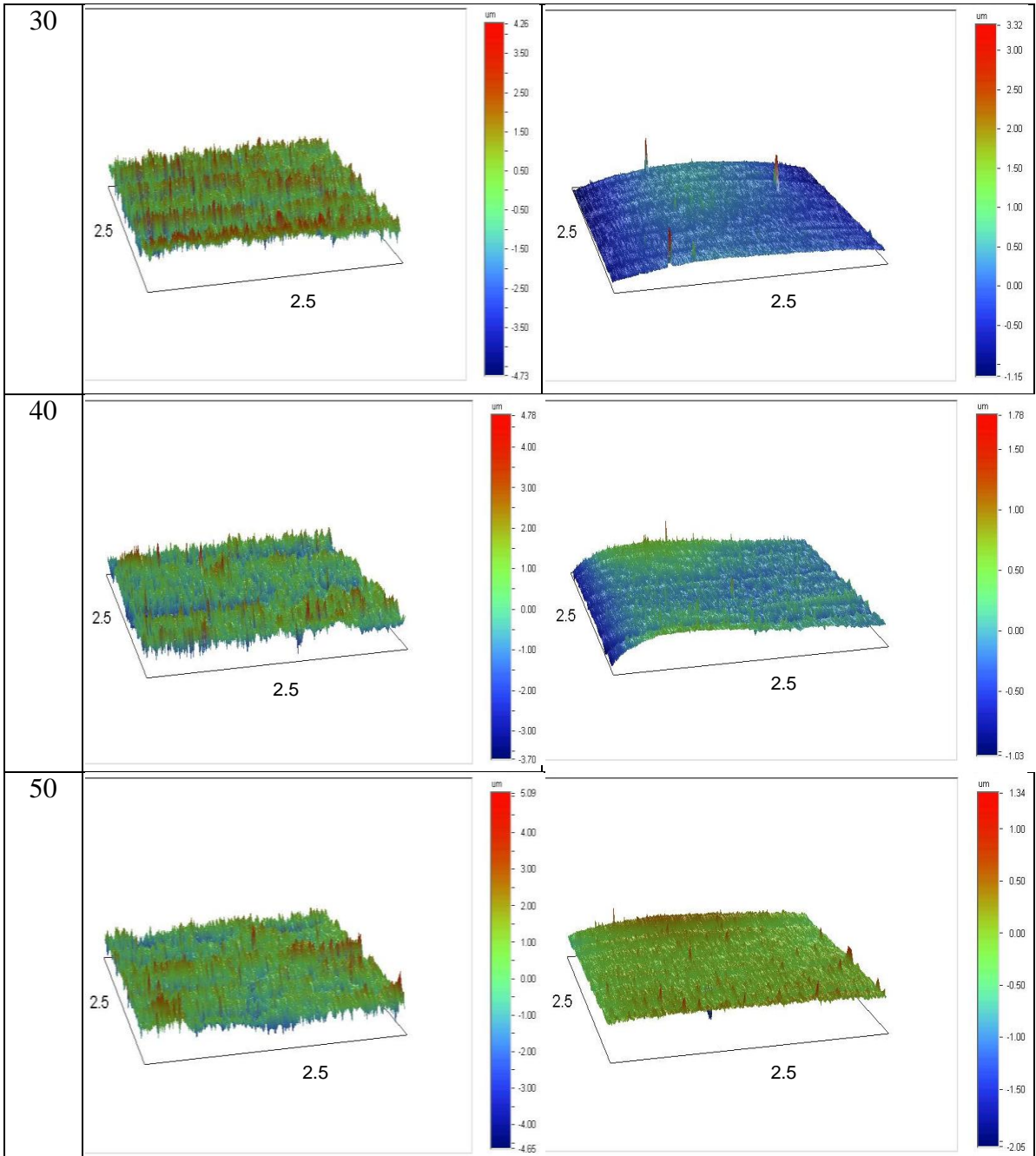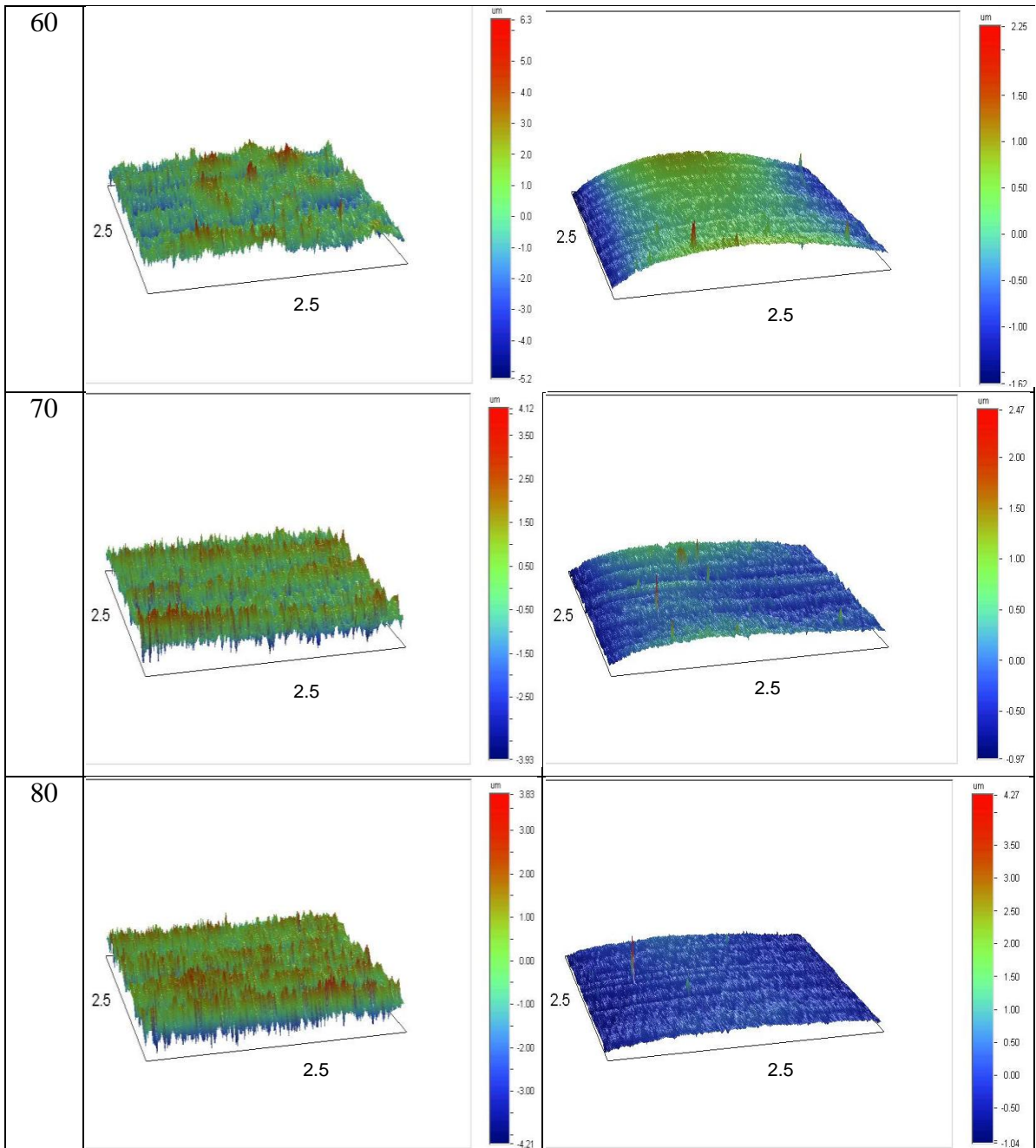
Table 12. Three-dimensional (3D) profilometry profiles of two sets of samples; (i) etched, and etched and coloured and (ii) polished, and polished and coloured Zr samples. Coloured samples (b − i) prepared at VAC = 10, 20, ..., 80 V. Passivation was performed in aqueous 10 wt.% Na_2SO_4 electrolyte for 10 s at $T = 298$ K.

V_{AC} (V)	3-D profile for Etched Zirconium	3-D profile for Polished Zirconium
0		
10		
20		

30		
40		
50		
60		

| 70 | | |
| 80 | | |
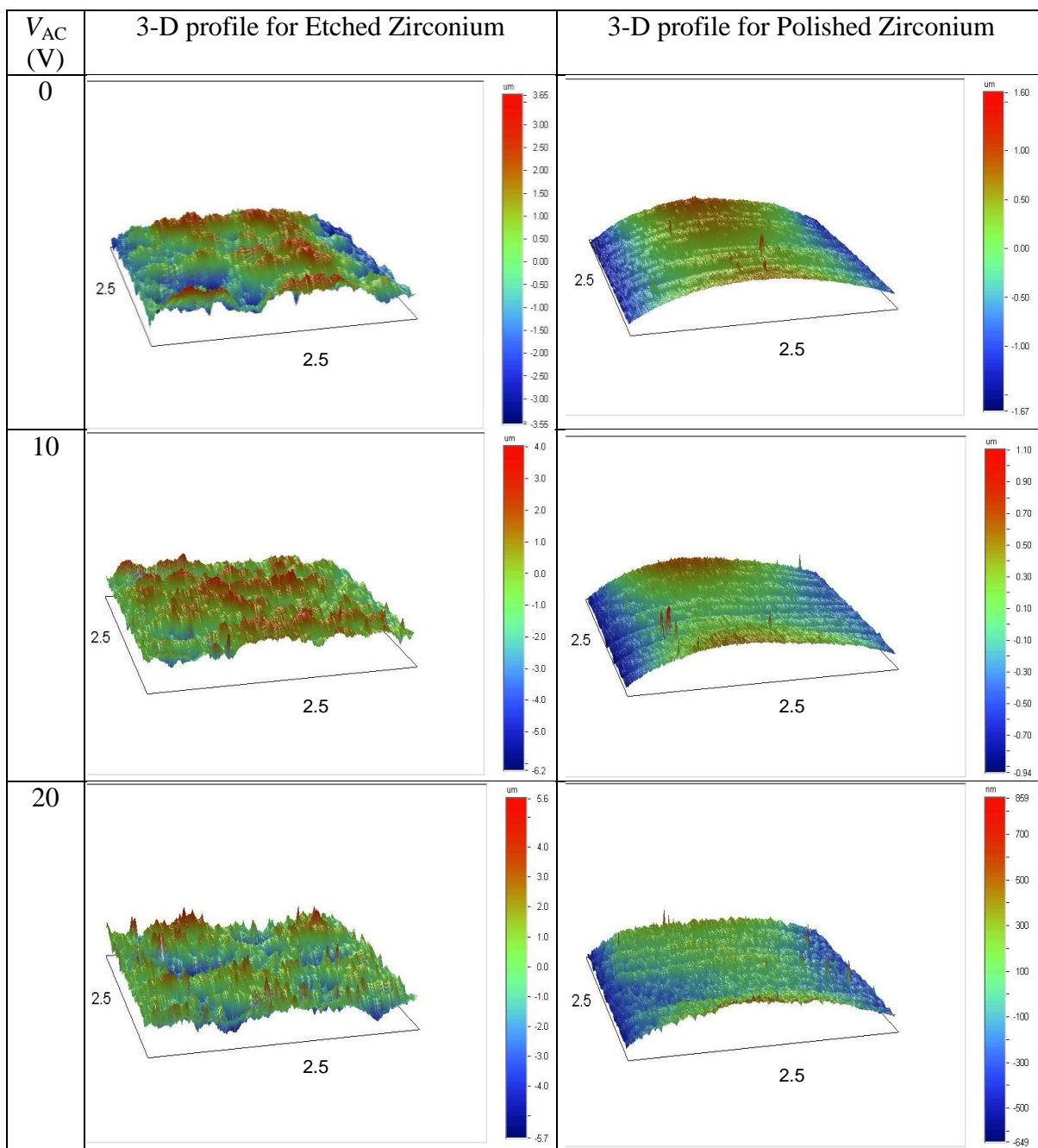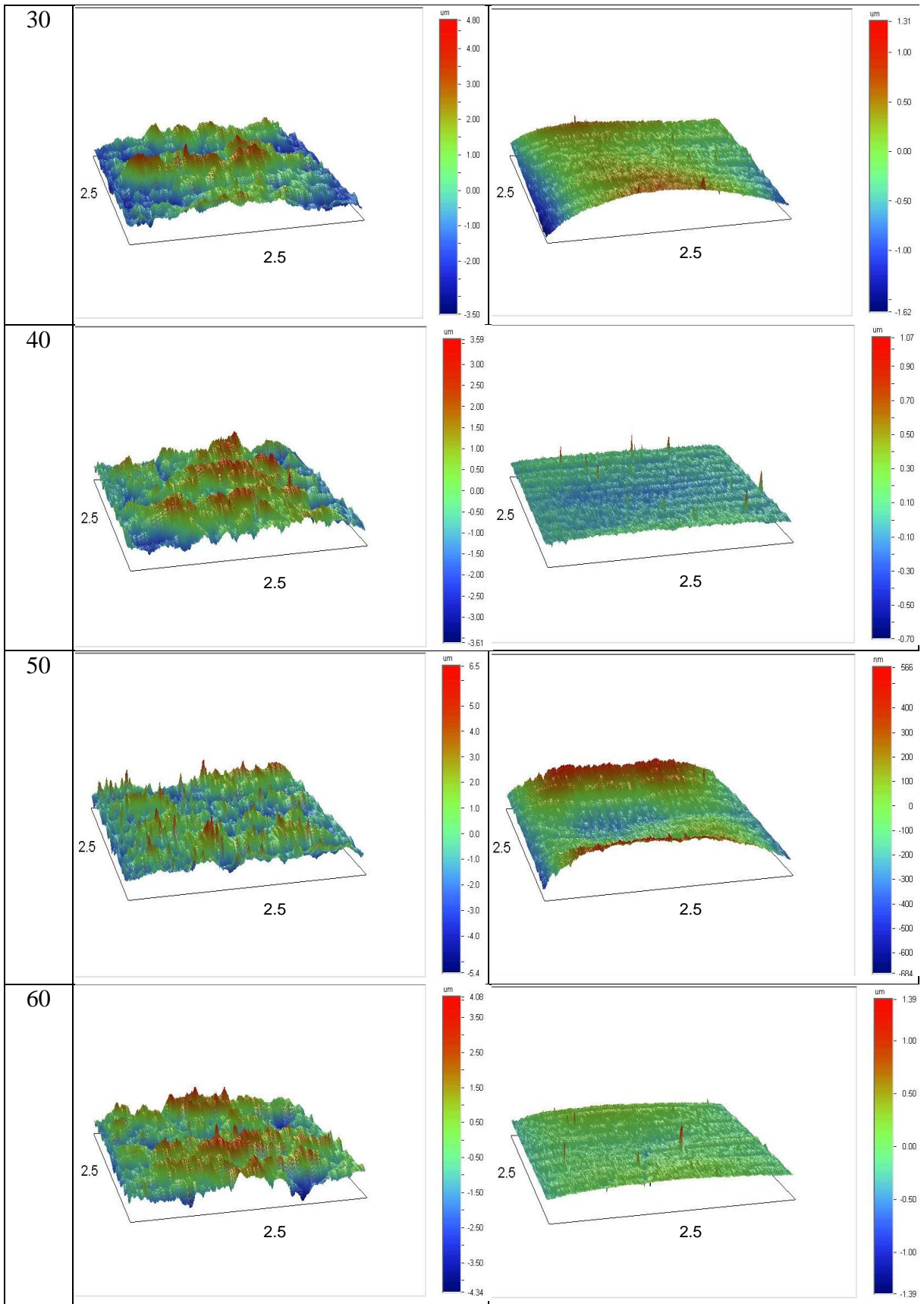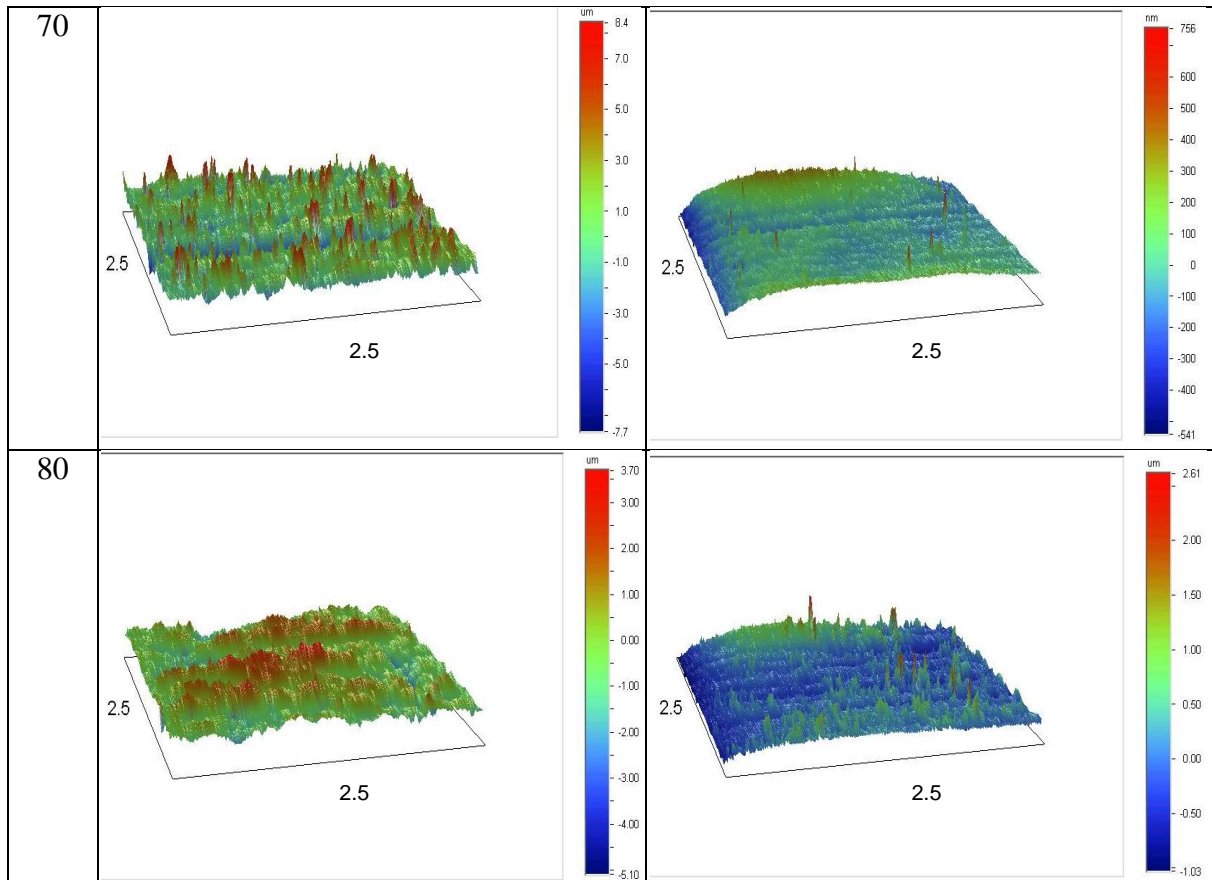
4.5 AFM

Atomic force microscopy experiments were performed on unpassivated etched, and etched and coloured Zr samples prepared at V_{AC} = 10, 20, ..., 80 V. Surface morphology (topography) maps of the samples were taken in three different dimensions (x,y = 1,2,5, and 15 μm, z = 50-500 nm depending on sample depth). The height of the sample (z) is dependent upon the surface structure present at various x, y coordinates. The largest of the surface morphology maps (15 μm x 15 μm x up to 500 nm) are shown as three-dimensional profiles in Figure 60. The three-dimensional profiles illustrate a change in morphology occurring with the increase in passivation voltage. With

138

increasing V_{AC}, a smoother surface is obtained until V_{AC} = 60 V is reached. From V_{AC} =

60 to 80 V, small pores appear, in agreement with VLM measurements (

Figure 50), which revealed surface defects that are most likely derived from localized

electrochemical breakdown.[32,33] Although porosity is not an objective of this project, the

results show that, if needed, porosity could be introduced in a controlled manner.

g.

h.

i.
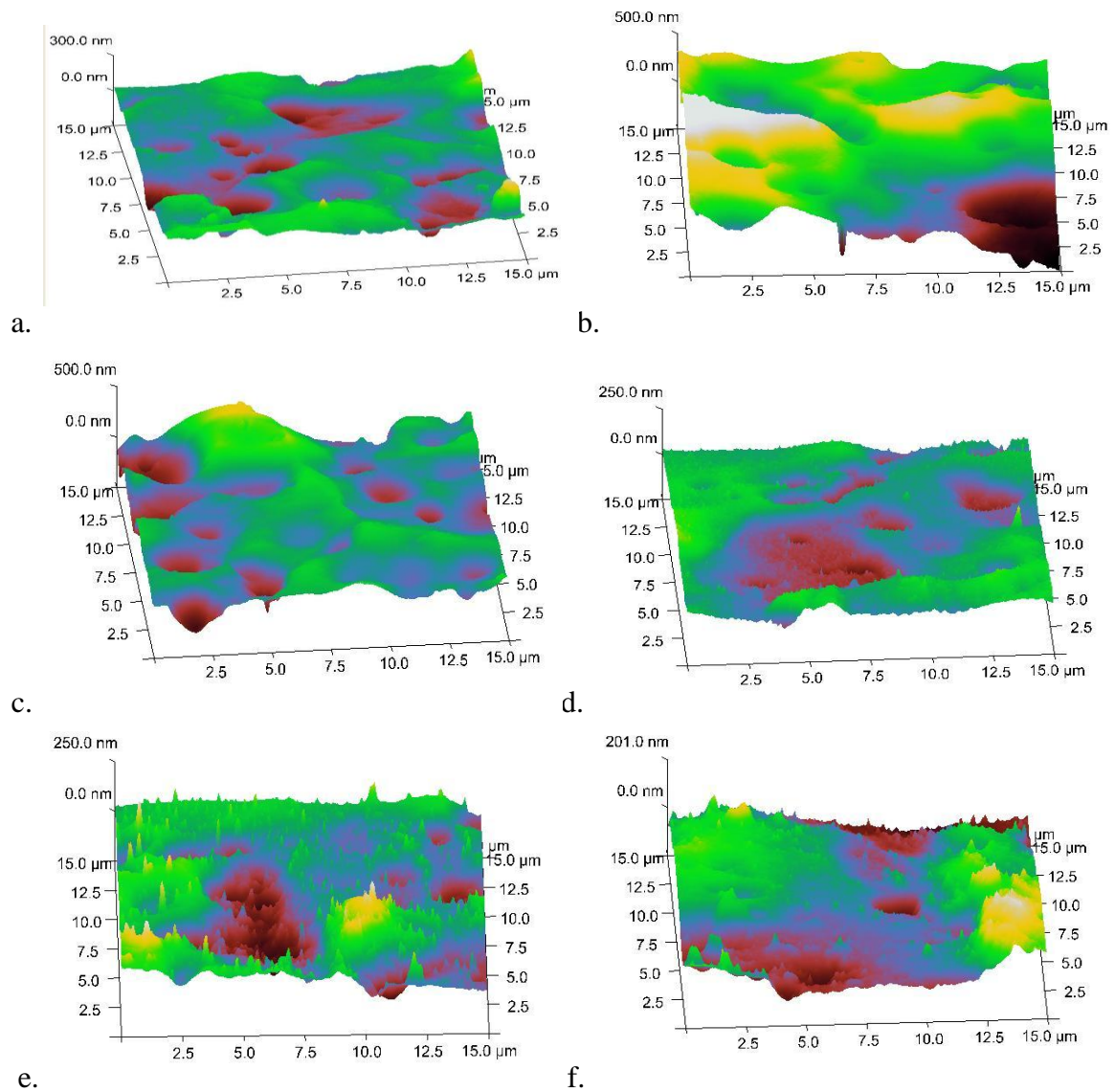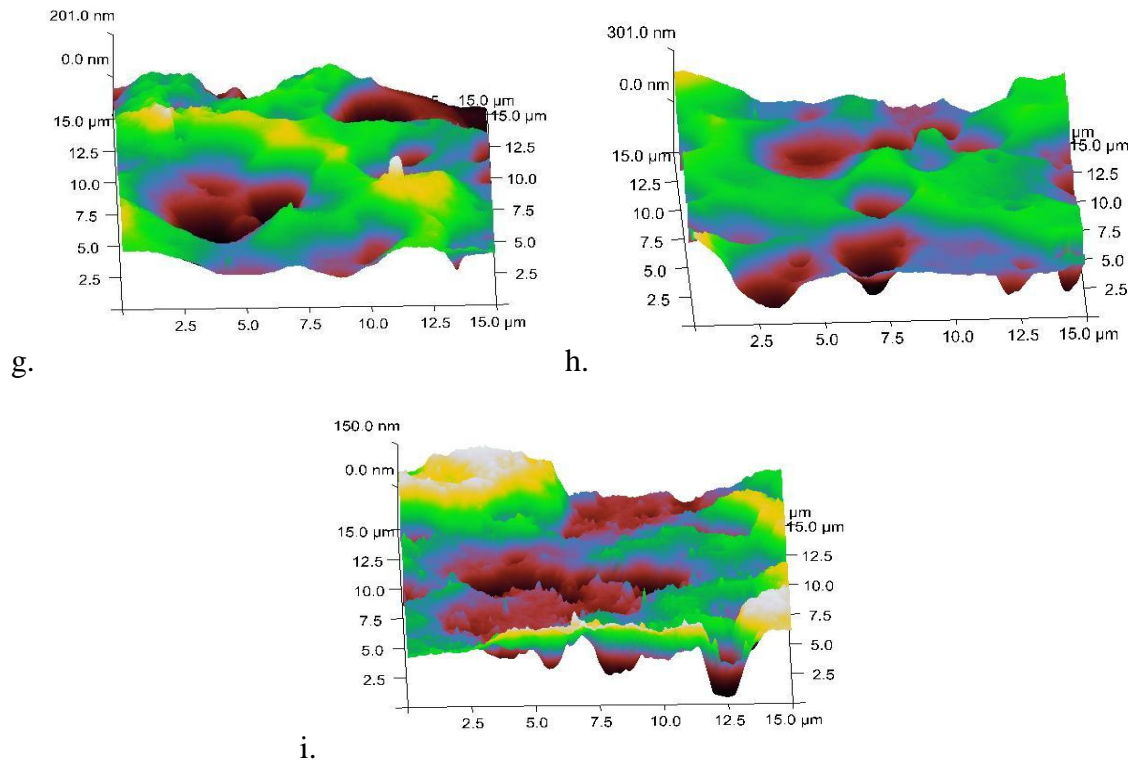
Figure 60. AFM profiles of the etched (a), and etched and coloured Zr (b – i) samples.

From b to i, the passivation voltage is $V_{AC} = 10, 20, ... , 80$ V. Passivation was performed

in aqueous 10 wt.% Na_2SO_4 electrolyte for 10 s at $T = 298$ K.
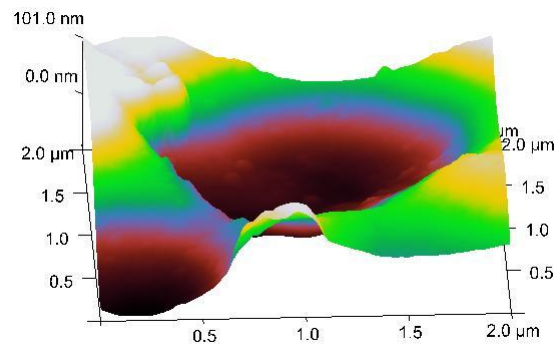
Figure 61. AFM 3-D image taken of etched Zr sample prepared at $V_{AC} = 60$ V, with a

map size of x,y = 2 µm. Pore shown roughly 1.7 µm in diameter.
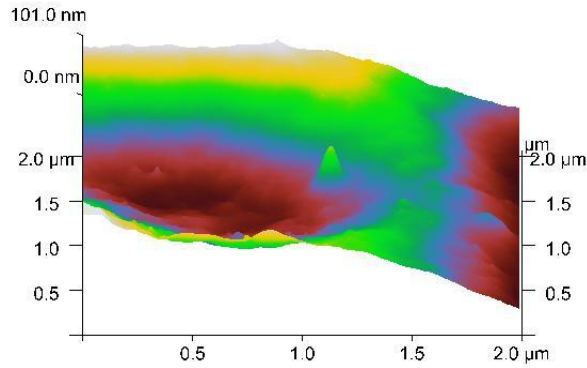
Figure 62. AFM 3-D image taken of etched Zr sample prepared at $V_{AC} = 70$ V, with a map size of x,y = 2 µm. Pore shown roughly 2.6 µm in diameter.
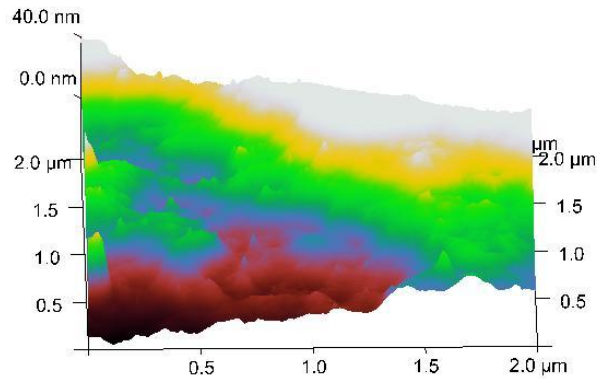
Figure 63. AFM 3-D image taken of etched Zr sample prepared at $V_{AC} = 80$ V, with a map size of x,y = 2 µm. Pore partially shown roughly 8 µm in diameter.

Three-dimensional images shown in Figures 61 to 63 illustrate the increase in pore dimensions with increasing applied AC voltage. This is most likely due to the enlargement of pores, or the clustering of pores in the same area, combining to make larger pores. For the sample prepared at $V_{AC} = 60$ V, the pore diameter is roughly 1.7 µm, and the measured pore depth is 22.3 nm ± 0.5 nm. The sample prepared at $V_{AC} = 70$ V shows a slightly larger pore, which is roughly 2.6 µm in diameter, with a measured pore

depth of 35.3 nm ± 0.5 nm. Finally, the sample prepared at V_{AC} = 80 V has a pore diameter of about 8 μm, with a measured pore depth of 43.1 nm ± 0.5 nm. There is clearly an increase in pore diameter and depth as the applied AC voltage is increased, and becomes nearer to the electrochemical breakdown voltage.

Table 13. Relation between roughness, R_a, values taken using AFM (surface morphology maps shown in Figure 60), and V_{AC}.

V_{AC} (V)	R_a (nm)
0	43.3 ± 3.9
10	111.3 ± 8.6
20	100.4 ± 8.0
30	39.2 ± 6.8
40	47.2 ± 5.9
50	48.0± 6.6
60	53.9 ± 3.7
70	67 ± 11
80	70.4 ± 5.8

Roughness results from AFM measurements are shown in Table 13, and were similar in trend to those obtained using profilometry: (i) higher values of R_a for the samples prepared at V_{AC} = 10 and 20 V; (ii) higher roughness for the samples prepared at V_{AC} = 60, 70 and 80 V because pores are prevalent across the surfaces of these samples. This trend was observed by Zhao,[26] as was previously stated, as well as by Lausmaa.[81] Since rougher surfaces have been proven to enable osseointegration of implants, the ideal pre-treatment for medical and dental implant materials would be chemical etching, followed by high voltage AC passivation.

4.6 SEM/FIB/TEM/EBSD

Scanning electron microscopy, FIB, and TEM measurements were performed by a technician (Hubert Schulz) using an AURIGA® Cross Beam instrument at the Zeiss Application Laboratory in Oberkochen, Germany. This instrument includes all three techniques (SEM, FIB and TEM), enabling extensive analysis on a single instrument. Thickness measurements were performed on all etched, and etched and coloured Zr prepared at V_{AC} = 10, 20, ..., 80 V. Due to the advanced and expensive nature of the experiments performed, detailed SEM, FIB and TEM analyses were conducted on one sample in particular (etched Zr passivated at V_{AC} = 80 V). Similar experiments on all sample types will ideally be performed in the future. A cross-sectional analysis was performed using an ion beam milled sample prepared at V_{AC} = 80 V. The sample studied in detail was first coated with Pt using first electron beam and then ion beam deposition.
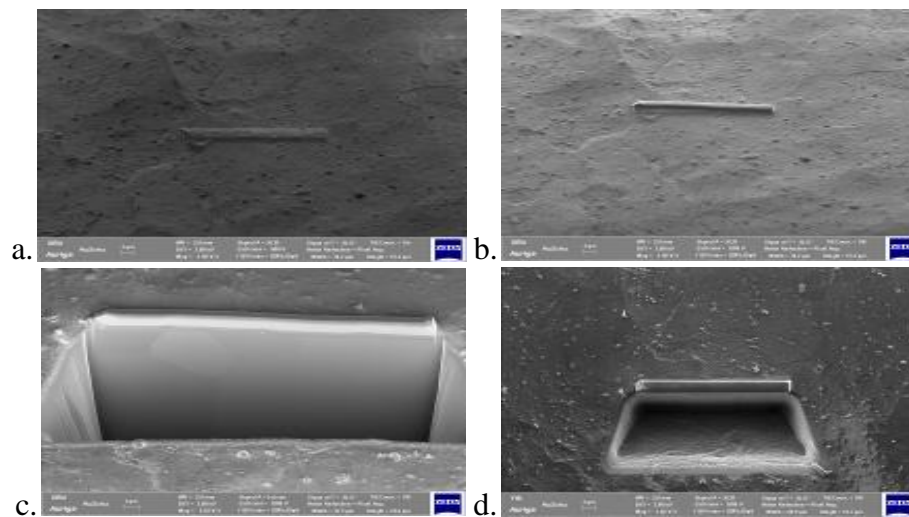
Figure 64. SEM/FIB images of the sample (V_{AC} = 80 V) during its preparation; (a) electron beam deposited platinum, (b) ion beam deposited platinum atop the previous electron deposited layer, and finally (c, d) the trench developing due to ion beam milling. FIB probe at 30 kV and 20 pA, 36° tilt angle to stage.

Figure 64 shows the sample prepared at $V_{AC} = 80$ V at various stages of ion beam milling. The Pt coating (Figure 64a, b) is placed atop the surface for protection. The platinum protective layer application processes, as well as the ion beam milling procedure, were described in detail in the experimental section (3.6). The trench observed is smooth in appearance due to the low beam current polishing performed after the ion beam milling process was completed. Thus, a smooth and even surface, which contains a minimal amount of gallium ion implantation and redeposited material, can be imaged and studied using the imaging capabilities of the electron beam.
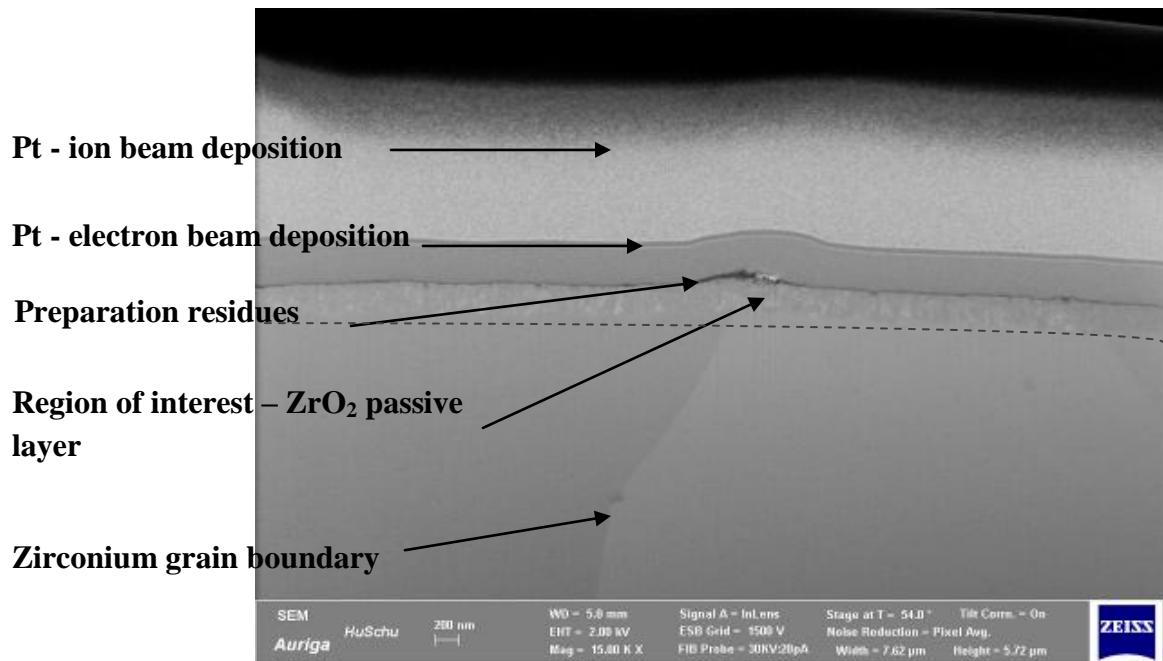
Figure 65. Image of the etched and coloured Zr sample prepared at $V_{AC} = 80$ V. This image illustrates the regions present: elemental Zr, passive oxide, residue from preparation, and finally Pt protective coatings (dashed line is used to emphasize the interface between metal and passive layer).

Figure 65 shows the underlying Zr metal, the desired region under study (passive layer), as well as the protective Pt layers. A clearly defined grain boundary can be seen in the Zr metal, as well as a difference in structural appearance between the Zr and the oxide layer atop the metal. Because the oxide layer had a very different appearance, a further study of the structural composition of the passive layer, was done using TEM. Prior to the application of the Pt protective layer, the sample clearly picked up some surface residue, during handling, transfer, air exposure, etc. between sample preparation in a clean environment and its study. Finally, the two Pt protective layers are apparent atop the surface residue and have a different appearance, with the electron beam deposited

145

layer being darker and more compact, and the ion beam deposited layer being much broader. These two Pt layers protect the underlying sample from gallium ion implantation, as well as redeposition of material across the surface of interest.
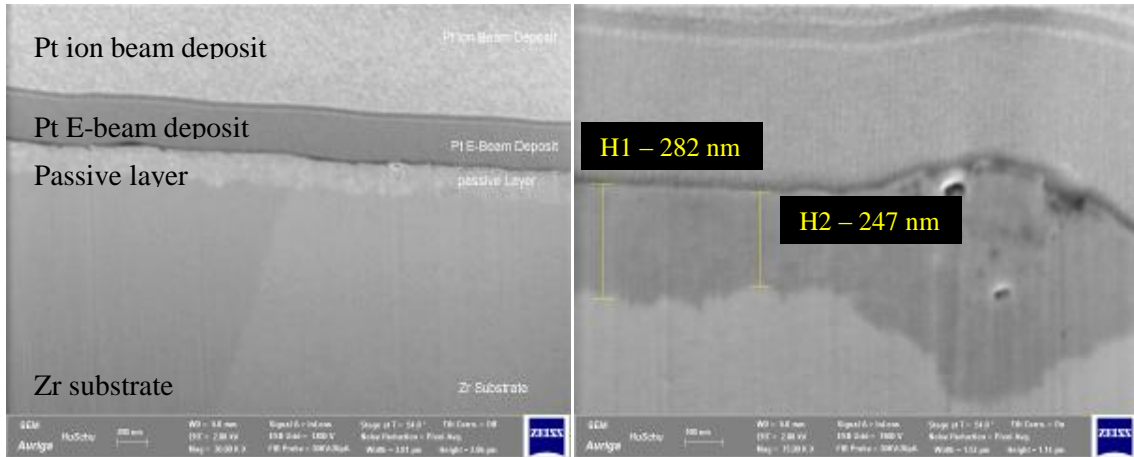
Figure 66. SEM/FIB images of etched and coloured Zr sample prepared at V_{AC} = 80 V, where ZrO_2 layer thickness varies between 240 nm–300 nm.

Thickness measurements were also performed using electron beam imaging for etched and coloured Zr samples (V_{AC} = 10, 20, ..., 80 V). Figure 66 shows the approach employed for measurement of passive layer thicknesses. Using the electron beam for imaging of the ion beam polished surface, the passive layer can be measured in different regions and an average taken, with the corresponding standard deviation between the measurements used to express variation. Thicknesses of all of the etched and coloured Zr samples were measured using this method, and are summarized in Table 14.

Table 14. Thicknesses of Zr etched and coloured passive layers. Coloured samples prepared at V_{AC} = 10, 20, ..., 80 V)

Sample V_{AC}	Thickness	Variation (m = 5)
0 V	0	± 0
10 V	51 nm	± 4 nm
20 V	68 nm	± 4 nm
30 V	126 nm	± 6 nm
40 V	136 nm	± 6 nm
50 V	184 nm	± 6 nm
60 V	192 nm	± 10 nm
70 V	237 nm	± 10 nm
80 V	264 nm	± 15 nm

Figure 67 shows a linear increase in thickness with applied AC voltage, as was found for Ti samples in previous work.[4,78] In order to clearly represent these results, the trend was graphed in Figure 67.
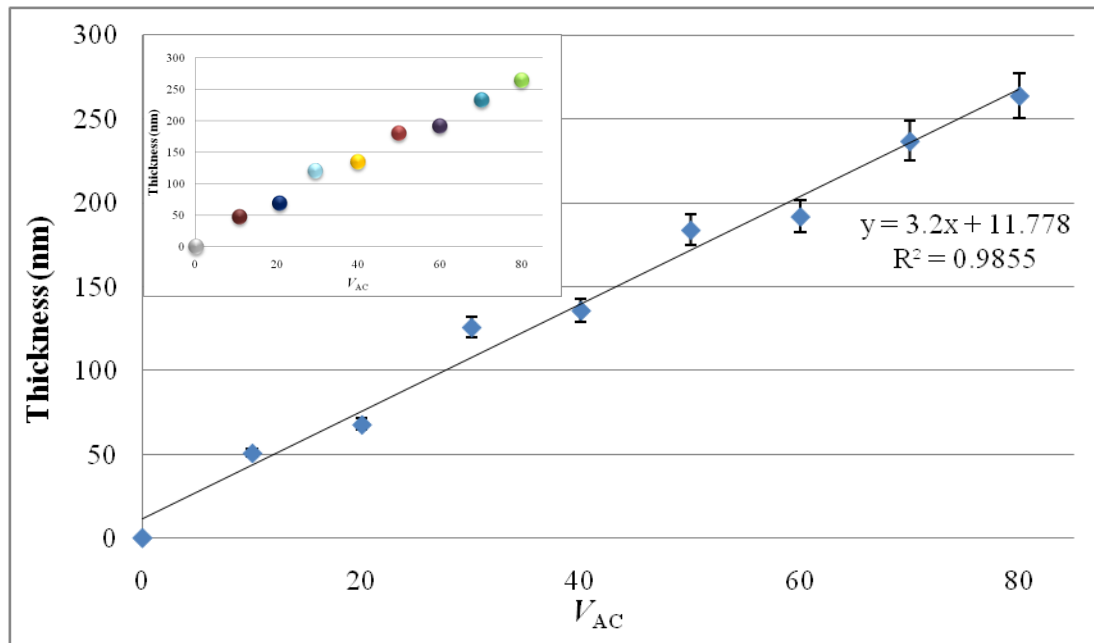
Figure 67. Thicknesses in relation to applied voltage for etched and coloured Zr samples prepared at V_{AC} = 10, 20, ..., 80 V.

Zirconium passive layers are also expected to be thinner than Ti passive layers because there is only one oxide layer (ZrO_2) [37] instead of two in the case of Ti (TiO_2 and Ti_2O_3).[78] As was stated by Zhao,[26] Ti passive layers prepared using DC voltage has one oxide layer (TiO_2), whereas those prepared using AC voltage in the same electrolyte have two oxide layers (TiO_2 and Ti_2O_3), and are thicker than those prepared using DC voltage. Thus, it stands to reason that the layers prepared using AC voltage on Ti would most likely be thicker than those prepared on Zr. In any case, colouration being dependent upon iridescence, as the passive layer thicknesses increased, their observed colour changed.

148
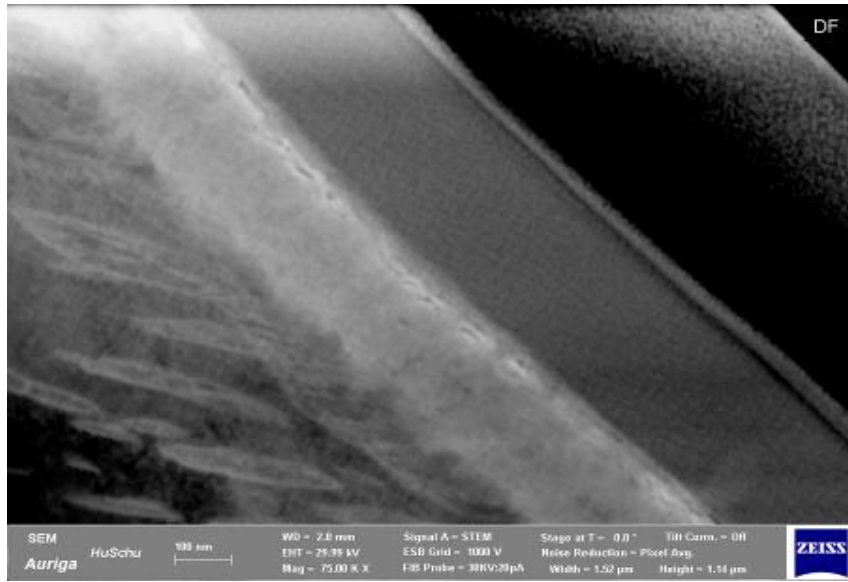
Figure 68. STEM investigation of etched and coloured Zr sample (V_{AC} = 80 V).

Through the use of scanning STEM, a more detailed and magnified region of the passive layer, is obtained in Figure 68. The passive layer appears crystalline, which was confirmed by EBSD in Figure 69 using diffraction mapping and Kikuchi lines.
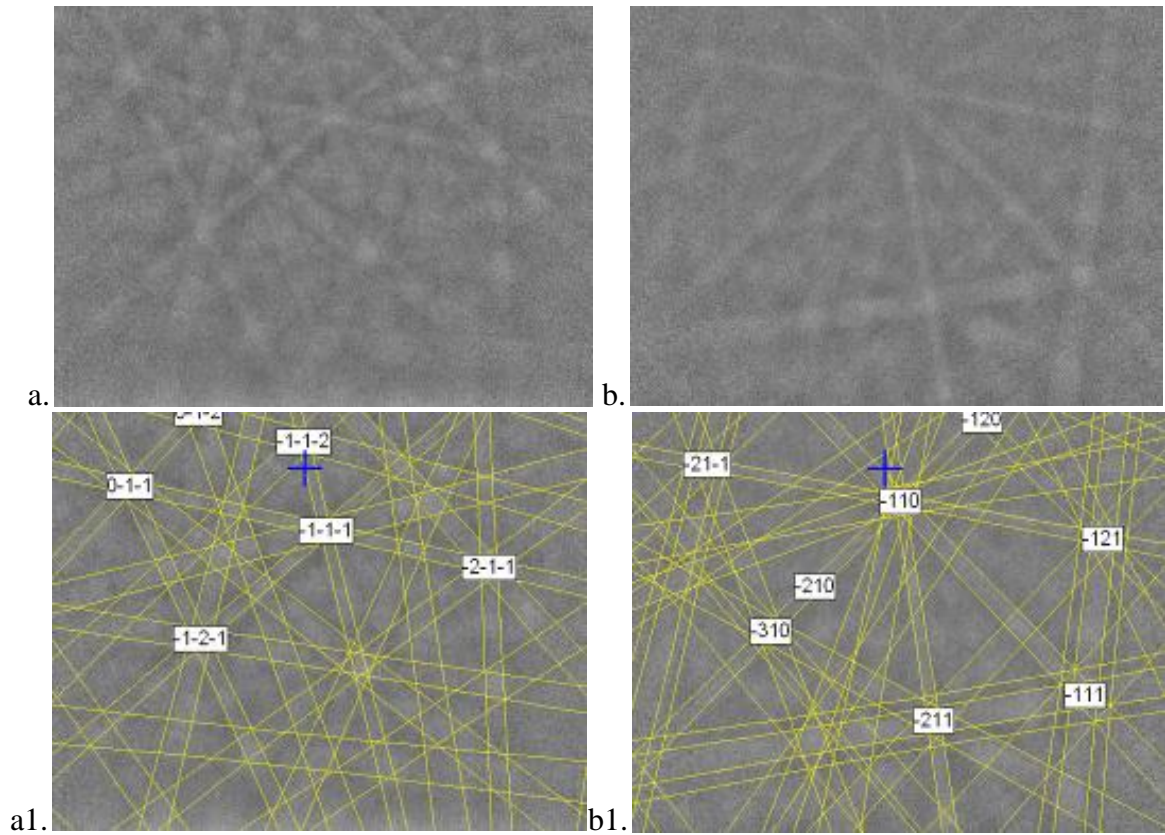
Figure 69. EBSD investigation of etched Zr substrate (a, a1) as well as etched and coloured Zr oxide layer (b, b1), on etched and coloured sample prepared at $V_{AC} = 80$ V.

The passive layer is known to be composed of zirconium oxide (ZrO_2).[37] It was previously proposed that, with thicker passive layers, the structure of the underlying metal disappeared, and thus the oxide layer must be amorphous.[37] However, this is clearly incorrect, as Figure 69 shows that the oxide layer has crystalline properties, and is thus not an amorphous layer.

150

4.7 ICP-MS

Inductively coupled plasma mass spectrometry studies were performed on four sets of samples; (i) etched, and etched and coloured Ti, (ii) etched, and etched and coloured Zr, (iii) polished, and polished and coloured Ti and (iv) polished, and polished and coloured Zr. Coloured samples were placed in 25 mL of a 1% aqueous NaCl solution to analyse their stability in saline media. The samples remained in solution over time increments of 24 hours, 7 days, 14 days, 1 month and finally 2 months. External calibrations (seen in Figures 38 and 39) were employed to find the concentration of ions released into solution over the time periods stated above. The results from sample immersion in the saline solution over time are shown in Figures 71 through 74.
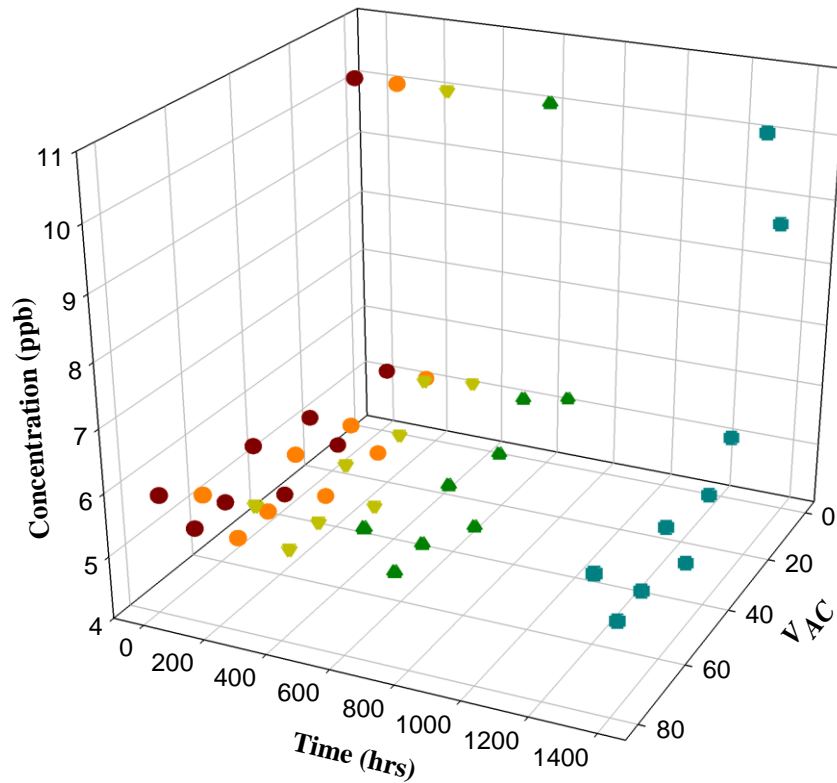
Figure 70. Three dimensional relationship between released Ti concentration, time (24 hours, 7 days, 14 days, 1 month and 2 months), and applied AC voltage, for etched, and etched and coloured Ti samples. Concentrations were obtained by ICP-MS for samples immersed in 1% NaCl solution over time. Coloured samples were prepared at V_{AC} = 10, 20, ..., 80 V. Passivation was performed in aqueous 7.5 wt.% NH_4BF_4 electrolyte for 10 s and at T = 298 K.
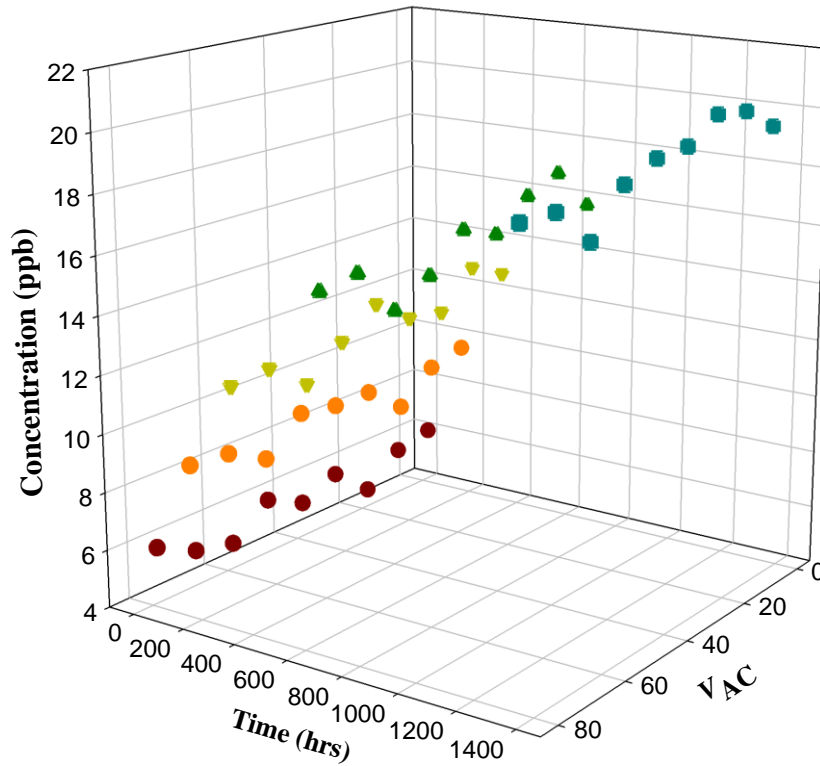
Figure 71. Three dimensional relationship between released Ti concentration, time (24 hours, 7 days, 14 days, 1 month and 2 months), and applied AC voltage, for polished, and polished and coloured Ti samples. Concentrations were obtained by ICP-MS for samples immersed in 1% NaCl solution over time. Coloured samples were prepared at $V_{AC} = 10$, 20, ..., 80 V. Passivation was performed in aqueous 7.5 wt.% NH_4BF_4 electrolyte for 10 s and at $T = 298$ K.
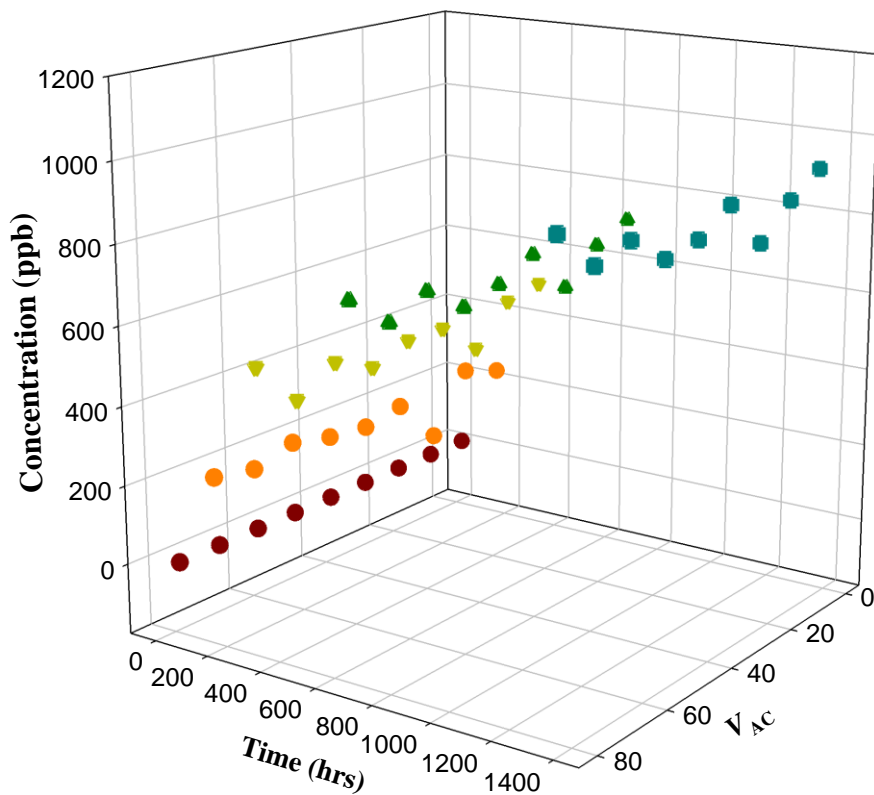
Figure 72. Three dimensional relationship between released Zr concentration, time (24 hours, 7 days, 14 days, 1 month and 2 months), and applied AC voltage, for etched, and etched and coloured Zr samples. Concentrations were obtained by ICP-MS for samples immersed in 1% NaCl solution over time. Coloured samples were prepared at V_{AC} = 10, 20, ..., 80 V. Passivation was performed in aqueous 10 wt.% Na_2SO_4 electrolyte for 10 s and at T = 298 K.
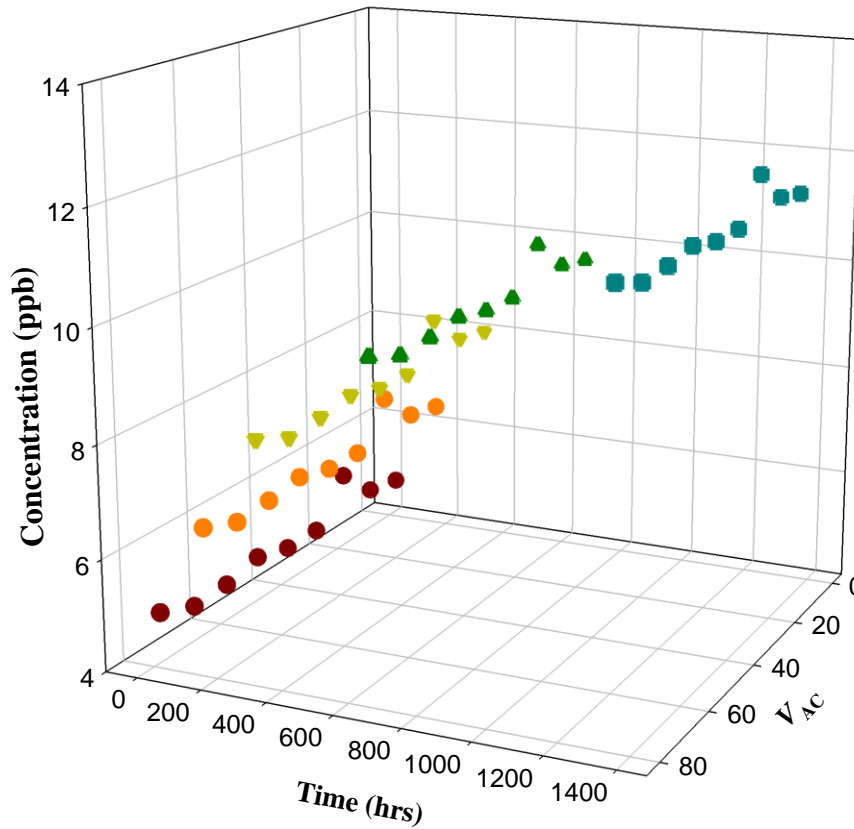
Figure 73. Three dimensional relationship between released Zr concentration, time (24 hours, 7 days, 14 days, 1 month and 2 months), and applied AC voltage, for polished, and polished and coloured Zr samples. Concentrations were obtained by ICP-MS for samples immersed in 1% NaCl solution over time. Coloured samples were prepared at $V_{AC} = 10$, 20, ..., 80 V. Passivation was performed in aqueous 10 wt.% Na_2SO_4 electrolyte for 10 s and at $T = 298$ K.

The results for Ti samples show that the polished samples experienced more corrosive dissolution than the etched Ti samples. This is expected because chemical etching retains the underlying metallic structure, whereas polishing evasively removes

structure atop the metal, creating disorder in order to have a shinier finish. Thus, polished Ti is more likely to corrode than etched Ti, which is in contrast to Zr samples. Indeed, Zr released a significantly higher concentration of Zr ions into solution with etched than polished samples. Archibald and Leach discovered that anodic oxides formed on fluoride-etched Zr developed large internal stresses.[82] Mogoda found that chemically-etched Zr experienced a greater dissolution rate than polished Zr.[83] These results confirm the corrosive dissolution of etched Zr into solution, since HF is an etchant component that would weaken the overall oxide structure. Hackerman and Cecil determined that significant dissolution of anodic Zr occurs in aqueous NaCl media.[84] Further studies lead to confirmation that the presence of chloride ion leads to a substantial corrosion of Zr.[85] Magoda found that, up to a 0.1 N concentration of chloride ions, a large amount of dissolution and localized attack occurs, whereas, over this concentration, the ions adsorb on the oxide surface and retard dissolution.[25] These results were confirmed for the etched samples, which experienced substantial corrosive dissolution into solution. However, the polished samples were fairly resistant to corrosion in chloride-containing solution.

Figure 74. Visible light microscopy images of etched (a), and etched and coloured (b − i) Ti samples after 2 months in 1% aqueous NaCl solution. From b to i, the passivation voltage is $V_{AC} = 0$, 10, ..., 80 V. Passivation was performed in aqueous 7.5 wt.% NH_4BF_4 electrolyte for 10 s at $T = 298$ K.

After immersion in an aqueous NaCl solution for two months, all samples were removed from the saline solution and studied using VLM. In Figure 74, VLM images of etched, and etched and coloured Ti samples show no visible surface defects. The surface

remaining uniformly coated and protected. The colouration is consistent across these samples.

Figure 75. Visible light microscopy images of polished (a), and polished and coloured (b – i) Ti samples, after 2 months in 1% aqueous NaCl solution. From b to i, the passivation voltage is $V_{AC} = 0, 10, ..., 80$ V. Passivation was performed in aqueous 7.5 wt.% NH_4BF_4 electrolyte for 10 s at $T = 298$ K.

VLM images of polished, and polished and coloured Ti samples can be seen in Figure 75. These samples do not have the same uniform colouration across their surfaces, as the etched Ti samples, and have new features. This colouration difference is due to corrosion of the oxide layer, thinner areas of oxide having different colouration. The thickness affects colouration since the colours originate from iridescence, constructive light interference. The samples prepared at $V_{AC} = 30$, 60 and 70 V show a leafy pattern of discolouration, whereas the sample prepared at $V_{AC} = 80$ V has a dendrite-like pattern across its surface. Interestingly, these discolouration patterns are crystal-like in appearance. Mechanical polishing produces a disordered, strained surface structure, which is more susceptible to corrosion and abrasion. Thus, polished samples release metal from their disordered surface structure, revealing the underlying crystalline metallic oxide.
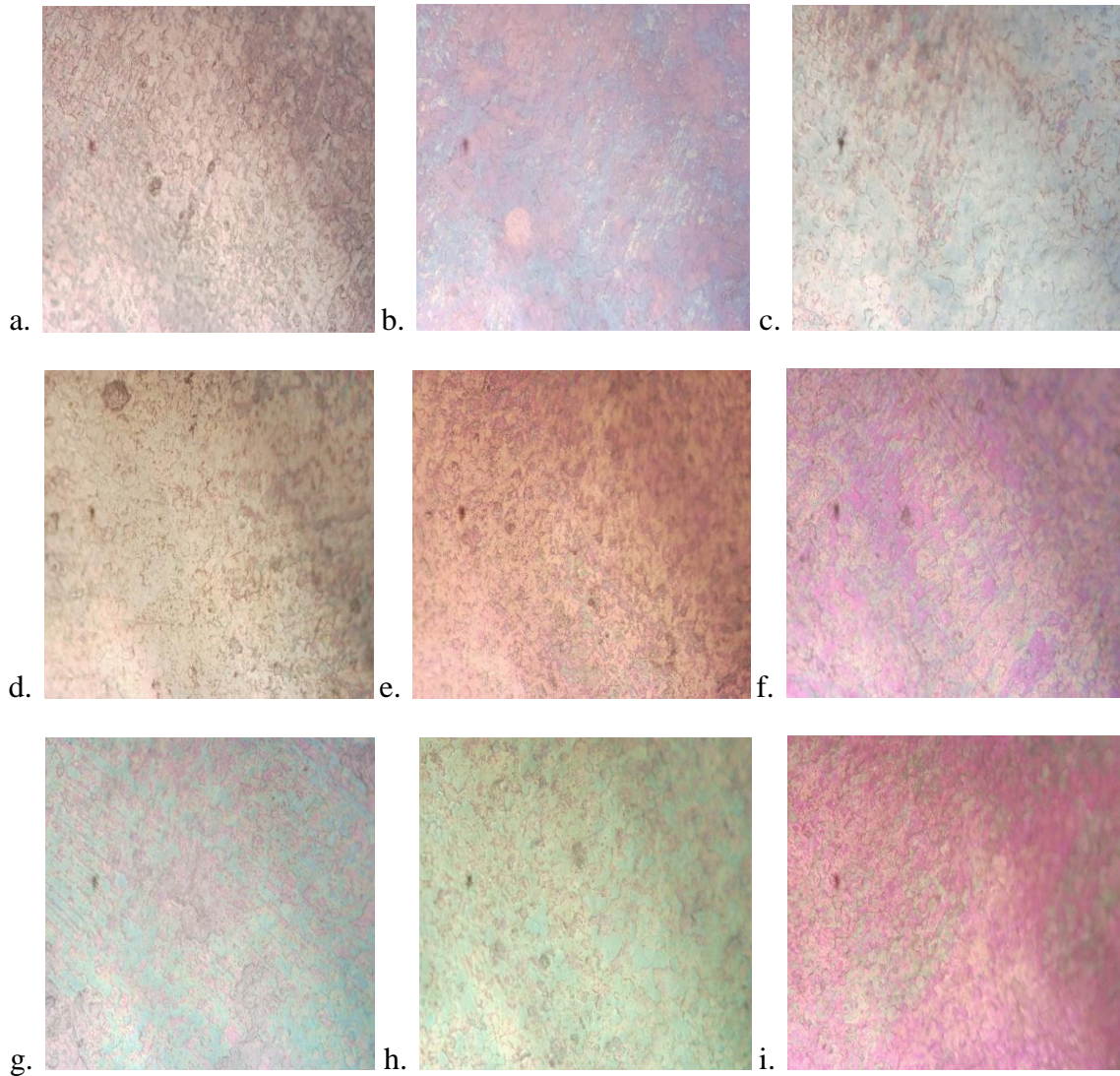
Figure 76. Visible light microscopy images of etched (a), and etched and coloured (b – i) Zr samples, after 2 months in 1% aqueous NaCl solution. From b to i, the passivation voltage is $V_{AC} = 0, 10, ..., 80$ V. Passivation was performed in aqueous 10 wt.% Na_2SO_4 electrolyte for 10 s at $T = 298$ K.

The VLM images of etched, and etched and coloured Zr samples in Figure 76 show that the passive films have different colouration across their surfaces, and thus they have decreased in thickness in some areas. The sample prepared at $V_{AC} = 60$ V has

emerging colours that are similar to those of the sample prepared at V_{AC} = 50 V. This trend is also observed for the sample prepared at V_{AC} = 80 V, which has emerging colouration of the sample prepared at V_{AC} = 70 V.
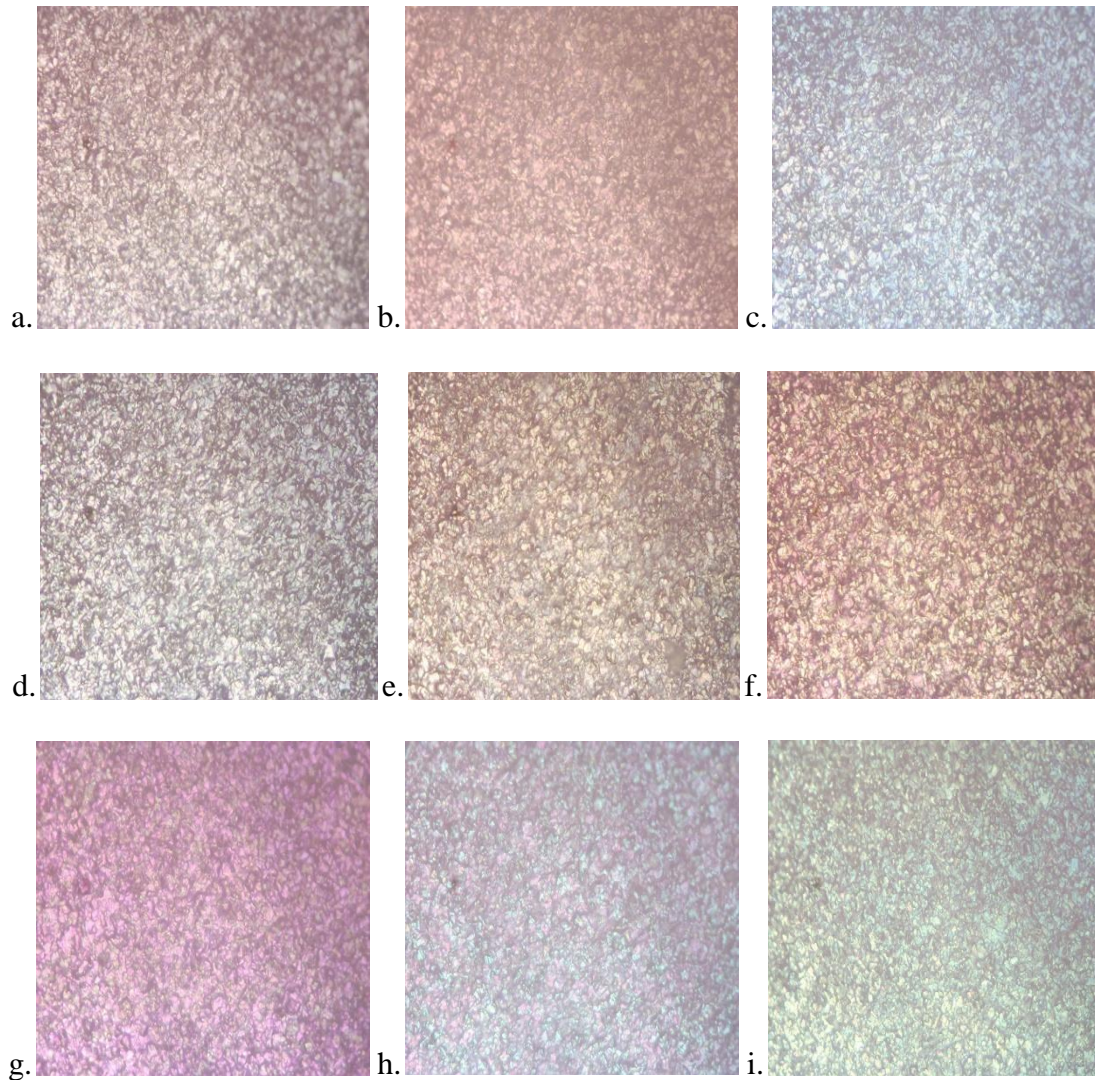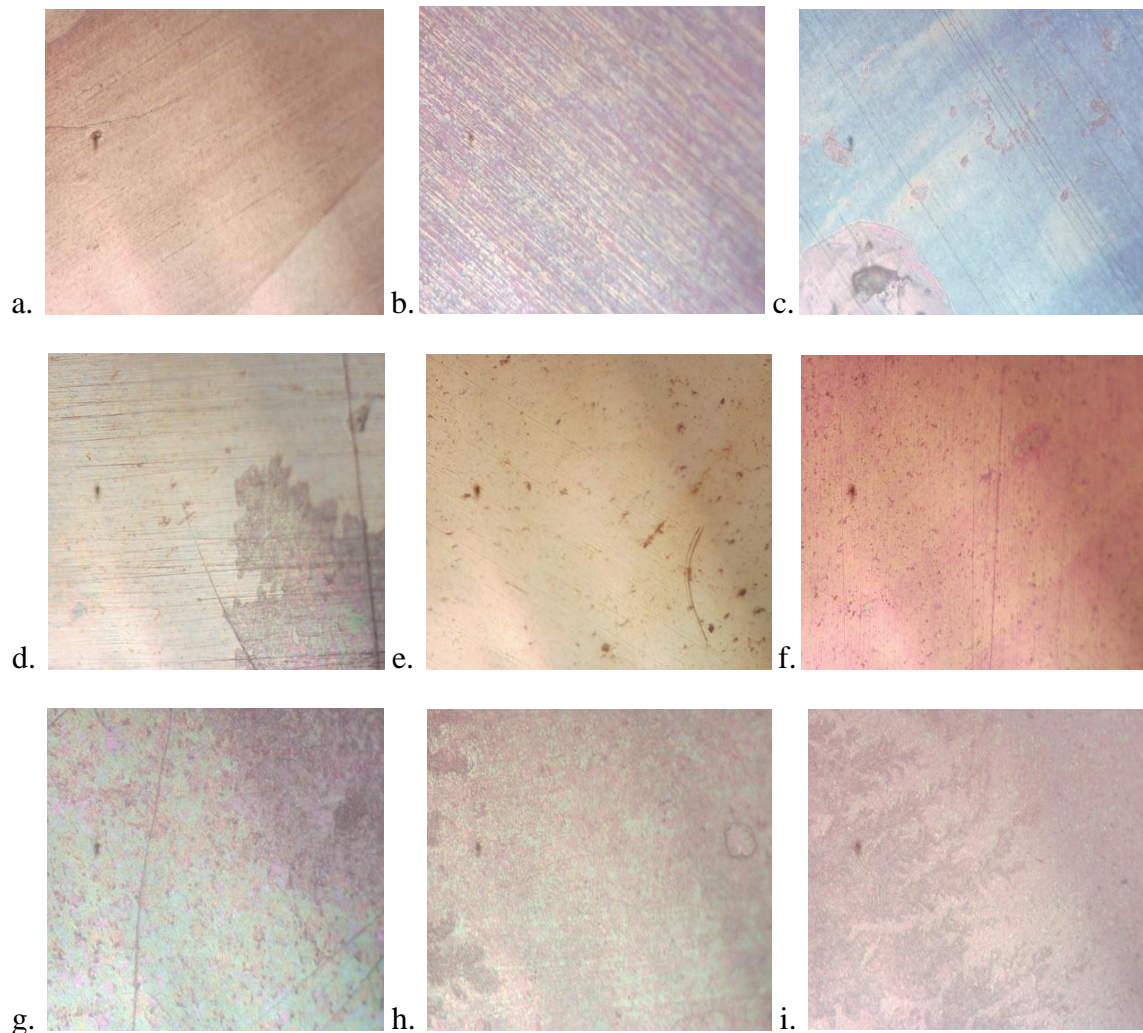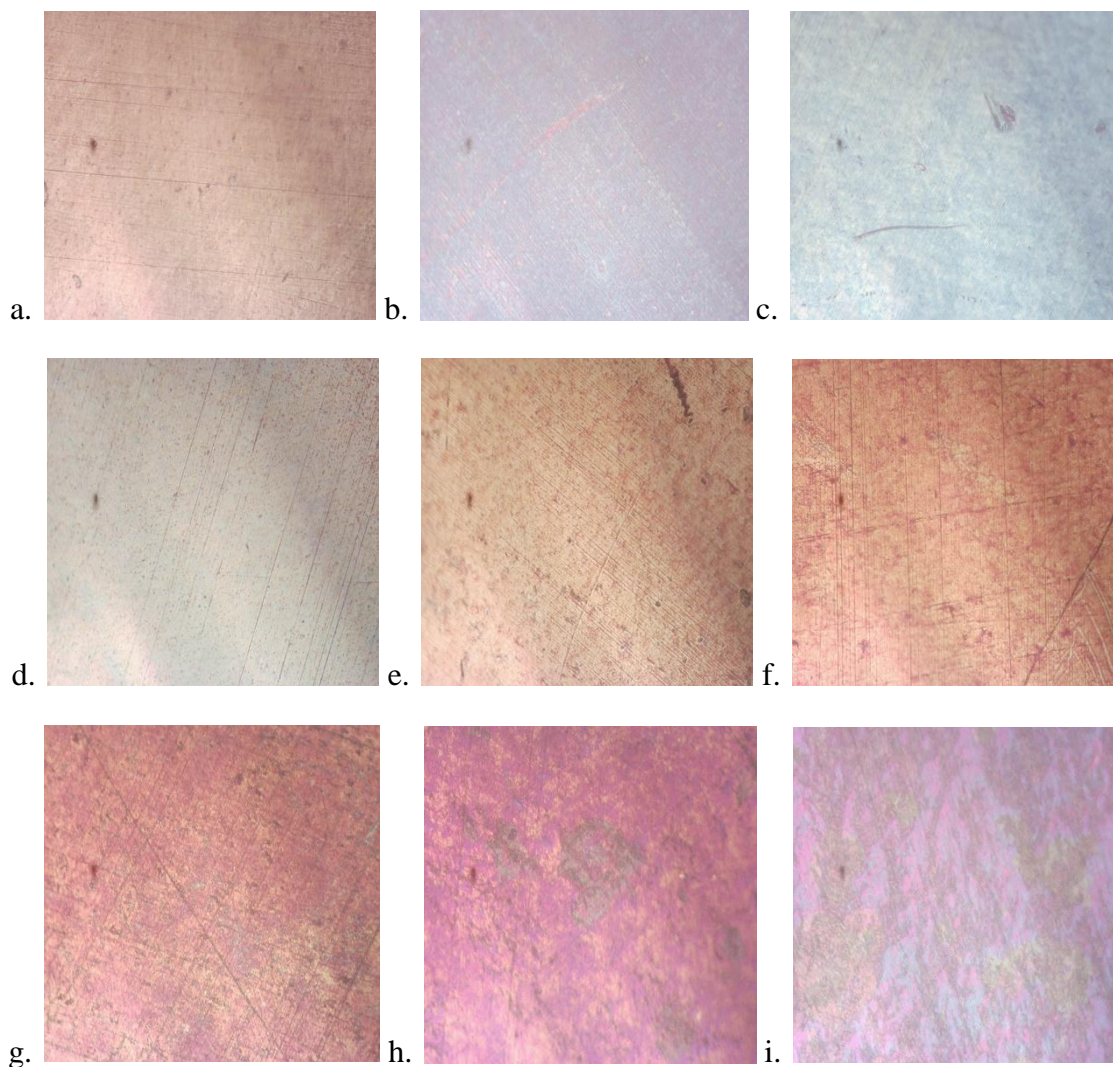

Figure 77. Visible light microscopy images of polished (a), and polished and coloured (b – i) Zr samples, after 2 months in 1% aqueous NaCl solution. From b to i, the passivation voltage is V_{AC} = 0, 10, ..., 80 V. Passivation was performed in aqueous 10 wt.% Na_2SO_4 electrolyte for 10 s at T = 298 K.

Finally, the VLM images of polished, and polished and coloured Zr samples, in Figure 77, show a more consistent colouration across the surface than the etched Zr samples exhibited. However, the samples prepared at V_{AC} = 60, 70, and 80 V begin to show non-uniformities in colouration. In particular, the samples at higher voltages have areas with a thinner oxide layer atop the metal than other areas of the passive layer.

The VLM images for Ti specimens showed more imperfections on polished samples than on etched samples, which is consistent with the ICP-MS results, where polished Ti experienced slightly more corrosive dissolution into solution than etched Ti. The opposite trend was observed for Zr, where the etched samples show more imperfections on their surfaces than the polished samples. There were also shallow areas found on samples prepared at V_{AC} = 60 through 80 V. This was confirmed by the results from Zeiss VLM experiments as well as AFM experiments on Zr. These higher voltages produce pores in the structure of the oxide layer due to electrochemical breakdown. The pores do not, however, affect the corrosion rates according to ICP-MS immersion tests and polarization curve experiments, which are discussed in the following section.

4.8 Polarization Curves

Polarization curve measurements were carried out using a 1% wt. aqueous solution of NaCl, which served as the electrolyte and was common with ICP-MS measurements for consistency. Polarization curve measurements were taken on two sets of samples; (i) etched, and etched and coloured Ti, and (ii) etched, and etched, and coloured Zr. The measurements were performed seven times per sample type, in order to

assure accuracy in results. This is necessary since non-noble metals such as Ti and Zr often produce inaccurate results in electrochemical studies due to impurities or other poorly understood phenomena. Reproducibility of potential measurements in the study of Ti is difficult to obtain due to the dependence upon surface conditions of the metal, as well as the nature, composition, thickness and conductivity of the oxide layer atop the metal.[35] From the most negative applied potential to the most positive, polarization curves have the following regions: hydrogen generation, active, active-passive transition, passive, and finally transpassive with oxygen evolution and oxide dissolution. These regions, and their potential ranges display characteristics about the material under scrutiny. The results can be seen in Figures 79 through 88.
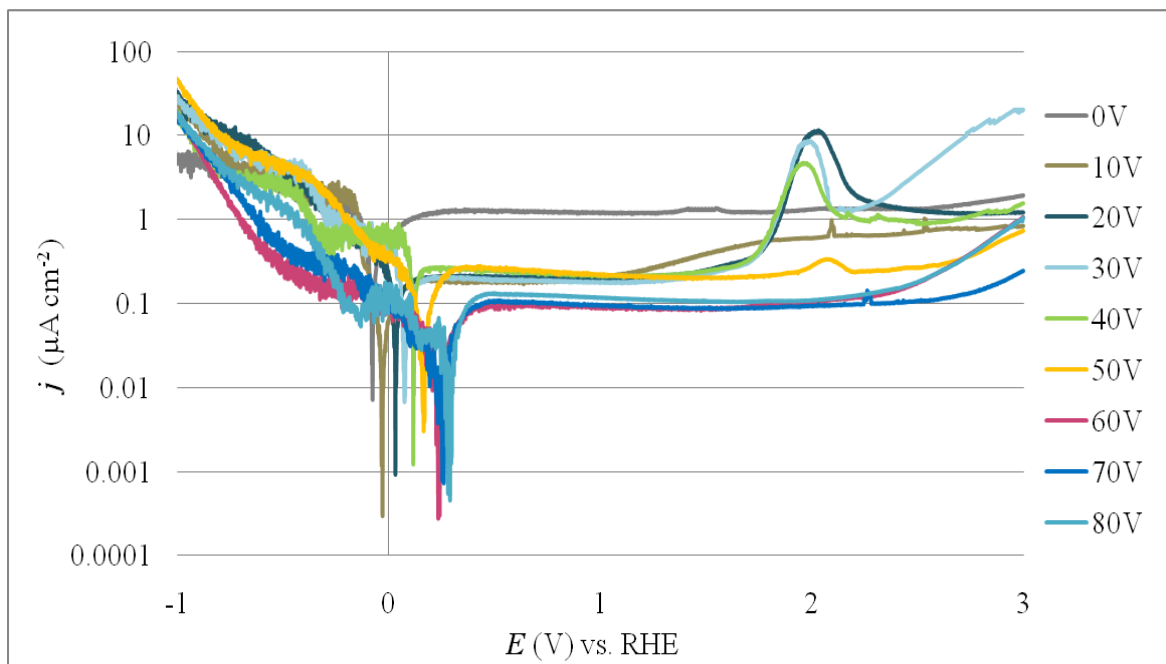
Figure 78. Comparative graph of polarization curves for etched and etched and coloured Ti samples. Coloured samples were prepared at V_{AC} = 10, 20, ..., 80 V, and were studied in a 1% aqueous NaCl solution. Passivation was performed in aqueous 7.5 wt.% NH_4BF_4 electrolyte for 10 s at T = 298 K. The scan rate used was 1 mV s^{-1}, and the potential range was from -1 to 3 V.
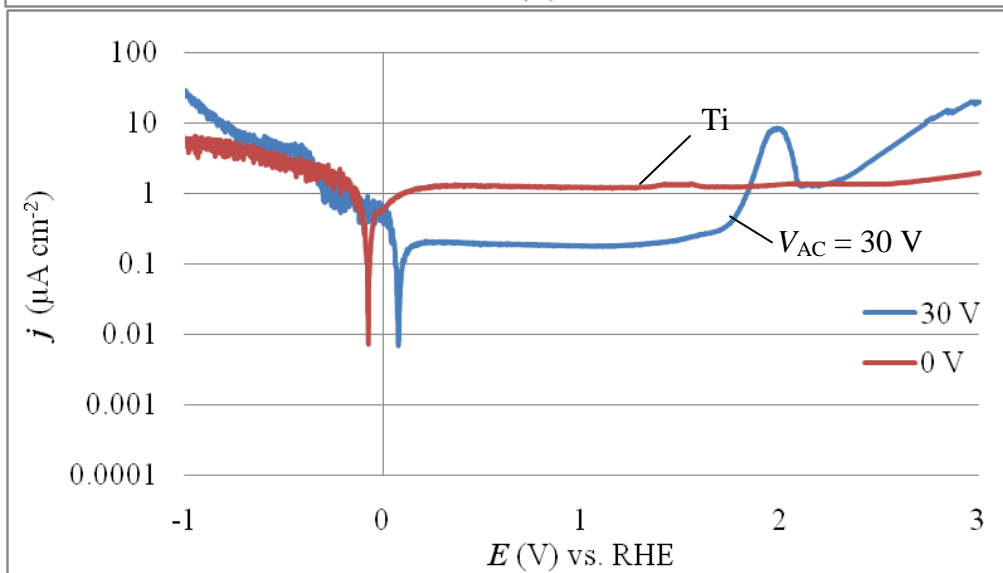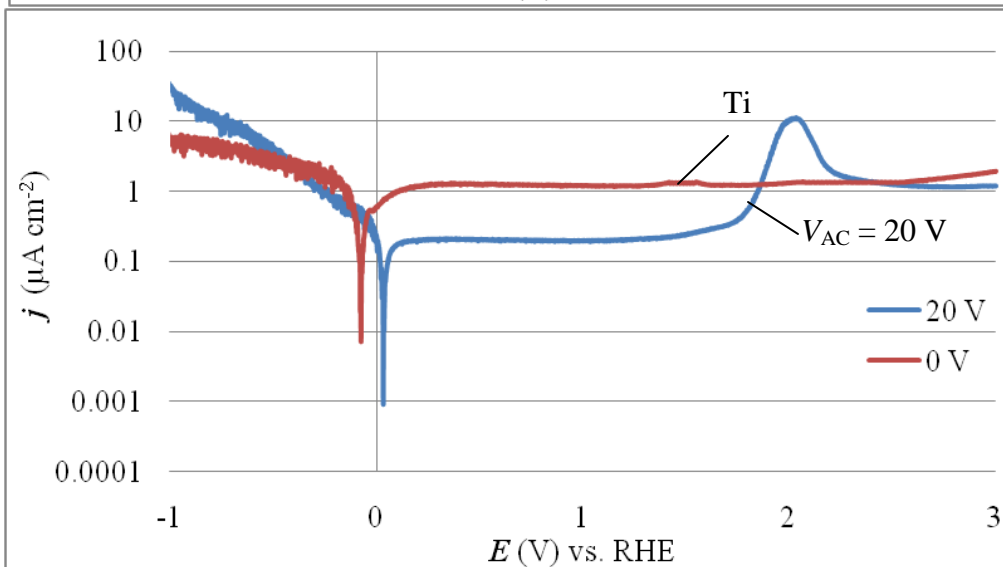
Figure 79. Individual polarization curves (each compared to that of unpassivated Ti) for etched and etched and coloured Ti samples. Coloured samples were prepared at V_{AC} = 10, 20, ..., 80 V, and were studied in a 1% aqueous NaCl solution. Passivation was performed in aqueous 7.5 wt.% NH_4BF_4 electrolyte for 10 s at T = 298 K. The scan rate used was 1 mV s^{-1}, and the potential range was from -1 to 3 V.

Figure 79 shows polarization curves for the passive films on Ti , which reveal the following: (i) the overall shape of the polarization curves for passive films is similar to that of Ti, (ii) the hydrogen generation region exhibits current density variations due to oscillatory behaviour or bubble blocking, (iii) the current density values of passive layer polarization curves are lower than that of Ti by a factor of 10^1, (iv) the corrosion potential (E_{corr}) values increase with applied AC voltage, thus indicating that the passive layers are becoming more stable with increasing thickness and V_{AC}, (v) the critical current density (j_{cc}) decreases from 0.686 µA cm^{-2} for chemically etched Ti (confirmed by Zhao,[26] in Hank's Balanced Salt Solution), to 0.0569 µA cm^{-2} for the passive film formed at V_{AC} = 80 V, resulting in the conclusion that it becomes easier for Ti to enter the stable passive state as V_{AC} increases. Passivation also occurs almost immediately, showing no transition into the passive region. This is most likely due to passivation of Ti occurring during exposure to open air for short periods of time while performing manipulations, thus resulting in samples being passivated with a nanoscopic TiO_2 layer prior to being introduced into the system.

The samples prepared at V_{AC} = 10, 20, ..., 50 V show a peak in a region that is most likely a passive-active-passive transition, because a passivated sample shows an increased activity over a narrow potential range, and afterwards a new passive state develops. This peak was analysed for peak current density (j_{peak}), as well as its peak potential (E_{peak}). The results are shown in Figures 81 and 82.
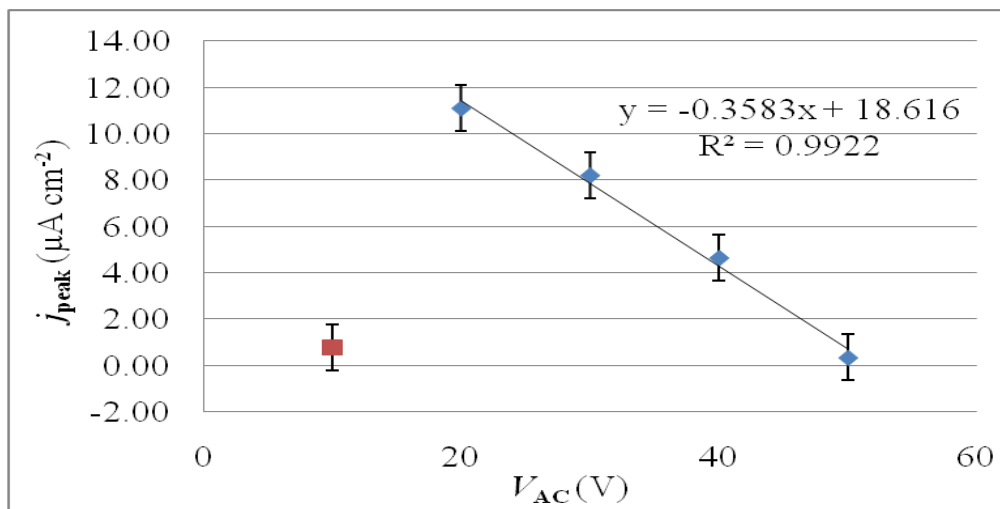
Figure 80. Peak current density values of the passive-active-passive transition in Ti polarization curves of the samples prepared at V_{AC} = 10, 20, ..., 50 V. Samples were studied in a 1% aqueous NaCl solution. Passivation was performed in aqueous 7.5 wt.% NH_4BF_4 electrolyte for 10 s at T = 298 K. The scan rate used was 1 mV s^{-1}, and the potential range was from -1 to 3 V.
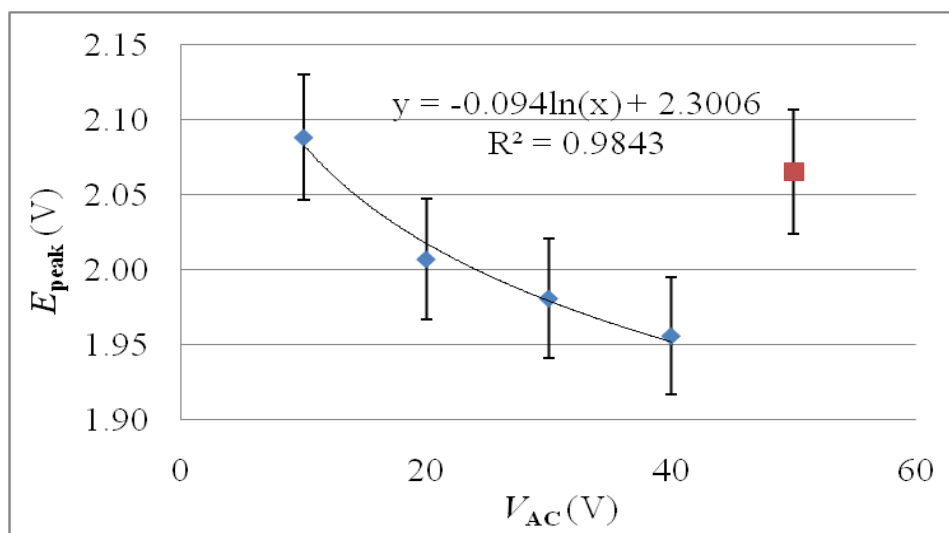
Figure 81. Peak potential values of the passive-active-passive transition in Ti polarization curves of the samples prepared at V_{AC} = 10, 20, ..., 50 V. Samples were studied in a 1% aqueous NaCl solution. Passivation was performed in aqueous 7.5 wt.% NH_4BF_4 electrolyte for 10 s at T = 298 K. The scan rate used was 1 mV s^{-1}, and the potential range was from -1 to 3 V.

The values of j_{peak} show an increase between the sample prepared at V_{AC} = 10 V to that prepared at V_{AC} = 20 V, followed by a linear decrease to the sample prepared at V_{AC} = 50 V. These results indicate that the peak present in the polarization curve for coloured Ti prepared at V_{AC} = 10 V may merely be an artifact. The values of E_{peak} show a trend of monotonous decrease for the samples prepared at V_{AC} = 10, 20, ..., 40 V. However, the sample prepared at V_{AC} = 50 V instead increases in peak potential. The potential at which the peak is found could be decreasing with increasing V_{AC}, as the current density was decreasing, up to the point of return to the original position.
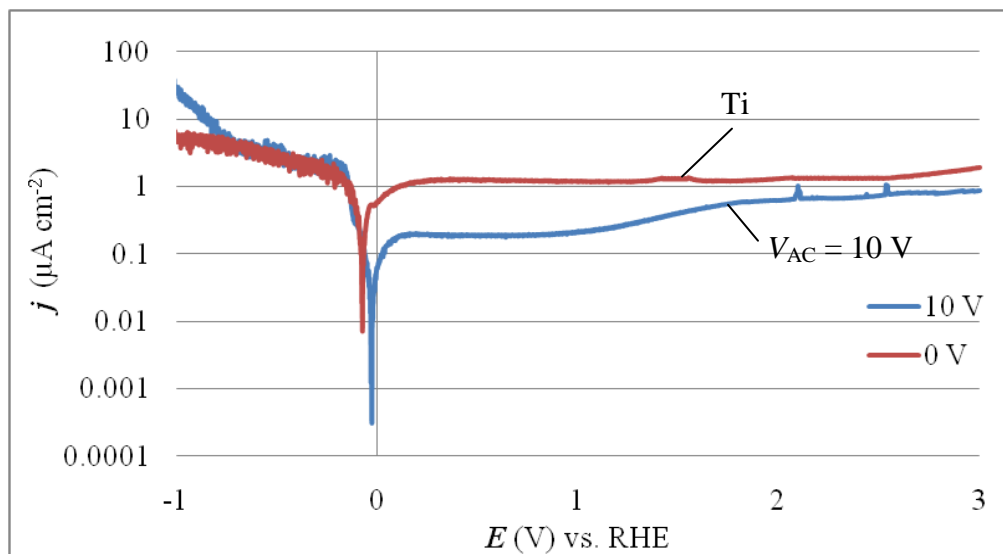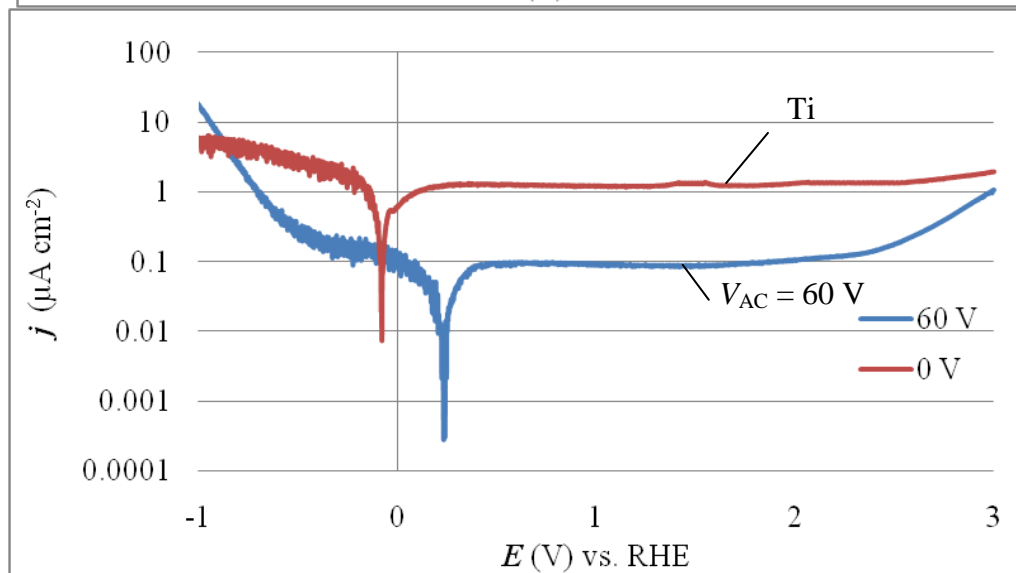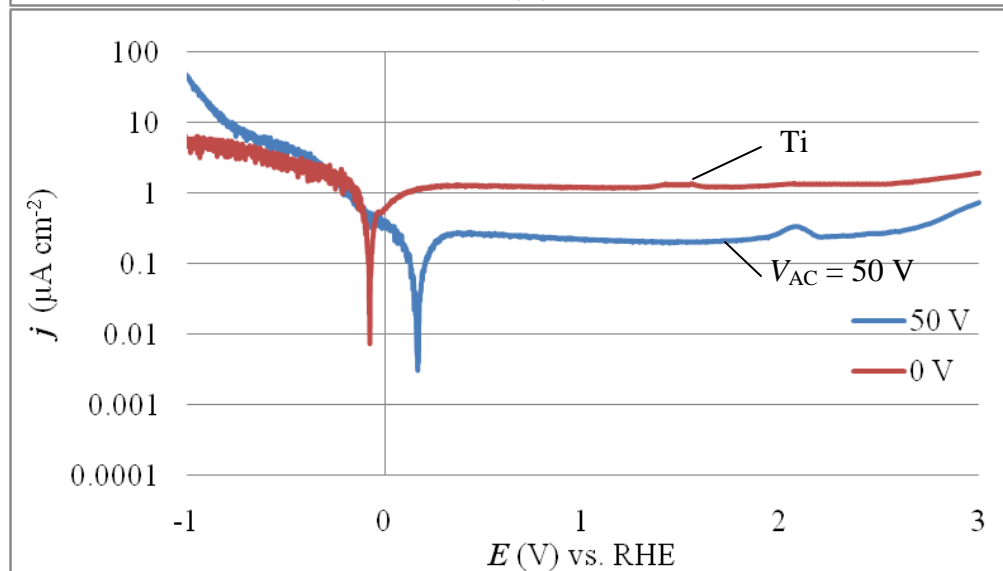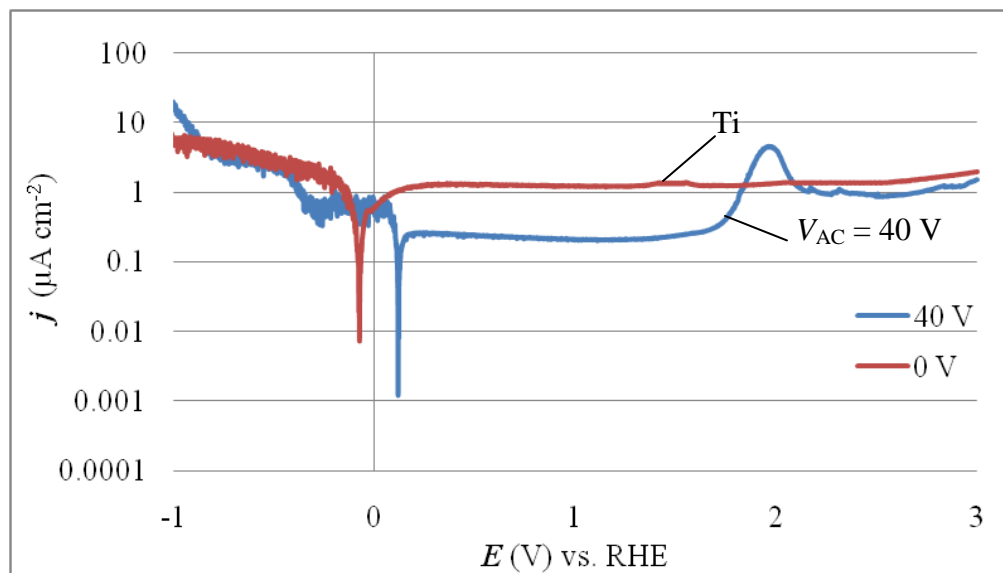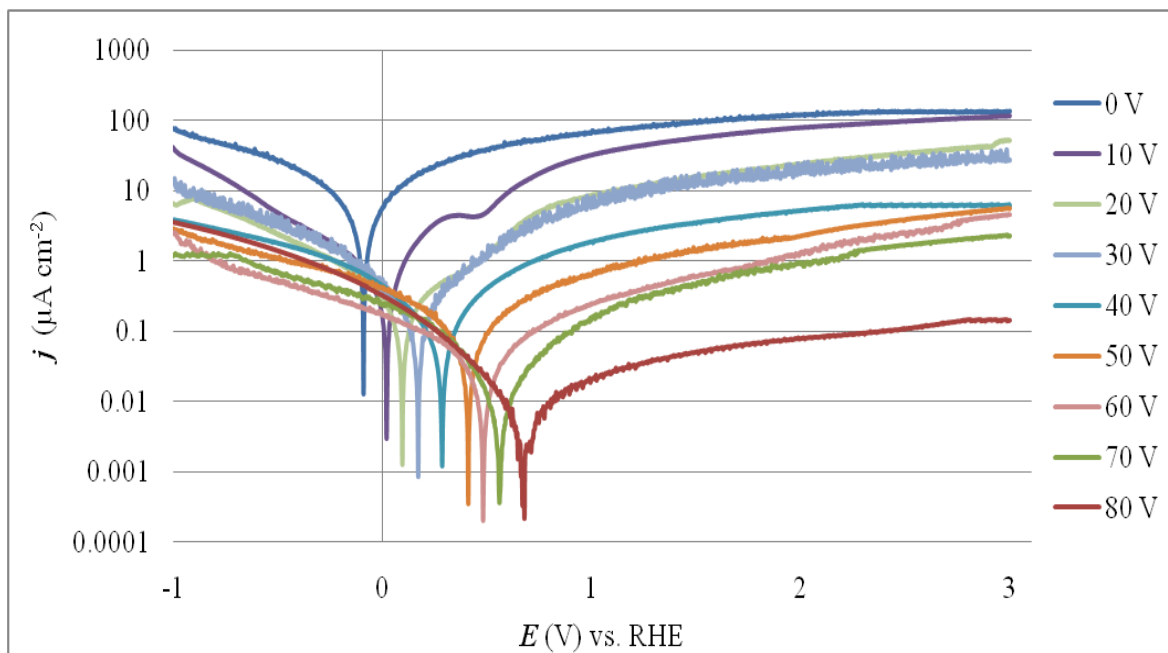
Figure 82. Comparative graph of polarization curves for etched and etched and coloured Zr samples. Coloured samples were prepared at V_{AC} = 10, 20, ..., 80 V, and were studied in a 1% aqueous NaCl solution. Passivation was performed in aqueous 10 wt.% Na_2SO_4 electrolyte for 10 s at T = 298 K. The scan rate used was 1 mV s^{-1}, and the potential range was from -1 to 3 V.
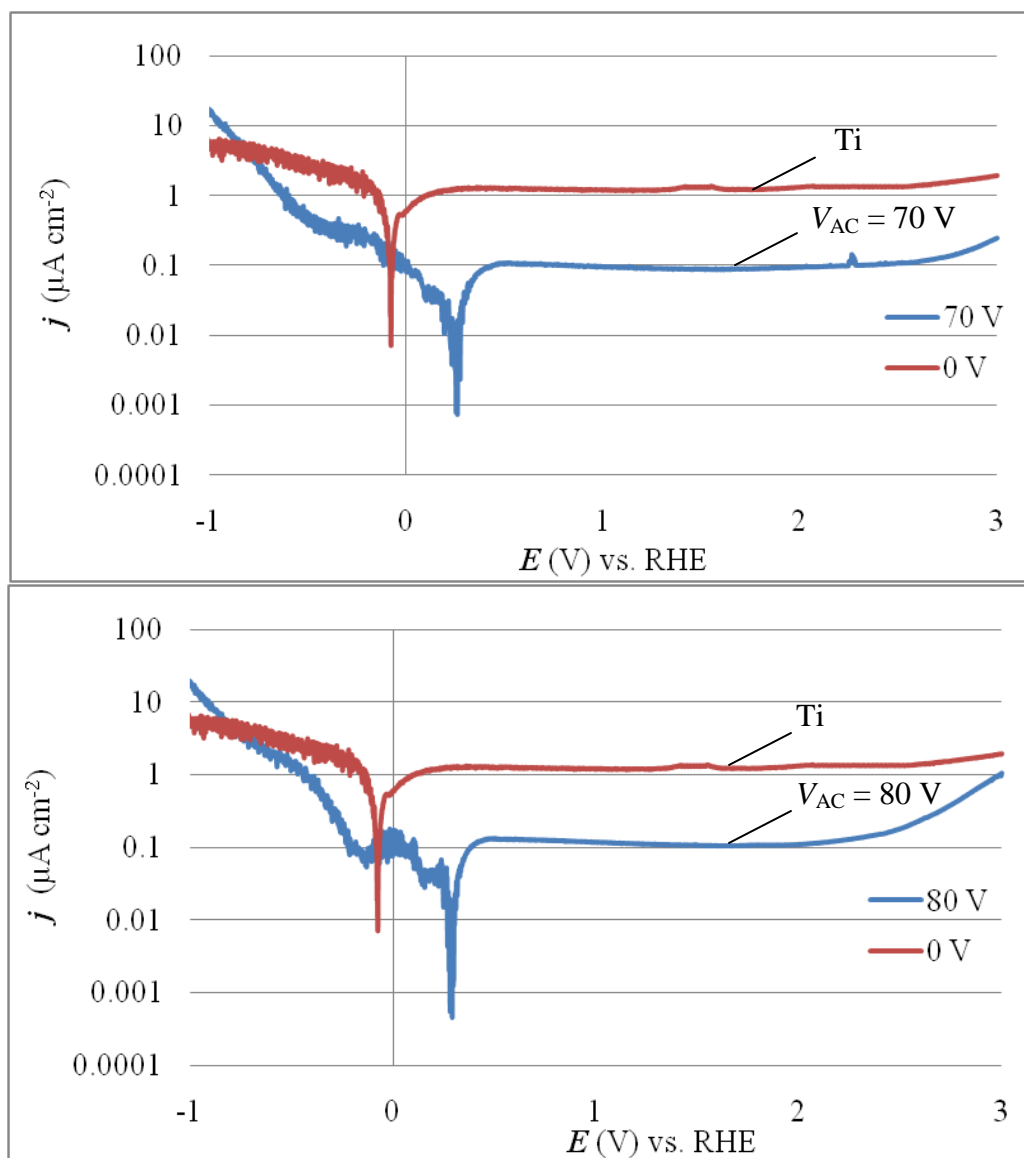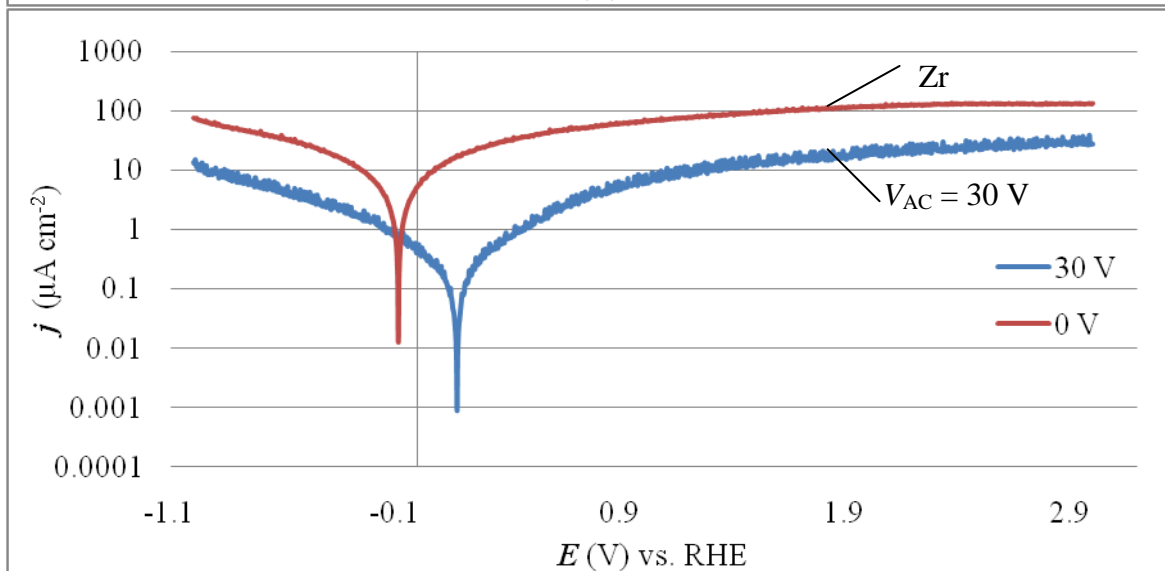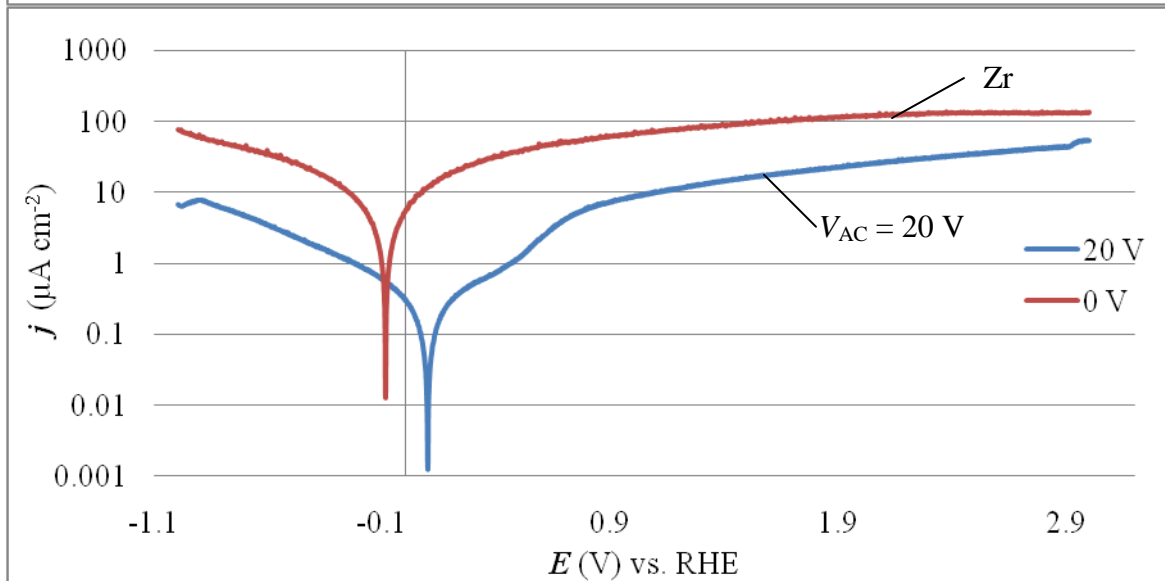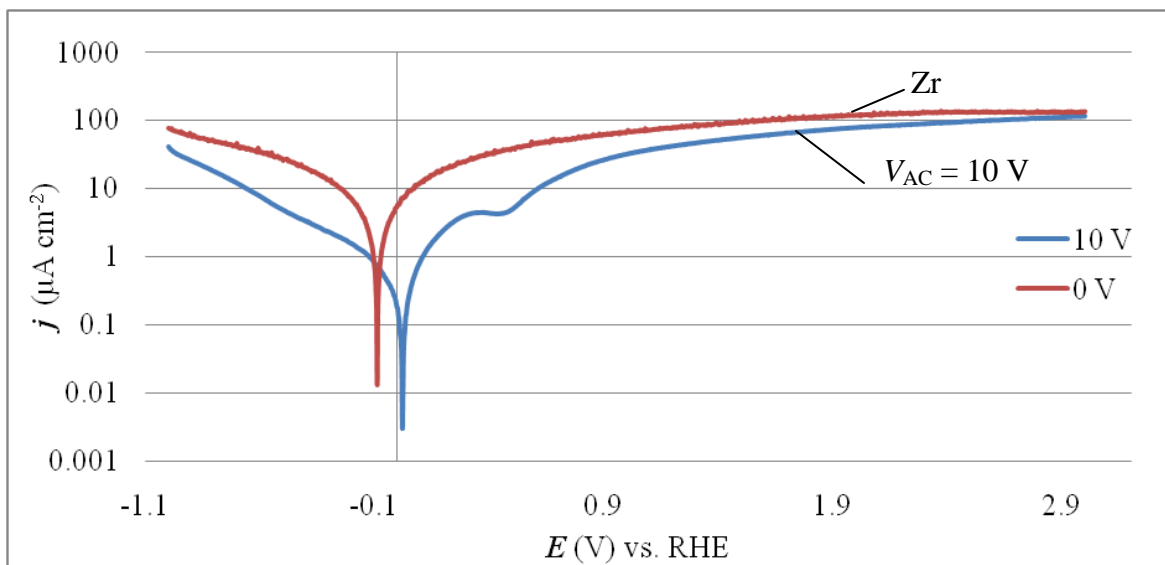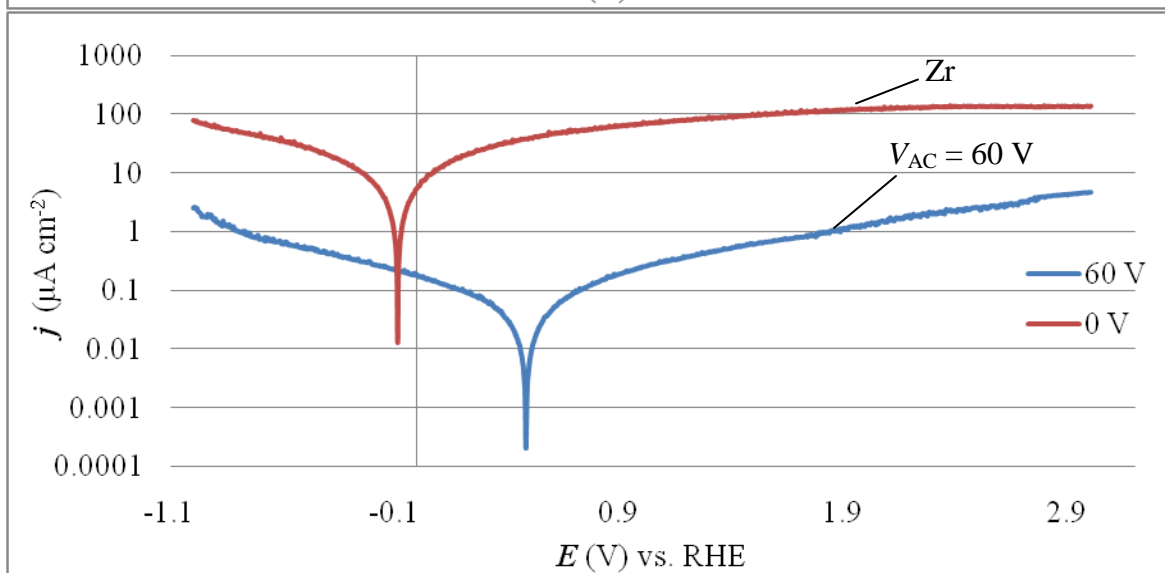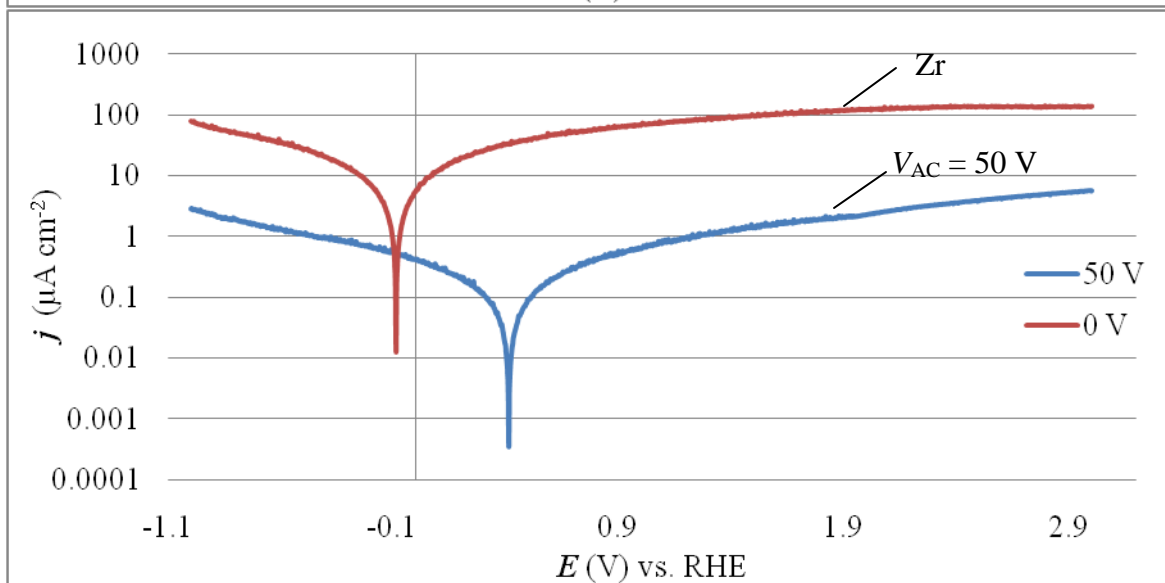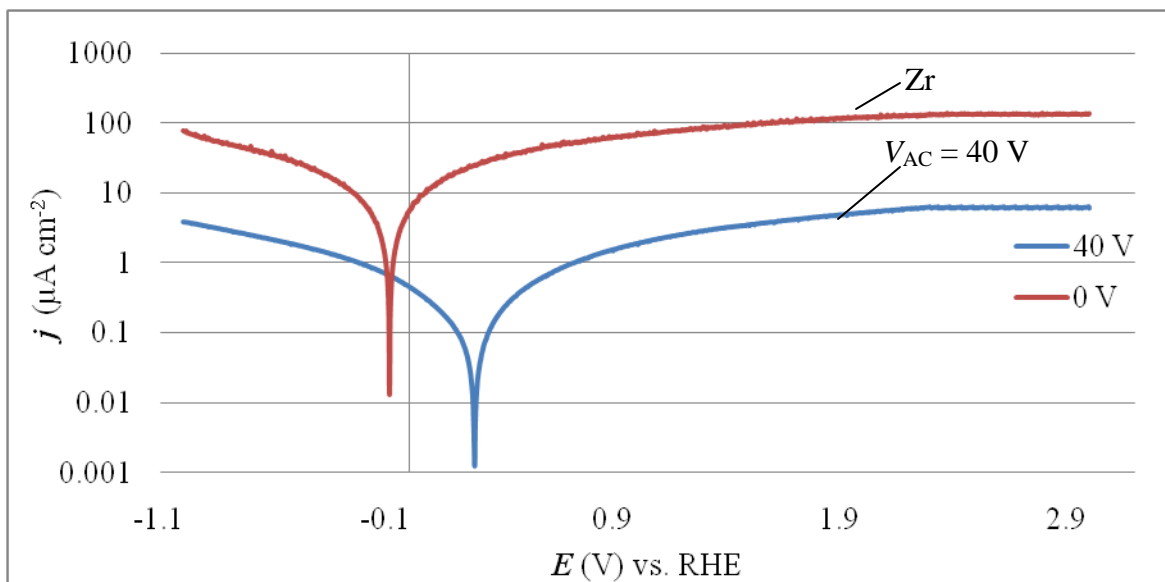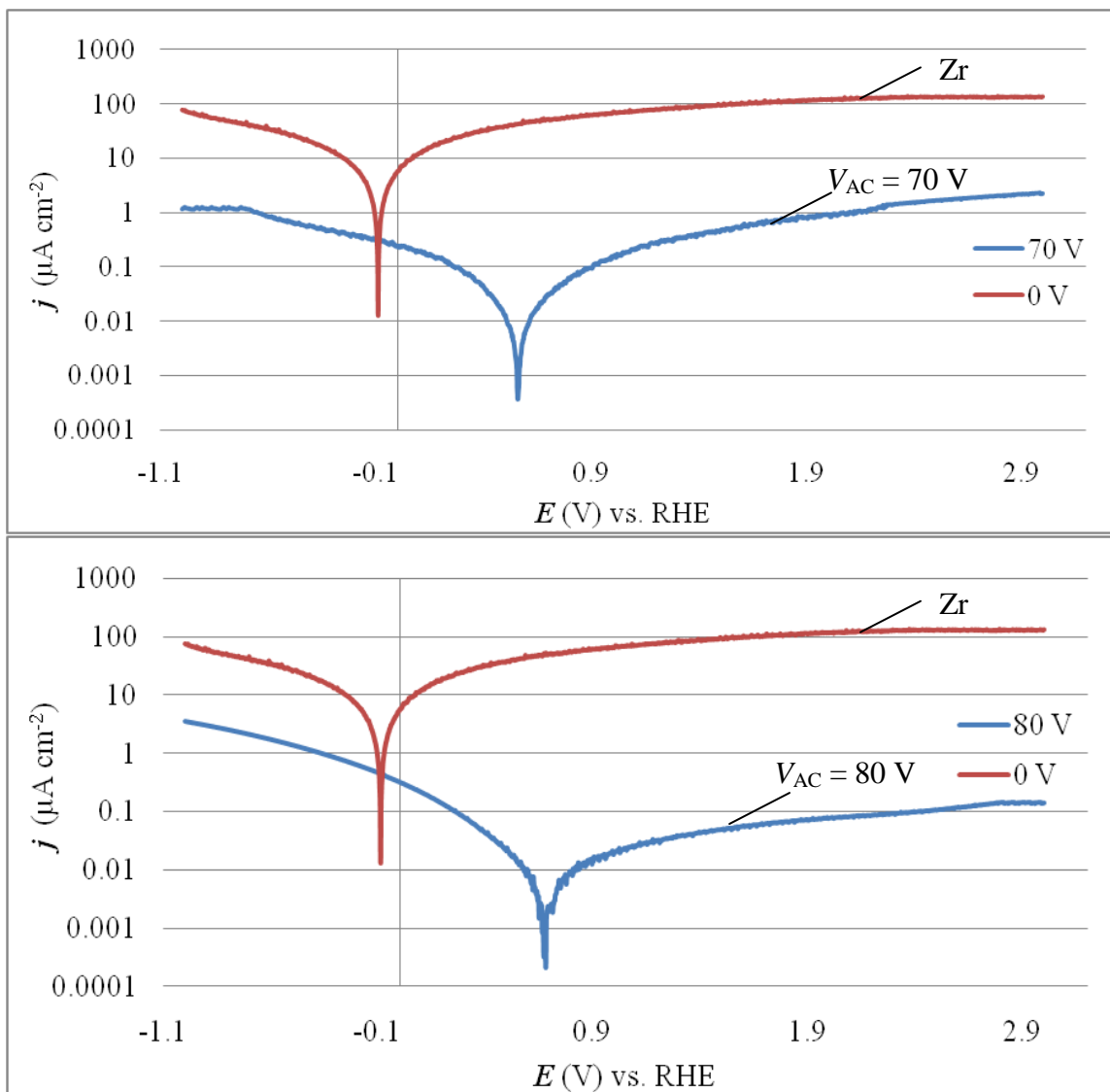
Figure 83. Individual polarization curves (each compared to that of unpassivated Zr) for etched and etched and coloured Zr samples. Coloured samples were prepared at $V_{AC} = 10, 20, ..., 80$ V, and were studied in a 1% aqueous NaCl solution. Passivation was performed in aqueous 10 wt.% Na_2SO_4 electrolyte for 10 s at $T = 298$ K. The scan rate used was 1 mV s^{-1}, and the potential range was from -1 to 3 V.

Figure 83 shows polarization curves for pure Zr and the passive films on Zr formed at V_{AC} = 10, 20, ..., 80 V, respectively. These transients for the passive films reveal the following characteristics: (i) the overall shape of the polarization curves for passive films is similar to that of Zr, (ii) the hydrogen generation region does not exhibit current density variations due to oscillatory behaviour or bubble blocking as was observed with Ti, (iii) the current density values of passive layer polarization curves are lower than that of Zr by up to a factor of 10^3, (iv) the corrosion potential (E_{corr}) values increase with applied AC voltage, indicating that the passive layers are becoming more stable with increasing V_{AC} and thickness. These results are consistent with those for Ti, with the passive layer becoming more stable as V_{AC} is increased. As was observed for Ti, passivation occurs almost immediately, showing no transition into the passive region. This is due to passivation of Zr occurring in open air during seconds of exposure, and thus the samples were passivated prior to being introduced into the electrochemical cell.

The trend observed for both Ti and Zr passive layers is a shift towards less negative values of the corrosion potential (E_{corr}), as the applied AC voltage increases. The results show that, as the passive layers increase in thickness, they become less susceptible to corrosion in this medium and thus increasingly provide more protection of the underlying metal. A less negative corrosion potential value illustrates a more stable passive layer (more noble), as well as further resistance of the metal to corrosion in 1% aqueous NaCl. Both Ti and Zr have shown the same trend towards corrosion resistance with higher V_{AC} and thickness of passive layers. This shows that the defects shown using profilometry and AFM, which become prevalent across the surface at V_{AC} = 60 to 80 V, do not affect the corrosion properties of the passive layer. Thicker layers are still more

protective of the underlying metal, even if their surfaces contain many defects. In order to clearly view the corrosion potential differences, E_{corr} values are graphed to exhibit the trend in Figures 85 and 86.
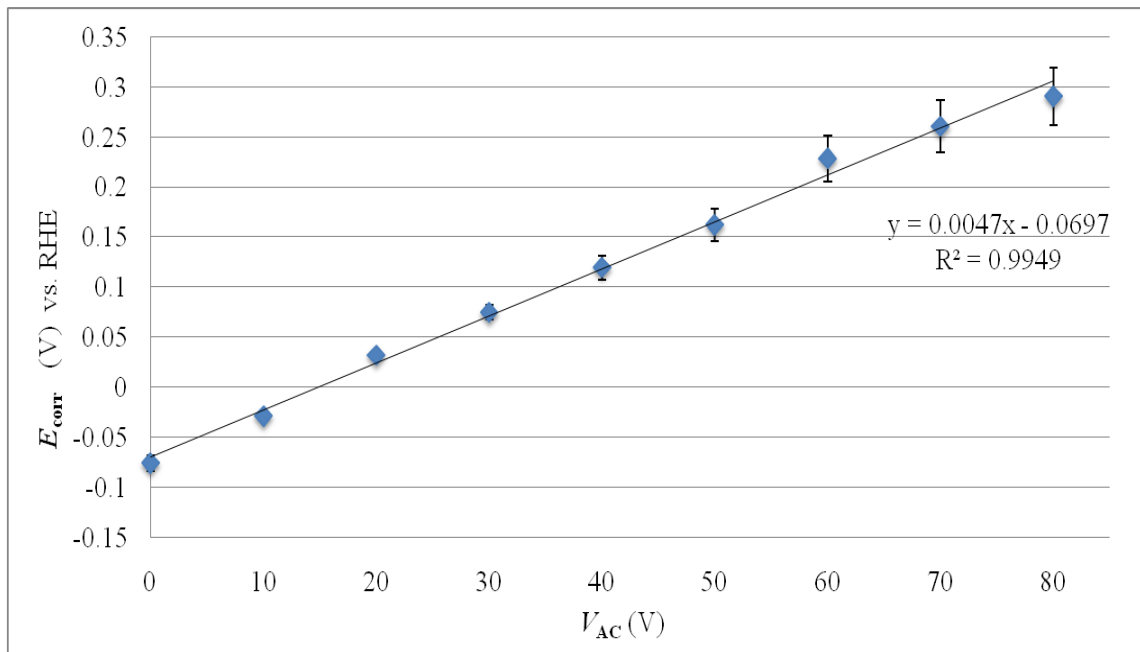
Figure 84. Corrosion potential values for etched, and etched and coloured Ti samples. Coloured samples were prepared at V_{AC} = 10, 20, ..., 80 V, and were studied in a 1% aqueous NaCl solution. Passivation was performed in aqueous 7.5 wt.% NH_4BF_4 electrolyte for 10 s at T = 298 K. The scan rate used was 1 mV s^{-1}, and the potential range was from -1 to 3 V.
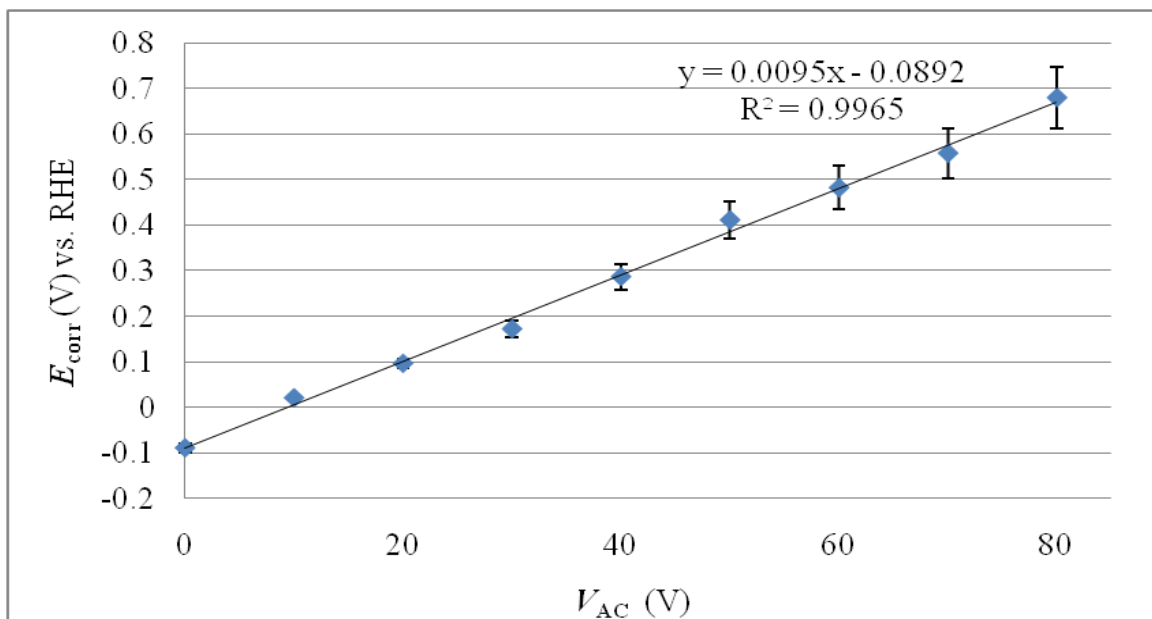
Figure 85. Corrosion potential values for etched, and etched and coloured Zr samples. Coloured samples were prepared at V_{AC} = 10, 20, ..., 80 V, and were studied in a 1% aqueous NaCl solution. Passivation was performed in aqueous 10 wt.% Na_2SO_4 electrolyte for 10 s at T = 298 K. The scan rate used was 1 mV s^{-1}, and the potential range was from -1 to 3 V.

Figures 85 and 86 reveal a linear increase of corrosion potential for both Ti and Zr with V_{AC}. The corrosion potential values for Ti samples varied by 366 mV, from the unpassivated metal to the sample prepared at V_{AC} = 80 V. The corrosion potential values for Zr samples varied by 769 mV, from the unpassivated metal to the sample prepared at V_{AC} = 80 V. The corrosion current density (j_{corr}) values decrease from pure Ti to the passivated samples, where they become relatively constant (Figure 86). This was also true for Zr, where the value of j_{corr} is higher for pure Zr than for the passivated samples (Figure 88). There is a minimum in the corrosion current densities around 10^{-10} A cm^{-2}

177

for Zr, and 10^{-9} A cm^{-2} for Ti. The value of j_{corr} is lower for passivated samples than for the pure metal, showing less material dissolution, and therefore less corrosion in solution with passivation.
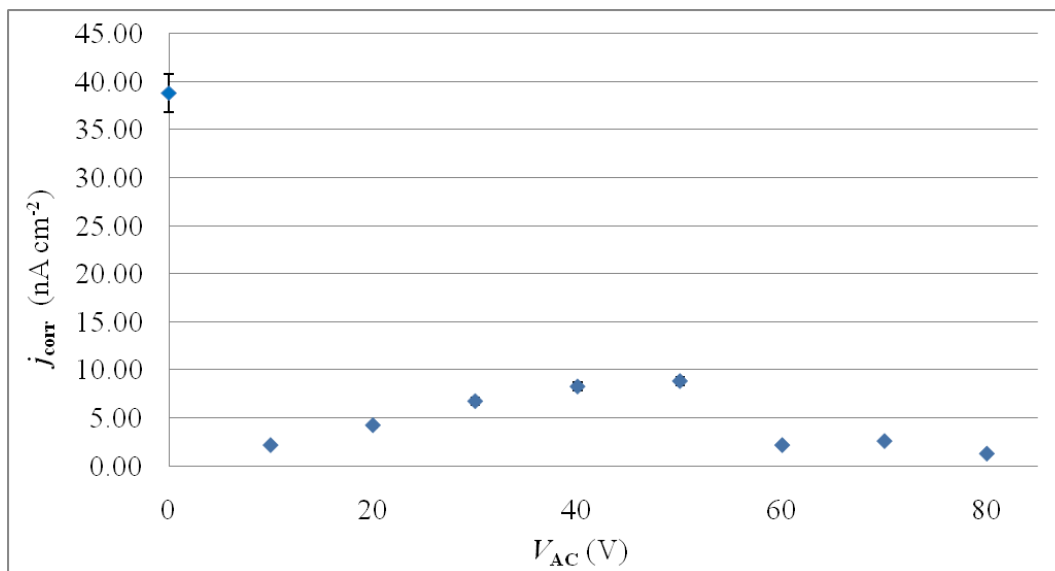
Figure 86. Corrosion current density values for etched, and etched and coloured Ti samples. Coloured samples were prepared at V_{AC} = 10, 20, ..., 80 V, and were studied in a 1% aqueous NaCl solution. Passivation was performed in aqueous 7.5 wt.% NH$_4$BF$_4$ electrolyte for 10 s at T = 298 K. The scan rate used was 1 mV s^{-1}, and the potential range was from -1 to 3 V.
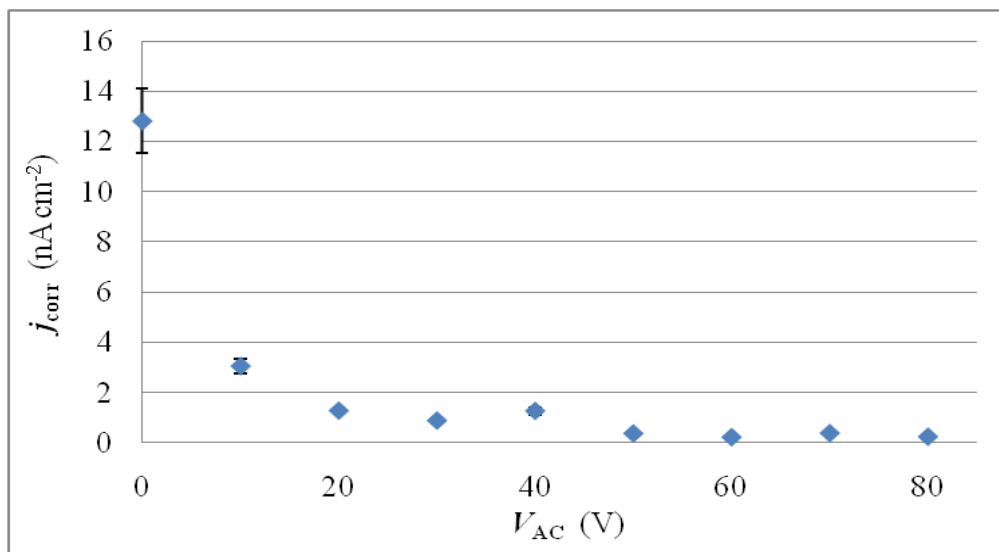
Figure 87. Corrosion current density values for etched, and etched and coloured Zr samples. Coloured samples were prepared at V_{AC} = 10, 20, ..., 80 V, and were studied in a 1% aqueous NaCl solution. Passivation was performed in aqueous 10 wt.% Na_2SO_4 electrolyte for 10 s at T = 298 K. The scan rate used was 1 mV s^{-1}, and the potential range was from -1 to 3 V.

5.0 Conclusions

Titanium and Zr AC polarization results in the formation of passive layers which reveal a wide spectrum of bright, well-defined, and uniform colours. Their colouration, which originates from constructive thin-layer light interference, depends on the applied AC voltage. Important information about these passive layers has been obtained through the use of techniques such as: VLM, NIR-UV-Vis reflectance spectroscopy, profilometry, AFM, SEM, FIB, TEM, EBSD, ICP-MS and electrochemical polarization curve experiments.

Visible light microscopy analyses showed that the coloured passive layers are compact and free of fractures or cracks. This is important for protection of the underlying metal, as, with a fully coating passive layer, there will be reduced contact between the metal and the outside environment. These experiments also revealed the difference in surface structure derived from pre-treatment methods (chemical etching versus mechanical polishing). Although polished samples of Ti and Zr were similar in appearance under VLM, the etched samples showed a distinct difference in surface structure and roughness. Etched Zr samples were much smoother in appearance than the etched Ti samples, which were very rough and uneven due to the difference in grain structure between the two metals, which is dependent upon both nucleation processes as well as their machining properties. Because the process of chemical etching retains the underlying grain structure, clear differences between Ti and Zr grains can be observed in the etched samples. Mechanical polishing, however, obtains a mirror-like surface through abrasion, thus not revealing underlying differences between the two metals.

There were also high-resolution VLM experiments performed at Zeiss application laboratories in Oberkochen, Germany. These experiments employed a high-resolution VLM in order to study etched, and etched and coloured Zr samples, revealing the colouration of their grains. These grains were differently coloured because of their different surface orientations as a result of a variation in their growth rates. Thus, varied granular growth rates lead to different grain thicknesses; which result in different grain colours. The grain colours were representative of the overall appearance of the samples seen by the naked eye. These images also revealed pores in samples prepared at $V_{AC} = 60$

to 80 V, which became more prevalent across the surface with higher applied AC voltage, but did not appear to reach the underlying metal in depth.

From NIR-UV-Vis reflectance results, two distinct trends became apparent: (i) the regions of high reflectance intensity and their corresponding wavelength values were consistent with the surface colouration observed using VLM experiments, and (ii) there was a red-shift as the applied AC voltage was increased, where waves were reappearing in the UV region as soon as they became depleted beyond the IR region. The wave pattern was thought to be due to thin film interference reinforcing and cancelling certain wavelengths as the oxide layer became thicker. [42] There was also a difference between the R intensities overall for etched and polished Ti, with the mirror-like polished samples being much more reflective than rough etched samples. In contrast, etched Zr samples were smooth and almost mirror-like in sheen, and had similar intensities of R to the polished Zr samples. As a result, Zr and Ti showed different trends between the colourations of their etched and polished samples. Because Ti has two oxide layers, while Zr only has one, it is possible that the passive layer thicknesses on Ti are more consistent in formation, even with different surface pre-treatments. Thus, colourations caused by iridescence would be the same for polished and etched Ti samples prepared at the same V_{AC}.

Profilometry was employed for roughness measurements and surface morphology mapping, which showed that mechanical polishing created a contoured, but smooth surface due to uneven applied pressure. The roughness values were higher overall for the samples prepared at V_{AC} = 60, 70, and 80 V due to the surface pores present, which appeared to cluster together to become larger with higher applied AC voltage. These

pores were previously observed using VLM. An overall greater value of roughness was observed with increased V_{AC}, a trend which was also observed by Zhao.[26]

AFM was able to explore, on a smaller scale, the surface defects observed through VLM and profilometry experiments. These defects would most likely be derived from localized electrochemical breakdown.[32,33] The pores were confirmed to appear on the surfaces of samples prepared at V_{AC} = 60 to 80 V, and their dimensions were explored. Images taken using AFM showed that the pores became larger with higher applied AC voltage. Although porosity is not an objective of this project, the results show that, if needed, porosity could be introduced in a controlled manner. This would be desirable for medical and dental implant fabrication, as bone tissue adhesion requires uneven surface structures and pores for cells to osseointegrate. Roughness measurements taken using AFM confirmed the trends measured by profilometry, where roughness values increased with applied AC voltage. This trend was observed by Zhao,[26] as well as by Lausmaa.[81] Since rougher surfaces have been proven to enable implant osseointegration, the ideal pre-treatment for implant materials would be chemical etching, followed by AC passivation at a voltage between V_{AC} = 60 and 80 V.

The thicknesses of etched Zr samples were measured using SEM and FIB, and found to increase with V_{AC}. Thus, the wave pattern of incident light changes as it passes through the passive layers, depending on their thicknesses. Thicknesses of etched and coloured Zr passive layers varied from 51 nm (V_{AC} = 10 V) to 264 nm (V_{AC} = 80 V). TEM experiments were also performed on the etched Zr sample prepared at V_{AC} = 80 V, and found a crystalline appearance in the structure of the passive layer on Zr, which was confirmed using EBSD experiments for analysis of the crystal structure.

Inductively coupled plasma mass spectrometry was employed to perform experiments on the corrosion-induced metallic dissolution into solution of Ti and Zr samples. Overall, less dissolution was observed as the applied AC voltage of passive layers increased. There was also less dissolution for etched Ti as compared to polished Ti, as expected because chemical etching retains the underlying surface structure. However, etched Zr was found to dissolve more into solution than polished samples. Archibald and Leach discovered that anodic oxides formed on fluoride-etched Zr developed large internal stresses.[82] These results confirm the corrosive dissolution of etched Zr into solution, the HF etchant component weakening the overall oxide structure.

The defects found using VLM, AFM and profilometry did not change the corrosion resistance of the passive layer. Passive layers became more resistant to corrosion with higher V_{AC}, and therefore with increased passive layer thickness. Electrochemical polarization curve experiments, performed in order to measure the corrosion resistance of passive layers on Ti and Zr, revealed similar results to ICP-MS, with the passive layers becoming more stable and resistant to corrosion with increased V_{AC} and therefore thickness.

Based on these results, it can be concluded that AC passivation of Ti and Zr provides a unique method of colouration and protection of the underlying metal. This method would be beneficial for use in medical and dental implant manufacture since the passive layers can be controlled in their roughness, porosity and corrosion properties, as well as in automotive, marine, aerospace and many other industries where colouration and resistance to saline-based corrosion are desired.

6.0 Works Cited

1. Delplancke, J. L.; Degrez, M.; Fontana, A.; Winand, R. Self-colour anodizing of titanium. **1982,** *16* (2), 153-162.

2. Winanda, R.; Delplanckea, J. L. Galvanostatic anodization of titanium—II. Reactions efficiencies and electrochemical behaviour model. **1988,** *33* (11), 1551-1559.

3. Zhao, B.; Jerkiewicz, G. Electrochemically formed passive layers on titanium - preparation and biocompatibility assessment in Hank's balanced salt solution. **2006,** *84,* 1132-1145.

4. Jerkiewicz, G.; Strzelecki, H.; Wieckowski, A. A New Procedure of Formation of Multicolour Passive Films on Titanium: Compositional Depth Profile Analysis. *Langmuir* **1996,** *12,* 1005-1010.

5. Hrapovic, S.; Luan, B. L.; D'Amours, M.; Vatankhah, G.; Jerkiewicz, G. Morphology, Chemical Composition, and Electrochemical Characteristics of Colored Titanium Passive Layers. **2001,** *17,* 3051-3060.

6. Zhao, B.; Jerkiewicz, G.; Hrapovic, S.; Luan, B. Discovery of Reversible Switching of Coloration of Passive Layers on Titanium. **2008,** *20,* 1877-1880.

7. Donachie, M. J. *Titanium: A Technical Guide;* ASM International: Novelty, 2000.

8. Hammond, C. R. *CRC Handbook of Chemistry and Physics;* Taylor and Francis Group: Boca Raton, 2010-2011.

9. Lohrengel, M. M. Thin anodic oxide layers on aluminum and other valve metals: high field regime. **1993,** *R11,* 243-294.

10. Barksdale, J. *The Encyclopedia of the Chemical Elements: Titanium;* Reinhold Book Corporation: New York, 1968; p 732–738.

11. Emsley, J. Titanium. In *Nature's Building Blocks: An A-Z Guide to the Elements;* Oxford University Press: Oxford, 2001.

12. Lausmaa, J.; Kasemo, B. Surface spectroscopic characterization of titanium implant materials. *Applied Surface Science* **1990,** *44,* 133-146.

13. Binon, P. P.; Weir, D. J.; Marshall, S. J. Surface analysis of an original Branemark implant and three related clones. *International Journal of Oral & Maxillofacial*

Implants **1992,** *7,* 168-174.

14. Hansson, S.; Olefjord, I. Surface analysis of four dental implant system. *International Journal of Oral & Maxillofacial Implants* **1993,** *8,* 32-40.

15. Machnee, C. H.; Wagner, W. C.; Jaarda, M. C.; Lang, B. R. Identification of oxide layers of commercially pure titanium in response to cleaning procedures. *International Journal of Oral & Maxillofacial Implants* **1993,** *8,* 529–533.

16. Codell, M. Chemistry of Titanium. In *Analytical Chemistry of Titanium Metals and Compounds;* Interscience Publishers Inc.: New York, 1979; Vol. 9.

17. Askeland, D. R.; Phulé, P. P. *The Science and Engineering of Materials,* 5th ed.; Nelson: Toronto, 2006.

18. Boyer, R. R. Titanium and Titanium Alloys. In *Materials Properties Handbook;* ASM International, 1994; pp 575-588.

19. Kobayashi, E.; Matsumoto, S.; Yoneyama, T.; Hamanaka, H. Mechanical Properties of the Binary Titanium-Zirconium Alloys and their Potential for Biomedical Materials. *Journal of Biomedical Materials Research* **1995,** *29,* 943.

20. Yau, T. L. *Corrosion and corrosion protection handbook 2nd Ed. – Zirconium;* Marcel Dekker Inc.: USA, 1989.

21. Hayes, E. T. *Zirconium: Its Production and Properties;* United States Government Printing Office: Washington, 1956.

22. Miller, G. L. *Metallurgy of the Rarer Metals – 2 Zirconium;* Butterworths Scientific Publications: London, 1954.

23. Schlechten, A. W. *Rare Metals Handbook;* Reinhold Publishing Corp.: New York, 1954.

24. Meyer, R. E. Rotating Disk Study of the Dissolution of Zirconium in HF-HN03. *Journal of the Electrochemical Society* **1965,** *112,* 684-688.

25. Mogoda, A. S. Electrochemical Behaviour of Zirconium and the Anodic Oxide Film in Aqueous Solutions Containing Chloride Ions. *Thin Solid Films* **1999,** *357,* 202-207.

26. Zhao, B. *Electrochemical Surface Treatment and Characterization of Titanium-*

Based Biomaterials; PhD Thesis; Queen's University: Kingston, 2007.

27. Atkinson, A. Transport processes during the growth of oxide films at elevated temperature. *Rev. Mod. Phys.* **1985,** *57,* 437–470.

28. Burgers, W. G.; Claasen, A.; Zernicke, I. On the chemical nature of the oxide layers that form at anodic polarization on the metals aluminum, zirconium, titanium and tantalum. *Zeitschrift für Physik A Hadrons and Nuclei* **1932,** *74,* 593-603.

29. Charlesby, A. Ionic currents in thin films of zirconium oxide. *Acta Metallurgica* **1953,** *1,* 340-347.

30. Kalra, K. C.; Singh, K. C.; Singh, M. Electrical breakdown of anodic films on titanium in aqueous electrolytes. *Journal of Electroanalytical Chemistry* **1994,** *371,* 73-78.

31. Masson, J.; Loup, J. P.; Marchenoir, J. C. Study of porous layers formed by anodic oxidation of titanium under high tension. *Thin Film Stud* **1980,** *66* (3), 357-369.

32. Delplancke, J. L.; Winand, R. Galvanostatic Anodization of Titanium- I. Structures and Compositions of the Anodic Films. *Electrochimica Acta* **1988,** *33* (11), 1539-1549.

33. Hollander, L. E.; Castro, P. L. Dielectric Properties of Single-Crystal Nonstoichiometric Rutile (TiO2). *Journal of Applied Physics* **1962,** *33,* 3421.

34. Huber, F. Piezoeffects in p-n Junctions of Semiconducting Titanium Oxide Films. *Applied Physics Letters* **1963,** *2,* 76.

35. James, W. J.; Straumanis, M. E. Titanium. In *Encyclopedia of Electrochemistry of the Elements;* Bard, A. J., Ed.; Marcel Dekker Inc.: New York, 1976; Vol. V, pp 305-386.

36. Heitz, E.; Kreysa, G. *Principles of Electrochemical Engineering;* VCH, 1986.

37. Bolduc, S. Master's Thesis: Coloured Passive Films on Zirconium, Titanium and Alloys: Preparation, Characterization, Applications. **2003**.

38. Light, the Visible Spectrum, 2006. Encyclopedia Brittanica. http://www.britannica.com/EBchecked/topic/340440/light/258410/Electromagnetic-waves-and-the-electromagnetic-spectrum (accessed May 24, 2011).

39. Fairchild, M. *Colour Appearance Models;* Addison-Wesley: Reading, 1998.

40. Nassau, K. *The Physics and Chemistry of Color;* Wiley-Interscience: New York, 1983.

41. Jones, D. A. Principles and Prevention of Corrosion. **1992**.

42. Munro, A. *Master's Thesis: The Application and Characterization of Protective Polymer Layers on Electrochemically Passivated Zirconium and Titanium;* Queen's University: Kingston, 2006.

43. Davis, J. R.; Destefani, J. D.; Frissell, H. J.; Crankovic, G. M. *ASM Handbook,* 9th ed.; ASM International, 1987; Vol. 13.

44. Bass, M.; Van Stryland, E. W.; Williams, D. R.; Wolfe, W. L. *Handbook of Optics Volume 2: Devices, Measurements and Properties;* McGraw Hill Inc.: New York, 1995.

45. Johnson, B. K. *Optics and Optical Instruments;* Dover Publications Inc.: New York, 1960.

46. Williams, D. B.; Carter, C. B. *Transmission Electron Microscopy: A Textbook for Materials Science;* Springer: New York, 2004.

47. Microscope diagram, 2010. Digitals Microscopy. http://www.digitalsmicroscope.com/microscope-diagram/ (accessed Aug 10, 2011).

48. Grant, B. G.; Palmer, J. M. *The Art of Radiometry;* SPIE, 2009.

49. Matsubara, T.; Oishi, T.; Katagiri, A. Determination of Porosity of TiO2 Films from Reflection Spectra. *Journal of the Electrochemical Society* **2002,** *149* (2), C89-C93.

50. Burrows, L.; Kowalski, C.; Valencia, J. *Dektak 8 Advanced Development Profiler Manual;* Veeco Instruments Inc., 2003.

51. Degarmo, E. P.; Black, J. T.; Ronald, A. *Materials and Processes in Manufacturing;* Wiley: Hoboken, 2003.

52. Gewirth, A. A.; LaGraff, J. R. Atomic Force Microscopy. In *The Handbook of Surface Imaging and Visualization;* CRC Press, Inc.: Santa Barbara, 1995.

53. Butt, H. J. Measuring Electrostatic, Van der Waals, and Hydration Forces in Electrolyte Solutions with an Atomic Force Microscope. **1991,** *60,* 1438-1444.

54. Butt, H. J. Electrostatic Interaction in Atomic Force Microscopy. **1991,** *60,* 777-785.

55. Hartmann, U. Intermolecular and Surface Forces in Noncontact Scanning Force Microscopy. **1992,** *42-44,* 59-65.

56. Tortonese, M.; Barrett, R. C.; Quate, C. F. Atomic Resolution with an Atomic Force Microscope Using Piezoresistive Detection. **1993,** *62,* 834-836.

57. Kowalski, C.; Burrows, L.; Fitzgerald, C.; Thornton, J. *SPM Training Notebook;* Veeco Inc., 2003.

58. Yao, N. Focused Ion Beam: A Multifunctional Tool for Nanotechnology. In *I. Optical Microscopy, Scanning Probe Microscopy, Ion Microscopy and Nanofabrication*.

59. Stevie, F. A.; Giannuzzi, L. A.; Prenitzer, B. I. The Focused Ion Beam Instrument. In *Introduction to Focused Ion Beams;* Springer: Orlando/Raleigh, 2005.

60. Hubbard, A. T. *THe Handbook of Surface Imaging and Visualization;* CRC Press: Salem, 1995.

61. Dunlap, M.; Adaskaveg, J. E. *Introduction to the Scanning Electron Microscope: Theory, Practice & Procedures;* Facility for Advanced Instrumentation, UC Davis: Merced, 1997.

62. Giannuzzi, L. A.; Prenitzer, B. I.; Kempshall, B. W. Ion-Solid Interactions. In *Introduction to Focused Ion Beams;* Springer: New York, 2005.

63. Utlaut, M. Focused Ion Beams. In *Handbook of Charged Particle Optics;* Taylor and Francis Group, 2009.

64. Orloff, J.; Utlaut, M.; Swanson, L. *High Resolution Focused Ion Beams: FIB and its Applications;* Kluwer Academic/Plenum Publishers: New York, 2003.

65. Ishitani, T.; Tsuboi, H.; Yaguchi, T.; Koike, H. Transmission Electron Microscope Sample Preparation Using a Focused Ion Beam. *Journal of Electron Microscopy* **1994,** *43,* 322-326.

66. Scanning Electron Microscopy. In *Handbook of Analytical Methods for Materials;* Hanke, L. D., Ed.; Materials Evaluation and Engineering Inc.: Plymouth, 2009.

67. Humpherys, F. J. Review Grain and Subgrain Characterization by Electron Backscatter Diffraction. *Journal of Materials Science* **2001,** *3* (6), 3833-3854.

68. Humphreys, F. J. Characterisation of Fine-Scale Microstructures by Electron Backscatter Diffraction (EBSD). **2004,** *51,* 771-776.

69. Manning, T.; Grow, W. Inductively Coupled Plasma - Atomic Emission Spectroscopy. http://www.mrl.ucsb.edu/mrl/centralfacilities/chemistry/icp.pdf (accessed May 29, 2010).

70. Shoesmith, D. W. *ASM Handbook,* 9th ed.; ASM International, 1986; Vol. 13, pp 29-36.

71. Standard practice for conventions applicable to electrochemical measurements in corrosion testing. In *Annual Book of ASTM Standards,* 3rd ed.; American Society for Testing and Materials: Philadelphia, 1985; Vol. G.

72. Standard Practice for Conventions Applicable to Electrochemical Measurements in Corrosion Testing. In *Annual Book of ASTM Standards;* American Society for Testing and Materials: Philadelphia, 1985; Vol. G 3.

73. Dean, S. W. Electrochemical Methods of Corrosion Testing. *Symposium of Electrochemical Techniques for Corrosion,* 1977, 52-60.

74. Greff, R.; Peat, R.; Peter, L. M.; Robinson, J.; Pletcher, D. *Instrumental Methods in Electrochemistry;* Albion/Horwood Publishing Ltd., 2002.

75. Anisimov, M. P. Nucleation: theory and experiment. *Russian Chemical Reviews* **2003,** *72* (7), 591-628.

76. di Quarto, F.; Doblhofer, K.; Gerischer, H. Instability of Anodically Formed TiO2 Layers. *Electrochimica Acta* **1978,** *23,* 195-201.

77. Sul, Y.-T.; Johansson, C. B.; Petronis, S.; Krozer, A.; Jeong, Y.; Wennerberg, A.; Albrektsson, T. Characteristics of the Surface Oxides on Turned and Electrochemically Oxidized Pure Titanium Implants up to Dielectric Breakdown: The Oxide Thickness, Micropore Configurations, Surface Roughness, Crystal Structure and Chemical Composition. *Biomaterials* **2002,** *23,* 491-501.

78. Hrapovic, S. Coloured Titanium Passive Films: preparation, characterization, applications and surface modification. **2001,** *17,* 3051-3060.

79. Simmons, C. A.; Pilliar, R. M.; Valiquette, N. Osseointegration of sintered porous-surfaced and plasma spray–coated implants: An animal model study of early postimplantation healing response and mechanical stability. *Journal of Biomedical Materials Research* **1999,** *47* (2), 127-137.

80. Li, D. H.; Ferguson, S. J.; Beutler, T.; Cochran, D. L.; Sittig, C.; Hirt, H. P.; Buser, D. Biomechanical comparison of the sandblasted and acid-etched and the machined and acid-etched titanium surface for dental implants. *Journal of Biomed. Mater. Res.* **2002,** *60,* 325.

81. Lausmaa, J. Titanium in medicine: material science, surface science, engineering, biological responses and medical application. Brunette, D. M., Tengvall, P., Thomsen, P., Textor, M., Eds.; Springer: New York, 2001.

82. Archibald, L. C.; Leach, J. S. L. The anodic oxidation of zirconium—I. growth stresses in anodic ZrO2 films. *Electrochimica Acta* **1977,** *22,* 15.

83. Mogoda, A. S. Influence of Some Parameters on Passivation of Zirconium and the Stability of the Anodic Oxide Film. *Corrosion* **1999,** *55* (9), 877-882.

84. Hackerman, N.; Cecil, O. B. The Electrochemical Polarization of Zirconium in Neutral Salt Solutions. *Journal of the Electrochemical Society* **1954,** *101,* 419.

85. Maraghini, M.; Adams, G. B.; Van Rysselberghe, P. Studies on the Anodic Polarization of Zirconium and Zirconium Alloys. *Journal of the Electrochemical Society* **1955,** *101,* 400-409.

86. Tyndall National Institute. http://www.tyndall.ie/research/nanotechnology-group/facilities_ntg/lithography_fab.html (accessed Nov 02, 2009).

87. Taylor, G. Disintegration of Water Drops in an Electric Field. *Proceedings of the Royal Society of London. Series A, Mathematical and Physical Sciences* **1964,** *280* (1382), 383-397.

88. Chapter 2 - Film Characterisation Techniques. http://www.chm.bris.ac.uk/pt/diamond/stuthesis/chapter2.htm (accessed Nov 02, 2009).

89. Nastasi, M.; Mayer, J. W.; Hirvonen, J. K. Ion Solid Interactions: Fundamentals

and Applications. *Cambridge University Press,* 1996.

90. Ziegler, J. F.; Biersack, J. P.; Littmark, U. The Stopping Range of Ions in Solids. **1985**.

91. Townsend, P. D.; Kelly, R.; Hartley, N. E. Ion Implantation, Sputtering and Their Applications. **1976,** 137-142.

92. Andersen, H. H.; Bay, H. L. Sputtering Yield Measurements. In *Sputtering by Particle Bombardment I: Physical Sputtering of Single-Element Solids;* Springer: Berlin, 1981.

93. Behrisch, R. Introduction and Overview. In *Sputtering by Particle Bombardment I: Physical Sputtering of Single-Element Solids;* Springer: Berlin, 1981.

94. Sigmund, P. Sputtering by Ion Bombardment: Theoretical Concepts. In *Sputtering by Particle Bombardment I: Physical Sputtering of Single-Element Solids;* Springer: Berlin, 1981.

95. Adams, D. P.; Vasile, M. J.; Benavides, G.; Campbell, A. N. Micromilling of Metal Alloys with Focused Ion Beam-Fabricated Tools. **2001,** *25,* 107-113.

96. Davis, R. B. Preparation of samples for mechanical property testing using the FIB workstation. **1997,** *25,* 511-515.

97. Wittke, J. Stigmators and Scanning Coils, 1997-2003. North Arizona University. http://www4.nau.edu/microanalysis/microprobe/Column-Stigmators.html (accessed Nov 10, 2009).

98. Zier, M. Focused Ion Beam, 2007. Forschungszentrum Dresden-Rossendorf. http://www.fzd.de/DB/Cms?pOid=23615&pNid=0 (accessed Nov 10, 2009).

99. Young, R. J.; Moore, M. V. Dual-Beam (FIB-SEM) systems: Techniques and Automated Applications. In *Introduction to Focused Ion Beams;* Springer: New York, 2005.

100. Phaneuf, M. W. Applications of focused ion beam microscopy to materials science. **1999,** *30,* 277-288.

101. Benninghoven, A. **1976,** *6,* 291.

102. Leibl, H. **1967,** *38,* 5277.

103. Kuroda, K.; Takahashi, M.; Kato, T.; Tsuji, S.; Saka, H. Application of focused ion beam milling to cross-sectional TEM specimen preparation of industrial materials including heterointerfaces. *319,* 92-96.

104. Gianuzzi, L. A.; Stevie, F. A. A Review of Focused Ion Beam Milling Techniques for TEM Specimen Preparation. **1999,** *30,* 197-204.

105. Martel, L. M. V.; Taylor, G. J. Ion Microprobe. www.psrd.hawaii.edu/Feb06/PSRD-ion_microprobe.html.

106. Jerkiewicz, G. Coloured Passive Layer on Ti: Preparation, Morphology Analysis by OM and SEM, Electrochemical Characteristics, and Colour-Switching Effect. Benediktbeuern, 2009.

107. Lindhard, J.; Scharff, M.; Schiott, H. E. Range Concepts on Heavy Ion Ranges. **1963,** *33* (14), 15.

108. Notte, J.; Ward, B. Sample interaction and contrast mechanisms of the helium ion microscope. **2006,** *28* (13).

109. Smith, N. S. . S. W. P. . K. S. M. . K. D. E. . T. P. P. . S. O. . A. A. . B. R. W. High brightness inductively coupled plasma source for high current focused. **2006,** *B24* (6), 2902–2906.

110. Foles, S.; Claybourn, M.; Johansson, J. Raman Spectroscopy: A Strategic Tool in the Process Analytical Technology Toolbox. **2010**.

111. Pelletier, M. J. *Analytical applications of Raman spectroscopy;* Blackwell Science Ltd.: Oxford, 1999.

112. Bohning, J. J.; Choudhury, M.; Misra, T. N. The Raman Effect, 1998. American Chemical Society. [http://portal.acs.org/portal/acs/corg/content?_nfpb=true&_pageLabel=PP_ARTIC LEMAIN&node_id=924&content_id=WPCP_007605&use_sec=true&sec_url_var =region1&__uuid=78cfa52a-9ebc-4372-9779-8e3481629e78](http://portal.acs.org/portal/acs/corg/content?_nfpb=true&_pageLabel=PP_ARTICLEMAIN&node_id=924&content_id=WPCP_007605&use_sec=true&sec_url_var=region1&__uuid=78cfa52a-9ebc-4372-9779-8e3481629e78) (accessed March 13, 2011).

113. *A Review of Techniques for Electrochemical Analysis;* Princeton Applied Research: Princeton.

114. McAleer, J. F.; Peter, L. M. Instability of Anodic Oxide Films on Titanium. *Journal of the Electrochemical Society* **1982,** *129* (6), 1252-1260.

115. Laser, D.; Yaniv, M.; Gottesfeld, S. Electrochemical and Optical Properties of Thin Oxide Layers Formed on Fresh Titanium Surfaces in Acid Solutions. *Journal of the Electrochemical Society* **1978,** *125* (3), 358-365.

116. Schutz, R. W.; Covington, L. C. Effect of Oxide Films on the Corrosion Resistance of Titanium. *Corrosion* **1981,** *37,* 585-591.

117. Briars, J. D. Interpretation of Oxidation Colours on Titanium. *Optik* **1983,** *63* (4), 341-348.

118. Delplancke, J. L.; Winand, R. Galvanostatic Anodization of Titanium- II. Reactions Efficiencies and Electrochemical Behaviour Model. *Electrochimica Acta* **1988,** *33* (11), 1551-1559.

119. Huang, Y. Z.; Blackwood, D. J. Characterization of Titanium Oxide Film Grown in 0.9% NaCl at Different Sweep Rates. *Electrochimica Acta* **2005,** *51* (6), 1099-1107.

120. Lausmaa, J.; Kasemo, B.; Mattsson, H.; Odelius, H. Multi-technique Surface Characterization of Oxide Films on Electropolished and Anodically Oxidized Titanium. *Applied Surface Science* **1990,** *45,* 189-200.

121. da Fonseca, C.; Boudin, S.; da Cunha Belo, M. Characterization of Titanium Passivation Films by In-Situ AC Impedance Measurements and XPS Analysis. *Journal of Electroanalytical Chemistry* **1994,** *379,* 173-180.

122. Blackwood, D. J.; Chooi, S. K. M. Stability of Protective Oxide Films Formed on a Porous Titanium. *Corrosion Science* **2002,** *44,* 395-405.

123. Ektessabi, A. M. Ion Beam Assisted Sputter Deposition of Thin Oxide Films. *Surface and Coatings Technology* **1994,** *68/69,* 208-216.

124. Verhoeven, J. D. *Scanning Electron Microscopy;* Iowa State University.

125. Cai, Z.; Shafer, T.; Watanabe, I.; Nunn, M.; Okabe, T. Electrochemical Characterization of Cast Titanium Alloys. *Biomaterials* **2003,** *24,* 213-218.

126. Wisbey, A.; Gregson, P. J.; Peter, L. M.; Tuke, M. Effect of Surface Treatment on the Dissolution of Titanium-Based Implant Materials. *Biomaterials* **1991,** *12,* 470-473.

127. Oliveira, N. T. C.; Biaggio, S. R.; Rocha-Filho, R. C.; Bocchi, N. Studies on the

Stability of Anodic Oxides on Zirconium Biocompatible Alloys. *Journal of the Brazilian Chemical Society* **2002,** *13* (4), 463-468.

128. Petit, J. A.; Chatainier, G.; Dabosi, F. Inhibitors for the Corrosion of Reactive Metals: Titanium and Zirconium and Their Alloys in Acid Media. *Corrosion Science* **1981,** *21* (4), 279-299.

129. Lipp, S.; Frey, L.; Lehrer, C.; Demm, E.; Pauthner, S.; Ryssel, H. A Comparison of Focused Ion Beam and Electron Beam Induced Deposition Processes. *Microelectron. Reliab.* **1996,** *36* (11/12), 1779-1782.

130. Berlin, B.; Kay, P. *Basic color terms : their universality and evolution;* Center for the Study of Language and Information: Stanford, 1999.